Redox Signaling in Eukaryotic DNA Replication and Repair

Thesis by

Elizabeth O'Brien

In Partial Fulfillment of the Requirements
for the Degree of
Doctor of Philosophy in Chemistry

California Institute of Technology
Pasadena, CA
2018
(Defended June 1, 2018)

Elizabeth O’Brien
ORCID: 0000-0003-2889-1688

Acknowledgements

There are many people who have contributed to my thesis in some way over the past six years, as evidenced by the length of this segment. First and foremost, however, I must thank my advisor, Professor Jackie Barton, for all that she has done to make me a stronger scientist and a stronger person. Jackie, you always say our experiments take courage. Webster's dictionary defines courage as 'mental or moral strength to venture, persevere, and withstand danger, fear, or difficulty' and you have pulled more scientific courage out of me than I knew I had. We have been through a lot in the last six years, and you have always given me honest, kind and constructive advice. My time in your lab has changed me for the better. I will take your scientific and personal example with me to Berkeley and beyond.

I would like to thank my committee chair, Professor Harry Gray, for always bringing insight and levity to my committee meetings. You, along with Professors Doug Rees and Dave Tirrell, have given me honest and constructive feedback and truly made my ideas better. Not only do I learn a lot every time we meet, but I genuinely enjoy the conversation. I could not ask for a better committee!

Maureen Renta, Elisha Okawa, and Elizabeth Garcia have all kept the non-science elements of our group running during my time here, and for that I will always appreciate them. Thank you Elizabeth for the pep talks, computer advice, and sharing of the best cat and dog videos the internet has to offer. You have been a great help and a great friend over the past year; you have helped me power through the end of my degree and actually have a pretty good time while I do it.

Several Caltech staff members have been helpful in solving problems ranging from scientific to administrative. I would like to thank division coordinators Agnes Tong and Alison Ross, who have always kept an open door when I needed to pop in and ask a question. Joe Drew was a huge help every time we needed to renovate areas of the lab for a new instrument, and he continues to help keep the Signaling Center seminars running smoothly. Joe's help has contributed to me successfully juggling research and non-research responsibilities; I am sure this is true for many other students in the division.

I would also like to thank Dr. Paul Oyala and Dr. Angelo DiBilio for training me on the EPR instrumentation and keeping these machines running while we do experiments. Dr. Mona Shahgholi has always kept the extensive mass spectrometry facility running smoothly. The staff at the Kavli Nanoscience Institute, including Dr. Guy DeRose, Melissa Melendes, Steven Martinez, Bert Mendoza, and Alex Wertheim have all trained or helped me at some point during my time in the clean room. Their competence and dedication allows us to have the resources to fabricate our multiplexed electrodes, which make a big difference in our research.

I want to thank Professor John Bercaw and Professor Peter Dervan, for whom I was a TA during my time at Caltech. I learned about how to teach both undergraduate and graduate level chemistry from these experiences, and I appreciate the respect both of you show to your TAs and students.

My work at Caltech was possible because of fruitful collaborations with Vanderbilt University and the USC Norris Cancer Center. Professor Walter Chazin at Vanderbilt University, as well as his team of graduate students and postdocs, has been an incredible source of insight and guidance in the primase work. His postdocs, Matt Thompson and Aaron Ehlinger,

as well as his students Marilyn Holt and Lauren Salay, were instrumental in bringing the human primase story over the finish line. Lauren and Walter have also contributed a great deal to the yeast primase project, with the help of Professor Katherine Friedman and her student Esther Epum. Thank you to everyone at Vanderbilt! Dr. Kevin McDonnell, Dr. Stephen Gruber, and the entire team at USC and the University of Michigan who contributed to the MUTYH story, thank you for working so well with us and contributing to a fantastic piece of work.

I would like to thank Dr. Megan Bergkessel for patiently answering my questions about yeast genetics and growth as I ventured out of my scientific comfort zone. I want to thank Sarah Del Ciello for being a positive and collaborative partner in hosting IOS. I would like to thank my SURF student, Andreea Filip, who was a patient and willing participant in many marathon experiment days.

I have been fortunate to have many amazing labmates during my Ph.D. First, I want to thank Dr. Phil Bartels for showing me the ropes in the clean room, and being a driving force behind the MUTYH project and a handful of book chapters. Thank you Rebekah Silva and Dr. Yingxin Deng for being my other review article partners-in-crime, and great sources for feline internet content. Our postdocs, Edmund, Adela, Levi, Yingxin and Sandra all bring their expertise into our increasingly multidisciplinary lab. Phil, Bekah, Andy, Kelsey, and Stephanie have all been friendly and helpful around the lab consistently, even when things get super busy. Siobhan had been a wonderful deskmate and has done an amazing job taking over the Signaling Center talks. I am grateful for your fantastic attitude and tolerance of my making you watch more pug videos than necessary. Catrina Pheeney, Anna Arnold, and Mike Grodick trained me on various techniques when I first joined the lab, and I am grateful to them. Natalie Muren and I overlapped both in lab and at the (fantastic) Caltech swimming pool, and Natalie continues to be

a great friend and calming source of wisdom. She is kind and genuine person who leads by example. Thank you to all the fantastic Bartonites with whom I overlapped at Caltech!

I want to thank the teachers and professors who first sparked my interest in science. Suzanne Savner-D'Addio was my high school chemistry teacher and is both very knowledgeable and laugh-out-loud funny in her lectures. I still think of her verbal illustrations when trying to communicate about science. Elizabeth Savner, my high school physics teacher, has a kind but no-nonsense style that allowed me and many others to learn difficult concepts. I have no idea where I would be if I was never in their classes. Professor Ivan Dmochowski took me under his wing during my undergraduate years at the University of Pennsylvania. He is a kind and intelligent mentor who gave me the opportunity to do research and believed that I could get into a top-tier graduate school. I definitely would not have applied to Caltech if it were not for Ivan. Thank you so much for believing in me.

I have been lucky to be part of several amazing social groups at Caltech. I will always remember the parties at the 818 S. Lake house fondly. Holidays were always entertaining and creatively celebrated; it was like I never left New Jersey, except the weather was nicer. Team Inspector Gadget is a great group with whom I have enjoyed killing it at trivia over the last year. The Philz Phriday Phriend group was a great way to get in some time each week with wonderful people, and some steps! Finally, the early morning locker room/lunch in the park crew has been a wonderful part of my time at Caltech. You all keep me coming to the gym before the sun rises and make it the only place to start my day.

I have been fortunate to make some amazing friends during my degree. Samuel Ho is a passionate hard worker who is always down to grab an early morning coffee. Dr. Lauren

Chapman was a great buddy for coffee and/or Philadelphia rolls who I can't wait to visit in the Bay Area. Dr. Leanne Chen is my partner in dog petting and death hikes. Dr. JingXin Liang and Dr. Tanvi Ratani were my Sunday dumpling and movie buddies with whom I hope to continue sharing an offbeat sense of humor and love of food. Your friendship over the last six years has meant a lot to me.

Thank you to my interspecies friends, the pugs and manatees of the world. Your photos and videos put a smile on my face even when I am extremely stressed. I am grateful that something so simple can elevate my mood. I hope your species thrive for many centuries to come.

I want to thank my great friends from Jersey, who have remained in my life for over a decade despite the physical distance. Kim Stivers got me out of my bubble to finally go wine tasting in California. Karen Choucrallah and Marie Graboso fill my winter breaks with cool new adventures. Gayatri Desai is my forever On the Border buddy and fellow Doug the Pug enthusiast.

I want to thank the Nieskens family for everything they have done for me over the years. Kristina, you have been the Patrick to my Spongebob since before that cartoon was on the air! You are the sister I never had; being your friend for the last 22 years has been like seeing ten pugs every day. I am inspired by the warmth, creativity, and curiosity you bring to my life. Mrs. Nieskens, thank you for being my 3am ride to the airport and my future pug nanny. You are the first one to take me out to California and have always treated me like your own. Mr. and Mrs. Nieskens, Mila, and Abs, thank you for continuing to welcome me into your home. I love you all very much.

I want to thank my expansive and enthusiastic family for all of their love and support over the past 28 years. My mom is an amazing person who has passed on the desire to dive deep into a topic of interest. You have done more for me than I can imagine or probably deserve, and you have generously tolerated my nonsense for more than two decades. Thank you for being a calm and loving voice of reason and supporting me in all that I do. And putting up with all the silly nicknames we insist on giving you. I love you Shelly! My brother Joe is an intelligent, capable, and supportive person who is pursuing his passion and has always encouraged me to pursue mine. Thank you for always sharing your knowledge and opinions with me; I look forward to seeing what you do in the future. My dad, who passed away during my first year at Caltech, always encouraged me to pursue the most challenging path. Thank you for recognizing that I would be bored and restless doing anything else. My aunts, uncles, and cousins on both sides are always fun to visit. There is never a dull moment or a subpar cocktail. I love you all. To Debbie, Dr. W.P. will continue to work for you. Rest in peace.

Abstract

DNA-mediated charge transport chemistry (DNA CT) offers an intriguing regulatory mechanism in biology, as it is long-range, rapid, and sensitive to mismatches and perturbations to base stacking. DNA-processing enzymes in all three domains of life moreover have been shown to contain [4Fe4S] clusters, commonly redox cofactors. Bacterial [4Fe4S] repair proteins have been shown to signal one another using long-range DNA-mediated charge transport (DNA CT), facilitating the redistribution to damaged genomic DNA in cells. The role of metabolically expensive, [4Fe4S] cluster cofactors in eukaryotic systems, however, was less clear than in prokaryotes.

Here we examine the chemical role of the [4Fe4S] cluster in eukaryotic DNA primase and the human base excision repair glycosylase, MUTYH. The primase cluster functions as a redox switch regulating DNA binding and redox signaling activity in humans and yeast. Yeast moreover require the primase redox switch for viability. Human MUTYH, a bifunctional glycosylase which repairs oxidative DNA lesions, performs DNA-mediated redox signaling, similarly to the bacterial homologue MutY. The MUTYH mutation which destabilizes the [4Fe4S] cluster during redox signaling, C306W, promotes degradation and loss of activity, associated with hereditary colorectal cancer.

To assess the redox role of the human primase [4Fe4S] cluster, we perform anaerobic DNA electrochemistry on the [4Fe4S] domain of human primase (p58C), which independently binds DNA. On DNA-modified Au electrodes, we compare the redox activity of electrochemically oxidized and electrochemically reduced p58C. Oxidized $[4Fe4S]^{3+}$ p58C is electrochemically active, and reduced $[4Fe4S]^{2+}$ p58C state is redox-inert. This redox-driven switch is electrochemically reversible, and is mediated by a triad of conserved tyrosines between the DNA binding interface and [4Fe4S] cluster. Mutation of residues Y309, Y345, and Y347 to phenylalanine causes attenuation of redox switching on DNA. Single-atom mutations in the redox pathway moreover compromise initiation and truncation of primer synthesis but do not affect RNA polymerase activity. We find that primase truncation is gated by DNA CT *in vitro*; a single mismatch in the nascent primer abrogates truncation of primase products. As

primase is tethered to DNA polymerase α, a putative [4Fe4S] enzyme to which primase hands off the RNA-primed template, we propose that DNA-mediated signaling between primase and polymerase α chemically regulates this handoff during the first steps of replication.

Eukaryotic primase must bind both DNA and nucleotide triphosphates (NTPs) in order to convert to active form. Using DNA electrochemistry we show that p58C, and full-length DNA primase, display a robust, semi-reversible NTP-dependent signal on DNA, centered near 150mV vs. NHE. This signal is dependent on the tyrosine redox pathway. The presence of reversible redox activity at a physiological potential when primase is bound to DNA and NTPs suggests that reversible redox switching from the $[4Fe4S]^{2+}$ to the $[4Fe4S]^{3+}$ state is important for the activity of primase during replication.

The cluster serves as a redox switch governing DNA binding in yeast primase, just as in human primase. Mutation of tyrosines 395 and 397 in yeast primase moreover, alters the same electron transfer chemistry as the mutation of their orthologues, Y345 and Y347, respectively, alters in human primase. Although these tyrosines are arranged differently in the yeast and human proteins, they perform the same reaction to affect the switch. The single-atom Y395F mutation causes some sensitivity to chemically induced oxidative stress in yeast, and single-residue mutation Y397L confers lethality in yeast cells. A constellation of tyrosines for protein-DNA electron transfer mediates the redox switch in eukaryotic primases, regulates the affinity for RNA-primed DNA template, and is required for primase function *in vivo*.

We finally characterize a novel mutation in the [4Fe4S] human base excision repair protein, MUTYH, which destabilizes the cluster environment and has pathogenic consequences. The MUTYH C306W mutation alters one of the cysteines coordinating the cluster to tryptophan. This mutation moreover is associated with hereditary colorectal cancer and causes defective DNA binding and enzymatic activity. We perform DNA electrochemistry on WT MUTYH, as

well as C306W and two cancer-associated mutants, Y197C and G396D, which have an unaltered cluster environment. MUTYH variants participate in redox signaling, but C306W is destabilized upon oxidation from the $[4Fe4S]^{2+}$ to the $[4Fe4S]^{3+}$ state during signaling on DNA, leading to degradation to a $[3Fe4S]^{+}$ cluster and loss of DNA binding and activity. A [4Fe4S] human DNA repair enzyme performs redox signaling on DNA; dysregulation of this signaling activity is linked to tumorigenesis.

Published Content and Contributions

O'Brien, E., Silva, R.M.B., Barton, J.K. (2016). Redox Signaling through DNA. In : *Isr. J. Chem.* 56, pp 705-723. doi : 10.1002/ijch.201600022.

Review article with E. O'Brien as first author, text and figures adapted for Chapter 1.

Barton, J.K., Bartels, P.L., Deng, Y., O'Brien, E. (2017). Electrical Probes of DNA-Binding Proteins. *Methods in Enzymology*, Academic Press, 591, pp. 355- 414. doi: 10.1016/bs.mie.2017.03.024.

Chapter, co-authored by E. O'Brien, text adapted for Chapter 1.

O'Brien, E., Holt, M.E., Thompson, M.K., Salay, L.E., Ehlinger, A.C., Chazin, W.J., Barton, J.K. (2017). The [4Fe4S] cluster of human DNA primase functions as a redox switch using DNA charge transport. *Science*, 355(6327), eaag1789. doi: 10.1126/science.aag1789

Research article adapted for Chapter 2. E. O'Brien wrote the manuscript, performed all electrochemistry experiments and analysis, and performed all primase activity experiments and analysis.

List of Figures

Chapter 1

Chapter 2

Chapter 3

Chapter 4

Chapter 5

List of Tables

Chapter 1

Chapter 2

Chapter 3

Chapter 4

Chapter 5

Chapter 1: Chemistry of FeS Proteins in Repair and Replication

Adapted from: O'Brien, E., Silva, R.M.B., Barton, J.K. Redox Signaling through DNA. *Israel J. Chem.*, **2016**, *56*, 705-723.; Barton, J.K., Bartels, P.L., Deng, Y., O'Brien, E. Electrical Probes of DNA-Binding Proteins. *Methods in Enzymology*, **2017**, Academic Press, *591*, 355-414.; O'Brien, E., Silva, R.M.B., Barton, J.K. Chemistry of FeS Proteins in Repair and Replication., *Annu. Rev. Biochem.*, **2018**, draft.

Introduction

Iron sulfur clusters are modular, tunable metal cofactors which often serve as one-electron redox donors and acceptors (*1,2*). These cofactors operate over a wide range of physiological potentials, from approx. -500mV vs. NHE to 300mV vs. NHE. (*3*) One type of iron-sulfur cofactor is the [4Fe4S] cluster, a remarkably tunable cluster which is operable in a range of redox conditions. (**Figure 1.1**) The redox potentials of these clusters vary depending on the environment of the cofactor within a protein, the electrostatic environment, and the solvent exposure of the metal cofactor. (*4*) The [4e4S] clusters moreover are found in proteins across all three domains of life, bacteria, archaea, and eukaryotes, in both cytosolic and membrane-bound proteins. (*1*) These cofactors can generally access three different oxidation states in the cellular environment. The resting state is the $[4Fe4S]^{2+}$ redox state; High potential iron protein (HiPIP)-like [4Fe4S] clusters can be oxidized to the $[4Fe4S]^{3+}$ state and ferredoxin-like [4Fe4S] clusters can be reduced to the $[4Fe4S]^{+}$ state. (*5*) These cubane-like cofactors mediate redox reactions in processes such as nitrogen fixation and respiration (*6,7*), often acting as redox mediators in a chain of metal cofactors within an otherwise insulating protein matrix environment. (*8*)

These metal cofactors likely arose during prebiotic conditions on Earth, when an abundance of ferrous iron and sulfide would have been present in the atmosphere. (*2*) They are generally coordinated by conserved cysteine motifs, and are metabolically expensive to assemble and load into their recipient proteins.(*9-11*) Biogenesis and assembly proteins, chaperone proteins for transport, and in the case of eukaryotes, a targeting complex comprising of three proteins (CIA1, CIA2, and MMS19) (*9-12*) are all required to load the cofactor into its recipient protein.

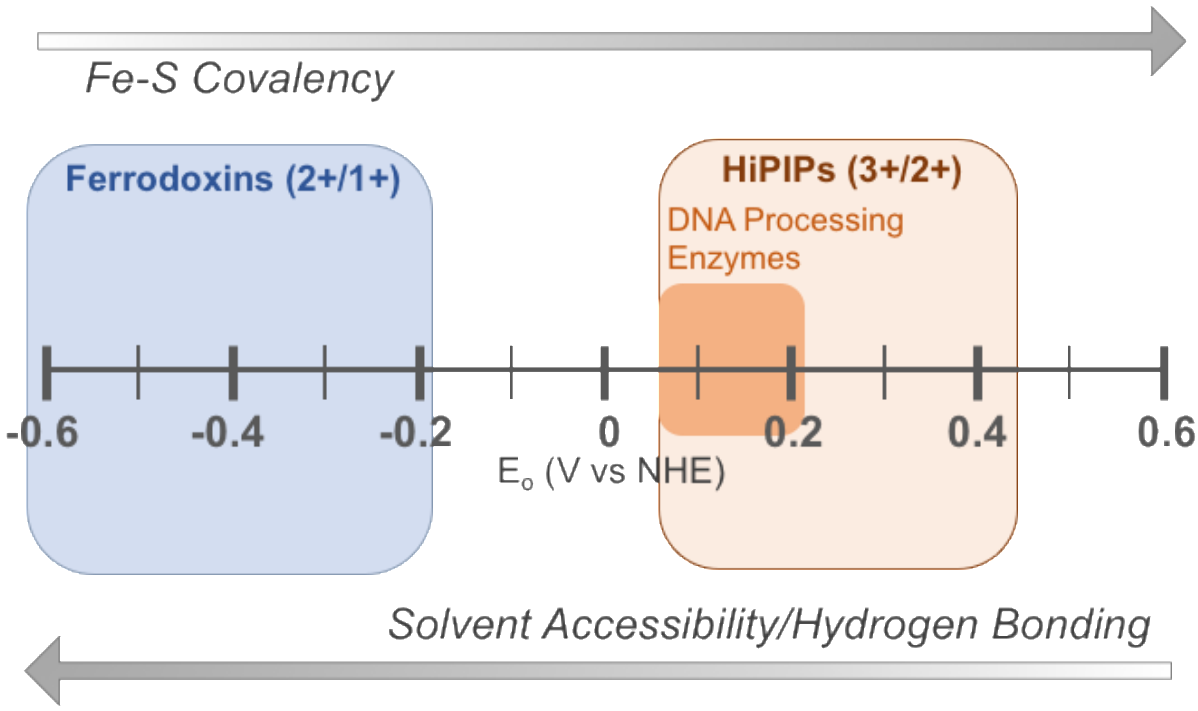

Figure 1.1. The potential of the [4Fe4S] cluster cofactor is tunable over a wide range of physiological redox potential values. Ferredoxins access the $[4Fe4S]^{2+/1+}$ couple, upon reduction from the resting $[4Fe4S]^{2+}$ state. (blue) High potential iron proteins (HiPIPs) access the $[4Fe4S]^{3+/2+}$ couple upon oxidation to the $[4Fe4S]^{3+}$ state from the resting $[4Fe4S]^{2+}$ state. (red) DNA-processing enzymes with [4Fe4S] cofactors have DNA-bound redox potentials which fall within the HiPIP $[4Fe4S]^{3+/2+}$ potential range, at approximately ~65-150mV vs. NHE. The solvent accessibility and hydrogen bonding/electrostatic environment of the cluster all contribute to tuning the redox potential of the cofactor. (*5*)

The general process for iron-sulfur biogenesis and loading is summarized in **Figure 1.2**. In bacteria, the ISC assembly machinery is generally responsible for cofactor generation, though the NIF system has been identified as part of the maturation pathway for the iron-sulfur containing enzyme nitrogenase and the SUF assembly system is implicated in biogenesis during oxidative stress. (*9*) In eukaryotes, the ISC assembly machinery and mitochondrial ISC export system are necessary for biogenesis of the cofactor (*13*) and the cytosolic iron-sulfur assembly (CIA) machinery is required for cluster maturation. (*14,15*) Inorganic sulfur is acquired from a cysteine desulfurase (IscS) in bacteria or exported from the mitochondria by Atm1, (*13,16*) then bound by a cysteine desulfurase (NFS1) in eukaryotes. Cysteine desulfurase activity converts cysteine to alanine, generating a persulfide which is then transported directly or indirectly to scaffold proteins (IscU in bacteria, ISU in eukaryotes) for cluster assembly. Ferrous iron is donated by a protein source, and electron transfer occurs to reduce S^0 to S^{2-} present in iron-sulfur clusters. After the *de novo* biosynthesis of a labile cluster coordinated by scaffold protein cysteine residues, the cluster-containing scaffold associates with chaperone proteins (HscA/HscB in bacteria, HSC20/HSPA9 in eukaryotes). ATP hydrolysis likely drives a conformational change in order to keep the labile cluster shielded during delivery to the recipient protein,(*9,10*) and direct or indirect transfer of the cofactor to the recipient protein occurs.

Although the presence of iron-sulfur cofactors in proteins responsible for nitrogen fixation (*6*) and photosynthesis (*17*) had been demonstrated in previous decades, the surprising discovery of a [4Fe4S] cluster in the Base Excision Repair (BER) glycosylase Endonuclease III (*E. coli*) (*18*) in 1989 led to the investigation of several important questions about the role of these cofactors in DNA repair: Are [4Fe4S] clusters present in other DNA repair enzymes? Do they serve a structural or a biochemical purpose? Perhaps the cluster was simply an ancestral

Prokaryotes

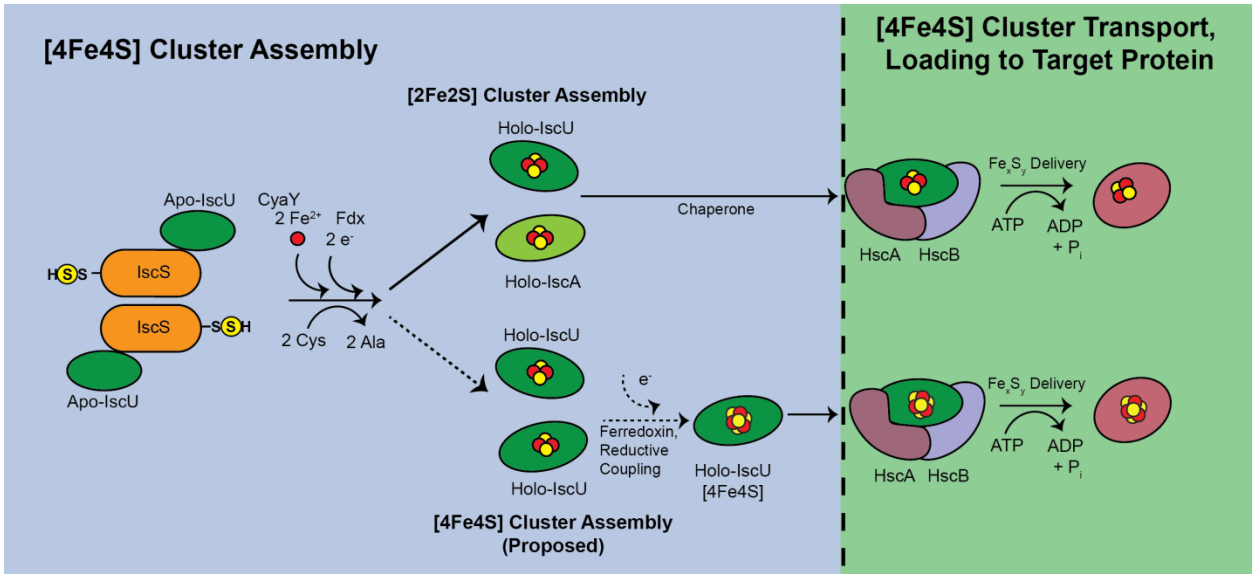

Eukaryotes

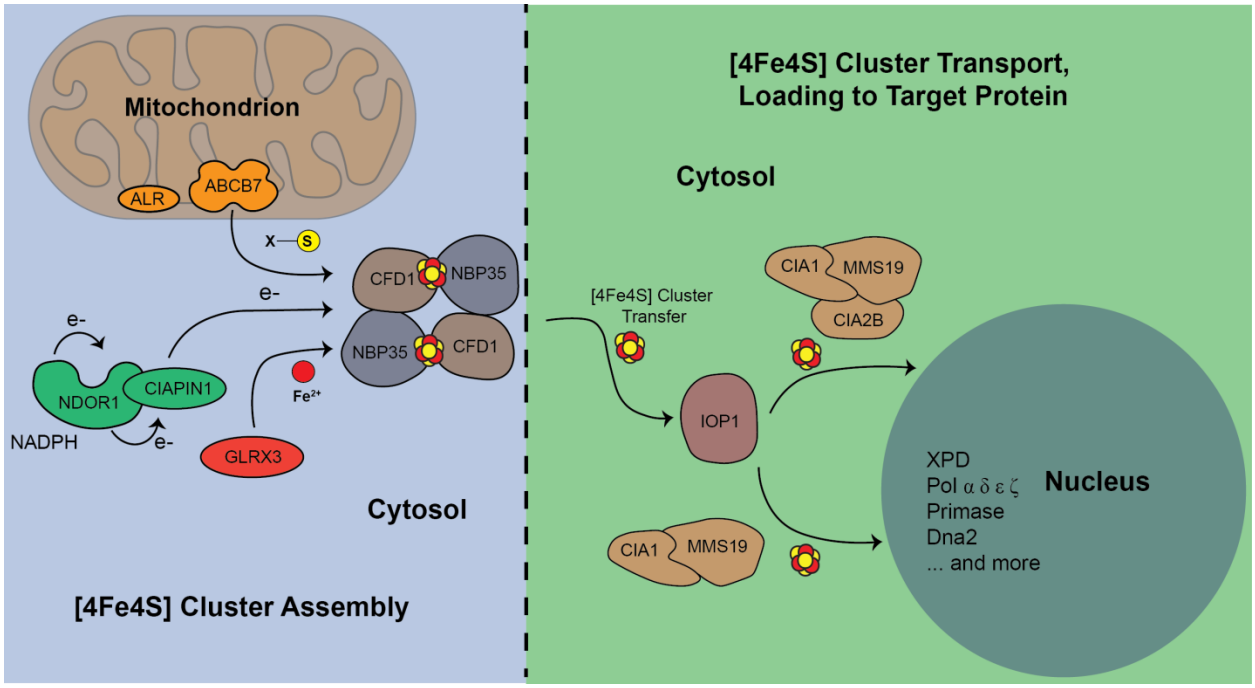

Figure 1.2. [4Fe4S] cluster biogenesis and loading into client prokaryotic (above) and eukaryotic (below) proteins. Scaffold proteins, together with cysteine desulfurases and ferrous iron sources, assemble the cluster and bind chaperone machinery to then transport the cluster to target proteins and machinery responsible for cluster delivery. This process is not identical in bacteria and eukaryotes, however each process requires the concerted action of several specialized proteins and requires significant metabolic expense for the cell. (*9-11*)

relic with no function at all. The discovery of this cluster in Endonuclease III led to the prediction that it was also present in the homologous BER glycosylase MutY, (*19*) which, similar to Endonuclease III, catalyzes the removal of oxidative damage products from genomic DNA. (*20*). The [4Fe4S] cluster would eventually be shown to exist in several BER enzymes, including Endonuclease III, MutY (*21*), and Uracil DNA Glycosylase (UDG) in *A. fulgidus* (*22*). The question of what role the [4Fe4S] clusters played, however, was less straightforward. These cofactors are often associated with biological redox chemistry (*1,2*), yet early studies were unable to demonstrate a redox function.

Studies of DNA repair enzymes containing [4Fe4S] clusters repeatedly demonstrated that the proteins were isolated in an EPR-silent, $[4Fe4S]^{2+}$ oxidation state (*18,22, 23*) and resistant to a change in cluster redox state even upon addition of powerful chemical oxidants and reductants to the protein solution. A Resonance Raman study performed with Endonuclease III moreover showed that the spectroscopic signature of the $(Cys)_4$-ligated [4Fe4S] cluster cofactor was not significantly perturbed upon binding thymine glycol, the native substrate lesion of the enzyme. (*24*) These results led to the early conclusion that the [4Fe4S] cluster played a structural rather than functional role. (*18,24,25*) In the case of MutY, a BER glycosylase with significant homology to Endonuclease III (*19*), however, biochemical evidence challenged the early conclusion of a structural role for the cluster. When Porello and coworkers chemically denatured and refolded MutY from *E. coli*, in the presence and absence of ferrous iron and sulfide ions necessary to form a [4Fe4S] cluster, they observed that the circular dichroism spectra were very similar for cluster-loaded protein and apoprotein, indicating similar structures. (*26*) The cofactor clearly served a purpose other than maintenance of the structural integrity in MutY. A substrate-sensing role was proposed for the cluster in light of this discovery, but a chemical role for the

cofactor still eluded observation. Over the next two decades, more DNA-processing enzymes across several pathways in all kingdoms of life were shown to contain [4Fe4S] cofactors. Table 1.1 summarizes the enzymes across bacteria, eukaryotes, and archaea that contain a [4Fe4S] cofactor. (*27-29*)

Cells invest a significant amount of energy and engage several protein systems to form and load [4Fe4S] clusters into certain DNA-binding proteins. Placing an iron-containing cofactor in a DNA-binding protein could additionally place the bound nucleic acid at risk of damage. A labile ferrous iron from the cofactor could react with hydrogen peroxide in the cellular environment; this Fenton chemistry creates reactive oxygen species (**Figure 1.3**) which could damage nearby DNA bases. Why then does Nature spend the requisite energy incorporating a redox-active inorganic cofactor into a DNA-processing enzyme?

Characterizing the Fundamental Properties of DNA-Mediated Charge Transport

DNA, the native substrate of these [4Fe4S] enzymes, was moreover predicted to have conductive properties. DNA was first predicted to conduct charge in the dry, solid state by Eley and Spivey (*30*). The nitrogenous bases of duplex DNA stacked in an arrangement which resembles stacked graphene sheets, a known conductive material. (**Figure 1.4**) (*30*) In order to assess whether DNA molecules conducted charge in the aqueous, biologically relevant state, new methods of assessing the redox properties of DNA were necessary. Across all of the platforms developed, consistent features of DNA CT are observed: charge transport through duplex DNA is dependent on the coupling of redox donors and acceptors to the π-stacked bases; DNA CT can occur over long molecular distances with shallow distance dependence; and DNA CT is attenuated in the presence of even minor perturbations in π-stacking interactions between the

[4Fe4S] Protein			Pathway	Function
Bacteria	**Archaea**	**Eukarya**		
Endonuclease III		NTHL1, Ntg2	Base Excision Repair	Bifunctional glycosylase, removal of oxidized pyrimidine bases
MutY		MUTYH	Base Excision Repair	Glycosylase, removes adenines mispaired with 8-oxo-guanine
	XPD	XPD, Rad3	Nucleotide Excision Repair	5'-3' helicase, unwinds DNA surrounding TT dimers
DinG			Replication-Coupled Repair	Helicase, unwinds R-loop structures
		FANCJ	Replication-Coupled Repair	5'-3' helicase, generates ssDNA overhangs for homologous recombination
Rtel1			Telomere processing, meiotic crossover	5'-3' helicase, unwinds specialized DNA structures
AddAB			Replication-Coupled Repair	Helicase-nuclease with 5'-3' nuclease activity, generates 3'-ssDNA overhangs
		Dna2	Replication-Coupled Repair	Helicase-nuclease, ssDNA-dependent ATPase, Okazaki fragment processing/double-strand break repair
		DNA Primase	Replication	DNA-dependent RNA polymerase, synthesizes 8-14nt RNA primer on ssDNA
		DNA Polymerase α	Replication	Extends RNA primer by 10-20nt
		DNA Polymerase δ	Replication	Lagging Strand DNA polymerase, 3'-5' exonuclease
		DNA Polymerase ε	Replication	Leading Strand DNA polymerase, 3'-5' exonuclease
		DNA Polymerase ζ	Replication	Translesion synthesis polymerase
	RNA Polymerase	Elp3	Transcription	Template-directed RNA synthesis
Cas4			CRISPR adaptive immunity	5'- 3' exonuclease
PhrB			Photoreactivation DNA repair	Repair of UV-induced cyclopyrimidine dimers

Table 1.1. DNA-processing, [4Fe4S] enzymes are found in all three domains of life (prokaryotes, archaea, and eukaryotes). These enzymes are found in different pathways, such as repair, replication, and transcription, and perform specialized, distinct tasks in cells.

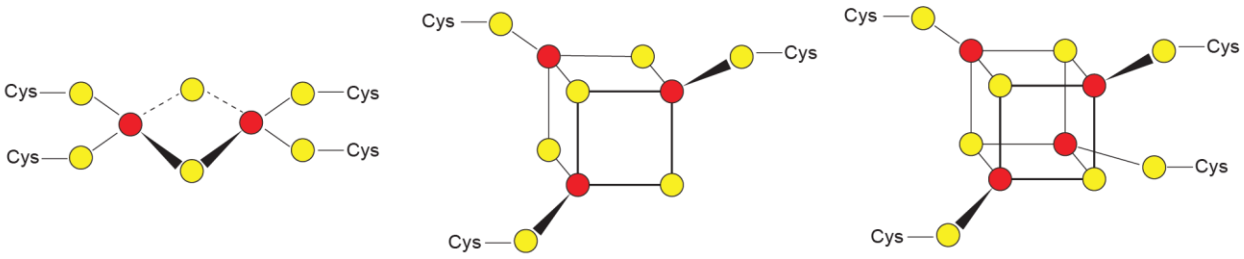

[2Fe2S] [3Fe4S] [4Fe4S]

$$Fe^{2+} + H_2O_2 \longrightarrow Fe^{3+} + OH^- + OH^\bullet \longrightarrow \text{DNA Damage}$$

Figure 1.3. (Above) Structures of common iron-sulfur cofactors, the rhomboid [2Fe2S] cluster, the [3Fe4S] cluster, and the cubane [4Fe4S] cluster. (below) A redox-active cofactor containing iron could potentially react with DNA bases with chemistry such as the Fenton reaction shown, in which oxidation of ferrous iron by hydrogen peroxide creates reactive oxygen species that in turn damage DNA.

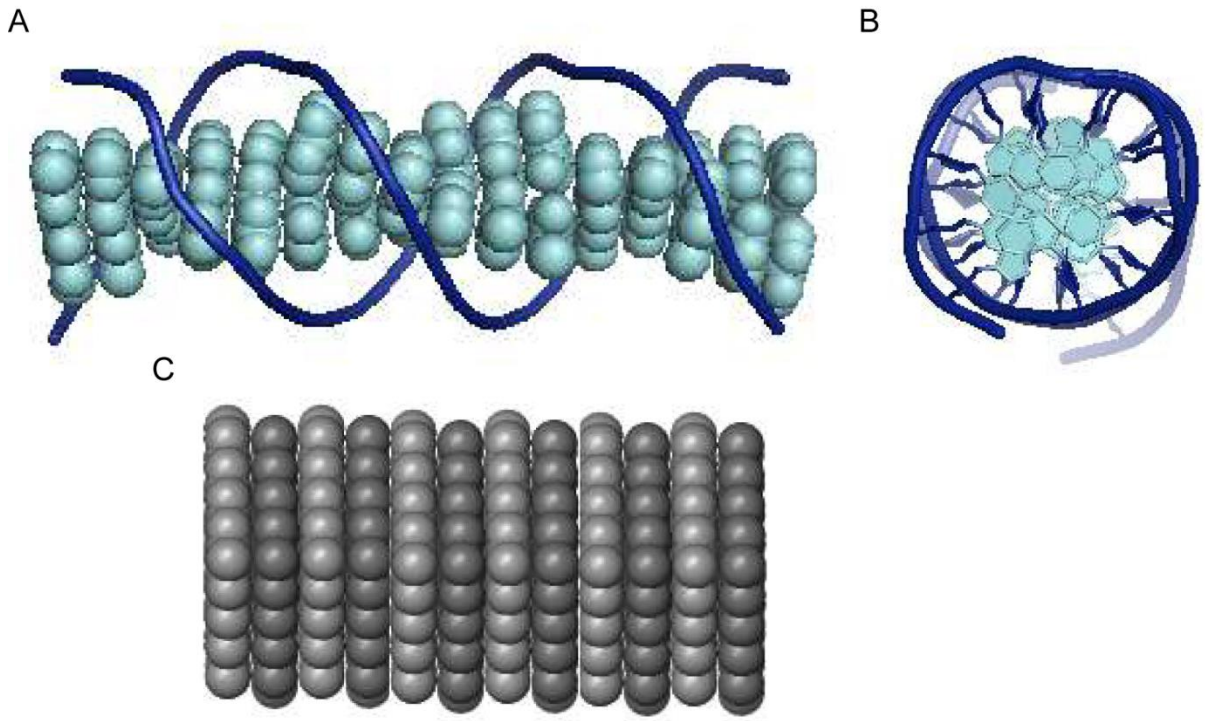

Figure 1.4. The structure of DNA facilitates long-range, rapid electron transfer. A) Side view of DNA. The aromatic bases at the center of the DNA helix are oriented so that the π orbitals of adjacent bases overlap with one another in the duplex DNA structure. This structural property suggests that DNA charge could pass through the π-stacked base pairs of DNA. (*30-34*) B) Front view of aromatic base pairs (light blue) stacked in 3.4Å layers at the center of DNA. C) Crystal structure of graphite a known conductive material. Upon noting the structural similarity between the graphene layers and the DNA base stacking, (*28*) it was predicted that DNA would conduct charge. DNA crystal structure PDB ID **3BSE**.

intervening DNA bases. Photophysical studies using DNA-intercalating redox donors and acceptors were first used to characterize the conductive properties of DNA. Metal complexes $[Ru(phen)_2dppz]$ (phen= 1,10 phenanthroline, dppz = dipyrido[3,2-*a*:2',3'-*c*]-phenazine) and $[Rh(phi)_2(phen)]^{3+}$ (phi = 9,10-phenanthrenequinone diamine) were covalently tethered to a short, 15-bp oligonucleotide. Upon irradiation, $[Ru(phen)_2dppz]^{2+}$ acts as an electron donor, which is quenched through electron transfer through the DNA by the $[Rh(phi)_2(phen)]^{3+}$ acceptor. A poor DNA intercalator cannot quench the luminescence, suggesting that efficient charge transport through DNA is dependent on intercalation of donors and acceptors. (*31*) The luminescence of fluorescent base analogues 2-aminopurine (A_2) and 1,N^6-ethenoadenine (A_ε) can also be quenched by guanine (G) or deazaguanine (Z) through DNA charge transport. (*32*) Fluorescence quenching of a DNA-intercalated ethidium donor by a $[Rh(phi)_2(bpy)]^{3+}$ acceptor through a 17-bp DNA duplex, moreover, is fivefold less efficient in the presence of a single CA base pair mismatch, relative to a well-matched duplex. (*32*) Using DNA-intercalating photooxidants, oxidative DNA damage has also been observed at a distance. An intercalating oxidant such as $[Rh(phi)_2(bpy')]^{3+}$ (bpy'= 4-butyric acid, 4'-methylbipyridine) can be tethered to one end of a 63-bp duplex DNA substrate and photoexcited, oxidizing low-potential guanine bases at the 5'- end of a 5'-GG'-3' doublet sequence. (*33*) Photolysis leads to the oxidation product 7,8-dihydro-8-oxo-2'-deoxyguanosine (8-oxo-G) to form in a DNA-mediated manner, observed up to 200 Å from the site of intercalation of the photooxidant. These reactions additionally have been demonstrated to occur on the picosecond timescale;(*34*) charge can move 10 times the single-step tunneling distance through protein in a miniscule fraction of the time! DNA CT has thus consistently been demonstrated to occur over large molecular distances, in a manner that is rapid and sensitive to perturbations in base-stacking interactions.

Continuous stacking of DNA bases is important for efficient DNA-mediated charge transport. Proteins that bind and sharply kink the DNA duplex, for example, attenuate charge transport through the bound bases. The restriction enzyme R.*Pvu*II is a TATA binding protein that kinks DNA when bound, attenuating DNA mediated guanine oxidation at a 5'-**G**G-3' site. Long-range guanine oxidation by a covalent Rh (III) photooxidant is attenuated in the presence of a TATA binding protein (*35*), which disrupts the π-stacking interaction and inhibits DNA charge transport to prevent guanine oxidation at a distal site.

In order to study DNA CT in a truly biological context, however, a platform to study this chemistry in the ground electronic state was necessary. (*36-38*) To this end, DNA electrodes were developed, which facilitate the study of DNA charge transport using readout from DNA-intercalating redox probes (*36-38*) as well as redox-active, DNA-bound proteins (*23, 39-42*). Complementing the information from previous studies concerning the redox behavior of DNA-dissociated [4Fe4S] repair proteins, (*18,24)* we were now able to measure the *DNA-bound* redox potentials of these enzymes.

DNA Electrochemistry

DNA-modified Au electrodes are a useful platform for assessing whether a DNA-processing, [4Fe4S] enzyme is redox-active when bound to its substrate. This method is adaptable and can be used to assess redox activity on a variety of DNA substrates on a single Au surface (*37,38,43*). Using DNA electrochemistry, we can importantly measure DNA-bound redox potentials of [4Fe4S] proteins. BER glycosylases MutY (*E. coli*), Endonuclease III (*E. coli*), and Uracil DNA Glycosylase (UDG) (*A. fulgidus*), for example, were studied on this platform and displayed reversible redox signals in the physiological redox potential range, near ~85mV vs. NHE, corresponding to cycling between the $[4Fe4S]^{2+}$ and $[4Fe4S]^{3+}$ oxidation

states. (*23*) This initial study of BER proteins was followed by electrochemical studies on several other repair and replication enzymes (*39-42*,*44*), which have been central to the prediction and discovery of redox signaling between DNA-bound [4Fe4S] enzymes across different repair pathways. The platform can be used to characterize redox-deficient mutants of proteins, such as DNA primase and Endonuclease III (*23*,*42*), used as controls in biochemical and genetics experiments. This platform can also be used to oxidize and reduce a sample of protein electrochemically (*41*,*42*,*44*).

DNA electrochemistry allows for observation of redox activity under physiologically relevant conditions and is adaptable to important control experiments for characterization of the redox signal. DNA charge transport is sensitive to base-pair mismatches and apurinic sites (*47*), so a duplex substrate on the DNA-modified electrode containing a mismatch or apurinic site attenuates a DNA-mediated redox signal. This control allows for confirmation that the protein redox activity is mediated by DNA CT. Finally, proteins that bind nucleotide triphosphates, such as ATP, in their active form can be tested in the presence and absence of their cofactors (*39*,*40*). A DNA-modified electrode surface is constructed using alkanethiol-modified DNA duplex substrates, which are incubated on an Au surface. A self-assembling monolayer of duplex DNA assembles on this surface overnight. After washing the surface and passivating the surface with β-mercaptohexanol to prevent direct interaction between the electrode surface and the protein solution in the experiment, the surface can be used to perform DNA electrochemistry on a [4Fe4S] enzyme.

DNA electrochemistry was initially performed on single surfaces; an Atomic Force Microscopy surface served as the Au working electrode with a platinum counter electrode and Ag/AgCl reference. (*23*,*39*) A multiplexed electrode setup (*37*,*38*) was recently adapted for

DNA-bound, redox-active protein electrochemistry (*43*) so that measurements and their controls can be examined in parallel. (**Figure 1.5**) The multiplexed setup complements the single electrode platform, with sixteen Au electrodes at the center of a silicon chip, which can be patterned and fabricated using standard photolithography and metal evaporation techniques. (*37,38,43*) These electrodes are uniform in area and physically divided into four quadrants, so redox activity on as many as four different DNA substrates can be compared on a single surface. DNA charge transport is sensitive to base-pair mismatches and apurinic sites (*47*), so signal on a DNA duplex substrate containing a mismatch or apurinic site can be compared to a signal on well-matched duplex DNA on a multiplexed chip. This control allows for confirmation that the protein redox activity is mediated by the DNA duplex; charge is flowing through the DNA from the electrode to the cluster.

Cyclic voltammetry (CV) is an electrochemical technique which involves sweeping a range of potential values from the in one direction (positive to negative potentials, e.g.) and then in the opposite direction. Although CV provides a wealth of information about DNA-mediated redox reactions, other techniques such as Square Wave Voltammetry (SWV) and Differential Pulse Voltammetry (DPV) can complement CV. DPV and SWV are both types of linear sweep voltammetry; unlike CV, these techniques involve sweeping the potential in a single direction, observing either reduction or oxidation in one scan. (*48*) These linear sweep techniques both measure only Faradaic current, or current resulting from oxidation or reduction of a species on the working electrode, and are thus more sensitive than CV, which also measures charging, or background, current. These sensitive techniques are useful for observing smaller signals from redox-active proteins on DNA electrodes. (*49-51*) Reduction and oxidation sweeps in SQWV or DPV should both be analyzed in a single experiment. Finally, bulk electrolysis (BE) can be

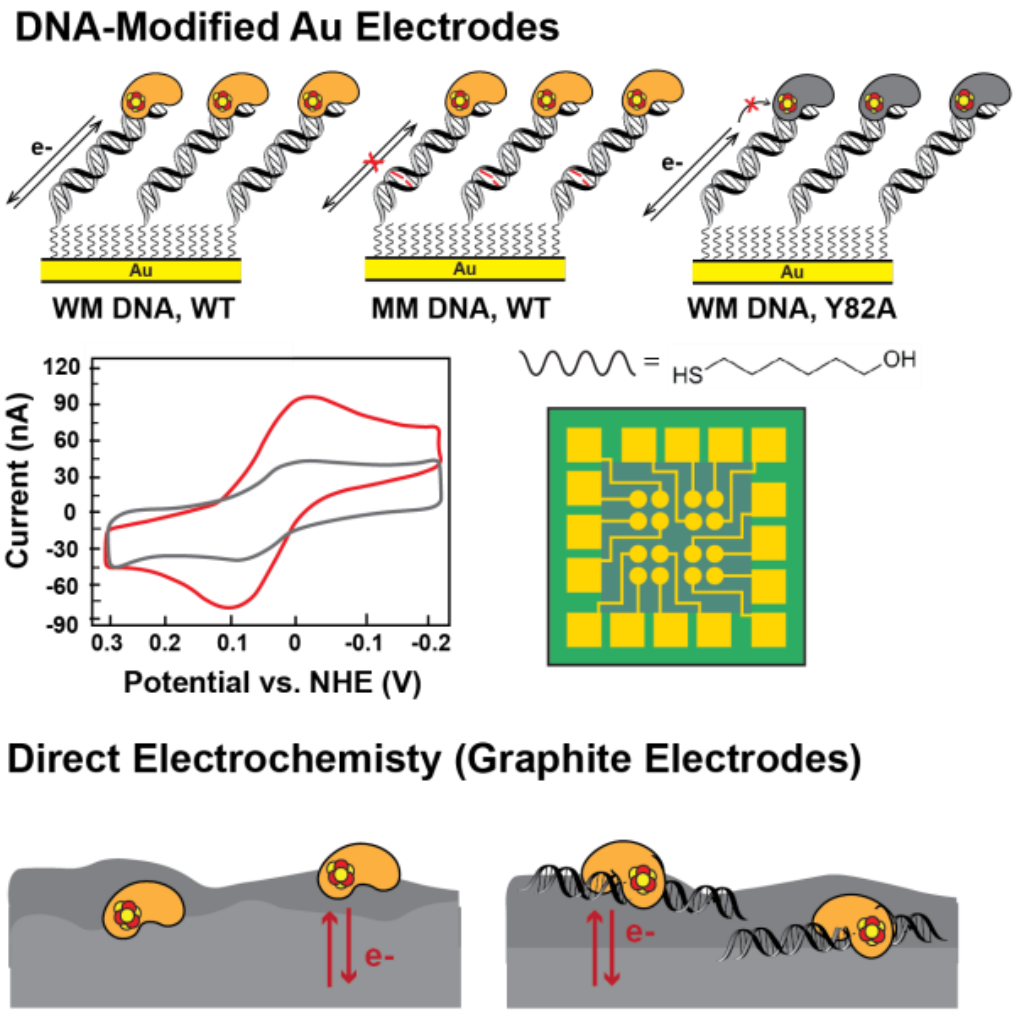

Figure 1.5. Electrochemical methods to measure the redox potential of DNA-bound (top) and DNA-free (below) [4Fe4S] enzymes. DNA electrochemistry on Au electrodes can be used to assess redox signals from DNA-bound, [4Fe4S] proteins. Signals are attenuated when mismatches in the duplex are present, and when the redox pathway within the [4Fe4S] protein has been inhibited through site-directed mutagenesis. A multiplexed chip platform (center, right) has now been adapted to measure [4Fe4S] protein signals on different DNA substrates, with replicates on a single surface. (*37*, *38*, *43*) Direct electrochemistry on pyrolytic graphite edge (PGE) electrode surfaces can be used to compare DNA-bound and DNA-dissociated [4Fe4S] protein potentials. (*46*)

applied to oxidize or reduce a sample of redox-active protein uniformly at the DNA/solution interface of this platform. An applied potential $\geq$100mV positive of the midpoint potential for the redox couple creates an oxidized sample; an applied potential $\geq$100mV negative of the midpoint generates an electrochemically reduced sample. (*23,42*) These oxidized and reduced species can then be compared electrochemically by CV or assayed in a spectroscopy experiment (EPR) or an activity study. (*41,51*)

A Shift in Potential on Binding the DNA Polyanion

DNA electrochemistry is performed predominantly on Au electrode surfaces (*39-45, 51*), which are amenable to measuring physiological potentials in the range of approx. -200mV vs. NHE to +500mV vs. NHE. Scanning beyond this potential regime is necessary in some cases to observe a redox signal from a protein in the absence of DNA, which has higher (more reductive) midpoint potential due to the absence of the bound DNA polyanion. (*41,45,49*) In order to measure the potential of DNA-dissociated [4Fe4S] proteins, graphite electrodes are very useful. To directly compare the redox activity of Endonuclease III in the presence and absence of DNA, highly oriented pyrolytic graphite (HOPG) electrodes were used. (*49*) Pyrene-modified duplex DNA was incubated on the electrode surface to generate a monolayer similar to the monolayers formed on Au electrodes. Reversible, DNA-mediated redox signals similar to those observed on Au were measured on this platform. In the absence of DNA, an irreversible redox signal, shifted approximately 200mV positive of the DNA-bound protein signal, was observed for Endonuclease III. This shift corresponds to an approximately 1000-fold tighter binding affinity for the oxidized $[4Fe4S]^{3+}$ EndoIII relative to the reduced $[4Fe4S]^{2+}$ EndoIII.

The advantages of PGE surfaces for protein electrochemistry have been thoroughly characterized (*52*,*53*). Armstrong and coworkers, for example, showed using porosimetry and scanning electron microscopy that the surface area of a polished PGE surface is ~10^3-10^4 times the geometric surface area of the electrode. (*53*) The pore sizes in the PGE surface moreover were on average ~10nm wide, large enough to accommodate the volume of an enzyme. These characteristics make PGE an optimal surface for protein adsorption, relative to HOPG, which is hydrophobic and has a smooth surface. Protein films can be made by depositing layers of protein sample onto PGE electrode surfaces and drying these samples with argon, with a Nafion film to seal the film onto the electrode surface. To aid protein adsorption, charged species such as neomycin can be added to the surface, promoting electrostatic interactions with a surface-charged protein (*53*). Single-walled carbon nanotubes can also be added to the surface, providing increased surface area and a conductive material on the surface to which the protein is attached.

PGE electrodes have been used to measure potential changes of [4Fe4S] enzymes in response to a change in the cluster environment. Mutation of a distal loop in *M. laminosus* ferredoxin, for example, induces a change in cluster environment so substantial that direct electrochemistry of WT and mutant ferredoxin showed a 57mV shift in redox potential as measured on PGE. (*54*) The HiPIP-like DNA-processing [4Fe4S] repair enzymes have also been assayed using PGE electrode surfaces. EndoIII and MutY (*E. coli*) display DNA-bound and DNA-dissociated redox potentials similar to those observed on HOPG, corroborating the observation that the oxidized $[4Fe4S]^{3+}$ protein is stabilized in the presence of DNA. The shift in electrostatic environment upon binding the DNA polyanion thus induces a significant shift in redox potential, indicating stabilization of the $[4Fe4S]^{3+}$ species in the presence of DNA (*46*).

This was consistently and robustly observed on PGE surfaces, corroborating and improving upon the signals observed for Endonuclease III initially on HOPG. (*49*)

Chemical oxidation or photooxidation are other common methods of assessing redox potential for [4Fe4S] proteins, both bound to and dissociated from DNA. The presence of a [4Fe4S] cluster cofactor in a protein, for example, is often demonstrated using EPR spectroscopy. In the resting $[4Fe4S]^{2+}$ state, the cluster is diamagnetic and thus does not generate an EPR signal. Chemical oxidants such as potassium ferricyanide ($K_3Fe(CN)_6$) and reductants such as sodium dithionite ($Na_2S_2O_4$) can convert the [4Fe4S] cluster into a paramagnetic species (reduced to $[4Fe4S]^{+}$ or oxidized to $[4Fe4S]^{3+}$) which can be observed in EPR. The [4Fe4S] domain of DNA primase in yeast and humans, for example, was demonstrated using EPR and treatment with potassium ferricyanide. (*55,56*) Hinks and coworkers characterized the *A. fulgidus* uracil deglycosylase enzyme with sodium dithionite and potassium ferricyanide, observing the reduced $[4Fe4S]^{+}$ and oxidized $[4Fe4S]^{3+}$ forms (*22*).

Electrochemical observations of DNA-processing [4Fe4S] enzymes are complemented by spectroscopic analysis, using techniques such as electron paramagnetic resonance (EPR). EPR analysis of [4Fe4S] enzymes requires chemical or electrochemical conversion of the resting, paramagnetic $[4Fe4S]^{2+}$ enzymes to the oxidized $[4Fe4S]^{3+}$ or reduced $[4Fe4S]^{+}$ redox state. To convert a DNA-bound [4Fe4S] cluster protein to the oxidized form photochemically, a DNA-intercalating oxidant can be employed (*23,41*). Anthraquinone has been tethered to a DNA and, upon irradiation, can convert [4Fe4S] DNA-bound polymerase δ from the resting $[4Fe4S]^{2+}$ state to the $[4Fe4S]^{3+}$ state. This oxidized sample can then be assayed for activity and compared to a native or reduced protein sample (*41*). DNA, in the presence of intercalating photooxidant $[Co(phen)_3]Cl_3$, has also been used to oxidize DNA-bound [4Fe4S] repair enzymes, in order to

observe an EPR signal of the DNA-bound $[4Fe4S]^{3+}$ protein. (*23*) There are thus several methods for oxidizing or reducing [4Fe4S] enzymes in order to assess their redox potentials and biophysical properties in different cluster oxidation states.

Though the DNA-dissociated form of the [4Fe4S] DNA-processing enzymes is essentially completely in the $[4Fe4S]^{2+}$ state, binding of the DNA polyanion stabilizes the oxidized $[4Fe4S]^{3+}$ state of these proteins. (**Figure 1.6**) This stabilization is primarily an electrostatic effect (*45*); electrostatic modeling calculations based on the crystal structures of DNA-bound MutY and EndoIII suggests that DNA binding accounts for the stabilization of a [4Fe4S] species with an added positive charge in both proteins. Sulfur K-edge absorption spectroscopy analysis of MutY and Endonuclease III (*57*) recently demonstrated that a large increase in iron-sulfur bond covalency occurs upon binding DNA. This change in covalency is consistent with stabilization of the $[4Fe4S]^{3+}$ protein and contributes largely to the shift in potential. In a cluster environment which is destabilized by a mutation or other perturbation, however (*51*), oxidation of the cluster to the $[4Fe4S]^{3+}$ form after DNA binding can lead to oxidative degradation to a $[3Fe4S]^{+}$ product, as observed with the pathologic mutant of human MUTYH, C306W. The degradation product is thus a direct consequence of the cluster being oxidized to the $[4Fe4S]^{3+}$ state during DNA-mediated redox activity, occurring only when the protein has been switched into a tighter binding state through redox chemistry. We have now demonstrated this redox switch in EndoIII using both electrochemical methods (*46,49*) and microscale thermophoresis to assess binding of electrochemically oxidized and native reduced EndoIII (*45*). (**Figure 1.6**)

[4Fe4S] Proteins in DNA Repair

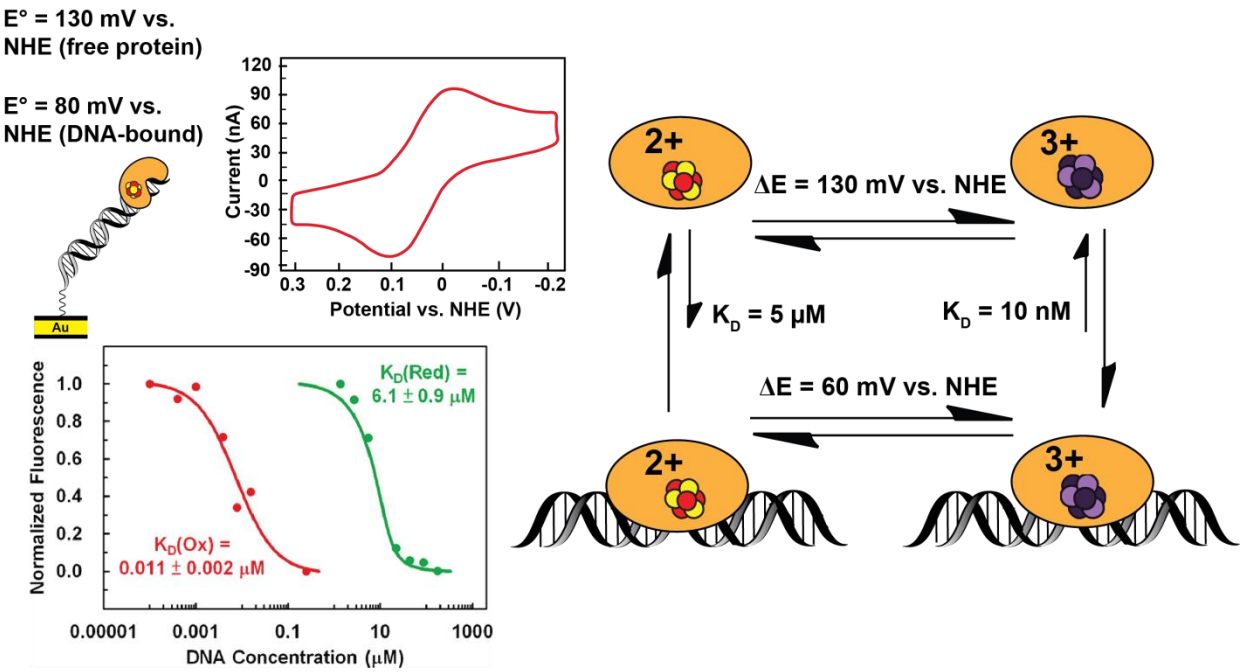

Figure 1.6. DNA binding shifts the potential of [4Fe4S] cluster enzymes. Endonuclease III (above, left) has a redox potential of approximately 80mV vs. NHE for the $[4Fe4S]^{2+/3+}$ couple measured on a DNA-modified Au electrode. This is a negative shift from the ~130mV vs. NHE potential for this couple when the protein is dissociated from DNA. This corresponds thermodynamically to a stabilization of the oxidized $[4Fe4S]^{3+}$ state upon binding the DNA polyanion. Microscale thermophoresis (MST) on electrochemically oxidized and native reduced Endonuclease III indicates that a ~550-fold increase in DNA binding affinity is associated with the conversion from $[4Fe4S]^{2+}$ to the $[4Fe4S]^{3+}$ state. (*45*)

DNA Charge Transport Signaling By Base Excision Repair Glycosylases coordinating a [4Fe4S] Cluster

The first [4Fe4S] enzymes assayed for DNA-bound redox potentials were glycosylases from the base excision repair (BER) pathway, which resolves smaller DNA lesions which do not distort the helix. Some BER substrates include, for example, apurinic/apyrimidinic sites, 7,8-dihydro-8-oxo-2′-deoxyguanosine (8-oxo-G):A mismatches, alkylated or oxidized bases, and uracil that has been incorrectly incorporated into the genome.(*58*) Endonuclease III (EndoIII), an N-glycosylase and AP-lyase from *E. coli* that senses damaged pyrimidines, was the first DNA repair enzyme containing a [4Fe4S] cluster to be discovered in 1989. EndoIII coordinates the cluster in a Cys-X_4-Pro-X-Cys-X_2-Cys-X_5-Cys loop located near the C terminal domain (CTD).(*18*) The cluster is strongly conserved in all domains of life. The presence of the cluster was initially a surprise, but the discovery of the cluster in EndoIII was quickly followed by prediction and demonstration of a cluster in a homologous *E. coli* enzyme, MutY, a glycosylase which resolves 8-oxo-G:A lesions, and like EndoIII, is strongly conserved in prokarya, eukarya, and archaea.(*19,26*) The third BER enzyme, family 4 Uracil-DNA glycosylase (UDG) from the thermophilic bacterium *Archeoglobus fulgidus*, was additionally found to coordinate a [4Fe4S] cluster.(*22*) Thermophilic Family 4 UDGs are the only known UDGs to contain a [4Fe4S] metallocenter, but it is interesting that cytosine deamination, which generates uracils within DNA, is overwhelmingly favored at the higher temperatures of thermophiles.

Structural characterization of the BER glycosylases has been instrumental in efforts to understand why a metabolically expensive and potentially reactive [4Fe4S] metallocenter would be found in enzymes that interact directly with DNA.(*25,59,60*) First, structures for EndoIII, MutY, and UDG from *Thermus thermophilus* (TfUDG, homologous to AfUDG) consistently

show that the cluster is located remotely from the enzymatic active site, where a base is flipped out and excised; it is therefore unlikely that the cluster is directly involved in active site catalysis. (*61*) The DNA-free and DNA-bound structures of EndoIII and MutY are moreover remarkably similar, so a large conformational change is not associated with DNA binding. Secondly, for DNA-bound crystal structures of EndoIII, MutY, and TtUDG, the cluster is consistently located roughly 15-20 Å away from the double helix with a pathway of aromatic amino acids sandwiched between the cluster and the DNA substrate.(*23*,*62*,*63*) The aromatic residues are highly suggestive of an electron transfer pathway from the DNA to the cluster. (*8*) Hence, given these characteristics of the clusters in the repair enzymes, we were prompted to begin determining if the [4Fe4S] clusters coordinated by DNA repair proteins were redox-active and could participate in DNA CT chemistry.

Initial attempts to oxidize and reduce the EndoIII cluster, which suggested the cofactor was redox-inert under physiological conditions (*59*), were carried out in the absence of DNA. However, we considered the more relevant redox potential to examine was that for the protein bound to DNA. Our approach was to adapt the DNA-modified gold electrode platform we had developed to probe DNA CT for protein electrochemistry, using EndoIII, MutY, and AfUDG rather than small molecules as the redox probes.(*23*,*63*) Interestingly, reversible redox activity for all three glysosylases in the presence of DNA was seen by cyclic voltammetry (CV), with positive, midpoint potentials between 60 and 100 mV vs. NHE, which is characteristic of high iron potential [4Fe4S] proteins (HiPIPs) (**Figure 1.6**) (*23*) Critically, there was not any observed degradation of the cluster under these conditions. Interestingly, redox activity could not be observed in the absence of DNA and was greatly attenuated in the presence of an abasic site. Though abasic sites are not direct substrates of EndoIII, MutY, or UDG, the redox sensing of this

DNA lesion by the BER glycosylases was an exciting discovery, and together, these data indicated that the redox-activity of the [4Fe4S] cluster was facilitated and mediated by DNA. The redox characteristics of the protein could be probed or signaled through DNA CT.

While there is not a marked conformational change associated with DNA binding based on crystallographic studies (*21,25*, *64,65*) protein binding to DNA appears to have a dramatic effect on the potential of the $[4Fe4S]^{3+/2+}$ couple. The $[4Fe4S]^{2+}$ resting state of the HiPIP-like glycosylases appeared to be activated toward oxidation within a potential range that is biologically accessible and does not damage the DNA bases, even within guanine repeat sequences.(*66,67*) On a graphite electrode, where DNA-bound and dissociated forms can be compared directly, the shift in potential was found to be ~70-100 mV negative on DNA binding.(*46,49*) The oxidation state of [4Fe4S] clusters is known to vary widely depending on the local environment,(*68,69*) and the shift in potential with the BER glycosylases is readily explained by the change from a solvent-exposed cluster in the DNA-free state to the more negatively-charged local environment in the DNA-bound state.(*23*) Certainly the application of [4Fe4S] clusters in these enzymes offered an opportunity to tune the potential of the cluster to a redox-active form at cellular potentials when bound to DNA.

DNA CT Signaling Activity by DNA Helicases with [4Fe4S] Clusters

Concurrent with the initial characterization of the BER glycosylases, several proteins involved in genome maintenance from repair, replication, recombination, and transcription were reported to coordinate a [4Fe4S] cluster (*12, 47*), providing opportunity to study more repair proteins in the context of DNA-mediated redox chemistry. XPD is a [4Fe4S] helicase, an essential component of the transcription factor IIH (TFIIH) machinery that unwinds DNA during nucleotide excision repair (NER) and transcription in archaea and eukarya.(*70*) Mutations in the

XPD gene are associated with trichothiodystrophy, Cockayne syndrome, and Xeroderma pigmentosum. As with the BER glycosylases, many mutations in XPD associated with genetic diseases are known, but how some of these mutations lead to disease remained poorly understood.(*39,44*) Interestingly, evidence now points to an association between cluster destabilization and disease development. The second helicase we examined, DinG, is an *E. coli* SOS-inducible protein that shares some sequence homology with XPD, most strongly in the [4Fe4S] cluster domain.(*71,72*) DinG is responsible for resolving R-loops (DNA:RNA duplexes) and is required for maturation of R-loops at stalled replication forks.

When XPD from the archaeal species, *Sulfolobus acidocaldarius* (SaXPD), and DinG were studied electrochemically on the DNA-modified gold electrode platform, both helicases were found to participate in DNA CT chemistry.(*39,40*) Furthermore, they shared the same DNA-bound redox potential as the BER glycosylases, approximately 80mV vs. NHE.(*39,40*) Consistent with the previous studies of BER [4Fe4S] enzymes, the signal was attenuated, but not shifted, in the presence of an intervening lesion. Remarkably redox signaling is attenuated in the presence of mismatches and abasic sites, which perturb DNA CT but are not native substrates for these enzymes. DNA CT facilitates detection of a wide range of DNA damage by these repair enzymes. Further probing of the CT activity found that in the presence of ATP, the signal for SaXPD and DinG quite stunningly increased in a concentration-dependent manner without any shift in the midpoint potential. Hence, it appears that helicase activity increases the electrochemical signal and coupling of the cluster to the π-stacked DNA bases, indeed signaling electrochemically that the helicase is active. This electrical detection of redox-independent enzymatic activity by the helicases on DNA substrates is thus yet another intriguing indication of a redox role for the [4Fe4S] cluster and DNA CT in DNA biology. Indeed, two mutants of

SaXPD, G34R and L325V (L461 in human XPD), associated with disease, were both found to be CT-deficient, but enzymatically active.(*39,44*) Additional studies will be instructive as to how CT signaling of enzymatic activity might be utilized *in vivo*.

A Model for Lesion Detection Using DNA CT

With the discovery that DNA binding shifts the redox potential, and that the cluster can be accessed through DNA CT, we sought to explore roles for this chemistry within the cell. One essential protein function DNA CT chemistry seemed well suited for was the ability to detect damaged bases. We had seen that DNA electrochemistry could be used to detect a variety of naturally occurring base lesions (*73*). Repair proteins are challenged with the enormous task of discriminating the billions of unmodified bases from the thousands of damage sites generated per day, many of which are structurally very similar to their undamaged counterparts.(*74*) The protein traffic on DNA in the form of transcription factors, other repair proteins, RNA polymerases, DNA polymerases, and histones (in eukaryotes) adds layers of complexity to the processes that must be coordinated in order to maintain genomic integrity. Furthermore, the copy numbers of MutY and EndoIII per cell are limiting: MutY is expressed at ~30 copies/cell and EndoIII is expressed at ~500 copies/cell.(*47*) Indeed, a basic model of genome scanning that includes facilitated diffusion constants for the *E. coli* genome (4.6×10^6 base pairs) and a protein copy number of 30 under the assumption of instantaneous lesion detection and no protein traffic predicts a search time of 46 minutes to find a single lesion, far too long for an organism with an average doubling time of 20-30 min.(*75*) Hence other factors must facilitate efficient lesion detection.

Detection of damaged lesions through DNA CT, which is exquisitely sensitive to base stack perturbations even in the absence of perturbation to the overall helix structure, is an

excellent reporter of base stack integrity and could enhance DNA damage search efficiency. This idea is especially relevant for proteins expressed at low copy numbers. Utilization of DNA CT in the cell for efficient lesion detection could explain why many DNA repair enzymes coordinate a redox-active [4Fe4S] cofactor. As such, a new model for DNA-mediated sensing and signaling *as a first step* in lesion detection was proposed based on the DNA-bound redox behavior and the shared midpoint potential of the [4Fe4S] repair enzymes (**Figure 1.7**).(*23*,*47*,*75*) In this model, iterative signaling across the genome involves redox communication between a protein donor in the $[4Fe4S]^{2+}$ state and a distally-bound acceptor, oxidized to the $[4Fe4S]^{3+}$ state. We have seen that guanine radicals, presumably generated under oxidative stress, can oxidize the clusters of DNA-bound repair proteins, generating the $[4Fe4S]^{3+}$ state.(*23*) Upon binding to DNA, the donor is activated toward oxidation and can reduce the distally bound acceptor protein in a self-exchange electron transfer reaction if the intervening DNA is free of lesions. The acceptor, now in the $[4Fe4S]^{2+}$ state, can more easily diffuse away to another region of the genome due to the decreased binding affinity of the protein for DNA once in the reduced state. This iterative process can repeat to facilitate communication between [4Fe4S] proteins in the same repair pathway or in different repair pathways. If, however, there is a DNA CT-attenuating lesion between the donor and acceptor pair, redox signaling is disrupted and the lesion is effectively sensed by the cluster proteins on either side of the lesion. The DNA-bound [4Fe4S] proteins bound flanking the lesion are tightly bound on the DNA in the $[4Fe4S]^{3+}$ state, and these proteins can then move processively on the double helix to localize to the precise location of the lesion. Proteins bound tightly on the damaged regions can also recruit other protein complexes necessary for timely repair. This model serves to redistribute the repair proteins in the vicinity of lesions. Including a CT search component in the model of genome

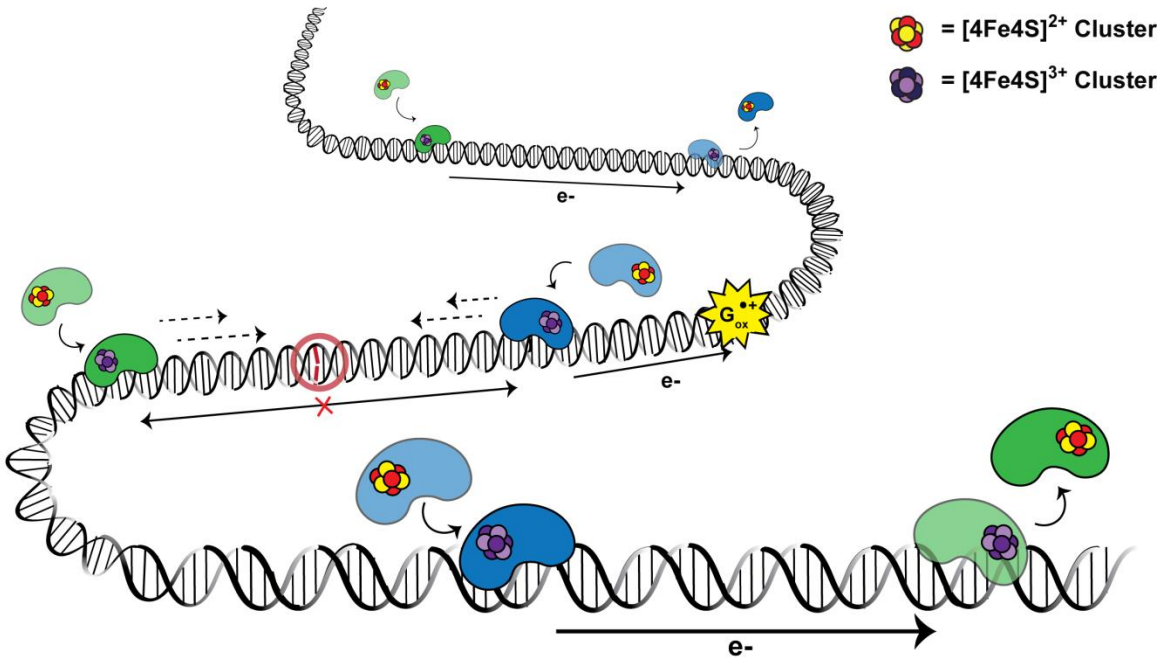

Figure 1.7. A model for DNA-mediated redox signaling between repair proteins. Enzymes with the cluster in the native $[4Fe4S]^{2+}$ first bind DNA, causing the cluster to become activated toward oxidation. Oxidative stress initiates the damage search when highly reactive species such as the guanine radical cation are formed; these can oxidize DNA-bound proteins in their vicinity. Oxidation of the cluster to the $[4Fe4S]^{3+}$ form leads to a 1000-fold increase in DNA binding affinity, so oxidized proteins remain bound and diffuse along the DNA. When another [4Fe4S] proteins binds at a distant site, it can send an electron through the DNA base stack to reduce the oxidized protein. At this point, the reduced protein binds less tightly to DNA and diffuses away, while the newly oxidized protein continues the damage search. This process of redox exchange continues until a segment of DNA containing a lesion is approached. Since even subtle lesions can disrupt base stacking, CT is attenuated and any nearby oxidized proteins remain bound. Thus, DNA CT allows repair proteins to scan large sections of the genome and focus their time on areas containing damage.

scanning with CT distances of only a few hundred bases predicts that a protein with a copy number as low as 10 can find a lesion in 6 minutes, which is within reason for *E. coli*.(*75*)

Cooperative Redox Signaling Between [4Fe4S] Proteins Across Pathways

A key component of the proposed CT scanning model is the localization of CT-proficient, [4Fe4S] cluster proteins in the vicinity of damage, after scanning undamaged regions of the genome. A way to visualize and test how [4Fe4S] proteins distribute onto damaged versus undamaged DNA was developed using AFM.(*75*) (**Figure 1.8**) For the AFM redistribution assay, two sets of DNA substrates, one which includes long, well-matched (WM), 3.8 kb duplex DNA and one which includes long, mismatched (MM) DNA (3.8 kb) engineered to contain a single C:A MM but is otherwise identical to the WM strand, are prepared. Both WM and MM DNA samples also include shorter strands (1.6 and 2.2 kbp) of undamaged DNA. EndoIII, SaXPD, and DinG were all studied as uniform samples and in mixtures with other [4Fe4S] repair proteins using the AFM redistribution assay. An increased density of protein, moreover, was consistently found on long, MM DNA relative to the shorter, undamaged DNA substrates. (*44,62,75*) Remarkably, comparable binding density ratios of approximately 1.5 (MM/WM) were observed for all CT-proficient repair proteins studied thus far, even though C:A MMs are not native substrates for any of the enzymes studied thus far. In stark contrast to the WT [4Fe4S] proteins, all the CT-deficient mutants visualized by AFM, EndoII Y82A, EndoIII Y75A, and SaXPD L325A, were found to have a binding density ratio of 1 MM/WM, showing no preference for the strand containing the single base mismatch. Indeed, a direct correlation was found between the electrochemical signal of a given protein cluster on the DNA-modified electrode, a measure of DNA CT ability, and the binding density ratio seen in the redistribution assay, a measure of the ability of the repair protein to find the mismatched strand.(*62*) Moreover,

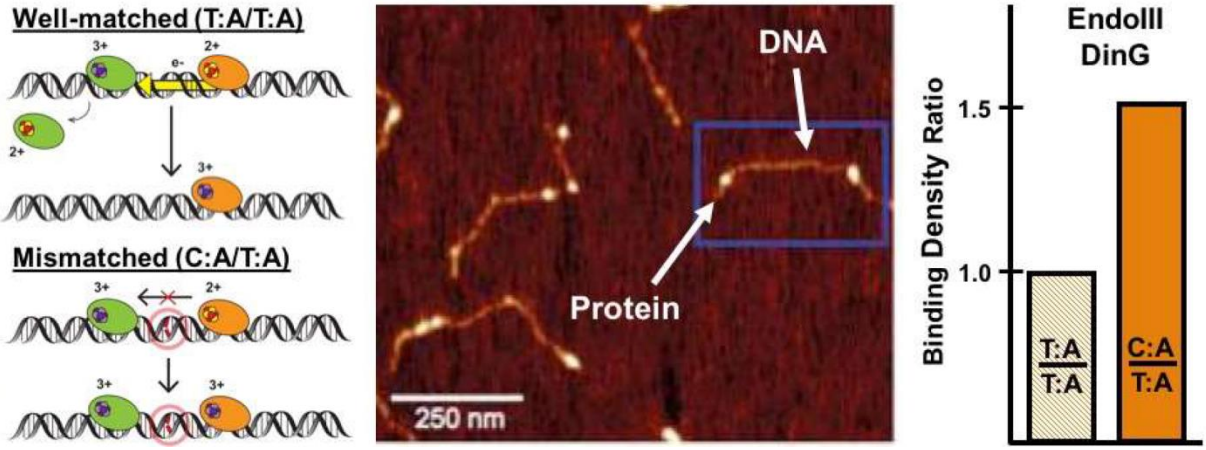

Figure 1.8. (*40,44,62*) Visualization of Protein Localization onto Damaged DNA by Atomic Force Microscopy (AFM). In the AFM redistribution assay, [4Fe4S] protein or protein mixtures are incubated with DNA substrates which contain either long, WM or MM strands (3.8 kbp), and short, undamaged DNA stands (1.6 and 2.2 kbp) (left) and imaged (middle). The proteins bound to long strands of DNA are counted, normalized, and expressed as a binding density ratio (right). Consistently, CT-proficiency determines if redistribution to damaged substrate occurs.

mixtures of wild type protein and CT-deficient mutants, for example EndoIII:Y82A and wild type EndoIII or XPD mixed with XPD:L325V, also were found to have a binding density ratio of 1, consistent with the idea that CT-deficient mutants cannot participate in signaling to another protein.(*44,75*)

We have additionally used the AFM redistribution assay to monitor communication between signaling partners from *distinct* repair pathways.(*40*) Binding density ratios of samples containing mixtures of BER glycosylase EndoIII and R-loop repair helicase DinG were found to be comparable to binding density ratios found for samples containing only EndoIII, DinG, or XPD (**Figure 1.8**). Consistent with these findings, protein mixtures containing DinG and CT-deficient Y82A (**Figure 1.8**), did not show a preference for damaged DNA. In fact, AFM studies with signaling partners from *different* organisms, EndoIII (*E. coli*) and XPD (*S. acidocaldarius*), showed a higher density of proteins on the mismatched strands of DNA, again with a binding density ratio of 1.5, just as were found for mixtures of proteins from the same organism.(*40*) Furthermore, no preference for damaged DNA was seen in protein mixtures containing XPD: EndoIII Y82A, EndoII: XPD L325V, and EndoIII Y82A: XPD L325V. These findings were remarkable, and suggested to us that signaling between [4Fe4S] cluster proteins is not dependent on the type of protein (endonuclease, glycosylase, or helicase) or even on the native organism. What forms the basis for the long range signaling is the ability of these proteins to bind DNA and couple their clusters electronically to the π-stacked bases in the DNA duplex. Thus these results are fully consistent with a model of lesion detection through long-range, DNA-mediated, redox signaling between [4Fe4S] repair proteins. CT deficient mutants that cannot fully participate in DNA CT chemistry are unable to unable to sense the lesions electrochemically, which impairs the search efficiency (redistribution onto damaged strands).

After observing robust and consistent evidence for DNA-mediated redox signaling *in vitro*, we began to probe for DNA-mediated signaling *in vivo*. We employ several different genetics assays, the general strategy of which is to select a strain of *E. coli* that relies on the repair protein for its survival, then genetically knockout a putative signaling partner containing the [4Fe4S] cluster, and monitor how the lack of the signaling partner affects activity/survival (**Figure 1.9**). If DNA-mediated CT is used to scan the genome for lesions, then decreasing the number of signaling partners in the cell should have a measurable effect on growth. Any growth defects should also be reversible, and to pinpoint the basis for rescue, complementation plasmids are introduced into the knockout strains to express either the wild type signaling partner or mutants that are CT-deficient or redox-active but enzymatically inactive.

The first *in vivo* assay we developed reports on the repair activity of MutY in the CC104 strain of *E. coli*.(*75*) The CC104 strain contains a cytosine rather than an adenine in the lacZ gene at the Glu-461 codon which is essential for metabolizing lactose (**Figure 1.9**).(*76*) When MutY activity is impeded, an increase in GC-to-TA transversions occurs, restoring the lacZ gene and growth (revertants) on minimal media where the only carbon source is lactose. When the EndoIII (*nth*) gene is knocked out of the CC104 strain, a significant, but not dramatic (roughly two-fold) increase in revertants is observed (**Figure 1.9**).(*75*) To test if the wild type phenotype could be restored, complementation plasmids were introduced expressing either Y82A, the CT-deficient but catalytically active EndoIII mutant, or D138A, which is a catalytically inactive but CT-proficient mutant of EndoIII. Consistent with our CT scanning model, the Y82A plasmid could not restore the wild type phenotype, but the D138A plasmid could restore the wild phenotype for both EndoIII and DinG knockout strains. Thus, the ability of MutY to find lesion

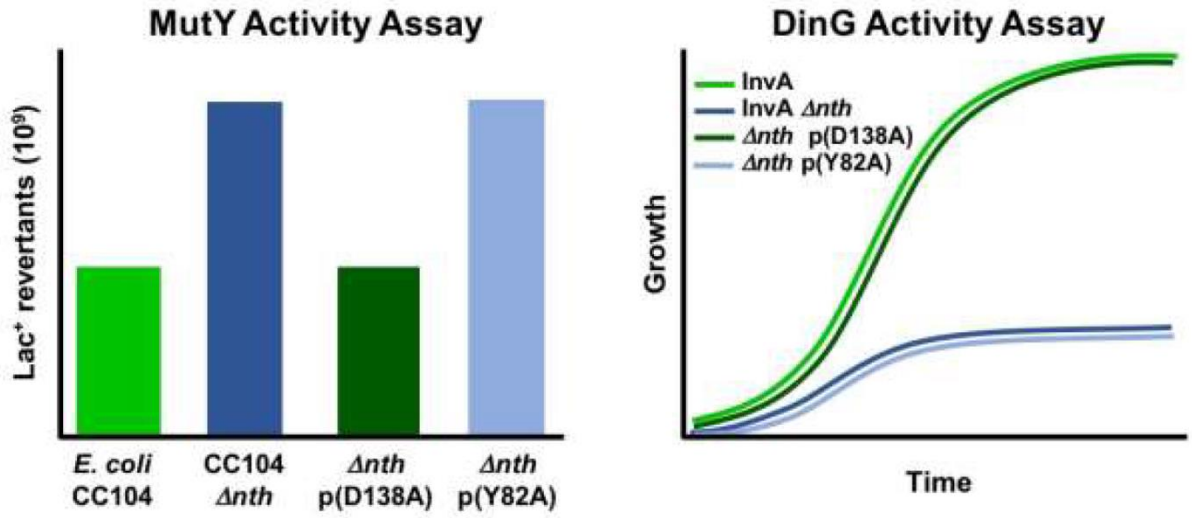

Figure 9. (*40,75*) Genetic Assays for Detection of DNA CT Signaling Among *E. co*li [4Fe4S] Repair Proteins. *E. coli* parent and knockout (KO) strains that report on the activity of MutY and DinG have been used to probed for DNA-mediated communication between putative signaling partners *in vivo*. Complementation plasmids expressing CT-proficient (pD138A) or CT deficient (pY82A) versions of EndoIII are introduced to KO strains to evaluate if the parent phenotype can be rescued. In the MutY Activity assay, impaired MutY activity in the CC104 strain leads to an increase in GC to TA transversions at the *lacZ* gene and to an increase in growth (revertants) on lactose-only media. In the DinG activity assay, impaired activity of DinG in the InvA strain, which has been engineered such that there is an increased frequency of R-loop formation at collisions between transcription and replication machinery, leads to a dramatic growth defect. Knocking out EndoIII (*Δnth*) impaired both MutY and DinG Activity (dark blue bar, left, and dark blue curve, right). Rescue in both assays could only be achieved by addition of CT-proficient, but enzymatically-inactive protein (green bar, left, and green curve, right), strongly indicating that DNA-mediated redox signaling is necessary for lesion detection (light blue bar, left, and light blue curve, right).

relies on redox signaling with EndoIII (*75*) and DinG(*40*) to find lesions, and moreover, the enzymatic functions of EndoIII and DinG do not appear to be relevant to this process.

To probe the signaling network further, another, more sensitive *in vivo* assay was developed that reports on the repair activity of DinG in the Inverted A (InvA) strain of *E. coli*.(*77*) In the InvA strain, the highly-transcribed rrnA operon in inverted, which increases the frequency of collisions between transcription and replication machinery and the formation of R-loops (**Figure 1.9**). DinG is required for resolving these types of lesions, and so, to test if DNA-mediated CT signaling is needed for DinG repair activity, the EndoIII gene was knocked out in the InvA strain, and growth rescue was attempted with plasmids expressing Y82A or D138A. The growth of the InvA *Δnth* mutant strain is severely compromised, but, growth can be completely rescued with the D138A plasmid, whereas the Y82A plasmid did not have a measurable effect on growth (**Figure 1.9**).(*75*) Like MutY, DinG also appears to rely on DNA CT chemistry to repair lesions. The ability of a catalytically inactive EndoIII enzyme (D138A) to rescue growth to wild type levels appears to be achieved simply through the increase of cellular concentration of redox-active [4Fe4S] protein to help in scanning the genome. Results from genetics assays reporting on both MutY (*44,75*) and DinG (*40*) activity thus highlight the power of DNA CT that is only now beginning to be realized in DNA and RNA biological processes. As other DNA-processing proteins containing [4Fe4S] clusters are discovered, we will be able to continue testing how DNA CT may be used in redox signaling networks.

[4Fe4S] Enzymes in Eukaryotic DNA Replication

Overview and Initial Steps in Replication.

Several diverse and specialized enzymes play a role in duplicating eukaryotic genomes ranging from ~10^6-10^9 bp (*78*) in size, with exceptionally low error rates (*78,79*). Many of the enzymes which are integral to this process working efficiently and correctly are [4Fe4S] cluster enzymes. All of the major polymerases, DNA polymerase α,δ, and ε, (*11*) as well as DNA primase (*55,56*), which initiates replication on duplex DNA through synthesis of a short RNA primer, contain this cofactor. Dna2, a helicase-nuclease integral in Okazaki fragment processing (*80*), as well as the translesion polymerase ζ (*11*), also contain this cofactor. These [4Fe4S] enzymes each contain multiple subunits (*81-84*), and they are a central part of a larger array of biological machinery affecting the bidirectional duplication of eukaryotic genomes on the leading and lagging strands. Along with the replicative helicase (CMG) (*85,86*), processivity factors such as proliferating cell nuclear antigen (PCNA), replication factor c (RFC), and single-stranded binding protein Replication Protein A (RPA), (*85,86*) these polymerases synthesize DNA in a manner which is spatiotemporally controlled and exquisitely high fidelity.

Before polymerases can synthesize new DNA, replication origin sites in the genome must be identified and licensed by the cellular machinery. (*87*) The hexameric origin recognition complex (ORC) consists of five AAA+ ATPase proteins, Orc 1-5, (*88*) and Orc6, which is required for replication initiation in eukaryotes but has not ATPase similarity (*89*). After origins are bound by Orc1-6, the Cdc6 and Cdt4 proteins will bind at the origin site and load the Mcm2-7 complex in an ATP-dependent manner. The origins sites are then licensed for replication. Loading of additional factors including Sld2, Sld3, Dpb11, Cdc45, the GINS complex, and DNA polymerase ε then allows for formation of the pre-initiation complex. (*86,87*) MCM 2-7 is not an active helicase in the absence of two accessory factors, GINS (Sld5 and Psf1-3) and Cdc45 (*90-92*); these form a complex at the origin site in cells to form the CMG helicase. CMG then

anneals AT-rich DNA at origin sites, to begin bidirectional replication on the two parent strands of genomic DNA. The spatiotemporal resolution of the binding and activity steps in the initiation of replication are largely controlled by phosphorylation of different components by the cyclin dependent kinase (CDK) and the Dbf4-dependent kinase (DDK). This process has now been reconstituted *in vitro* using 16 purified components of the budding yeast (*Saccharomyces pombe*) replication machinery. (*86*) After origin firing and DNA annealing to create lagging and leading strand templates, polymerases can then begin the dynamic and coordinated process of genome duplication.

DNA Polymerase-α-Primase Begins Genome Duplication through a Coordinated Association-Dissociation-Transfer Sequence.

DNA polymerase-α-primase (pol-prim) is the heterotetrameric complex responsible for RNA-DNA primer synthesis which precedes the processive synthesis by DNA polymerase ε on the leading strand and polymerase δ on the lagging strand (*93*). This complex consists of four subunits, two of which putatively contain a [4Fe4S] cluster. (*11,55,56,93*) RNA polymerase subunit p48 and regulatory subunit p58 comprise the primase heterodimer, which synthesizes a 8-14nt RNA primer on the ssDNA template (*94-96*) DNA polymerase subunit p180 and auxiliary subunit p70 (*97*) comprise the DNA polymerase α enzyme, which synthesizes a ~10-30nt DNA segment downstream of the RNA primer, once primase has completed RNA primer synthesis. This heterotetramer is flexibly tethered (*97*), allowing for movement in the cell during concerted RNA/DNA primer synthesis. The C-terminal domain of the primase auxiliary subunit (p58C) and the C-terminal domain of the polymerase α p180 catalytic subunit (*11,55,56*) contain the two putative [4Fe4S] cofactors.

Primer synthesis requires a series of association, dissociation, and transfer steps by the low-fidelity, relatively weakly binding primase and polymerase α enzymes (*93*) in order to synthesize the RNA/DNA primer and begin genome duplication. First, DNA primase binds the ssDNA template and two nucleotide triphosphates (NTPs). After substrate binding and synthesis of a phosphodiester bond between the two NTPs, primase is converted to the active form in the rate-limiting initiation step of primase activity. Primase then rapidly elongates the primer, and finally truncates the primer during a termination step which involves primase dissociation and handoff of the primed template to DNA polymerase α. (*94-97*) After the transfer step, polymerase α then binds the RNA/DNA template and deoxynucleotide triphosphates (dNTPs), then polymerizes ~10-30 dNTPs downstream of the RNA primer. After this sequence is completed, polymerase-α-primase then hands off the substrate to DNA polymerases δ and ε, which synthesize longer stretches of genomic DNA on the leading and lagging strand, respectively. Although this sequence of events beginning primer synthesis is well-characterized structurally and biochemically (*97-100*), the chemistry driving the coordinated binding and dissociation of primase and polymerase α was previously not well understood.

Primase and polymerase α, although they contain [4Fe4S] clusters, are otherwise structurally and functionally distinct from the other replicative DNA polymerases, δ and ε. These enzymes are both heterodimers containing catalytic and regulatory subunits. They are additionally both relatively low-fidelity, with error rates of ~10^{-2} (*94-96*) and ~10^{-4}-10^{-5} (*93*). Low fidelity is due in part to the fact that neither of these polymerase enzymes contain an exonuclease domain to 'proofread' replication errors. Polymerase α and primase also do not interact with the PCNA processivity clamp, unlike DNA polymerase ε and δ. Primase [4Fe4S] cluster assembly and fidelity moreover is negatively affected by oxidative stress conditions in the

cell (*101*), suggesting that cluster stability could be linked to the redox environment. Chemical and biophysical characterization of this cofactor in DNA primase has illuminated previously unclear chemistry performed by the pol-prim complex. (*42*)

The [4Fe4S] cluster of DNA primase was recently discovered to function as a redox switch, regulating DNA binding and redox signaling activity. The [4Fe4S] domain of primase, p58C, has the intrinsic ability to bind DNA substrates modestly, in the absence of the rest of the primase enzyme. (*100,101*) On a DNA-modified electrode, this protein was electrochemically oxidized or reduced using bulk electrolysis in an anaerobic environment. Subsequent CV scans showed that the oxidized $[4Fe4S]^{3+}$ p58C protein was redox-active on DNA, and the reduced $[4Fe4S]^{2+}$ form was redox-inert. (*42*) This electrochemically controlled switch in p58C binding and redox activity moreover is mediated by conserved tyrosines in both human and yeast p58C, positioned between the [4Fe4S] cluster and the DNA binding interface within this domain (*42,101*). Mutation of these tyrosines to phenylalanine or leucine attenuates redox activity of the oxidized protein on DNA electrodes and compromises initiation activity on ssDNA substrates in full-length primase. Interestingly, redox pathway mutations do not affect primase catalytic activity. Truncation of human primase moreover is gated by DNA CT *in vitro*, a single base mismatch in a nascent primer abrogates WT primase truncation on a primed substrate. Electron transfer activity is thus associated with the primase cluster, and a scheme for primase-polymerase α handoff has been proposed in light of these findings. Oxidized $[4Fe4S]^{3+}$ primase is coupled into the primed RNA/DNA duplex, tightly bound, and redox-active. The oxidized enzyme synthesizes the RNA primer, until the reduced $[4Fe4S]^{2+}$ polymerase α cluster is able to come into contact with the RNA/DNA duplex. Polymerase α can become oxidized through DNA CT through the RNA/DNA primer of appropriate length, which converts polymerase α to a tightly

binding oxidized form and the initially oxidized primase to the $[4Fe4S]^{2+}$ form. Primase is reduced and dissociates from the substrate, allowing polymerase α to bind and synthesize the DNA segment downstream of the original RNA primer. (Figure **1.10**) Redox switching driven by the [4Fe4S] cofactor, in the proposed model, facilitates the sequence of binding and dissociation events at the center of RNA/DNA primer synthesis.

DNA Polymerase ε and δ Perform Specialized Tasks on Opposite Strands of the Replication Fork

Polymerases ε and δ are the larger, high-fidelity multisubunit polymerases responsible for the synthesis of DNA on the leading and lagging strands, respectively. (*93*,*102*) This division of replicative labor has been debated and studied by several groups (*103*-*106*), primarily through the use of error-prone polymerase variant studies. In cell lines with RnaseH knocked out of the genome, ribonucleotide incorporation by a variant of polymerase ε prone to ribonucleotide incorporation, *pol2*M644G, can be measured and was demonstrated to localize on the leading strand (*103*,*104*). This result suggested that the leading strand synthesis is primarily performed by DNA polymerase ε. On the other hand, mutation analysis in cells expressing a low fidelity variant of polymerase δ (L612M) found the majority of errors localized on the lagging strand of nascent DNA (*105*). Although polymerase δ can replicate the leading strand templates under certain conditions (*106*), it is generally thought that polymerase ε synthesizes the leading strand and polymerase δ synthesizes the lagging strand under standard cellular conditions.

Both polymerase ε and polymerase δ, which are distinct enzymes specialized for the strands which they duplicate, have significantly higher fidelity than polymerase α primase.

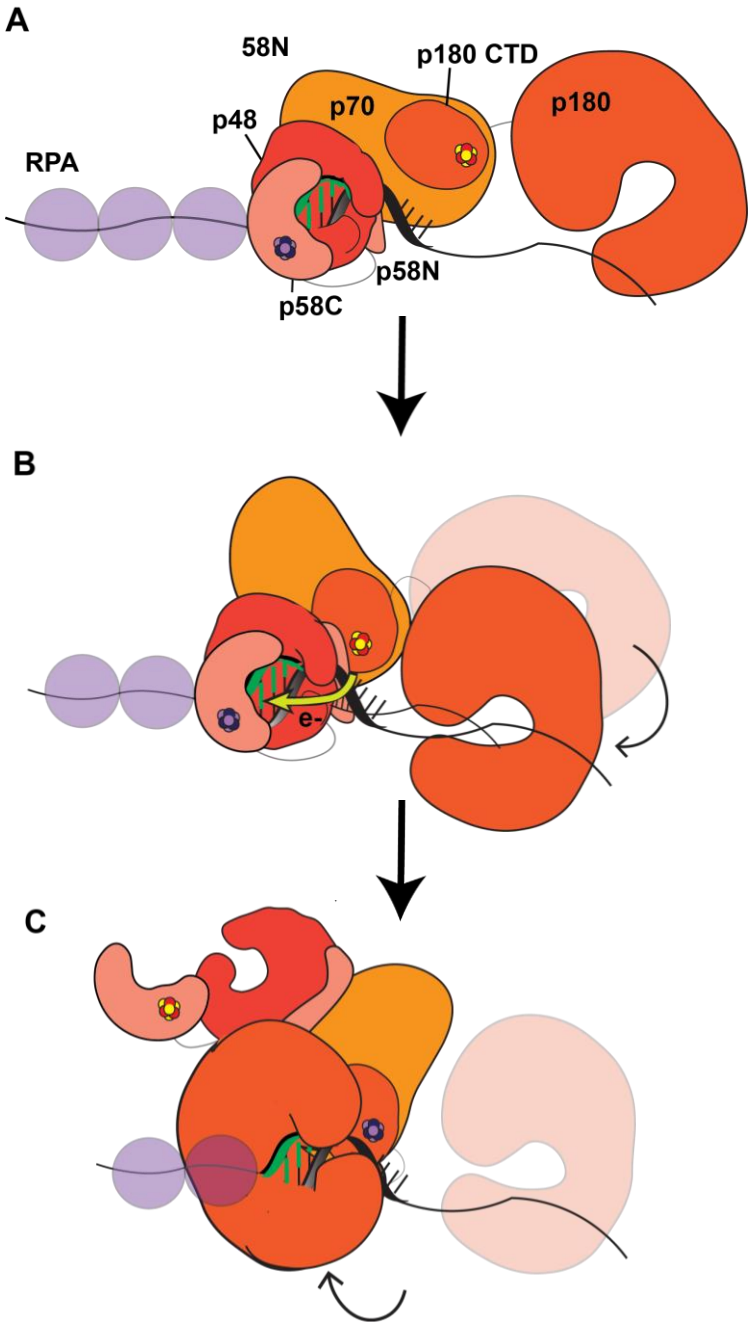

Figure 1.10. Model for primase-polymerase α handoff through redox switching. A) Oxidized $[4Fe4S]^{3+}$ primase is bound to the RNA/DNA primer during primer synthesis. Polymerase α is DNA-dissociated and reduced but flexibly tethered to primase. B) When the RNA primer reaches appropriate length, polymerase α orients in a position where the [4Fe4S] cluster is coupled into the RNA/DNA substrate and can be oxidized by DNA CT through this segment, sending an electron through the primed template to reduce DNA primase. C) Reduced primase dissociates from the RNA-primed DNA, and oxidized polymerase α can then synthesize DNA downstream of the primase product.

Polymerase ε has a mutation rate of ~10^{-5}-10^{-6} and polymerase δ has a rate of ~10^{-4}-10^{-6}. (*93*) Both of these enzymes have a 3'-5' exonuclease domain, which proofreads errors in DNA synthesis. Both polymerases also associate with PCNA; PCNA binding greatly enhances the moderate intrinsic processivity of DNA polymerase δ and somewhat enhances the already strong intrinsic processivity of polymerase ε. As polymerase ε synthesizes kb-scale products on the leading strand and polymerase δ synthesizes ~100-200nt Okazaki fragments, their relative processivities are consistent with their function in cells. The higher intrinsic fidelity than observed for pol-α-primase is furthermore consistent with the more permanent nature of these products; pol-α-primase products are removed during Okazaki fragment maturation (*94-96*). Thus nucleotide misincorporation in these cases does not necessarily cause mutagenic phenotypes.

Polymerase ε is a four-subunit enzyme which coordinates at least one [4Fe4S] cluster cofactor. (*11,107*) The polymerase ε holoenzyme has a large polymerase subunit, Pol2, which has been shown to contain a [4Fe4S] cluster which is essential for the polymerase activity within the domain but dispensable for the exonuclease activity (*107*). The Dpb2 subunit of polymerase ε is associated with the C-terminus of Pol2 and is essential for replisome assembly and checkpoint activation (*93*). The Dpb3 and Dpb4 subunits are not catalytic, but they likely enhance polymerase ε processivity, as does association of the enzyme with PCNA. The C-terminal domain of Pol2 and Dpb2 both interact with several subunits of the CMG helicase (*108-110*); polymerase ε can displace pre-bound polymerase δ at a replication origin. In addition to the [4Fe4S] cluster in the active polymerase domain of Pol2, polymerase ε has been purified with a [4Fe4S] cluster ligated in the Pol2 C-terminal domain, which was stabilized by coordination with Dpb2. (*11*) The role of these putative clusters in the context of polymerase ε activity is not

yet clear, but this enzyme represents a prime opportunity to discover new potential roles for DNA-mediated redox signaling in coordinating replication.

Polymerase δ, the lagging strand polymerase, is a three-subunit protein with a [4Fe4S] cluster bound in the Pol3 catalytic domain. Polymerase δ also contains auxiliary subunits Pol31, which associates with Pol3 to stabilize the cluster (*11*) and Pol32. (*93*,*102*) After replication factor C (RFC) loads the PCNA clamp onto DNA, polymerase δ can coordinate with PCNA and extend the Okazaki fragments begun by pol-α-primase synthesis. (*111*,*112*) The precise sequence of events between polymerase α dissociation from DNA and polymerase δ binding are still being investigated, but association of PCNA and polymerase δ is known to greatly enhance the processivity of the enzyme. The Pol3/Pol31 interface interacts with PCNA when the clamp is loaded onto DNA, but the QxxLxxFF binding domain within the Pol32 subunit governs polymerase δ/PCNA interaction off DNA, suggesting that a potential switch in conformation or general function occurs. (*102*) Polymerase δ moreover is capable of strand displacement synthesis, unlike polymerase ε or pol-α-primase. (*93*) This result is consistent with the role of polymerase δ in Okazaki fragment maturation, along with, among other proteins, helicase-nuclease Dna2. Several [4Fe4S] cofactors in these replication enzymes have been proposed to sense changes in the redox environment (*101*,*107*). DNA polymerase δ is known to be stabilized in the presence of stalled forks during replication stress (*113*). Does this enzyme play a role in cellular response to adverse redox environments?

The chemical role of the polymerase δ [4Fe4S] cluster was, until recently, not clear. Bartels and coworkers measured the DNA-bound redox potential of polymerase δ in the presence of PCNA on a DNA electrode and showed that this enzyme is redox-active, with a potential near 100mV vs. NHE, in the presence of a primed DNA substrate similar to those encountered by

polymerase δ in cells (*40*). The robust electrochemical signal was observed even at very low concentrations of protein, and it was attenuated by an abasic site in the DNA duplex, indicating that the signal is DNA-mediated. Electrochemical oxidation of polymerase δ using a DNA electrode platform, or oxidation using a tethered anthraquinone photooxidant, slowed polymerase δ activity in the presence of a primer-labeled DNA substrate, single-stranded DNA binding protein RPA, PCNA, RFC, ATP, and dNTPs. The oxidized enzyme synthesized significantly fewer products, especially at earlier time points, than the native, reduced enzyme. These findings moreover inspired a model by which PCNA-bound, reduced polymerase δ actively synthesizes products on a DNA template. When oxidizing conditions are present in cells, however, the polymerase δ cluster can be oxidized to the $[4Fe4S]^{3+}$ form, binding very tightly in the presence of PCNA and effectively stalled on the DNA. Since re-reducing the protein restores native activity in these polymerase assays, it was proposed that polymerase δ can remain stalled in the oxidized form on DNA and can be reduced again after damage resolution. (**Figure 1.11**)

Many More Possible [4Fe4S] Cluster Redox Roles in DNA Processing

In addition to the primary replicative eukaryotic DNA polymerases(*11*), several other replication and transcription enzymes have now been discovered to contain [4Fe4S] cofactors. (*11,114,115*) Dna2, for example, is a [4Fe4S] helicase-nuclease enzyme important in DNA double strand break repair, Okazaki fragment maturation, and processing of stalled replication forks (*116*). The cluster in Dna2 is located in the nuclease domain, approximately 10Å from the bound ssDNA substrate in a recent crystal structure (*116*). The 5' to 3' endonuclease activity of Dna2 is primarily associated with long flap processing during Okazaki fragment maturation, when RNA primers are removed from the lagging strand and replaced with products synthesized by the high-fidelity polymerase δ. (*93*) The endonuclease function of Dna2 also plays a role in

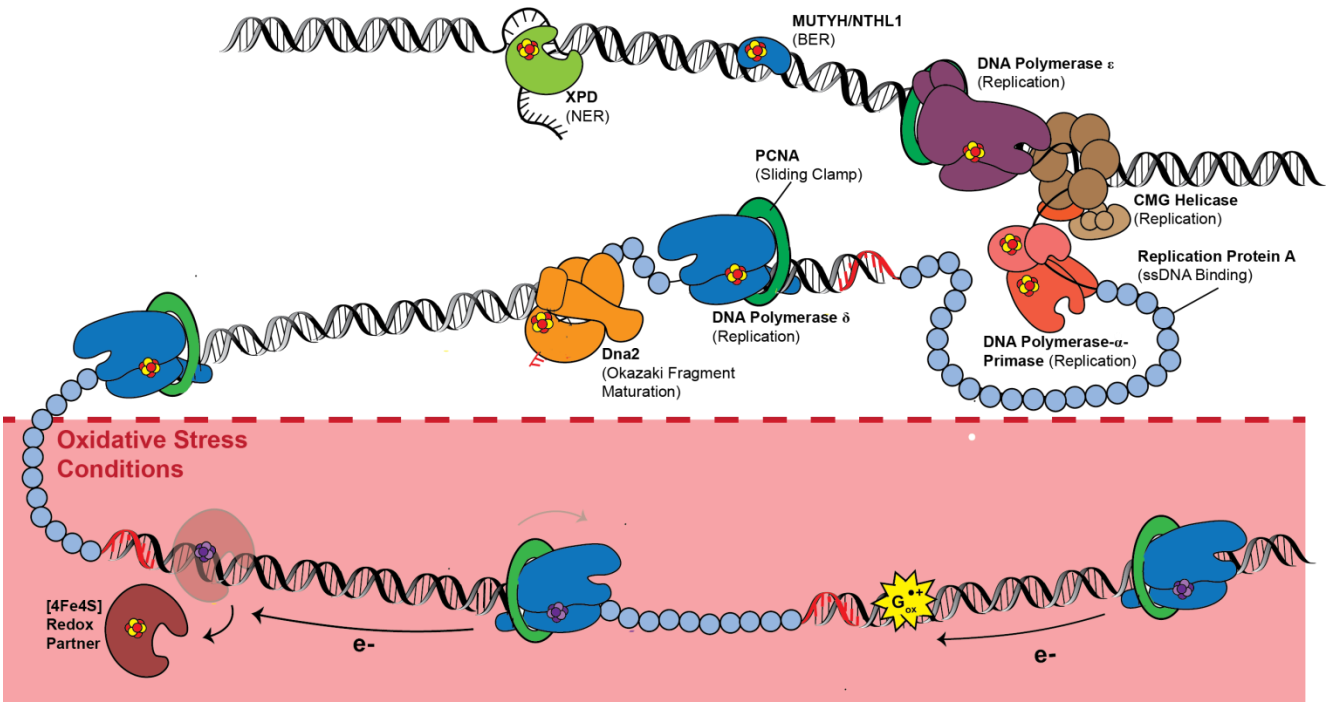

Figure 1.11. [4Fe4S] enzymes in eukaryotic repair and replication. B-family polymerases, DNA primase, Dna2 helicase-nuclease, BER/NER enzymes such as MUTYH, NTHL1, and XPD, all coordinate a [4Fe4S] cluster cofactor. Several of these proteins have been demonstrated to participate in DNA-mediated redox signaling; characterization of their redox roles is ongoing. (Below) Under oxidative stress conditions, polymerase δ may be conerted to the $[4Fe4S]^{3+}$ state as a means to stall synthesis under poor cellular conditions. Polymerase δ can be reversibly oxidized and reduced through DNA CT, which may regulate polymerase activity on the lagging strand.

preventing regression of stalled replication forks, however, and the enzyme has weak ATP-dependent helicase activity (*117,118*). These biochemical details of these functions are still not completely understood; [4Fe4S] redox signaling may play a role in coordinating the enzymatic activities of Dna2. The multisubunit translesion polymerase ζ also contains a [4Fe4S] cluster, which is coordinated in the Rev3 catalytic subunit of the enzyme. (*11,119*) The Rev3 domain is largely homologous to the other B-family polymerase catalytic subunits containing a cluster (*11*), and this enzyme contains two subunits, Pol31 and Pol32, which are also found in the DNA polymerase δ holoenzyme. Together with the Rev7 subunit, this tetrameric enzyme is responsible for mutagenic polymerase activity in the presence of lesions that stall replication fork progression.(*119*) This low-fidelity translesion synthesis polymerase does not contain an exonuclease proofreading domain, as found in DNA polymerases δ and ε. It does have important interaction partners, such as PCNA and the mutasome assembly factor Rev1 in cells, however, which may suggest a role for redox signaling in coordination of activities. (*119*) Finally, RNA polymerase II in several species of archaea have now been demonstrated to contain [4Fe4S] cofactors. (*120*) This enzyme is responsible for RNA synthesis on a DNA template during transcription, and the cluster has been suggested to play a role in stabilizing assembly of the protein complex, which in many organisms contains more than 10 subunits. (*114, 119*) The redox signaling capacity of this [4Fe4S] enzyme, however, is unclear and requires further electrochemical and biophysical investigation.

Summary and Perspectives

Long-range, DNA-mediated redox signaling provides a biochemical means to coordinate activity between replication and repair machinery across the nucleus, between enzymes from different pathways. DNA CT provides a more rapid means through which [4Fe4S] repair

enzymes can locate lesions which they are responsible for removing, but which do not perturb the overall DNA helix structure. The redox switching function associated with a change in the cluster oxidation state, moreover, provides a means of controlling enzyme association and dissociation with the DNA substrate. This capacity is an integral part of the DNA CT-driven lesion search in [4Fe4S] repair proteins, as well as a potential mechanism for regulating polymerase handoff and oxidative stress response in replication machinery. The change in cluster redox potential which occurs upon binding the DNA polyanion, and the capacity of these DNA-bound proteins to cycle between the $[4Fe4S]^{2+}$ and $[4Fe4S]^{3+}$ redox states at physiological potentials, are common biochemical properties which orchestrate different functions in the array of DNA-processing [4Fe4S] enzymes. More investigations of redox chemistry performed by these diverse and specialized proteins will illuminate several exciting new discoveries of the role this chemistry plays in cells.

References

1. Beinert, H.; Holm, R.H.; Münck, E. Iron-Sulfur Clusters: Nature's Modular, Multipurpose Structures. *Science* **1997**, *277*, 653-659.

2. Rees, D.C., Howard, J.B. The Interface Between the Biological and Inorganic Worlds: Iron-Sulfur Metalloclusters., *Science*, **2003**, *300*, 929-931.

3. Meyer, J. Iron-sulfur protein folds, iron-sulfur chemistry, and evolution. *J. Biol. Inorg. Chem.*, **2008,** *13*, 157-170**.**

4. Dey, A., et al. Solvent tuning of electrochemical potentials in the active sites of HiPIP versus ferredoxin. *Science,* **2007**, *318*, 1464-1468.

5. Bertini, I.; Gray, H.B.; Lippard, S.J.; Valentine, J.S. *Bioinorganic Chemistry*. University Science Books, 1994. Print.

6. Mortenson, L.E., Valentine, R.C., Carnahan, J.E. An electron transport factor from *Clostridium pasteurianum*. *Biochem. Biophys. Res. Commun.*, **1962**, *7*, 448-452.

7. Sands, R.H., Beinert, H. Studies on mitochondria and submitochondrial particles by paramagnetic resonance (EPR) spectroscopy. *Biochem. Biophys. Res. Commun.*, **1960**, *3*, 47-52.

8. Gray, H.B., Winkler, J.R. Electron flow through metalloproteins. *Biochim. Biophys. Acta, Bioenerg.*, **2010**, *1797*, 1563-1572.

9. Lill, R. Function and biogenesis of iron–sulphur proteins. *Nature*, **2009**, 460, 831-838.

10. Rouault, T.A. Mammalian iron-sulphur proteins: novel insights into biogenesis and function. *Nat. Rev. Mol. Cell Biol.*, **2015,** *16*, 45-55**.**

11. Netz, D.J.A., Stith, C.M., Stümpfig, M., Köpf, G., Vogel, D., Genau, H.M., Stodola, J.L., Lill, R., Burgers, P.M.J., Pierik, A.J. Eukaryotic DNA polymerases require an iron-sulfur cluster for the formation of active complexes. *Nature Chemical Biology*., **2012**, *8,* 125-132.

12. Fuss, J.O., Tsai, C., Ishida, J.P., Tainer, J.A. Emerging critical roles of Fe-S clusters in DNA replication and repair. *BBA*, **2015**, *1853*, 1253-1271.

13. Kispal, G., Csere, P., Prohl, P., Lill, R. The mitochondrial proteins Atm1p and Nfs1p are essential for biogenesis of cytosolic Fe/S proteins. *EMBO J.*, **1999**, *18*, 3981-3989.

14. Lill, R., Muhlenhoff, U**.** Iron-sulfur protein biogenesis in eukaryotes: components and mechanisms. *Annu. Rev. Cell Dev. Biol.*, **2006**, *22*, 457-486.

15. Vickery, L.E., Cupp-Vickery, J.R. Molecular Chaperones HscA/Ssq1 and HscB/Jac1 and Their Roles in Iron-Sulfur Protein Maturation. *Crit. Rev. Biochem. Mol. Biol.*, **2007**, *42*, 95-111.

16. Gerber, J., Neumann, K., Prohl, C., Muhlenhoff, U., Lill, R. The Yeast Scaffold Proteins Isu1p and Isu2p Are Required inside Mitochondria for Maturation of Cytosolic Fe/S Proteins. *Mol. Cell Biol.*, **2004**, *24*, 4848-4857.

17. Arnon, D.I., Whatley, F.R., Allen, M.B. Triphosphopyridine Nucleotide as a Catalyst of Photosynthetic Phosphorylation. *Nature*, **1957**, 180, 182-185.

18. Cunningham, R.P., Asahara, H., Bank, J.F., Scholes, C.P., Salerno, J.C., Surerus, K., Munck, E., McCracken, J., Peisach, J., Emptage, M.H. Endonuclease III is an iron-sulfur protein. *Biochemistry,* **1989**, *28*, 4450-4455.

19. Michaels, M.L., Pham, L., Nghiem, Y., Cruz, C., Miller, J.H. MutY, an adenine glycosylase active on G-A mispairs, has homology to endonuclease III. *Nucleic Acids Research*, **1990**, *18*, 3841-3844.

20. Kim, Y.-J., Wilson III, D.M. Overview of Base Excision Repair Biochemistry. *Curr. Mol. Pharmacol.*, **2012**, *5,* 3-13.

21. Guan, Y., Manuel, R.C., Arvai, A.S., Parikh, S.S., Mol, C.D., Miller, J.H., Lloyd, R.S., Tainer, J.A. MutY catalytic core, mutant, and bound adenine structures define specificity for DNA repair enzyme superfamily. *Nat. Struct. Biol.,* **1998**, *5*, 1058-1064.

22. Hinks, J.A., Evans, M.C.W., de Miguel, Y., Sartori, A.A., Jiricny, J., and Pearl, L.H. An Iron-Sulfur Cluster in the Family 4 Uracil-DNA Glycosylases. *J. Biol. Chem.,* **2002**, *277*, 16936-16940.

23. Boal, A.K., Yavin, E., Lukianova, O.A., O'Shea, V.L., David, S.S., Barton, J.K. DNA-Bound Redox Activity of DNA Repair Glycosylases Containing [4Fe-4S] Clusters. *Biochemistry,* **2005**, *44*, 8397-8407.

24. Fu, W., O'Handley, S., Cunningham, R.P., Johnson, M.K. The Role of the Iron-Sulfur Cluster in *Escherichia coli* Endonuclease III: A Resonance Raman Study. *J. Biol. Chem.*, **1992**, *267*, 16135-16137.

25. Thayer, M.M., Ahern, H., Xing, D., Cunningham, R.P., Tainer, J.A. Novel DNA binding motifs in the DNA repair enzyme endonuclease III crystal structure. *The EMBO J.,* **1995**, *14*, 4108-4120.

26. Porello, S.L., Cannon, M.J., David, S.S. A substrate recognition role for the $[4Fe\text{-}4S]^{2+}$ cluster of the DNA repair glycosylase MutY. *Biochemistry,* **1998**, *37*, 6465-6475.

27. Bartels, P.L., O'Brien, E., Barton, J.K. DNA Signaling by Iron-Sulfur Cluster Proteins. *Iron-Sulfur Clusters in Chemistry and Biology (ed. T. Rouault, de Gruyter, Berlin/Boston*), 2, 405-423 (2017).

28. Zhang, F., Scheerer, P., Oberpichler, I., Lamparter, T., Krauβ, N. Crystal structure of a prokaryotic (6-4) photolyase with an Fe-S cluster and a 6,7-dimethyl-8-ribityllumazine antenna chromophore. *Proc. Natl. Acad. Sci. USA*, **2013**, *110*, 7217-7222.

29. Zhang, J., Kasciukovic, T., White, M.F. The CRISPR Associated Protein Cas4 Is a 59 to 39 DNA Exonuclease with an Iron-Sulfur Cluster. *PLoS ONE,* **2012**, *7*, e47232.

30. Eley, D.D., Spivey, D.I. Semiconductivity of organic substances. Part 9.—Nucleic acid in the dry state. *Trans. Faraday Soc.*, **1962**, *58*, 411-415.

31. Murphy, C.J., Arkin, M.R., Jenkins, Y., Ghatalia, N.D., Bossmann, S., Turro, N.J., Barton, J.K. *Science,* **1993**, *262*, 1025-1029.

32. Kelley, S.O., Barton, J.K. Electron transfer between bases in double helical DNA. *Science*, **1999**, *283*, 375-381.

33. Nunez, M.E., Hall, D.B., Barton, J.K. Long-range oxidative damage to DNA: effects of distance and sequence. *Chem. Biol. (Oxford, U. K.)*, **1999**, *6*, 85-97.

34. O'Neill, M.A., Becker, H.-C., Wan, C., Barton, J.K., Zewail, A.H. Ultrafast Dynamics in DNA-Mediated Electron Transfer: Base Gating and the Role of Temperature. *Angew. Chem. Int. Ed. Engl.*, **2003**, *42*, 5896-5900.

35. Rajski, S.R., Barton, J.K. How Different DNA-Binding Proteins Affect Long-Range Oxidative Damage to DNA. *Biochemistry,* **2001**, *40*, 5556-5564.

36. Kelley, S.O., Boon, E.M., Barton, J.K., Jackson, N.M., Hill, M.G. Single-base mismatch detection based on charge transduction through DNA. *Nuc. Acids Res.*, **1999**, *27*, 4830-4837.

37. Slinker, J. D., Muren, N. B., Gorodetsky, A. A., Barton, J. K. Multiplexed DNA-modified electrodes. *J. Am. Chem. Soc.,* **2010**, *132*, 2769-2774.

38. Slinker, J.D., Muren, N.B., Renfrew, S.E., Barton, J.K. DNA charge transport over 34 nm. *Nature Chem.* **2011**, *3*, 228-233.

39. Mui, T.P., Fuss, J.O., Ishida, J.P., Tainer, J.A., Barton, J.K. ATP-Stimulated, DNA-Mediated Redox Signaling by XPD, a DNA Repair and Transcription Helicase. *J. Amer. Chem. Soc.* **2011**, *133*, 16378-16381.

40. Grodick, M.A., Segal, H.M., Zwang, T.J., Barton, J.K. DNA-Mediated Signaling by Proteins with 4Fe-4S Clusters Is Necessary for Genomic Integrity. *J. Amer. Chem. Soc.* **2014**, *136*, 16470-16478.

41. Bartels, P.L., Stodola, J.L., Burgers, P.M.J., Barton, J.K. A Redox Role for the [4Fe4S] Cluster of Yeast DNA Polymerase δ. *J. Am. Chem. Soc.*, **2017**, *139*, 18399-18348.

42. O'Brien, E., Holt, M.E., Thompson, M.K., Salay, L.E., Ehlinger, A.C., Chazin, W.J., Barton, J.K. The [4Fe4S] cluster of human DNA primase functions as a redox switch using DNA charge transport. *Science*, **2017**, *355*, eaag1789.

43. Pheeney, C.G., Arnold, A.R., Grodick, M.A., Barton, J.K. Multiplexed electrochemistry of DNA-bound metalloproteins. *J. Am. Chem. Soc.,* **2013**, *135*, 11869-11878.

44. Sontz, P.A., Mui, T.P., Fuss, J.O., Tainer, J.A., Barton, J.K. DNA charge transport as a first step in coordinating the detection of lesions by repair proteins. *Proc. Natl. Acad. Sci. USA*, **2012**, *109*, 1856-1861.

45. Tse, E.C.M., Zwang, T.J., Barton, J.K. The Oxidation State of [4Fe4S] Clusters Modulates the DNA-Binding Affinity of DNA Repair Proteins. *J. Am. Chem. Soc*., **2017**, *139*, 12784-12792.

46. Bartels, P.L., Zhou, A., Arnold, A.R., Nunez, N.N., Crespilho, F.N., David, S.S., Barton, J.K. Electrochemistry of the [4Fe4S] Cluster in Base Excision Repair Proteins: Tuning the Redox Potential with DNA. *Langmuir.*, **2017**, *33*, 2523-2530.

47. Grodick, M.A., Muren, N. B., Barton, J. K., DNA charge transport within the cell. *Biochemistry*, **2015**, *54*, 962-973.

48. Bard, A.J., Faulkner, L.A. Electrochemical Methods: Fundamentals and Applications, 2nd Edition. New York, NY: John Wiley & Sons. 2001. Print.

49. Gorodetsky, A.A., Boal, A.K., Barton, J.K. Direct electrochemistry of Endonuclease III in the presence and absence of DNA. *J. Am. Chem. Soc.* **2006**, *128*, 12082-12083.

50. DeRosa, M.C., Sancar, A., and Barton, J.K. Electrically monitoring DNA repair by photolyase. *Proc. Natl. Acad. Sci. USA*, **2005**, *102*, 10788-10792.

51. McDonnell, K.J.,* Chemler, J.A.,* Bartels, P.L.,* O'Brien, E., Marvin, M.L., Ortega, J., Stern, R.H., Raskin, L., Li, G., Sherman, D.H., Barton, J.K., Gruber, S.B. A Novel Human MUTYH Variant Causing Colonic Polyposis through Redox Degradation of the $[4Fe4S]^{2+}$ Cluster. Nature Chemistry, **2018**, accepted.

52. Banks, C.E., Compton, R.G. New Electrodes for old: from carbon nanotubes to edge plane pyrolytic graphite. *Analyst*, **2006**, 131, 15-21.

53. Blanford, C.F., Armstrong, F.A. The pyrolytic graphite surface as an enzyme substrate: microscopic and spectroscopic studies. *J. Solid State Electrochem.*, **2006**, *10*, 826-832.

54. Nechushtai, R., et al. Allostery in the ferredoxin protein motif does not involve a conformational switch. *Proc. Natl. Acad. Sci. USA,* **2011**, *108*, 2240-2245.

55. Klinge, S., Hirst, J., Maman, J.D., Krude, T., Pellegrini, L. An iron-sulfur domain of the eukaryotic primase is essential for primer synthesis. *Nat. Struct. Mol. Biol.,* **2007**, *14*, 875-877.

56. Weiner, B.E., Huang, H., Dattilo, B.M., Nilges, M.J., Fanning, E., Chazin, W.J. An iron-sulfur cluster in the c-terminal domain of the p58 subunit of human DNA primase. *J. Biol. Chem.*, **2007**, *282*, 33444-33451.

57. Ha, Y., et al. Sulfur K-Edge XAS Studies of the Effect of DNA Binding on the [Fe_4S_4] Site in EndoIII and MutY. *J. Am. Chem. Soc.*, **2017**, *139*, 11434-11442.

58. David, S.S., Wiliams, S.D. Chemistry of Glycosylases and Endonucleases Involved in Base-Excision Repair. *Chem. Rev. (Washington, DC, U. S.)*, **1998**, *98*, 1221-1261.

59. Kuo, C.F., McRee, D.E., Fisher, C.L., O'Handley, S.F., Cunningham, R.P., Tainer, J.A. Atomic structure of the DNA repair [4Fe-4S] enzyme endonuclease III. *Science*, **1992**, *258*, 434-440.

60. Fromme, J.C., Verdine, G.L. Structure of a trapped endonuclease III–DNA covalent intermediate. *EMBO J.*, **2003**, *22*, 3461-3471.

61. Lukianova, O.A., David, S.S. A role for iron-sulfure clusters in DNA repair. *Curr. Opin. Chem. Biol.*, **2005**, *9*, 145-151.

62. Romano, C.A.,* Sontz, P.A.* Barton, J.K. Mutants of the Base Excision Repair Glycosylase, Endonuclease III: DNA Charge Transport as a First Step in Lesion Detection. *Biochemistry*, **2011**, *50*, 6133-6145.

63. Boon, E.M., Livingston, A.L., Chmiel, N.H., David, S.S., Barton, J.K. DNA-mediated charge transport for DNA repair. *Proc. Natl. Acad. Sci. U. S. A.*, **2003**, *100*, 12543-12547.

64. Lee, S., Verdine, G.L. Atomic substitution reveals the structural basis for substrate adenine recognition and removal by adenine DNA glycosylase. *Proc. Natl. Acad. Sci. USA*, **2009**, *106*, 18497-18502.

65. Woods, R.D., O'Shea, V.L., Chu, A., Cao, S., Richards, J.L., Horvath, M.P., David, S.S. Structure and stereochemistry of the base excision repaire glycosylase MutY reveal a mechanism similar to retaining glycosylases. *Nucleic Acids Research,* **2015**, *44*, 801-810.

66. Crespo-Hernández, C.E., Close, D.M., Gorb, L., Leszczynski, J. Determination of Redox Potentials for the Watson-Crick Base Pairs, DNA Nucleosides, and Relevant Nucleoside Analogues. *J. Phys. Chem. B*, **2007**, *111*, 5386-5395.

67. Paukku, Y., Hill, G. Theoretical Determination of One-Electron Redox Potentials for DNA Bases, Base Pairs, and Stacks.*J. Phys. Chem. A*, 2011, *115*, 4804-4810.

68. Cowan, J.A., Lui, S.M. Structure-Function Correlations in High-Potential Iron Proteins. *Adv. Inorg. Chem.*, 1998, *45*, 313-350.

69. Liu, J., Chakraborty, S., Hosseinzadeh, P., Yu, Y., Tian, S., Petrik, I., Bhagi, A., Lu, Y. Metalloproteins Containing Cytochrome, Iron–Sulfur, or Copper Redox Centers *Chem. Rev. (Washington, DC, U. S.)*, **2014**, *114*, 4366-4469.

70. Spivak, G. Nucleotide excision repair in humans. *DNA Repair*, **2015**, *36*, 13-18.

71. Voloshin, O.N., Vanevski, F., Khil, P.P. Camerini-Otero, R.D. Characterization of the DNA Damage-inducible Helicase DinG from *Escherichia coli. J. Biol. Chem.*, **2003**, *278*, 28284-28293.

72. Ren, B. Duan, X., Ding, H. Redox Control of the DNA Damage-inducible Protein DinG Helicase Activity via Its Iron-Sulfur Cluster *J. Biol. Chem.*, **2009**, *284*, 4829-4835.

73. Boal, A.K., Barton, J.K. Electrochemical Detection of Lesions in DNA. *Bioconj. Chem.*, **2005**, *16*, 312-321.

74. S. R. Rajski, B. A. Jackson, J. K. Barton, DNA repair: models for damage and mismatch recognition. *Mutat. Res., Fundam. Mol. Mech. Mutagen.*, **2000**, *447*, 49-72.

75. Boal, A.K., Genereux, J.C., Sontz, P.A., Gralnick, J.A., Newman, D.K., Barton, J.K. Redox signaling between DNA repair proteins for efficient lesion detection. *Proc. Natl. Acad. Sci. U. S. A.* **2009**, *106,* 15237-15242.

76. Cupples, C.G., Miller, J.H. A set of lacZ mutations in Escherichia coli that allow rapid detection of each of the six base substitutions. *Proc. Natl. Acad. Sci. U. S. A.*, **1989**, *86*, 5345-5349.

77. Boubakri, H., de Septenville, A.L., Viguera, E., Michel, B. The helicases DinG, Rep and UvrD cooperate to promote replication across transcription units in vivo. *EMBO J.*, **2010**, *2003*, 145-157.

78. Moran, U., Phillips, R., Milo, R. SnapShot: Key Numbers in Biology. *Cell*, **2010**, *141*, 1262.

79. Ganai, R.A., Johansson, E. DNA Replication- A Matter of Fidelity. *Mol. Cell*, **2016**, *62*, 745-755.

80. Budd, M.E., Choe, W.-C., Campbell, J.L. DNA2 Encodes a DNA Helicase Essential for Replication of Eukaryotic Chromosomes. *J. Biol. Chem.*, **1995**, *270*, 26766-26769.

81. Baranovskiy, A.G., Babayeva, N.D., Zhang, Y., Gu, J., Suwa, Y., Pavlov, Y.I., Tahirov, T.H. Mechanism of Concerted RNA-DNA Primer Synthesis by the Human Primosome. *J. Biol. Chem.*, **2016**, *291*, 10006-10020.

82. Johansson, E., Majka, J., Burgers, P.M.J. Structure of DNA Polymerase δ from *Saccharomyces cerevisiae*. *J. Biol. Chem.*, **2001**, *276,* 43824-43828.

83. Chilkova, O., Jonsson, B.-H., Johansson, E. The Quaternary Structure of DNA Polymerase ε from *Saccharomyces cerevisiae*. *J. Biol. Chem.*, **2003**, *278*, 14082-14086.

84. Nelson, J., Lawrence, C., Hinkle, D. Thymine-thymine dimer bypass by yeast DNA polymerase ζ. *Science,* **1996**, *272*, 1646-1649.

85. Makarova, K.S., Koonin, E.V. Archaeology of Eukaryotic DNA Replication. *Cold Spring Harb Perspect Biol*, **2013**, *5*, a012963.

86. Yeeles, J.T.P., Deegan, T.D., Janska, A., Early, A., Diffley, J.F.X. Regulated eukaryotic DNA replication origin firing with purified proteins. *Nature*, **2015**, *519*, 431-435.

87. Fragkos, et. al. DNA replication origin activation in space and time. *Nature Reviews Cellular and Molecular Biology,* **2015**, *16*, 360-374.

88. Iyer, L.M., Leipe, D.D., Koonin, E.V., Aravind, L. Evolutionary history and higher order classification of AAA+ ATPases. *J. Struct. Biol.*, **2004**, *146*, 11-31.

89. Duncker, B.P., Chenokov, I.N., McConkey, B.J. The origin recognition complex protein family. *Genome Biol.*, **2009**, *10*, 214.

90. Moyer, S.E., Lewis, P.W., Botchan, M.R. Isolation of the Cdc45/Mcm2-7/GINS (CMG) complex, a candidate for the eukaryotic DNA replication fork helicase. *Proc. Natl. Acad. Sci. USA*, **2006**, *103*, 10236-10241.

91. Pacek, M., Tutter, A.V., Kubota, Y., Takisawa, H., Walter, J.C. Localization of MCM2-7, Cdc45, and GINS to the site of DNA unwinding during eukaryotic DNA replication. *Mol. Cell*, **2006**, *21*, 581-587.

92. Labib, K., Gambus, A. A key role for the GINS complex at DNA replication forks. *Trends. Cell. Biol.,* **2007**, *18*, 521-527.

93. Burgers, P.M.J., Kunkel, T.A. Eukaryotic DNA Replication Fork. *Annu. Rev. Biochem.*, **2017**, *86*, 417-438.

94. Arezi, B., Kuchta, R.D. Eukaryotic DNA primase. *Trends in Biochemical Sciences*., **2000**, *25*, 572-576.

95. Kuchta, R.D., Stengel, G. Mechanism and evolution of DNA primases. *Biochimica et Biophysica Acta*. **2010**, *1804*, 1180-1189.

96. Frick, D.N., Richardson, C.C. DNA Primases. *Annu. Rev. Biochem.,* **2001**, *70,* 39-80.

97. Nunez-Ramirez, R., et al. Flexible tethering of primase and DNA Pol α in the eukaryotic primosome. *Nuc. Acids Res.*, **2011**, *39*, 8187-8199.

98. a) Sheaff, R.J., Kuchta, R.D., Ilsley, D. Calf thymus DNA polymerase-α-primase: "communication" and primer•template movement between the two active sites. *Biochemistry*. **1994**, *33*, 2247-2254. b) Sheaff, R.J., Kuchta, R.D. Misincorporation of nucleotides by calf thymus DNA primase and elongation of primers containing multiple noncognate nucleotides by DNA polymerase α. *J. Biol. Chem.* **1994**, *269*, 19225-19231.

99. a) Kilkenny, M.L., Longo, M.A., Perera, R.L., Pellegrini, L. Structures of human primase reveal design of nucleotide elongation site and mode of pol α tethering. *Proc. Natl. Acad. Sci. USA*., **2013**, *110*, 15961-15966. b) Perera, R.L., Torella, R., Klinge, S., Kilkenny, M.L., Maman, J.D., Pellegrini, L. Mechanism for priming DNA synthesis by yeast DNA polymerase α. *eLife*, **2013**, *2*, e00482.

100. a) Vaithiyalingam, S., Warren, E.M., Eichman, B.F., Chazin, W.J. Insights into eukaryotic priming from the structure and functional interactions of the 4Fe-4S cluster domain of human DNA primase. *Proc. Natl. Acad. Sci. USA*., **2010**, *107*, 13684-13689. b) Sauguet, L., Klinge, S., Perera, R.L., Maman, J.D., Pellegrini, L. Shared active site architecture between the large subunit of eukaryotic primase and DNA photolyase. *PloS One*. **2010**, *5*, e10083.

101. Liu, L., Huang, M. Essential role of the iron-sulfur cluster binding domain of the primase regulatory subunit Pri2 in DNA replication initiation. *Protein Cell*, **2015**, *6*, 194-210.

102. Garg, P., Burgers, P.M.J. DNA Polymerases that Propagate the Eukaryotic DNA Replication Fork. *Critical Reviews in Biochemistry and Molecular Biology*, **2005**, *40*, 115-128.

103. Nick McElhinny, S.A., Kumar, D., Clark, A.B., Watt, D.L., Watts, B.E., et al. Genome instability due to ribonucleotide incorporation into DNA. *Nat. Chem. Biol.*, **2010**, *6*, 774–781.

104. Lujan, S.A., Williams, J.S., Clausen, A.R., Clark, A.B., Kunkel, T.A. Ribonucleotides are signals for mismatch repair of leading-strand replication errors. *Mol. Cell*, **2014**, *50*, 437–443.

105. McElhinny, S.A., Stith, C.M., Burgers, P.M., Kunkel, T.A. Inefficient proofreading and biased error rates during inaccurate DNA synthesis by a mutant derivative of *Saccharomyces cerevisiae* DNA polymerase δ. *J. Biol. Chem.*, **2007**, *282*, 2324–2332.

106. Johnson, R.E., Klassen, R., Prakash, L., Prakash, S. A major role of DNA polymerase δ in replication of both the leading and lagging DNA strands. *Mol. Cell*, **2015**, *59*, 163–175.

107. Jain, R., et al. An Iron–Sulfur Cluster in the Polymerase Domain of Yeast DNA Polymerase ε. *J. Mol. Biol.*, **2014**, *426*, 301-308.

108. Sengupta, S., van Deursen, F., de Piccoli, G., Labib, K. Dpb2 integrates the leading-strand DNA polymerase into the eukaryotic replisome. *Curr. Biol.*, **2013**, *23*, 543–552.

109. Sun, J., Shi, Y., Georgescu, R.E., Yuan, Z., Chait, B.T., et al. The architecture of a eukaryotic replisome. *Nat. Struct. Mol. Biol.*, **2015**, *22*, 976–982.

110. Langston, L.D., Zhang, D., Yurieva, O., Georgescu, R.E., Finkelstein, J., et al. CMG helicase and DNA polymerase ε form a functional 15-subunit holoenzyme for eukaryotic leading-strand DNA replication. *Proc. Natl. Acad. Sci. USA*, **2014**, *111*, 15390–15395.

111. Tsurimoto, T., Stillman, B. Replication factors required for SV40 DNA replication in vitro. II. Switching of DNA polymerase αand δ during initiation of leading and lagging strand synthesis. *J. Biol. Chem.*, **1991**, *266*, 1961–1968.

112. Yuzhakov, A., Kelman, Z., Hurwitz, J., O'Donnell, M. Multiple competition reactions for RPA order the assembly of the DNA polymerase δ holoenzyme. *EMBO J.*, **1999**, *18*, 6189–6199.

113. De Piccoli, G., Katou, Y., Itoh, T., Nakato, R., Shirahige, K., Labib, K. Replisome stability at defective DNA replication forks is independent of S phase checkpoint kinases. *Mol. Cell*, **2012**, *45*, 696-704.

114. Hirata, A., Klein, B.J., Murakami, K.S., The X-ray crystal structure of RNA polymerase from Archaea Nature, **2008**, *451*, 851-854.

115. Pokharel, S., Campbell, J.L. Cross talk between the nuclease and helicase activities of Dna2: role of an essential iron–sulfur cluster domain. *Nuc. Acids. Res.*, **2012**, *40,* 7821-7830.

116. Zhou, C., Pourmal, S., Pavletich, N.P. Dna2 nuclease-helicase structure, mechanism and regulation by Rpa. *eLife*, **2015**, *4*, e09832.

117. Hu, J., Sun, L., Shen, F., Chen, Y., Hua, Y., Liu, Y., Zhang, M., Hu, Y., Wang, Q., Xu, W., Sun, F., Ji, J., et al. The intra-s phase checkpoint targets Dna2 to prevent stalled replication forks from reversing *Cell*, **2012,** *149*, 1221-1232.

118. Budd, M.E. The nuclease activity of the yeast Dna2 protein, which is related to the RecB-like nucleases, is essential in vivo. *Journal of Biological Chemistry*, **2000**, *275*,16518–16529.

119. Makarova, A.V., Burgers, P.M.J. Eukaryotic DNA Polymerase ζ. *DNA Repair*, **2015**, *29*, 47-55.

120. Jennings, M.E., et al. The [4Fe-4S] clusters of Rpo3 are key determinants in the post Rpo3/Rpo11 heterodimer formation of RNA polymerase in *Methanosarcina acetivorans MicrobiologyOpen*, **2017**, *6*, e00399.

Chapter 2: The [4Fe4S] Cluster of Human DNA Primase functions as a Redox Switch using DNA Charge Transport

Adapted from: **O'Brien E**, Holt ME, Thompson MK, Salay LE, Ehlinger AC, Chazin WJ, Barton JK (2017) The [4Fe4S] cluster of human DNA primase functions as a redox switch using DNA charge transport. *Science*. 355(6327): eaag1789.

E. O'Brien wrote the manuscript, performed all electrochemistry experiments and analysis, and performed all primase activity experiments and analysis. M.K. Thompson and L.E. Salay performed X-ray crystallography. M.E. Holt and A.C. Ehlinger prepared protein. M.E. Holt performed DNA binding assays and UV-Visible/circular dichroism spectroscopy.

Introduction

The ability of DNA to transport charge over long range represents an intriguing potential regulatory mechanism in biology. DNA charge transport (DNA CT) provides a rapid means of signaling among redox moieties coupled into the DNA duplex, as well as a mechanism to sense the integrity of DNA (*1-6*). Remarkably, [4Fe4S] clusters, inorganic cofactors often associated with biological redox chemistry (*7,8*), are now being identified in proteins involved in DNA replication (*9-17*). The eukaryotic DNA primase enzyme responsible for initiation of replication on single-stranded DNA, for example, is a [4Fe4S] cluster enzyme. The [4Fe4S] cluster in primase has been shown to be essential for activity (*9-16*), but the role of this cofactor was unclear.

Rapid and accurate copying of genomic DNA in humans and other higher eukaryotes is the product of high fidelity, processive, replicative DNA polymerases (*18-21*). While efficient, these enzymes are unable to initiate synthesis of the new complementary strand without a short primer on the single-stranded DNA (ssDNA) template. The task of initiating synthesis of the new DNA strand is the responsibility of a heterotetrameric complex of two specialized polymerases: DNA primase and DNA polymerase α (pol α), both of which were discovered to contain [4Fe4S] clusters (*9-11, 17)*. Primase, a DNA-dependent RNA polymerase, generates an initial 8-12 nucleotide RNA primer on ssDNA before handing the nascent primer-template off to pol α, which extends the primer by ~20 DNA bases before handoff to the more processive polymerases (δ and ε). X-ray crystal structures have been determined for all globular domains of primase and pol α as well as for the primase heterodimer and the heterotetrameric pol-α-primase (pol-prim) complex (*11-16*, *22-25*). However, limited structural data have been obtained about catalytically active conformations and architectural changes in the pol-prim tetramer as the primer is initiated,

elongated first by primase then by pol α, and subsequently handed off to a processive polymerase. In particular, although the mechanism and structure of the catalytic subunit of primase have been extensively studied (*15,16,26,27*), the chemistry behind primase transferring a nascent primer to pol α is poorly understood.

Eukaryotic primases are heterodimeric, composed of a catalytic subunit (p48) and a regulatory subunit (p58) (*28,29*). The regulatory subunit contains a C-terminal domain (p58C) that is unique to eukaryotes and contains the [4Fe4S] cluster cofactor required for efficient priming (*10*). The biochemical evidence of the role for the [4Fe4S] cluster in primase, in addition to the high energetic cost (*8*) paid by cells to assemble and load this cofactor into an enzyme, argues for a functional rather than structural role for the cofactor (*30*).

DNA-Mediated Electrochemistry

To study the DNA-bound redox properties of enzymes with [4Fe4S] clusters, we employ DNA-mediated electrochemistry, a robust method for directly measuring DNA CT in the ground state (*5,31,32*) (**Figure 2.1A, B**). An alkanethiol-terminated, annealed duplex DNA (dsDNA) substrate is deposited on a gold surface, facilitating covalent linkage of the DNA to the gold through the thiol moiety. The gold is passivated using β-mercaptohexanol and becomes the working electrode in a three-electrode cell, with an external Ag/AgCl reference electrode and a platinum counter electrode (*5,31,32*). Charge transport through the stacked bases of dsDNA between the gold surface and a redox-active species bound at the distal end of the DNA can be measured using this platform under solution conditions. Cyclic voltammetry (CV) is employed to measure changes in current over a range of applied potentials. Earlier electrochemical studies of the base excision repair glycosylase Endonuclease III (EndoIII) using CV have shown that

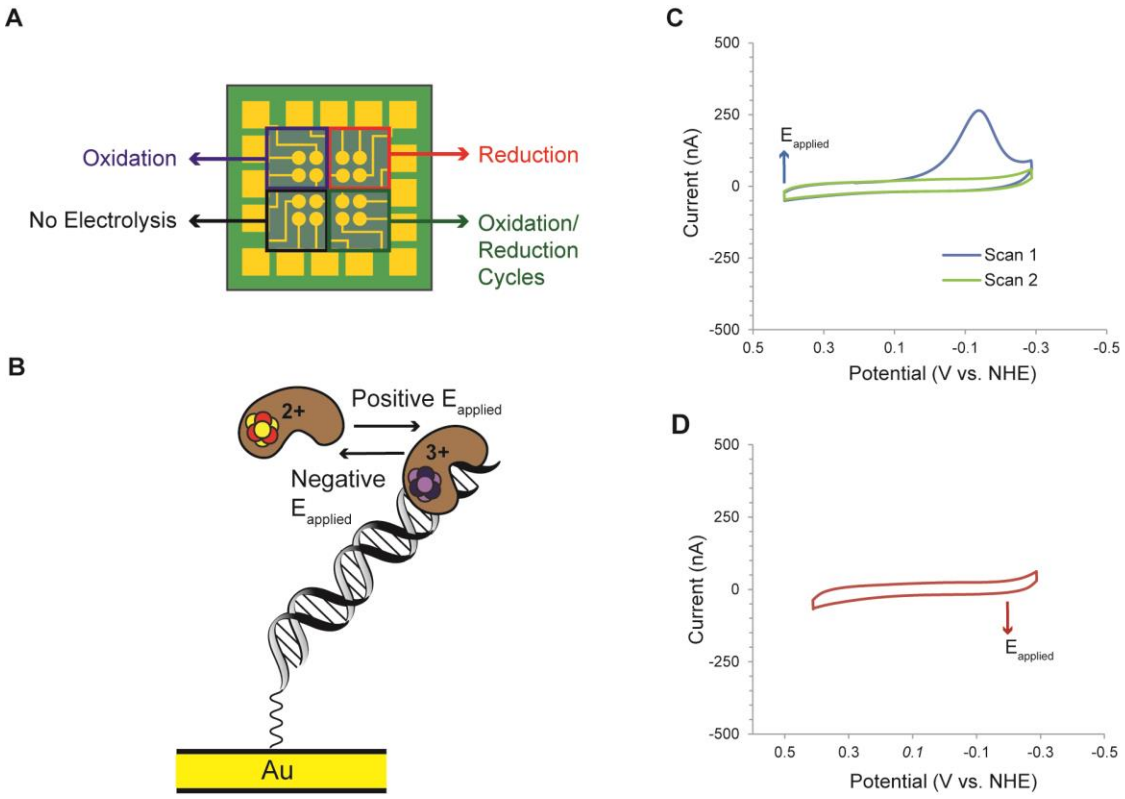

Fig. 2.1. **Oxidized [4Fe4S]$^{3+}$ and reduced [4Fe4S]$^{2+}$ p58C display different behavior on DNA-modified electrodes. A)** Multiplex chip with 16 DNA-modified Au electrodes (circles, center.) This platform facilitates direct comparison of oxidized, reduced, unaltered, and iteratively oxidized samples, on four separate quadrants of a single surface. **B)** The cartoon depicts the effects of electrochemical oxidation and reduction on p58C DNA binding and redox activity. **C)** CV of electrochemically oxidized p58C. After electrochemical conversion ($E_{applied}$ = 412mV vs. NHE) of the sample at the electrode/solution interface to the [4Fe4S]$^{3+}$ state, CV scans display a large cathodic peak only in the initial scan to negative, reducing potentials. **D)** CV of electrochemically reduced p58C. After electrochemical conversion ($E_{applied}$ = -188 mV vs. NHE) of the sample to the [4Fe4S]$^{2+}$ state, CV scans show no electrochemical signal on DNA. Electrochemistry was performed on 16μM p58C in 20 mM Tris, pH 7.2, 75 mM NaCl, 100mV/s for CV scans, using a Ag/AgCl reference electrode.

binding of the protein to the DNA polyanion shifts the redox potential of the [4Fe4S] cluster 200 mV negative to ~80 mV vs. NHE, into the physiological range of cellular potentials, activating the cluster for redox chemistry (*2*,*33*). Importantly, this potential shift corresponds thermodynamically to a 1000-fold increase in DNA binding affinity for the oxidized $[4Fe4S]^{3+}$ state of EndoIII relative to the reduced $[4Fe4S]^{2+}$ state.

Materials and Methods

Protein Expression and Purification. Recombinant WT and mutant p58C were expressed and purified as previously described (*11*). For crystallization of the proteins, an extra affinity purification step was added before size exclusion chromatography. Both WT and mutant p58C were buffer exchanged into 20 mM HEPES (pH 7.2), 2 mM DTT and 200 mM NaCl. Each protein sample was then loaded onto a HiTrap® Heparin column and eluted with a gradient of 20 mM HEPES (pH 7.2), 2 mM DTT and 1 M NaCl. To express primase, full-length p48 and p58 in the PBG100 and multiple cloning site 2 of the pETDuet vectors, respectively, were co-transformed into BL21 (RIL) D3 *E. coli*. The culture was grown in Terrific Broth at 37° C until it reached an O.D. of 0.5-0.8, at which point the growth was transferred to an 18° C incubator. This was allowed to continue growing until it reached an OD of 1-1.5, at which point protein expression was induced with 0.5 mM IPTG. The cells were harvested after expressing at 18° C for 20 hours. To purify primase, cells were lysed using a sonicator and spun at 50,000 rcf. Supernatant loaded onto a nickel column equilibrated in Buffer A (20 mM Tris, 300 mM NaCl, and 20 mM imidazole (pH 8.0). After washing with five column volumes of Buffer A, the primase was eluted with Buffer B (20 mM Tris, 300 mM NaCl, and 300 mM imidazole (pH 8.0). H3C protease was added to primase-containing fractions, and these were dialyzed in to Buffer A at 4° C overnight. Primase was separated from the cleaved 6xHis tag (and uncleaved protein) by

repassing over the nickel column. This sample was further purified by carefully diluting to 150 mM NaCl, loading onto a HiTrap® Heparin column, and eluting with a gradient of 20 mM HEPES (pH 7.2), 3% glycerol, and 1 M NaCl. This was followed by size exclusion chromatography with a Superdex S200 column from GE Healthcare. Primase was eluted into a final storage buffer containing 20 mM HEPES, 150 mM NaCl, 3% glycerol, pH 7.2.

Site Directed Mutagenesis. The Y309F, Y345F, and Y347F p58C mutants were created using a Q5 site directed mutagenesis kit from New England Biolabs. The following primers were supplied by Sigma Genosys to generate the mutant DNA plasmids. For Y309F, the forward primer was 5'-CCGAATGCAGTTTGGCCTATTTC-3' and reverse primers was 5'-CCTCCATGACGAAGATGG-3'. For Y345F, the forward primer was 5'-TGATAAAGGTTTCTCTTACAACATCC-3' and reverse primers was 5'-AACTTGTCTGGATCCATC-3'. For Y347F, the forward primer was 5'-AGGTTACTCTTTCAACATCCGTC-3' and reverse primers was 5'-TTATCAAACTTGTCTGGATCC-3'.

Oligonucleotide preparation. All standard or modified phosphoramidites and DNA synthesis reagents were purchased from Glen Research. Unmodified DNA and 2'-OMe RNA substrates used in electrochemical experiments or primase activity assays were purchased from Integrated DNA Technologies, Inc. DNA sequences for electrochemistry and primase activity assays are shown in **Table 2.1**. Thiol-modified DNA strands for electrochemistry were made on an Applied Biosystems 3400 DNA synthesizer, with a C6 S-S phosphoramidite incorporated at the 5'- terminus. Single-stranded DNA was purified using standard procedures as described previously. (5) Cleavage from the solid support should be performed with 0.3M NH_4OH (Sigma), using fresh reagent that is sealed with parafilm and stored at 4°C. Freshness can be

p58C Electrochemistry Substrates	Well-matched 5'-SH-GTCGTGCAACGTGTCTGCGC-3' 3'-CAGCACGTTGCACAGACGCGTAC-5'	Abasic Site 5'-SH-GTCGTGCAACGTGTCTGCGC-3' 3'-CAG_ACGTTGCACAGACGCGTAC-5'
Initiation Substrate	3'-AAAAAAAAAAAAAAAAAAAAAAAAAATAAAGAGAGAGAGAGAGAGAAAAGA-5'	
Well-Matched Elongation Substrate	3'-(U)$_{16}$(T)$_{15}$-5' 5'-AGAAAAGAGAGAGAGAGAGAGAAAAGAAT(A)$_{31}$-3'	
Mismatched Elongation Substrate	3'-(U)$_{16}$(T)$_{15}$-5' 5'-AGAAAAGAGAGAGAGAGAGAGAACAGAAT(A)$_{31}$-3'	
P58C Fluorescence Anisotropy Substrate	3'-GAGAGTTT-5' 5'-[Flc]-TCTCTCTCTCAAA-3'	
Primase Fluorescence Anisotropy Substrate	5'[Flc]-TTTTTTTTTTTTTTTTTTTTTTTTT-3'	

Table 2.1. Electrochemistry, primase activity assay, and fluorescence anisotropy DNA substrates used. Electrochemistry of p58C was performed on self-assembling monolayers of a 20-mer DNA duplex substrate with a 3-nt 5'- ssDNA overhang. A 50-nt ssDNA substrate with a single thymine base complementary to the α-^{32}P radiolabeled ATP was used in the primase initiation assay comparing wild type and CT-deficient full-length enzyme. A 2'-OMe RNA-primed ss/dsDNA substrate, containing a 31- nucleotide duplex segment and a 29- nucleotide 5'-ssDNA overhang was used to assay elongation. The mismatched elongation assay was performed with a cytosine engineered into the substrate (red) to promote a mismatch in the elongated primer segment. U = 2'-OMe rU, SH = -$(CH_2)_6$-SH, Flc = FITC.

assessed by pipetting reagent and determining whether the solution comes out of the pipet tip in droplets. This indicates fresh NH_4OH. High pressure liquid chromatography (HPLC) using a reverse-phase PLRP-S column (Agilent) was used, and oligonucleotide mass confirmed using MALDI-TOF Mass Spectrometry. The initial pressure on the column should be less than 60 bar; columns with higher initial pressure generally do not yield optimal results. Thiol-modified strands were reduced after the initial HPLC purification with 100mM dithiothreitol (Sigma) for 2-3 h in 50 mM Tris-HCl, pH 8.4, 50 mM NaCl. Reduced thiol-modified DNA was purified by size exclusion chromatography (Nap5 Sephadex G-25, GE Healthcare) and subsequent reverse-phase HPLC. Nap-5 columns should be loaded with sample after washing, then loaded with ~430-450μL of buffer. This will prime the column for elution of the thiolated DNA. Elute with volumes of 600-900μL. Single-stranded oligonucleotides were then desalted using ethanol precipitation and stored in low salt buffer (5 mM Phosphate, pH 7.0, 50 mM NaCl). During desalting, the final drying step *in vacuo* generally takes ~30-60 minutes. If the yield of DNA as assessed by HPLC (absorbance at 260nm) is low, resuspend the dried sample in a smaller volume of the appropriate buffer (25-30μL instead of 50-70μL). This will ensure that DNA concentrations are high enough to anneal and use the recovered sample for electrochemistry. Duplex DNA for electrochemistry and duplex 2'-OMe RNA/DNA was prepared by quantification of the complementary single-stranded oligonucleotides by UV-Visible spectroscopy, followed by annealing at 90 °C. A mixture of equimolar complementary single-stranded DNA/2'-OMe RNA (50 μM) was prepared in low salt buffer. Thiol-modified duplex DNA substrates were then deoxygenated by bubbling argon gas through the solution for 90 s. Duplex DNA was annealed on a thermocycler (Beckman Instruments) by initial heating to 90 °C, followed by slow cooling to 4 °C over 90 minutes. DNA was quantified using absorbance at 260

nm, with extinction coefficients at 260 nm for DNA or 2'-OMe RNA obtained using Integrated DNA Technologies online OligoAnalyzer tool. Single-stranded DNA substrates were quantified using UV-Visible spectroscopy and stored in low salt buffer at a stock concentration for activity assays.

Multiplexed Chip Fabrication. Multiplexed electrode platforms were prepared using standard photolithography techniques, adapted from established protocols (*5*,*31*,*32*). Nine 1 in. by 1 in. chips were patterned on 525 μm thick silicon wafers (SiliconQuest). A thermal oxide layer roughly 4000 Å thick was grown on the silicon wafers using a Tytan tube furnace (Tystar). S1813 photoresist (2 μm layer) was deposited onto the wafers for patterning of the chips before metal deposition. Electron beam evaporation (CHA Industries) was then used to deposit a 3nm titanium adhesion layer followed by a 100nm gold layer, without breaking vacuum between depositions. Metal lift-off using Remover PG (MicroChem) was performed overnight (10-12 h) at room temperature. Wafers were subsequently dried with a nitrogen gun and dehydrated at 140 °C for 10 minutes. A 3 μm layer of insulating SU-8 photoresist was deposited and patterned onto the wafer as described previously, (*5*,*31*,*32*) with connective wires between contact pads on the edges of the chips and working electrodes in the center were covered but the contact pads and working electrodes left exposed. This ensured a fixed working electrode surface area of 2 mm^2. SU-8 photoresist was cured (150 °C, 15 minutes) and wafers cleaved into individual chips using a Dynatex Scriber/Breaker. The Dynatex Scriber/Breaker does not always break the wafers. If the diamond tip is dull, multiple (3-5) scribings on this instrument help prime wafers for clean breakage. If the scriber/breaker cannot break the wafers, they should be broken manually.

DNA Modified Electrode Assembly/Preparation. Multiplexed chips were cleaned using sonication in acetone and isopropyl alcohol as described previously (*5*). Chips were then dried

using argon gas and ozone-cleaned for 15-20 minutes at 20 mW using a Uvo brand ozone cleaner. An older model of the Uvo cleaner generally requires ~20 minutes of cleaning. If retrieving the chip from the ozone cleaner proves difficult, use two pairs of tweezers, one to push the chip against the side of the cleaner and elevate it, and the other to physically clamp and pick up the chip by its edges. Clean chips were assembled onto polycarbonate holders with acrylic clamp and Buna-N rubber gasket according to previous protocols, with four quadrants in the chip separated by fastened gasket and clamp (5). Duplex DNA substrates, with a thiol modifier at the 5'- end, (25 μM) were deposited in a 20 uL volume onto each quadrant of the multiplex chip. Substrates incubated for 18-24 hours on the gold surface to allow formation of self-assembled DNA monolayer. DNA monolayers were washed with phosphate buffer (5mM phosphate, pH 7.0, 50mM NaCl, 5% glycerol) and subsequently backfilled with 1mM 6-mercaptohexanol (Sigma) in phosphate buffer for 45 minutes. Mercaptohexanol stocks should be stored under argon (~1m degassing a 100mM stock after each use) and 100mM stocks should be prepared on a monthly-bimonthly basis. (1mM mercaptohexanol is prepared on the day of experiments from 100-fold dilution of 100mM mercaptohexanol stocks.) Monolayers are then washed 10 times per quadrant with phosphate buffer and twice per quadrant with TBP buffer (5 mM phosphate, pH 7.0, 50 mM NaCl, 4 mM $MgCl_2$, 4 mM spermidine) to aid in formation of a monolayer with termini accessible for p58C binding. Assembled chips were transported into an anaerobic glove bag chamber (Coy Products) and washed 5 times per quadrant with p58C storage buffer (20 mM Tris-HCl, pH 7.2, 75 mM NaCl), which was previously deoxygenated by argon bubbling (approx. 1 hour per mL of buffer solution) and allowed to incubate at least 1-2 days in the chamber prior to the experiment. Initial cyclic voltammetry scans of the monolayers in p58C storage buffer were performed to ensure monolayer formation on each electrode. All washes

were performed with 20 μL buffer volumes on each quadrant. Before scanning, a 200 μL volume was deposited over the chip surface, a bulk solution well for completion of a three-electrode circuit with an external reference and counter electrode. The reference used (BasInc) is a solid state Ag/AgCl reference which is appended with a gel tip. 1g of agarose is mixed with 25mL of 3M NaCl and warmed in 3x 20s intervals in a microwave oven, with stirring between each interval, to create a uniform gel mixture. Gel is then injected with a syringe into a long gel-loading plastic pipette tip. Solid state references are then inserted into the gel-filled tip to make a continuous connection between the electrode and the end of the gel tip. These should be left to solidify and are often solid after ~30-60 minutes. Stretched parafilm is then used to wrap the electrode/tip interface to keep the reference secured in the glove bag chamber/during electrochemistry. Teflon tape is used to tightly wrap the Pt counter electrode (Pt wire) around the end of the plastic tip. Thicker Pt wire should be used, and no dramatic kinks or bends should be introduced to preserve the wire. New gel tips should be made every 1-2 weeks but Pt wire is reused until the metal becomes brittle and segments. Gel tip references are generally more reliable and consistent with measured midpoint potentials than solid-state no leak Ag/AgCl electrodes (Thermo Scientific). If stored in 3M NaCl, solid state electrodes for gel-tip references last for ~1-3 years.

Mutant Selection and Design. Mutations in the p58C domain of human DNA primase were designed based on previously determined structural data (*11*) and bioinformatics (*12*) compiled for conserved residues in this domain. PYMOL software was used to model the mutations in a 1.7 Å resolution structure of human p58C (*11*) (PDB 3L9Q). Mutagenesis and measurement tools were used to model possible point mutations and approximate distances between residues/cofactors. The COSMIC database (*34*) was used to search for somatic mutations of the

primase large subunit (PRIM2 gene) in cancer. The point mutation Y345C was found and selected for charge transfer and activity assays.

Circular Dichroism. The WT and mutants of p58C were concentrated to 2 mg⁄mL and buffer exchanged into 10 mM potassium phosphate (pH 7.2). The far-UV CD spectrum over the range 190–260 nm was acquired at room temperature using a Jasco J-810 spectrophotometer. Each spectrum is the average of three scans acquired with a scanning rate of 0.5 nm⁄s.

Fluorescence anisotropy. The binding of DNA to wild-type and mutant p58C and primase was measured by monitoring the change (increase) in fluorescence anisotropy as protein was added to a solution containing 5'-FITC labeled DNA (see **Table 2.1** for substrates). The p58C DNA substrate was annealed using a buffer containing 20 mM MES (pH 6.5) and 75 mM NaCl. In each case, an increasing concentration of protein was added to a solution containing DNA substrate at a concentration of 50 nM (p58C) or 20 nM (primase). Polarized fluorescence intensities were measured using excitation and emission wavelengths of 485 nm and 520 nm using a SpectraMax M5 microplate reader (Molecular Devices).

X-ray crystallography. Crystals of Y347F p58C were grown by hanging drop vapor diffusion at 21 °C from a drop composed of equal volumes of 75 mg/ml protein in 20 mM TRIS (pH 7.2) and 75 mM NaCl and reservoir solution containing 100 mM Tris (pH 8.5), 300 mM Li_2SO_4 and 20% PEG 3350. Crystals of Y345F p58C were grown in 20 mM MES (pH 6.5) and 50 mM NaCl and reservoir solution containing 100 mM Tris (pH 8.5) 150 mM Li_2SO_4 and 18% PEG 3350. Crystal growth was stimulated by streak seeding with WT. Prior to data collection, crystals were soaked in mother liquor containing 20% glycerol and flash frozen in liquid nitrogen. X-ray

data were collected at Sector 21 (Life Sciences Collaborative Access Team) of the Advanced Photon Source at Argonne National Laboratory. All data were processed by HKL2000. The Y347F crystals belong to the P3 space group and were twinned. The Y345F crystals were not twinned and belonged to the C2 space group. Prior to phasing, the twinned data set was de-twinned using the Detwin program of the CCP4 program suite (Collaborative Computational Project, 1994) by applying the twin law, h,-h-k,-l. Phasing of the diffraction data was done by molecular replacement using PHASER and PDB entry 3L9Q as the search model. Manual model building for the structure was performed using *Coot* model building software, and waters were placed with the *Coot* routine, Find Waters. The final model was obtained by iterative cycles of model building in *Coot* and structure refinement using Refmac5 in the CCP4 suite of programs. The final model of Y347F was a dimer of dimers with four Y347F p58C subunits in the asymmetric unit. The final model of Y345F was a dimer with two Y345F subunits in the asymmetric unit.

All protein figures were prepared with Chimera. Data collection and refinement statistics are given in **Table 2.2**.

Sample Preparation for Electrochemistry. Wild type and mutant p58C samples were stored prior to experiments in p58C storage buffer. Concentrations of [4Fe4S] cluster-containing p58C or mutants were measured using UV-Visible spectroscopy, by absorbance of the [4Fe4S] cluster at 410 nm (extinction coefficient = 17000 M^{-1} cm^{-1}) (*35*). Aliquots of stock samples (45-90 μL) were deoxygenated using argon bubbling for 4-5 minutes. Take care when using protein samples in glycerol-containing storage buffers to bubble argon at a slow and gentle rate; these buffers can otherwise bubble at the edges of the sealed tube and lead to sample loss. Centrifuge degassed protein for ~10s at 1200 rcf after deoxygenation to ensure all sample is at the bottom of the tube

Crystallographic data collection and refinement statistics.

PDB Entry	**517M**	**5DQO**
Protein Structure	Y345F	Y347F
Data Collection		
Space Group	C2	P31
Cell dimensions		
a, b, c (Å)	109.9, 52.7, 89.2	60.40, 60.40, 246.73
α, β, γ (°)	90, 115.25, 90	90, 90, 120
Temperature (K)	100	100
Wavelength (Å)	0.987	0.999
Resolution (Å)[a]	49.7-1.93 (1.96-1.93)	44.14- 2.48 (2.53-2.48)
Reflections		
Total	142, 467	184, 871
Unique	35, 604	41, 462
Completeness (%)[a]	99.9 (99.8)	99.1 (89.6)
R_{merge} (%)[a,b]	8.7 (58.4)	5.8 (49.3)
R_{pim} (%)[a]	0.048 (0.33)	2.9 (33.9)
$CC_{1/2}$ (%)[a]	(88.6)	(59.2)
I/σI	18.7 (2.1)	27.6 (2.1)
Redundancy	4.2 (4.0)	4.5 (2.9)
Refinement		
R_{work}/R_{free} (%)[c]	21.0/24.9	24.9/27.4
No. of residues		
Protein	314	628
4Fe-4S	2	4
Solvent	81	41
Average B-Factor (Å)		
Protein	28.8	53.69
4Fe-4S	21.5	46.16
Solvent	27.7	55.66
Wilson B-Factor (Å^2)	24.5	58.1
RMSD Bonds (Å)	0.02	0.02
RMSD Angles (°)	2.11	1.91
Ramachandran (%)		
Most favored	99%	98.5%
Allowed	1%	1.5%
Disallowed	0%	0%

[a] Values in parentheses are for the highest-resolution shell. [b] $R_{merge} = \Sigma(|I-\bar{I}|)/\Sigma I \times 100$. [c] $R_{work} = \Sigma |F_0-F_c|/\Sigma F_0 \times 100$, where F_0 is the observed structure factor amplitude and F_c is the calculated structure factor amplitude.

Table 2.2. Crystallographic Data for p58C Y345F (PDB 517M) and p58C Y347F (PDB 5DQO).

and can be easily diluted/ transferred to the electrode once in the glove bag. Samples were then transferred into the anaerobic chamber. Before deposition onto the gold electrode surface, p58C/mutant samples were diluted to a molar concentration of 16 μM [4Fe4S] p58C variant with previously deoxygenated p58C storage buffer. Samples were deposited onto multiplex chip quadrants in 20 μL volumes initially, with the remaining sample deposited in a well of bulk solution above the chip surface.

Wild Type/Mutant p58C Electrochemistry. All electrochemistry was performed using a CHI620D potentiostat and 16-channel multiplexer (CH Instruments), in an anaerobic glove chamber. Multiplex gold electrodes were part of a three electrode system with an external Ag/AgCl reference electrode (Bioanalytical Systems) and platinum counter electrode. The top panel of the custom multiplex chip electrochemical platform can be removed for clear observation of the gold pins on the multiplexer contacting the gold contact pads on the perimeter of the chip. This can be useful in directly observing whether a connection between all three electrodes in the cell is made, which is important when diagnosing issues that arise in scanning. The multiplexer Teflon adapter in which the pins are housed should be fastened onto the chip platform in a way which avoids bending or pressure application on the wires connecting to the potentiostat. This will prevent excessively tilted CVs and make signals more reliable and easier to measure. To ensure that the reference/counter electrode is connected correctly, clip the reference with a white alligator clip and the Pt counter electrode with a red alligator clip on the multiplexer. The clips used generally correspond to the 'Electrodes 1,2' portal on the potentiostat. The set of clips to use in experiments are the only pair of red/white clips not bound by zipties. Use tweezers with a thin end (available at VWR stockroom) to lower the clipped reference/counter setup into the electrode solution on a multiplex chip. Watch for a meniscus to

form in the solution; this indicates that the reference tip is in contact with the electrode solution. This is especially important in the anaerobic chamber, where vision of the setup is limited. Cyclic voltammetry scans were performed at 100 mV/s scan rates, over a potential range of +0.412 V to -0.288 V vs. NHE. Bulk electrolysis on DNA was performed at an applied potential of +0.412 V vs. NHE for all electrochemical oxidation reactions and -0.188 V vs. NHE for all electrochemical reduction reactions. The oxidizing potential was applied for 8.33 minutes for single oxidation reactions on a surface, and 5.83 minutes or 6.67 minutes for the iterative oxidation cycles of p58C variants. The reducing potential was applied for 8.33 minutes in all electrochemical reduction reactions. All bulk electrolysis and cyclic voltammetry was performed in previously deoxygenated p58C storage buffer (20 mM Tris, pH 7.2, 75 mM NaCl). Charge transfer (nC) in the cathodic peak of oxidized samples' CV scans was assessed using the area under the current wave of the reduction signal. All p58C variants were compared over three trials of oxidation at +0.412 V vs. NHE (two oxidation reactions after 500 s of applied potential, one reaction after 400 s of applied potential). The charge transfer in the bulk electrolysis curves was calculated as the area under the current curve plotted versus time for the bulk electrolysis reaction, as the current decays to a constant value. The percent recovery of bulk electrolysis charge in the CV peak after oxidation was averaged over three trials for each variant; error bars represent the standard deviation of the average fraction of charge recovered.

Full-Length Wild Type/Mutant Primase Initiation and Elongation Assays. All activity assays were performed in an anaerobic glove chamber (Coy Products) using previously deoxygenated buffer, protein, DNA substrates, and nucleotide triphosphates. All reagents were deoxygenated by argon gas bubbling after thawing from storage temperature immediately prior to assay. Buffer was deoxygenated by bubbling argon gas for several hours (approx. 1 hour per

mL buffer) and subsequent incubation in the glove chamber atmosphere for at least 1-2 days prior to the assay. Initiation assays were performed using the 50-nt Initiation Substrate listed in **Table 2.1**. Elongation assays were performed with the Elongation Substrate in **Table 2.1**, in which a 2'-OMe RNA/DNA primer is annealed to a 60-nt ssDNA complement strand. Initiation assays (18 μL total volume) contained 250 nM ssDNA Initiation Substrate, 1 μM [α-^{32}P ATP] (Perkin Elmer), 112 μM [CTP] (Sigma), 188 μM [UTP] (Sigma), and 400 nM primase or primase variant, in 50 mM Tris-HCl, pH 8.0, 3 mM $MgCl_2$. Reactions were initiated by the addition of primase or primase variant enzyme and incubated anaerobically at 37°C. Aliquots (5.5 μL) were removed from the primase reactions after 5 minutes, 10 minutes, and 30 minutes of incubation for wild type/mutant comparison assays and after 30 minutes, 60 minutes, and 120 minutes for wild type primase well-matched and mismatched primer comparison assays. All samples were quenched by addition of an equal volume of 1% SDS (Sigma), 25 mM EDTA (Sigma) solution. Samples were then removed from the glove chamber after quenching and heat denatured at 70°C. Products were then purified by size exclusion, using mini Quick Spin Oligo columns (Roche Diagnostics) for wild type/mutant comparison assays and Micro-Bio Spin™ P-6 columns (BioRad Laboratories) for wild type well-matched/mismatched primer comparison assays. Sometimes, samples should be processed with two rounds of spin columns. Free radiolabeled NTPs are not all removed from one purification round and can cause background issues in a gel assay if they are not run off the gel during electrophoresis. Radioactivity counts for products were measured using a LS5000TD scintillation counter (Beckman Instruments). The exposure times for gels were gauged based on the lowest recorded counts; free radiolabeled NTPs in solution prior to gel separation can cause artificially high counts in samples. Products were dried in vacuo, resuspended in 2 μL loading dye (Xylene cyanol, bromophenol blue), and

further annealed for 1 minute at 90°C before gel separation. Primase/mutant comparison elongation assays were performed under identical conditions, in the presence of 500nM Well-Matched Elongation Substrate, 120μM CTP (Sigma), 180μM UTP (Sigma), and 1μM α-^{32}P ATP (Perkin Elmer). The primase/variant concentrations used in elongation assays were 200nM, 400nM, 600nM, or 800nM. Primase assays for elongation in the presence of a mismatch were performed with 500μM Well-Matched Elongation Substrate or Mismatched Elongation Substrate, 200μM CTP (Sigma), 100μM UTP (Sigma), and 1μM α-^{32}P ATP (Perkin Elmer). Assays were performed anaerobically and quenched/purified in a manner identical to initiation assays.

Primase Assay Product Separation/Analysis. All primase/primase variant assay products were separated by denaturing polyacrylamide gel electrophoresis (20% polyacrylamide). When pouring gels, allow at least 1-2 hours for polyacrylamide polymerization/solidification after ammonium persulfate/TEMED addition. Generally only a very small amount of ammonium persulfate is required, if the reagent is fresh. Use a weighing boat containing excess polyacrylamide from gel preparation to assess whether the gel has solidified and is ready for use. Gels can be stored overnight at 4°C but should be allowed to return to room temperature before high voltage is applied to the setup. This avoids cracking of the gel casting plates. When prying gel plates apart after the gel has run, pry from a corner of one panel and proceed slowly, watching until one plate has completely separated from the gel. The plates will then be easily separated and this avoids ripping of the gel. Separated products were visualized using phosphorimagery on a Typhoon FLA 9000 imager (GE Healthcare) and quantified using ImageQuant TL software. Products synthesized by different primase variants were directly compared using measured ^{32}P counts detected by software. Initiation and Elongation Substrates

(**Table 2.1**) were designed to contain a single base complementary to the radiolabeled NTP, α-^{32}P ATP. Quantification could thus have a basis 1:1 product: radioactivity ratio, as the sole purine NTP and would be the strongly preferred site of initiation and an optimal 5'- elongation site (*36,37*). Product sizes were assigned by comparison with a 10/60 Oligo Length Standard (Integrated DNA Technologies). Single-stranded oligonucleotides in standard were labeled by incubation for 1 hour at 37°C with γ-^{32}P ATP (Perkin Elmer) and T4 polynucleotide kinase enzyme (Roche Diagnostics). Labeled standard was purified using size exclusion chromatography with mini Quick Spin Oligo columns (Roche Diagnostics). All product quantifications were averaged over three trials for p48/p58Y345F and p48/p58Y345C and six trials for p48/p58. Error bars represent the standard deviation of average values obtained over these trials.

Results

Oxidized and Reduced p58C Electrochemistry

The p58C domain of human DNA primase, independently of the rest of the enzyme, binds a primed template DNA (**Table 2.1**) with modest affinity ($K_d = 5.5 \pm 0.5\mu M$) when initially present as isolated in the reduced, EPR-silent $[4Fe4S]^{2+}$ state (*9,10*) (**Figure 2.2**). To investigate whether the p58C [4Fe4S] cluster oxidation state affects DNA binding, as observed in Endonuclease III, we used DNA electrochemistry. Experiments are carried out using a sixteen-electrode multiplexed chip, which allows for robust, reproducible, and internally consistent measurements of various conditions on a single surface (**Figure 2.1A**) (*5,6,31-33*). Bulk electrolysis is used to convert a sample to a uniform redox state in this setup, and it is performed by passage of current through the DNA at a constant applied potential. This technique facilitates the oxidation or reduction of the DNA-bound protein with a direct transfer

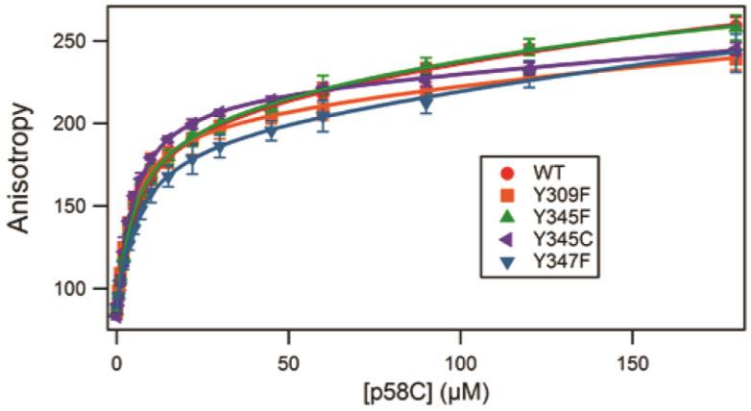

Dissociation constants for p58C

Construct	K_D (μM)
WT	5.5 ± 0.5
Y309F	4.1 ± 0.3
Y345C	4.6 ± 0.2
Y345F	4.9 ± 0.4
Y347F	4.1 ± 0.4

Fig. 2.2. DNA binding for WT and mutant p58C. WT and mutant p58C domains have similar DNA binding affinities with low micromolar dissociation constants. Affinities were measured in aerobic conditions by fluorescence anisotropy of FITC-labeled DNA substrates in 20 mM MES, pH 6.5, 50 mM NaCl. Background was subtracted from anisotropy values prior to plotting. K_D values are mean ± SD over n=3 measurements for each variant.

of electrons through the DNA, eliminating the need for exogenous chemical oxidants or reductants that could damage the protein.

For DNA electrochemistry on p58C, an alkane-thiol modified primed template DNA substrate (**Table 2.1**) was used. All experiments are performed in an anaerobic environment with deoxygenated reagents to prevent atmospheric cluster oxidation (*38*) and to ensure control of the redox state of the p58C samples on the electrode. As in earlier studies (*2*), we confirmed that p58C electrochemistry is DNA-mediated by observing a reversible p58C CV signal in the presence of ATP, which is attenuated when an intervening abasic site perturbs the base stacking of the duplex DNA substrate (**Figure 2.3**). The reversible redox signal observed when p58C is bound to both DNA and ATP is likely a result of the p58C [4Fe4S] cluster being better coupled into the DNA duplex for CT when bound DNA and a nucleotide triphosphate (NTP), both necessary substrates for primase activity. The improved coupling in the active form is likely associated with a large conformational change, but a structure of p58C bound to both DNA and a nucleotide triphosphate is necessary to confirm this. Increased coupling of the [4Fe4S] cluster to duplex DNA was previously observed for the [4Fe4S] helicase XPD (*S. acidocaldarius*) upon binding ATP, a substrate necessary for XPD activity. (*39*)

To electrochemically assay p58C in the presence of DNA only, oxidized and reduced samples are generated and subsequently compared on a single surface using bulk electrolysis followed by CV scanning. By passing sufficient current through the DNA-modified electrode at an oxidizing (412 mV vs. NHE) or reducing (-188 mV vs. NHE) potential, p58C is converted to the desired redox state (**Figure 2.1B**, **Figure 2.4**). We observe no redox signal by CV for electrochemically unaltered p58C, indicating that the EPR-silent, $[4Fe4S]^{2+}$ protein obtained upon isolation (*9*,*10*) is not electrochemically active on DNA (**Figure 2.5**). After oxidation by

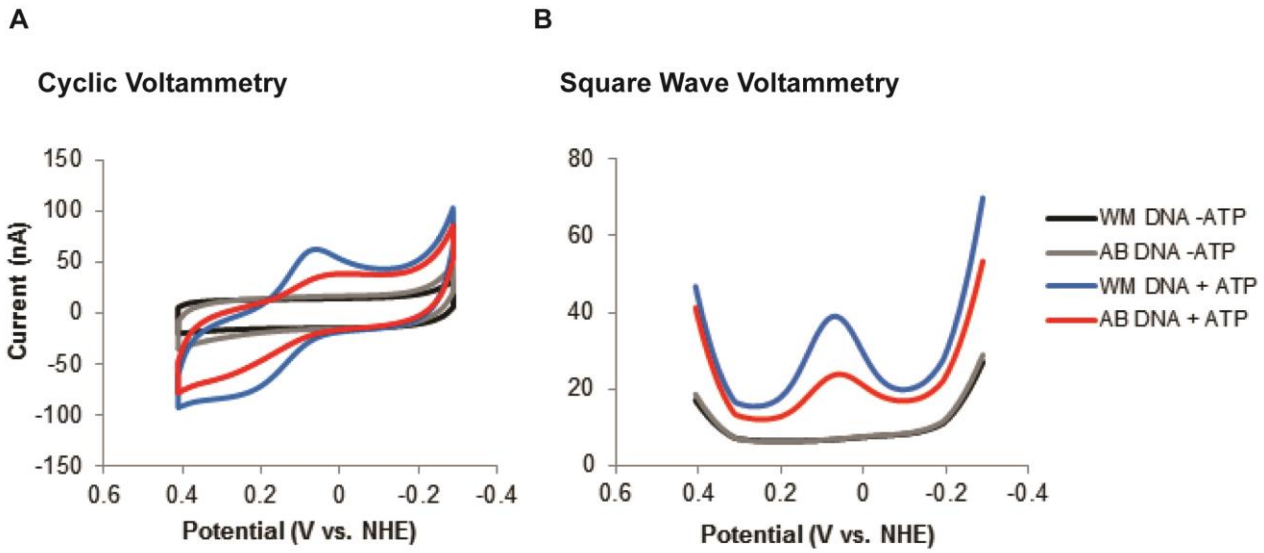

Fig. 2.3. Cyclic voltammetry (**A**) and Square Wave Voltammetry (**B**) signals of p58C bound to of well-matched (WM) DNA or DNA containing an abasic site (AB DNA) in the duplex segment, in the presence and absence of an NTP pool. The p58C domain displays a reversible redox signal centered at 140-150mV vs. NHE in the presence of ss/dsDNA and 500μM [ATP]. This suggests that the [4Fe4S] cluster in DNA primase is capable of undergoing reversible redox activity when the enzyme is in its active form, bound to DNA and NTPs. All electrochemistry was performed in anaerobic conditions with a Ag/AgCl reference, on 10μM [p58C] in 20mM Tris, pH 7.2, 75mM NaCl. Cyclic voltammetry scan rate: 100mV/s, square wave voltammetry scan frequency: 15 Hz.

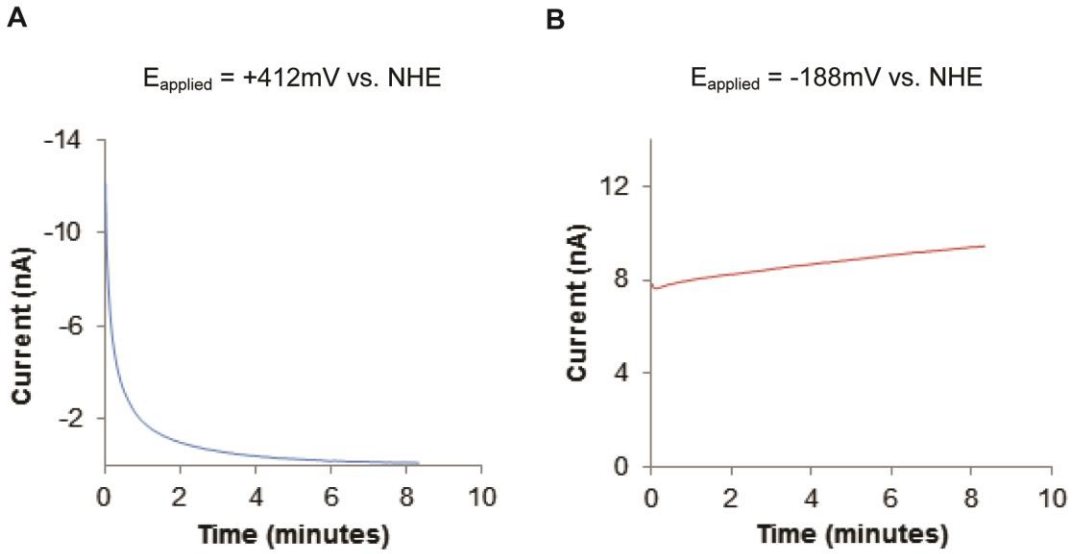

Fig. 2.4. Oxidation (**A**) and reduction (**B**) of p58C by bulk electrolysis on a DNA-modified multiplex Au electrode. Potentials shown on oxidation/reduction plots were applied to convert the sample at the DNA/solution interface to the desired [4Fe4S] cluster oxidation state. Bulk electrolysis is performed on 16μM p58C using a Ag/AgCl reference electrode, in 20 mM Tris buffer, pH 7.2, 75mM NaCl, in anaerobic conditions.

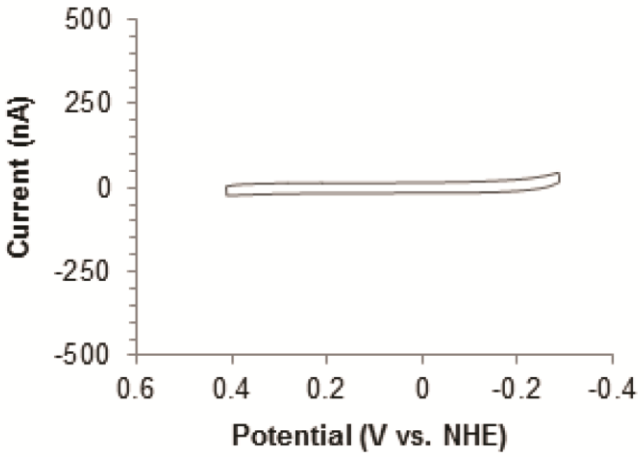

Fig. 2.5. P58C does not produce a redox signal on ss/dsDNA in the absence of electrochemical alteration. CV performed in anaerobic conditions on 16μM p58C using a Ag/AgCl reference electrode, in 20mM Tris buffer, pH 7.2, 75mM NaCl. CV scans were conducted at a 100mV/s scan rate.

bulk electrolysis, however, a large cathodic peak between -130 and -140 mV vs. NHE appears in CV (100 mV/s scan rate) during the initial scan to negative potentials (**Figure 2.1C**). Importantly, the electrochemical signal through DNA is lost after scanning to reducing potentials. The signal observed in the CV scan to negative potential for the oxidized p58C sample corresponds to a reduction event, which we assign to the electron transfer reaction in which the tightly bound, electrochemically active $[4Fe4S]^{3+}$ p58C is converted to a more weakly associated, electrochemically inactive $[4Fe4S]^{2+}$ state. Consistent with this observation, CV after reduction displays no redox signal (**Figure 2.1D**), as observed initially for the native protein, which we attribute to the lower affinity for DNA of the $[4Fe4S]^{2+}$ state.

To confirm assignment of the p58C redox signal, we employed iterative cycles of p58C electrochemical oxidation on a single electrode surface, followed each time by CV scanning (**Figure 2.6**). If scanning to negative potentials reduces the tightly bound $[4Fe4S]^{3+}$ p58C coupled to the DNA duplex for CT, to the weakly bound, uncoupled $[4Fe4S]^{2+}$ state, a second oxidation of the same sample should convert p58C again to the $[4Fe4S]^{3+}$ state and regenerate the CV signal as the protein rebinds tightly to the DNA. We performed five sequential bulk electrolysis reactions on a single electrode surface, followed each time by CV scanning (100 mV/s). We found each time that the p58C redox signal was not present after reduction during CV. However, upon conversion from the reduced to the oxidized state, the CV signal was regenerated. During the initial scan after oxidation, a cathodic peak between -130 and -140mV vs. NHE (100mV/s scan rate) consistently appears (**Figure 2.6B**). This reversible behavior suggests that the oxidation state of the [4Fe4S] cluster alters DNA binding by p58C; tighter DNA binding is associated with oxidation.

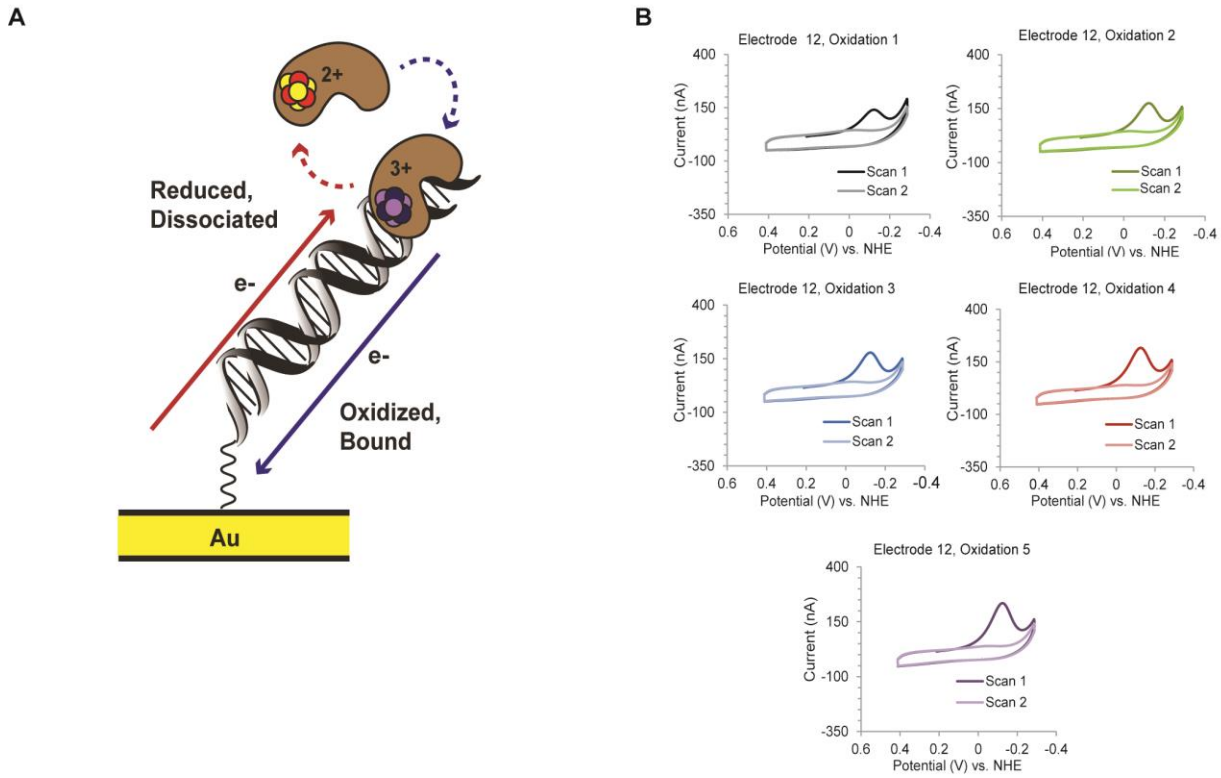

Figure 2.6. Iterative oxidation/reduction cycles of p58C on a single electrode surface. **A)** The scheme depicts the redox switch in p58C DNA binding. When oxidized, p58C is bound tightly to DNA. Reduction converts p58C to a weakly DNA-associated state. **B)** Cyclic voltammetry following five sequential oxidation reactions on one DNA-modified electrode of a multiplex chip. Electrolysis conditions ($E_{applied}$ = 412mV vs. NHE) are identical for each oxidation. A cathodic peak at ˉ130- ˉ140mV vs. NHE is regenerated each time in the first CV scan after oxidation. The cathodic peak corresponds to a reduction of tightly bound, oxidized p58C, to weakly associated p58C. Charge transfer values in the cathodic peaks for scans 1-5, in chronological order, are 65.4 nC, 112.4 nC, 116.4 nC, 151.1 nC, and 170.9 nC. Peak charge increases over trials due to increasing p58C at the solution/DNA interface. Electrochemistry was performed on 16 µM p58C in 20 mM Tris, pH 7.2, 75 mM NaCl, 100 mV/s scan rate for CV, using a Ag/AgCl reference electrode.

Progressively larger CV signals appear with each iterative oxidation performed under identical electrolysis conditions. The change in CV signal under constant oxidation conditions suggests that oxidation brings more molecules of p58C to the DNA substrate on the electrode each time that electrolysis is performed (**Figure 2.7**). Previously oxidized p58C molecules, together with newly oxidized p58C generated during each electrolysis at 412 mV vs. NHE, appear in the CV signal obtained after each oxidation. Moreover, it is not feasible on our experimental timescale that two serial protein diffusion events, diffusion of previously oxidized p58C molecules away from the DNA, followed by diffusion of a new sample to the DNA replacing them, can occur. This evidence therefore strongly suggests that the redox switch in the oxidation state of the [4Fe4S] cluster modulates DNA binding and coupling of the [4Fe4S] cluster into the DNA duplex for CT. The molecular basis for how oxidation controls this increase in DNA affinity is not known; progress to define this mechanism has been inhibited by the inability to produce sufficient quantities of uniformly oxidized, $[4Fe4S]^{3+}$ p58C, despite an extended and systematic survey of oxidizing agents and experimental conditions in an anaerobic environment.

Charge Transfer Pathway through p58C

Iterative, electrochemically controlled oxidation and reduction cycles demonstrate the ability of p58C to switch between weak and tight DNA binding upon a change in the oxidation state of the [4Fe4S] cluster under the control of DNA-mediated CT through the DNA electrode. For this DNA-mediated redox switch reaction to occur, however, a tunneling pathway (*40*) through p58C is necessary to move charge the ~25 Å distance between the primed template DNA binding site and the [4Fe4S] cluster cofactor (*11*,*22*). Residues within p58C must therefore shuttle charge through the insulating protein matrix to mediate the DNA binding switch reaction.

A

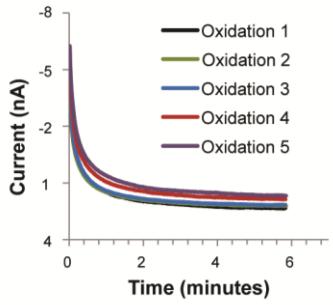

B

Oxidation Step	Cathodic Peak Charge Transfer (nC)
1	65.4
2	112.4
3	116.4
4	151.1
5	170.9

C

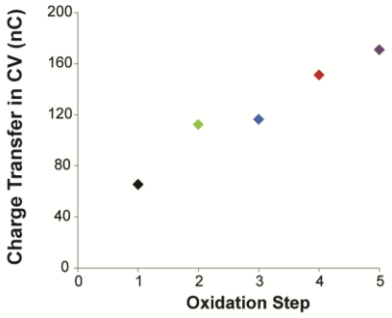

Fig. 2.7. **A**) Iterative oxidation reactions on a single DNA-modified multiplex electrode surface. Oxidation reactions of p58C indicate that charge passes, converting a reduced species to an oxidized species at an applied potential of +412mV vs. NHE. This shows that after reduction in CV, p58C can be oxidized again on a DNA-modified surface. **B**) Charge transfer (nC) in the cathodic peak signal for each CV scan of the iteratively oxidized p58C sample. Charge transfer increases during iterative oxidations, due to more p58C available at the DNA/solution interface during later trials. **C**) Plot of CV charge transfer for iterative oxidation steps. Charge transfer in CV peak increases over iterative scans, suggesting that electrochemical oxidation brings more p58C to the ss/dsDNA substrate. Electrochemistry performed on 16μM p58C in 20mM Tris, pH 7.2, 75mM NaCl. CV scans performed at 100mV/s scan rate.

In order for the protein-mediated redox reactions to occur on a feasible timetable over these distances, it is critical that residues with a low ionization potential are present in the electron transfer pathway (*40-42*). Tyrosine residues, whose aromatic rings can stabilize protein radicals, serve as redox mediators in a variety of proteins *(42*). Moreover, conservation of tyrosine residues across p58C domains of eukaryotic primases suggests potential participants in such a CT pathway through the protein to the DNA interface. In all structures of human p58C, three conserved tyrosine residues (Y309, Y345, Y347) form a pathway from the cluster to the putative DNA binding surface (Figures 3A, S6B). Given its low ionization energy of 8.5 eV in solution relative to 9.4 eV for phenylalanine (*43*) and an average of ~9.6 eV (*42*) for aliphatic residues, tyrosine is able to mediate electron/hole transfer through proteins. This is because the phenol side chain of tyrosine can more easily hold a radical than aliphatic residue side chains. Tyrosine residues have additionally been shown to mediate hopping reactions through other proteins to facilitate biological redox chemistry. (*42*) The chain of tyrosines in p58C is additionally within a feasible range for tunneling (*41,42*) between bound DNA and the [4Fe4S] cluster. For these reasons, the three conserved tyrosines in p58C were viewed as a likely conduit to facilitate electron transfer from the cluster to the DNA.

To test the proposed CT pathway, we designed and isolated three human p58C Y-F variants (Y309F, Y345F, Y347F), which were characterized in the same manner as the wild type protein. All three mutants are loaded with [4Fe4S] cluster to a similar degree as WT, as reflected in the UV-Visible absorbance 280 nm/410 nm ratio. To validate proper folding of the Y-F variants, circular dichroism was used to establish that the distribution of secondary structure is essentially identical to wild type (**Figure 2.8**). We also determined an X-ray crystal structure of p58C Y345F (**Table 2.2, Figure 2.9**). The presence of the cluster in the mutant and the RMSD

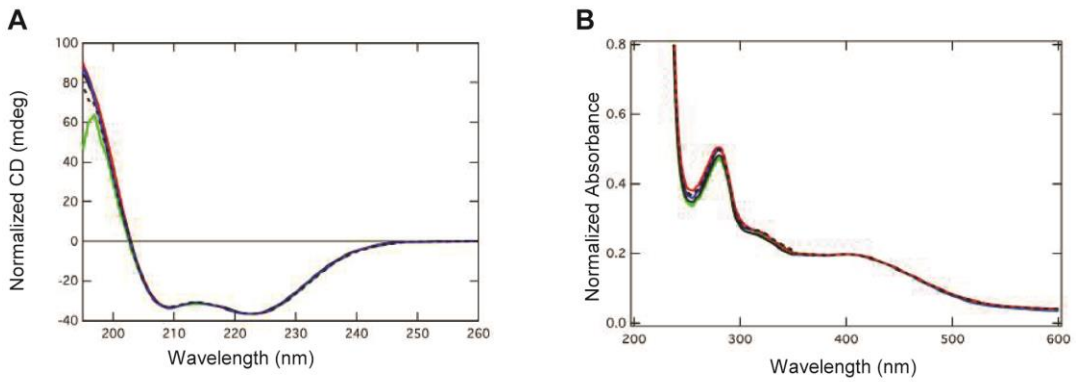

Fig. 2.8. WT and mutant p58C biophysical characterization. **A**) Circular dichroism (CD) spectroscopy of WT and mutant p58C indicate the mutations do not perturb any of the elements of secondary structure. All spectra normalized to WT at 222 nm. **B**) UV-Visible spectroscopy of WT and mutant p58C shows similar 280 nm/410 nm absorbance ratios, indicating similar degrees of [4Fe4S] cluster cofactor loading in all variants. All spectra normalized to WT at 410 nm.

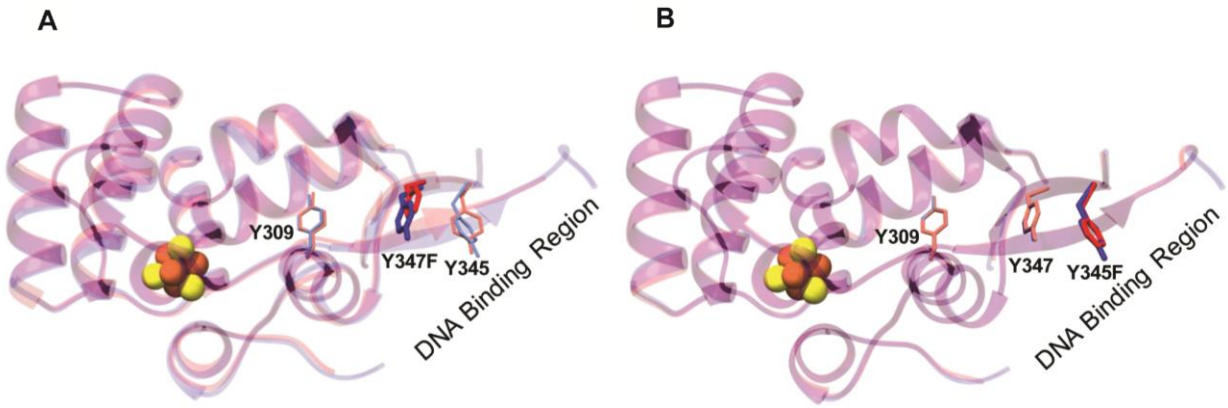

Fig. 2.9. Structural comparison of WT and mutant p58C. **A**)Superposition of the WT p58C (PDB 3L9Q) and Y347F p58C (PDB 5DQO) structures. **B**) Superposition of the WT p58C (PDB 3L9Q) and Y345F p58C (PDB 517M) structures. In both panels, WT p58C is colored blue and the tyrosine to phenylalanine mutant is red.

from the wild type protein of only 0.22 Å for the Y345F variant confirms that the structure is not perturbed. Critically, the crystal structure reveals that the F345 aromatic ring in the mutant adopts the same orientation as the Y345 ring in wild type p58C (**Figure 2.10B**). We also determined the X-ray crystal structure of the Y347F variant, with a similarly low RMSD (0.33Å) relative to wild type p58C (**Figure 2.9**). DNA binding measurements using *in vitro* fluorescence anisotropy (**Figure 2.2**) under aerobic conditions demonstrate that the mutations do not significantly affect the binding of p58C to a range of DNA substrates. Since the structures and biochemical properties of the mutants are the same as WT p58C, but the electron/hole transfer properties of tyrosine and phenylalanine are different, these single-atom mutations provide a powerful means to investigate the importance of the CT pathway through p58C and its effect on the DNA-mediated redox switch in primase.

Anaerobic electrochemical characterization was performed on all three Y-F variants (**Figure 2.11**). Oxidation and reduction using bulk electrolysis, followed by redox cycling during CV scanning (**Figure 2.12**), were performed on an identical multiplex chip surface as for wild type p58C (**Figure 2.10C**). Though the general DNA-mediated electrochemical behavior of the mutants is the same as for the WT protein, it was observed that all three mutants are charge transfer-deficient compared to WT p58C. As a control that the phenomena we observed are not unique to Y-F substitution, we also assayed p58C Y345C, a somatic mutation discovered in a gastric tumor (*34*). Oxidation of each mutant produces a cathodic peak at potentials similar to wild type in CV scanning after electrolysis, with a much smaller signal height (**Figure 2.11, 2.12**) and a slightly positive shift in average cathodic peak potential (**Figure 2.13**), both of which suggest that the charge transfer pathway facilitating conversion from the native reduced, $[4Fe4S]^{2+}$ state to the oxidized, $[4Fe4S]^{3+}$ state is attenuated with mutation. Although

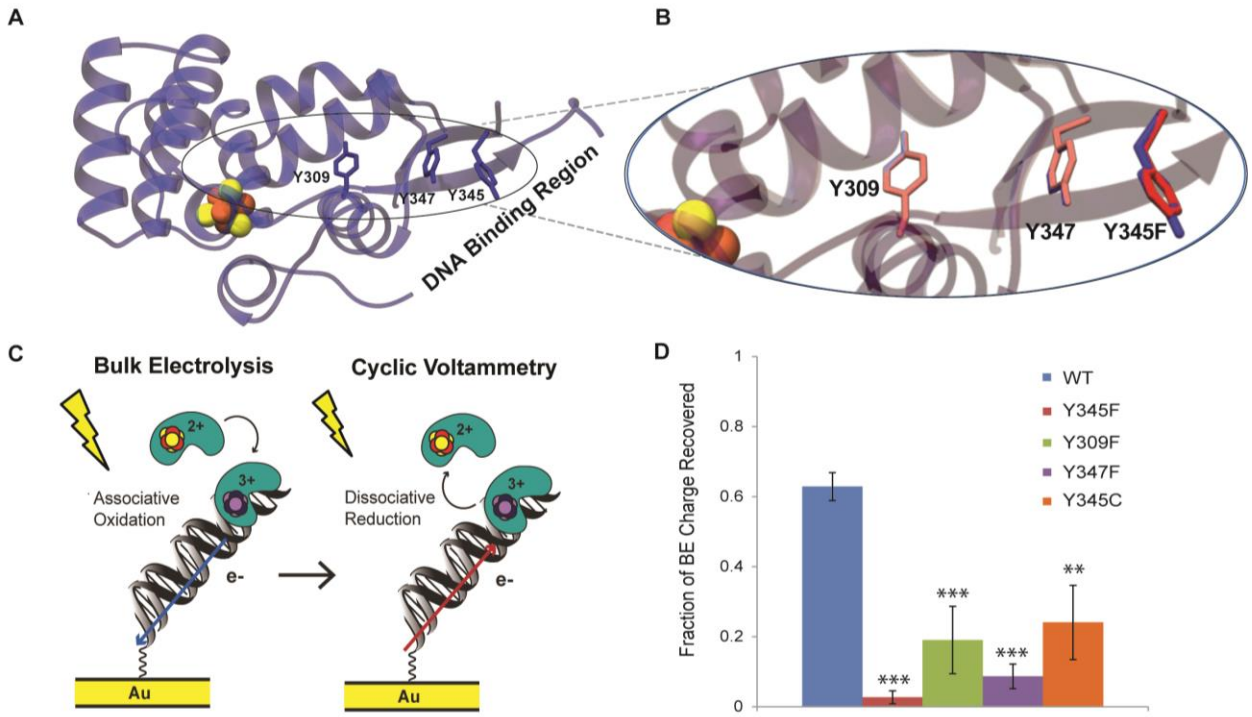

Fig. 2.10. DNA-binding, charge-transfer deficient p58C mutants. A) Tyrosine residues conserved in eukaryotic primase [4Fe4S] domain (Y309, Y345, Y347 in *H. sapiens*, blue sticks) are located between the [4Fe4S] cluster (orange and yellow spheres) and DNA-binding region. The DNA binding region, consisting of residues R302, R306, K314, and W327, is located ~20-30 Å from the cluster, necessitating electron transfer through the protein matrix for exchange of charge between the [4Fe4S] cofactor and bound DNA. **B)** Expanded region of the overlaid crystal structures of p58C (PDB 3L9Q, blue) and p58C Y345F (PDB 517M, red) demonstrates the minimal structural impact of the Y-F mutation; the phenylalanine residue in the mutant adapts the same orientation as the tyrosine in WT p58C. All mutants bind DNA with approximately the same affinity as WT p58C. **C)** Scheme depicts redox reactions in electrochemical assays with wild type and mutant p58C. Bulk electrolysis first oxidizes p58C and promotes tight DNA binding. CV then reduces the DNA-bound protein, converting it to the weakly associated, electrochemically inactive form. Both require the tyrosine charge transfer pathway and must be accounted for when comparing charge transfer proficiency. **D)** WT p58C recovers significantly more (63$\pm$4%) bulk electrolysis charge than the mutants, suggesting that perturbation of the charge transfer pathway diminishes DNA-bound redox chemistry and consequently affects the redox switch. All bulk electrolysis reactions and CV scans were performed on 16 µM p58C/mutant in 20 mM Tris, pH 7.2, 75 mM NaCl at a 100 mV/s scan rate for CV, using a Ag/AgCl reference electrode. Mean ± SD of n=3 scans per variant, ** = $0.001<p<0.0005$, *** = $p<0.0005$, student's t-test.

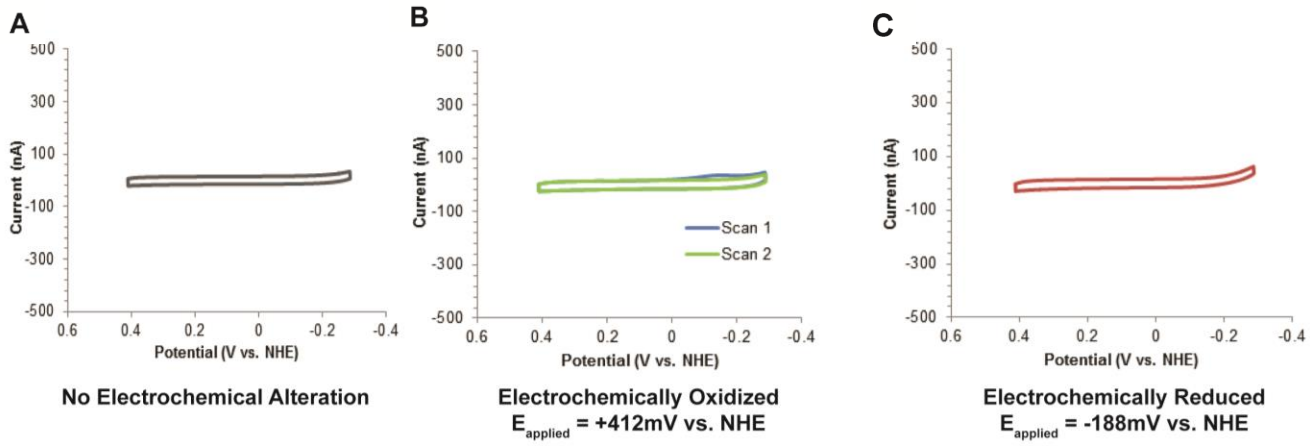

Fig. 2.11. CV scans of p58C Y345F. **A**) Electrochemically unaltered p58C tyrosine mutants display no electrochemical signal on DNA. **B**) Electrochemically oxidized p58C tyrosine mutants display a cathodic peak between -150mV and -160mV vs. NHE after oxidation at an applied potential of +412mV vs. NHE; the peak signal is smaller than that observed for wild type. **C**) Tyrosine mutants of p58C display no redox signal on DNA after electrochemical reduction at an applied potential of -188mV vs. NHE. All scans performed on 16μM p58C variant, in 20mM Tris, pH 7.2, 75mM NaCl, at a 100mV/s scan rate. P58C Y345F is shown as a representative example of the mutants.

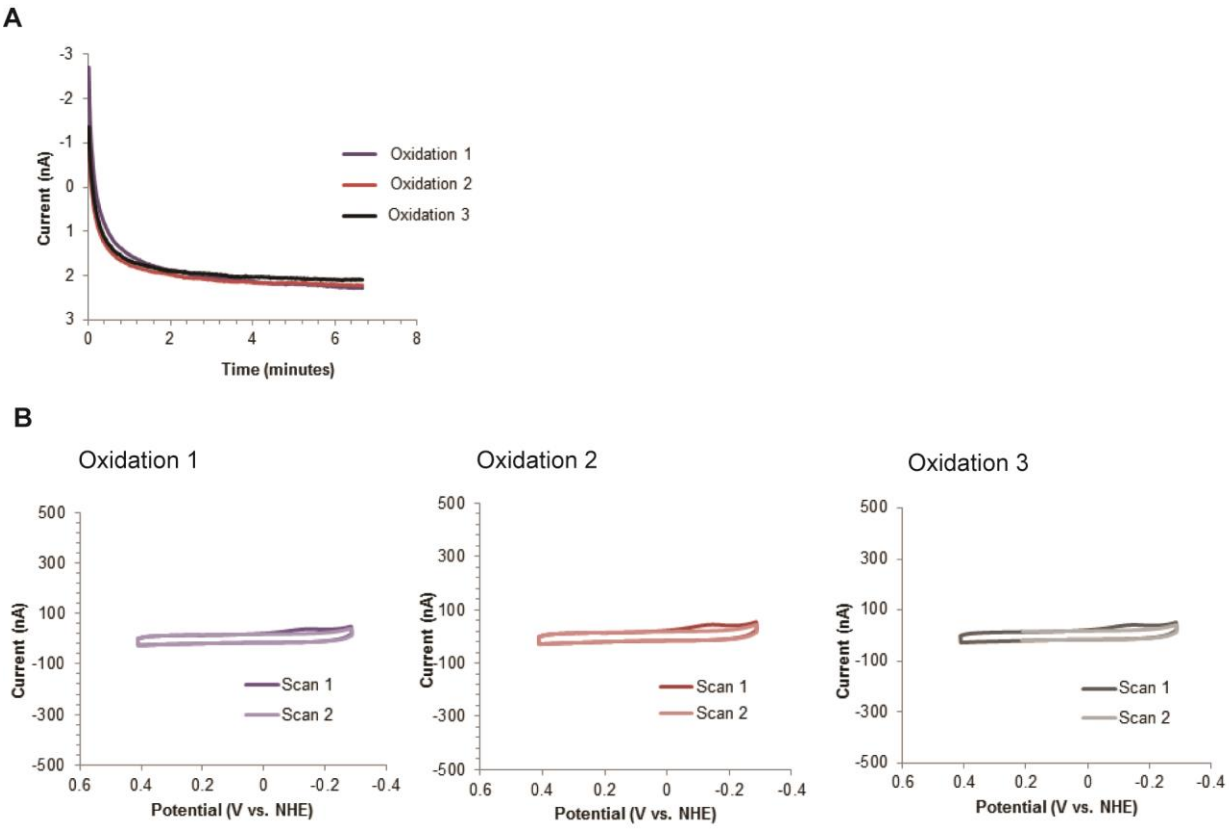

Fig. 2.12. Iterative Oxidations, followed by CV scans, of p58C Y345F on a single electrode surface. **A**) Three bulk electrolysis reactions at an applied potential of +412mV vs. NHE were performed in immediate succession on a single electrode surface. **B**) CV scans after each successive oxidation. Charge transfer in the cathodic peak was 4.1nC, 5.3nC, and 6.3nC during oxidations 1, 2, and 3, respectively. The mutant p58C thus shows the same general trend as WT but transfers less charge in bulk electrolysis and subsequent CV on the DNA-modified surface. All scans performed on 16μM p58C variant, in 20mM Tris, pH 7.2, 75mM NaCl, at a 100mV/s scan rate. P58C Y345F is shown as a representative example of the mutants.

A

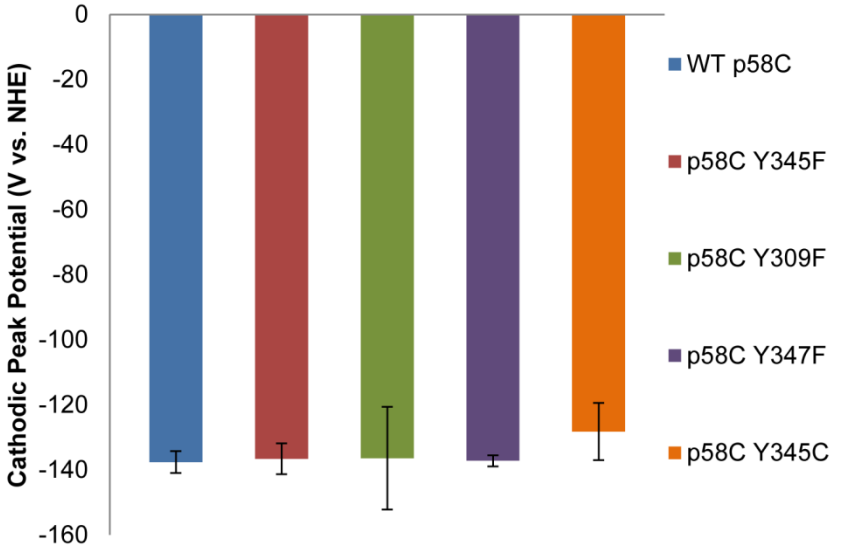

B

	E_{peak} (mV vs. NHE)
WT	-138±3.4
Y345F	-137±4.8
Y309F	-136±16
Y347F	-137±1.7
Y345C	-128±8.7

Figure 2.13. Change in potential value for cathodic peak after p58C oxidation, WT and tyrosine mutants of p58C. Potential measurements from three CV trials after p58C electrochemical oxidation show that the WT potential is more negative on average, but the difference between WT and mutant p58C cannot be determined to a significant degree outside the margin of error. This suggests that the mutants are more likely to be in the reduced $[4Fe4S]^{2+}$ state than the WT protein with an intact charge transfer pathway, as expected. Potential values are reported as mean ± SD over n= 5 trials.

perturbation of the CT pathway in p58C can be observed on DNA-modified electrodes, the rate-limiting step, tunneling of charge through the alkanethiol linker (*31*) appending the DNA to the gold surface, obscures a measurable difference in rate between wild type and mutant p58C redox switch pathways. When comparing the scan rate dependence of reductive peak potentials for WT p58C and a previously assayed tyrosine mutant, p58C Y345L, similar values calculated for the charge transfer coefficient, α (0.75 for WT p58C, 0.59 for p58C Y345L) demonstrate that charge transfer through the 6-carbon alkanethiol linker is still rate limiting on this platform (**Figure 2.14**). Nonetheless, redox proficiency of WT and mutant p58C may be compared using charge transfer values over a fixed time in bulk electrolysis and CV.

Conversion of the reduced $[4Fe4S]^{2+}$ p58C to the oxidized $[4Fe4S]^{3+}$ p58C in bulk electrolysis, and subsequent conversion of the oxidized $[4Fe4S]^{3+}$ p58C to the reduced $[4Fe4S]^{2+}$ p58C in CV, *both* require electron transfer through the protein, between bound duplex DNA and the [4Fe4S] cluster. If a pathway through conserved tyrosines mediates the redox switch, then less charge transfer in bulk electrolysis and CV should occur for the mutants. Diminished charge transfer through p58C during bulk electrolysis necessarily results in less oxidized mutant p58C being tightly bound to the DNA before CV scanning. This alone could produce the smaller CV signals observed. These signals, however, could also be diminished by the perturbed pathway impeding cluster oxidation in bulk electrolysis as well as reduction in CV. To assess whether charge transfer deficiency is additive for the mutants over both electrolysis and CV, we compare the percent of initial electrolysis charge observed in the CV signal for WT and mutant p58C. Wild type p58C recovers an average 63±4% of electrolysis charge in the CV peak, whereas the mutants recover an average of 24±11% (Y345C), 19±10% (Y309F), 9±4% (Y347F), and 3±2% (Y345F) of this charge under the same conditions (**Figure 2.10D**). The larger recovery

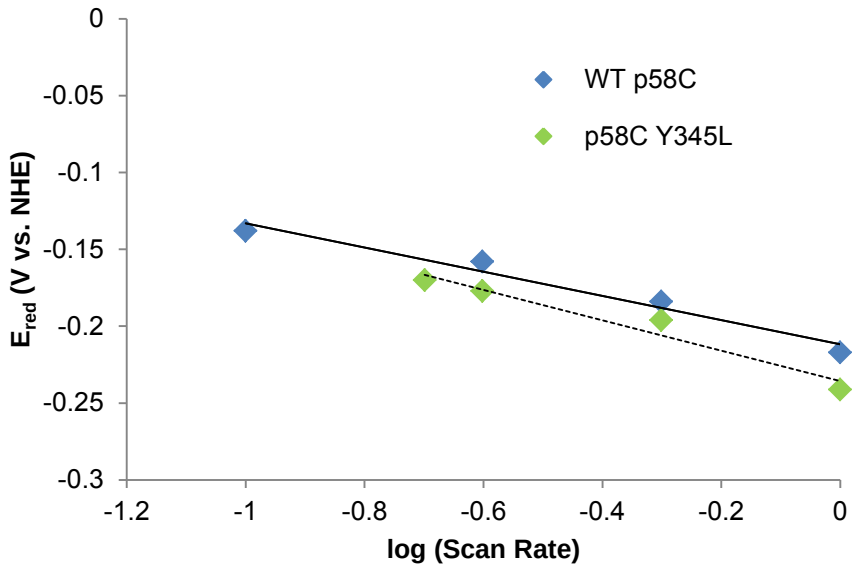

Figure 2.14. Scan Rate dependence of cathodic peak potential in p58C CV signal after electrochemical oxidation. The peak potential varies with the log of the scan rate for WT p58C (blue points, solid line) and for p58C Y345L (green points, dashed line), as is expected for an irreversible signal (*32*) in CV. The similar linear relationships of the potential and log of the scan rate for these two relationships demonstrate that the rate-determining step in generating this CV signal is tunneling through the alkanethiol linker tethering the DNA substrate to the gold electrode surface.

percentage measured for p58C Y345C may be due to transiently formed cysteine-thiyl radicals participating in a CT pathway through the protein with neighboring tyrosine residues (*44,45*), partially retaining redox switching capability. These attenuations are on the order of magnitude expected from the positive shift in cathodic peak potential (*2*). The p58C Y345L mutant was electrochemically assayed in the presence of ATP, producing a reversible signal similar to WT, again with decreased charge transfer. These data suggest that substrate binding and coupling of the [4Fe4S] cluster to duplex DNA are governed by similar biochemical properties in WT and mutant p58C. The p58C tyrosine mutants are CT-deficient, however, demonstrating that all three conserved tyrosine residues aid in shuttling charge between the [4Fe4S] cluster and bound DNA.

Redox Switch Required for Initiation but not Elongation

In order to investigate the connection between the DNA-dependent redox switch in p58C and priming activity, we assayed *in vitro* initiation and elongation activity of the full-length primase heterodimer and variants containing p58Y345F and p58Y345C mutations (**Figure 2.15A, B**). Anaerobic nucleotide incorporation assays were performed to test primase activity, measuring incorporation of α-^{32}P labeled ATP on ssDNA for initiation and 2'-OMe RNA-primed DNA for elongation. Anaerobic conditions for these assays are necessary when measuring the effect of the redox switch on priming because atmospheric oxygen can oxidize the cluster when the protein is not bound to DNA. In the absence of oxygen, the switch mediated by a pathway of conserved tyrosine residues is thus the sole means through which to convert the enzyme from its native $[4Fe4S]^{2+}$ state to its tightly bound, CT-active $[4Fe4S]^{3+}$ state. We additionally note that in our assays, primase cannot truncate its products by handing them off to pol α; instead, we observe a mixture of short primers and fully elongated 'primer-multimer' length products (**Figure 2.15A, 2.15B, 2.16A, 2.16B**) (*46,47*).

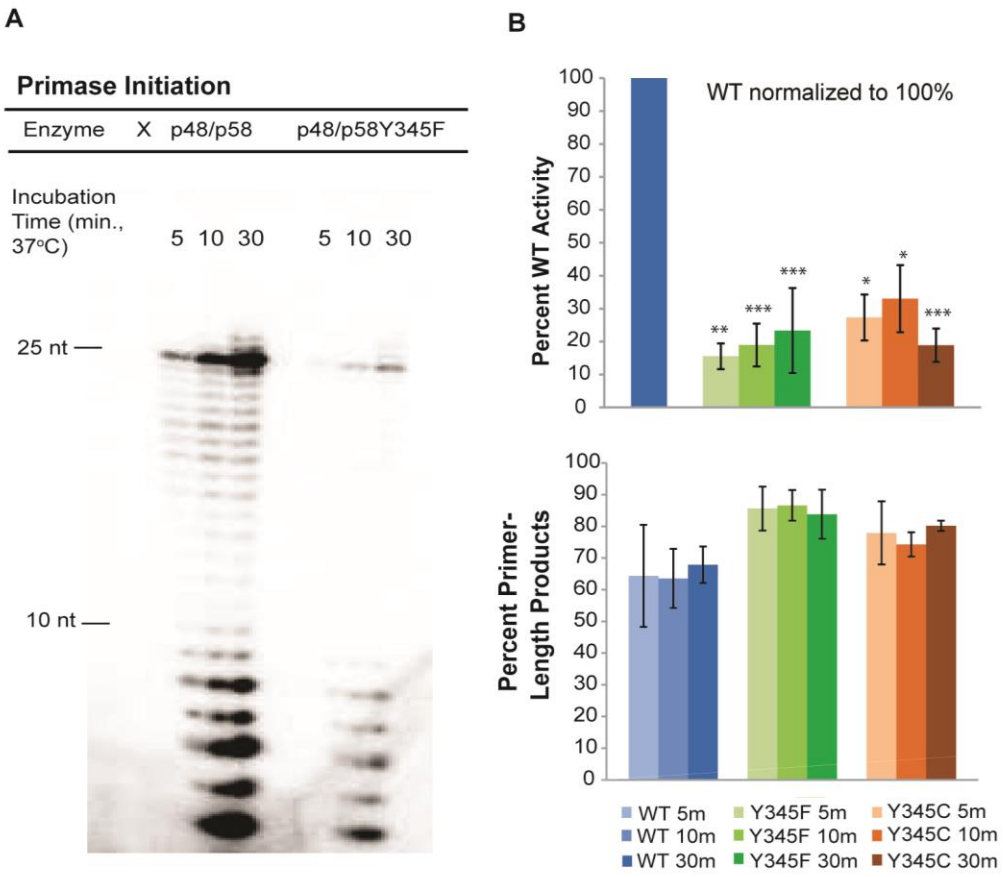

Fig. 2.15. Redox Switching Plays a Role in Primase Initiation. A) Gel separation of products for WT p48/p58 and p48/p58Y345F reactions on ssDNA. The WT enzyme is significantly more active on ssDNA than either mutant. **B)** Quantified products for WT p48/p58, p48/p58Y345F, and p48/p58Y345C initiation assays. Mutants synthesize 15-35% of WT products on average. Mutant primase synthesizes shorter products on average. Primer-length products in graph below are defined as products 7-10nt in length. Initiation assays were performed anaerobically, with 250nM ssDNA, 1 μM α-^{32}P ATP, 112 μM CTP, 188 μM UTP, 400 nM enzyme in 50 mM Tris, pH 8.0, 3 mM $MgCl_2$, at 37 °C. Quantifications shown are mean ± SD of n ≥ 3 trials, * = 0.001<p<0.005, ** = 0.001<p<0.0005, *** = p<0.0005, student's t-test.

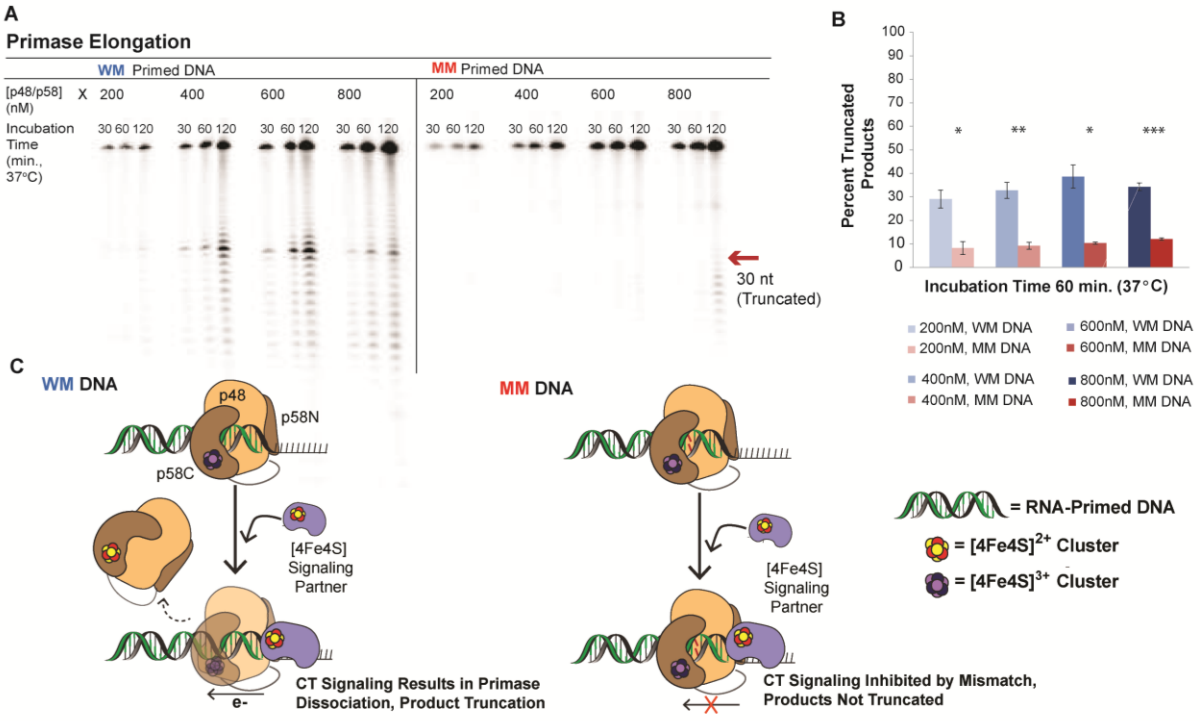

Fig. 2.16. A Mismatch in the Nascent Primer Inhibits Primase Truncation. A) Gel separation of elongation products on a 2'-OMe RNA- primed DNA substrate, when a well-matched (WM) or mismatched (MM) primer is synthesized by WT p48/p58. **B)** Average percent truncated products after 60 minutes of incubation at 37°C. WT primase synthesizes significantly more truncated products with a WM primer than a MM primer. **C)** Scheme illustrating the observed products in the mismatched primer elongation experiment. When p58C is in contact with the RNA/DNA primer, primase can signal another DNA-bound [4Fe4S] enzyme through a WM primer and dissociate from the template, truncating products. (bottom left) DNA CT is inhibited with a MM primer, precluding redox signaling and primer truncation. Elongation assays were performed anaerobically, with 500nM primed DNA, 1 μM α-^{32}P ATP, 200 μM CTP, 100 μM UTP, 200-800 nM p48/p58 in 50 mM Tris, pH 8.0, 3 mM $MgCl_2$, at 37 °C. Quantifications shown are mean ± SD of n = 3 trials, * = 0.001<p<0.005, ** = 0.001<p<0.0005, *** = p<0.0005, student's t-test.

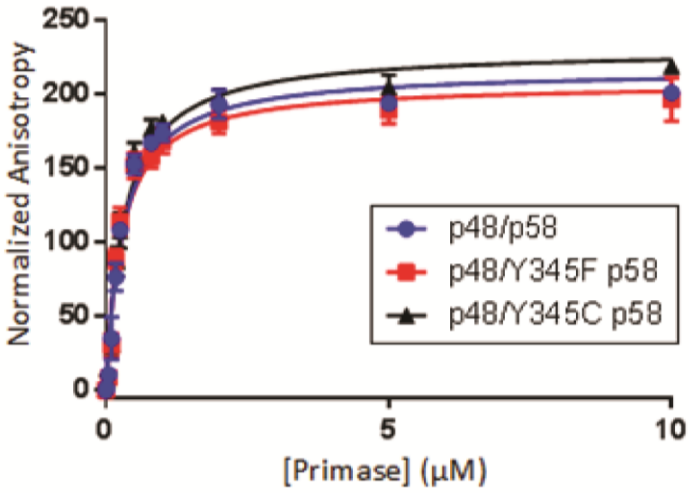

Dissociation Constants for p48/p58

Construct	K_D (μM)
p48/p58	0.30±0.03
p48/p58Y345F	0.28±0.04
p48/p58Y345C	0.32±0.04

Fig. 2.17. DNA binding for WT and mutant primase. WT and mutant primase have similar DNA binding affinities with high nanomolar dissociation constants. Affinities were measured by fluorescence anisotropy of FITC-labeled DNA substrates in the presence of atmospheric oxygen in 20 mM HEPES, pH 7.5, and 75 mM NaCl. Background was subtracted from anisotropy values prior to plotting. K_D values are mean ± SD over n=3 measurements for each variant.

To characterize initiation, we used a 50-nt ssDNA substrate (**Table 2.1**) containing exactly one complementary base for the radiolabeled nucleotide triphosphate, α-^{32}P ATP. We found that WT primase has much higher overall initiation activity than both mutants tested, including the single-atom p48/p58Y345F variant (**Figure 2.15A, 2.15B**). CT-deficient primase mutants are significantly less active on ssDNA, synthesizing only 15-35% of the WT initiation products over multiple trials. Compared to WT primase, a larger portion of the products synthesized by the mutants is < 10 nucleotides in length, suggesting that the rate-determining initiation step in product synthesis is inhibited for mutants deficient in the redox switch. The significant difference in initiation activity for the WT and CT-deficient mutant primase enzymes suggests that a redox switch changing the oxidation state of the [4Fe4S] cluster in p58C is crucial for the reaction to begin primer synthesis. Additionally, the difference in activity on ssDNA caused by a very subtle mutation in the CT pathway suggests that charge migration from bound DNA to the [4Fe4S] cofactor, through the insulating protein matrix of p58C, plays a significant role in mediating the rate-determining primase activation step on genomic template DNA, prior to the presence of duplex RNA/DNA.

We next tested the effect of a perturbation in the CT pathway through p58C on primase elongation. Primase can perform *de novo* primer synthesis on ssDNA, as well as elongation of an exogenous RNA primer on a duplex RNA/DNA substrate, *in vitro* (*9,16,48).* The enzyme binds ssDNA more tightly than duplex segments (*12*), and this substrate preference leads to a mixture of products from both elongation of the exogenous primer and initiation on the ssDNA segment of the primed substrate. We designed a primed substrate for anaerobic elongation assays with WT and CT-deficient primase (**Table 2.1**); a 31-nt 2'-OMe RNA/DNA primer was annealed to a 60-nt DNA complement strand so that the primed substrate would contain a 31-nt

RNA/DNA duplex sequence and a 29-nt 5'-ssDNA overhang. As expected, we observe a mixture of *de novo* initiation and primer elongation on these substrates with WT and mutant primase. We find that WT primase synthesizes more short, primer-length products through initiation on the ssDNA overhang and more truncated exogenous primers (**Figure 2.18**), slightly larger than 30-nt in length, while the CT-deficient mutant primase enzymes fully elongate the primer to 60-nt (**Figure 2.19**).

To examine the effect of additional copies of primase on the proportion of truncated versus fully elongated products formed, we repeated the experiment over a range of enzyme concentrations (200-800 nM). We had previously documented redox signaling using DNA CT between DNA repair proteins with [4Fe4S] clusters by atomic force microscopy (*3,4,6*), even using repair protein partners from different organisms. Hence, we hypothesized here that redox signaling between primases through DNA CT could lead to the product truncation we observe. Since DNA CT can occur through RNA/DNA duplexes (*49,50*), a redox-proficient partner for primase *in vitro* (i.e. another primase molecule), provides a means for the enzyme to change redox state, thus truncate synthesis and hand off the primer-template. Within the cell, the partner for primase handoff would presumably be DNA polymerase α, which also contains a [4Fe4S] cluster, rather than a second copy of primase. For these elongation assays, the products isolated were all at least 20 bp long, which is easily large enough for two copies of primase to bind simultaneously on the duplex, based on modeling from structural data (*11,22,26,51*), and be coupled into the duplex segment electronically. Quantification of products reveals that CT-proficient WT primase truncates products to a greater degree than the mutants, but the differences are small, especially between the WT and Y345F variants (**Figure 2.19**). This effect is not as striking as the difference seen between WT and mutant primase initiation activity, but

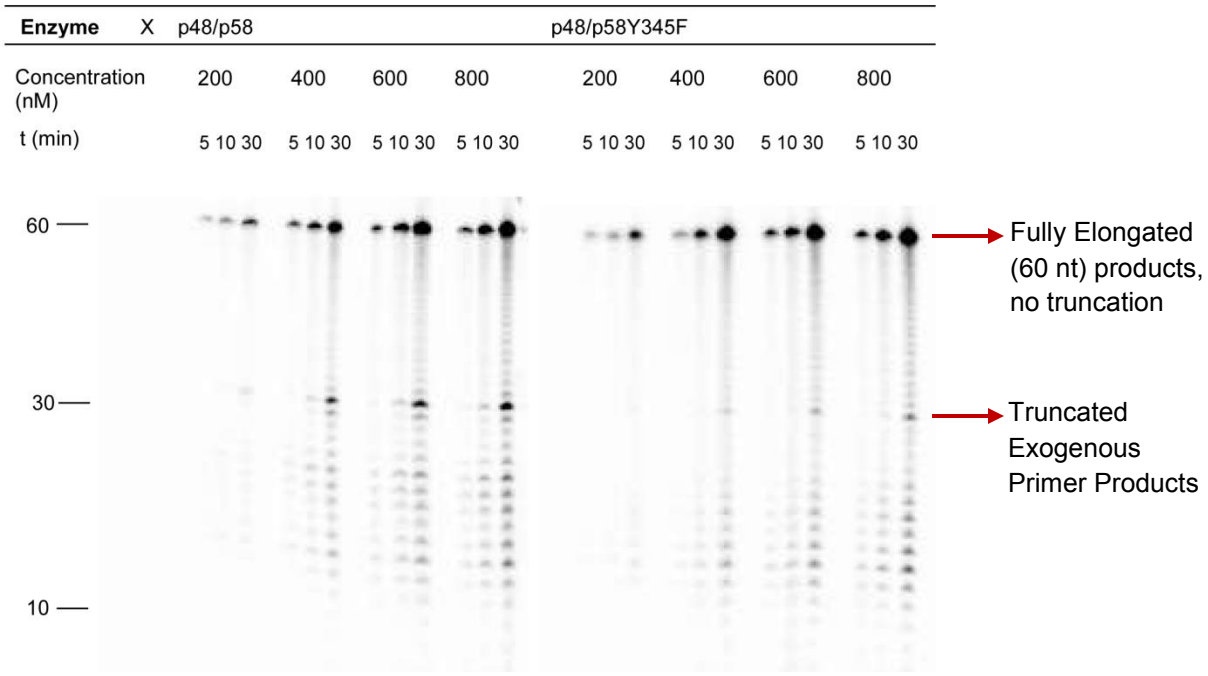

Figure 2.18. Gel separation of products for elongation reactions with increasing concentrations of p48/p58 and p48/p58Y345F on 2'-OMe RNA-primed DNA. WT primase, which has an efficient redox switching pathway between bound DNA and the [4Fe4S] cluster, synthesizes slightly more truncated products on average. The CT pathway through the protein is important for the redox switch, but it does not appear to be the sole mediator of primase product truncation. Elongation assays were performed anaerobically, with 500nM primed DNA, 1 μM α-^{32}P ATP, 120 μM CTP, 180 μM UTP, 200-800 nM enzyme in 50 mM Tris, pH 8.0, 3 mM $MgCl_2$, at 37 °C.

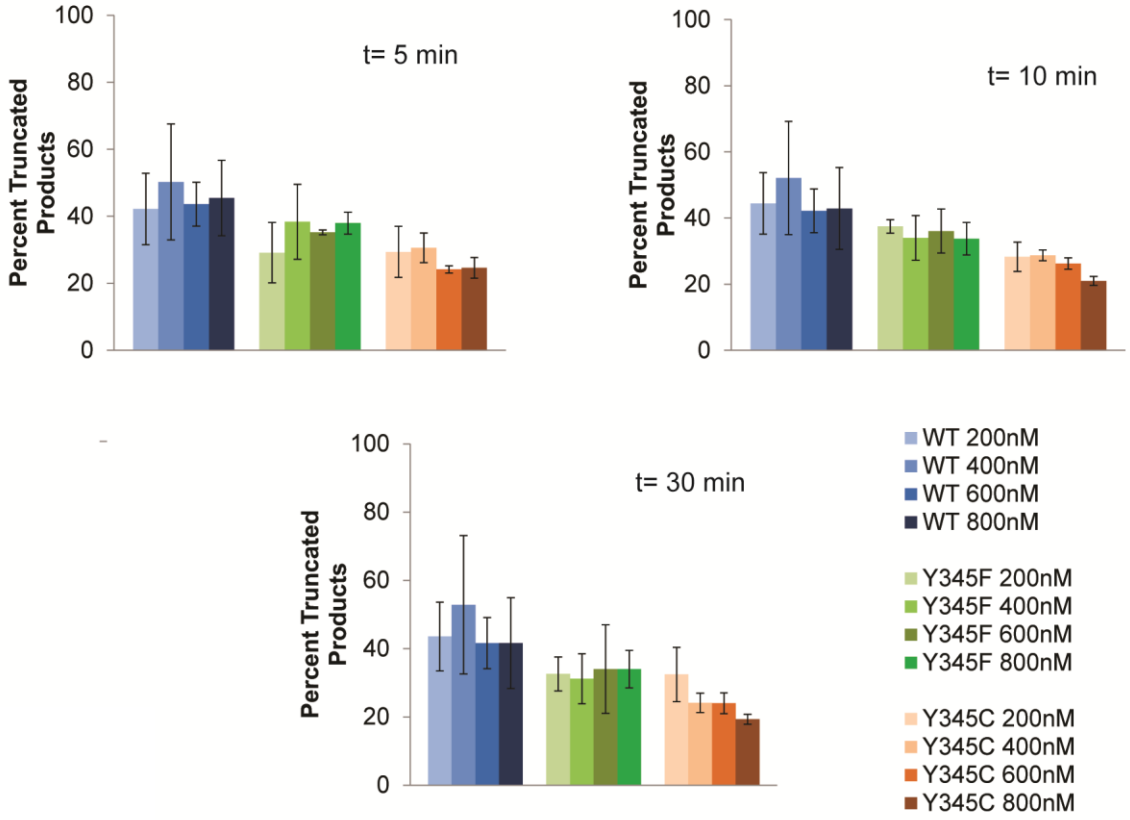

Fig. 2.19. Percent of primase products truncated by WT and CT-deficient variants at 5, 10, and 30 minutes of incubation at 37°C, under anaerobic conditions. Primase mutants are identified by the mutation in the p58C domain. WT and mutant primase elongation activity at t= 5 minutes (top left), t= 10 minutes (top right), and t= 30 minutes (bottom left) of incubation. Legend is shown on the bottom right. All measurements are mean ± SD for n= 3 trials.

the assay does underscore that CT proficiency is not critical to nucleotide polymerization in primase. Fully elongated, 60-nt products are synthesized by WT and mutant primase (**Figure 2.20**) to the same degree, within the margin of error.

DNA Charge Transport Regulates Truncation and Handoff

We next examined whether primase product truncation could be gated by DNA CT through the growing product duplex. This experiment provides a means to model substrate handoff by primase to pol α; the product duplex can mediate CT for the redox switch in protein binding and enable primer handoff, in this case between primase molecules (**Figure 2.21**). We designed and prepared an exogenously primed substrate nearly identical to the substrate used in the WT/mutant comparison assay; the only difference was a single cytosine base engineered into the 5'-ssDNA overhang. The new elongation substrate (**Table 2.1**), under conditions promoting synthesis of a primer containing a destabilizing C:C mismatch, should abrogate the CT signaling pathway through the RNA/DNA duplex and thus inhibit truncation of products by primase if DNA CT mediates the handoff. As anticipated, we observe that WT primase truncates significantly more products (**Figure 2.21A, 2.21B**) when the synthesized primer is well-matched than when the primer contains a single-base mismatch. This effect persists in anaerobic well-matched and mismatched primer elongation assays over a course of 30 to 120 minutes; we observe this effect over all concentrations of primase assayed (200 nM-800 nM) (**Figure 2.21B).** The striking difference in average percentage of truncated products (29-39% with a well-matched primer, 9-12% with a mismatched primer at t= 60 minutes) demonstrates that primase uses DNA CT as a means to modulate DNA binding through changing the redox state of its [4Fe4S] cluster.

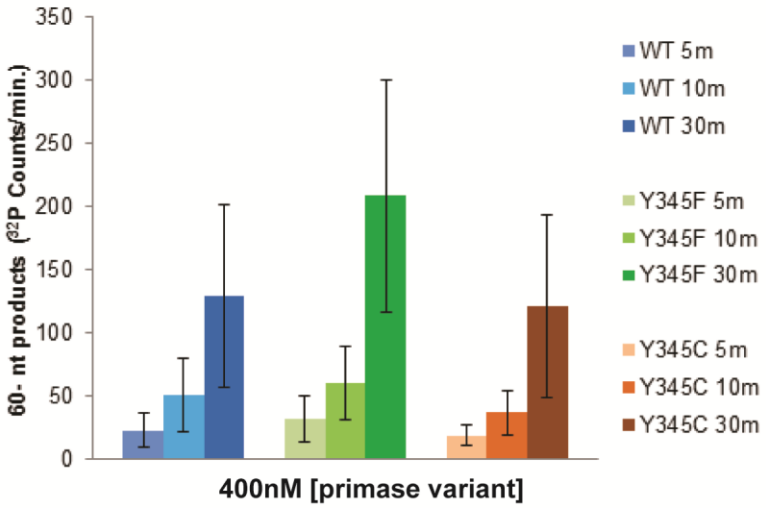

Fig 2.20. Quantification of 60-nt products synthesized by WT and CT-deficient variants at 5, 10, and 30 minutes of incubation at 37°C, under anaerobic conditions. The products, quantified by calculating ^{32}P counts/minute from α-^{32}P ATP incorporated into products separated by mass on a 20% PAGE denaturing gel, are identical between variants within error for each time point. The 60-nt products were quantified and compared to assess the nucleotide polymerization of each variant, as these products are independent of regulation by the redox switch. This demonstrates that CT-deficient primase retains the ability to polymerize nucleotides and elongate exogenous primers. Conditions are shown for 400nM enzyme concentration reactions. All measurements are mean ± SD for n= 3 trials.

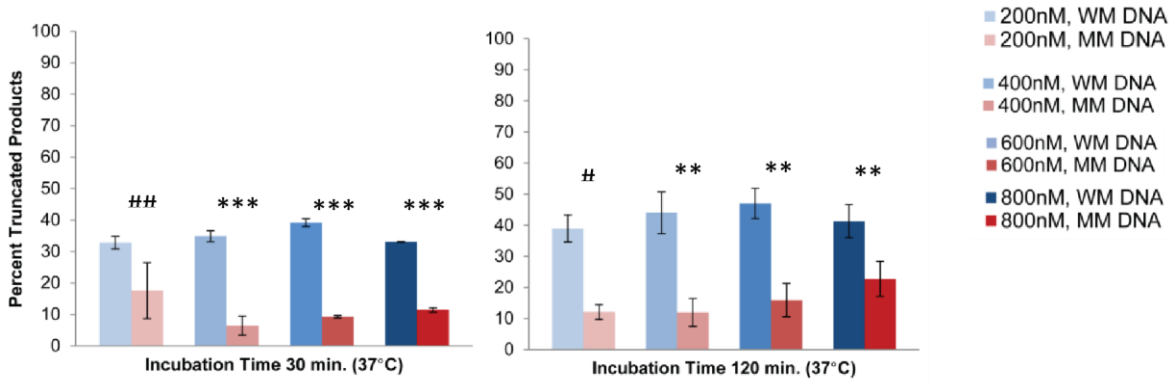

Figure 2.21. Percentage of WT primase truncated products for a) t = 30 minutes (left) and b) t = 120 minutes (right). Similar to the 60 minute time point (incubation at 37°C), these plots suggest that CT-proficient primase synthesizes significantly more truncated products on well-matched, primed DNA than in the presence of a single base mismatch within the RNA primer. When primase cannot participate in DNA CT, it favors product elongation to primer-multimer length, at all concentrations of CT-proficient primase assayed. Mean ±SD values are plotted for n= 3 trials, # = $0.025<p<0.01$, ## = $0.005<p<0.01$, ** = $0.001<p<0.0005$, *** = $p<0.0005$ (student's t-test).

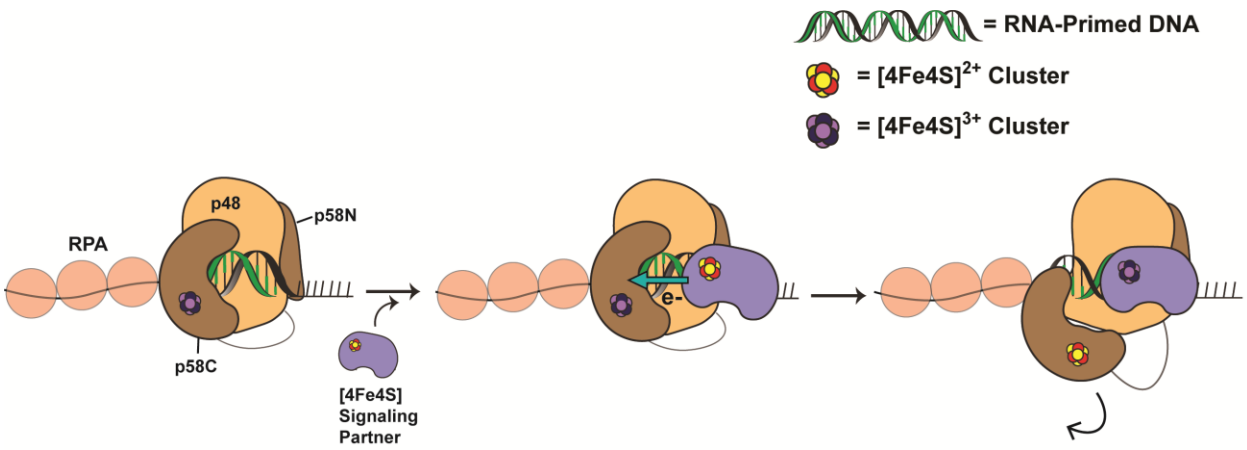

Figure 2.22. **Proposed Mechanism of Primer Handoff Driven by DNA Charge Transport Chemistry**. DNA primase elongates an RNA primer (green) to 8-12 nt length with both p48 and p58C contacting the nascent RNA/DNA duplex (left). When the nascent primer is large enough, another [4Fe4S] enzyme (purple), which we hypothesize to be DNA polymerase α *in vivo*, participates in DNA-mediated signaling through the primer-template duplex (middle). This promotes dissociation of p58C through reduction of the cluster from the $[4Fe4S]^{3+}$ state to the $[4Fe4S]^{2+}$ state; the next [4Fe4S] enzyme is then tightly bound and can continue elongation of the primer-template (right).

Discussion

Our initiation and elongation assays together suggest that DNA primase initiation and product truncation are both dependent on a redox switch changing the oxidation state of the [4Fe4S] cluster in p58C. The redox switch first activates primase to tightly bind DNA, initiating primer synthesis. DNA CT through the nascent RNA/DNA primer then mediates primase truncation. On the basis of the available structural and biochemical data (*9-12,16,22-25,47*), we propose a model for priming that incorporates this redox switch (**Figure 2.22**). As DNA primase elongates the RNA primer to 8-12 nt length, a second [4Fe4S] enzyme, DNA polymerase α, comes into contact with the exposed nascent RNA/DNA helix (*24*) and associates with the primer-template so that its cluster is able to serve as a redox donor/acceptor through primed DNA. A DNA-mediated redox event can then occur, promoting p58C dissociation from the duplex and pol α binding. Since most polymerases bind to their duplex DNA substrates with modest affinity, as we show is the case for primase, pol α is unlikely to effectively *take* the primed substrate from primase. DNA-mediated signaling, which modulates polymerase binding affinity through a change in the redox state of the [4Fe4S] cluster, would thus provide the key driver for efficient primer handoff.

We propose that DNA-mediated CT drives signaling between the [4Fe4S] cluster cofactors in DNA primase and DNA polymerase α, facilitating rapid handoff of the RNA/DNA primer. Synthesis of a short primer to initiate replication must occur repeatedly on the lagging strand of the replication fork. DNA CT occurs on a timescale (*52,53*) that could plausibly mediate this handoff; electron hopping through the protein matrix conversely occurs approximately 6 orders of magnitude more slowly (*41,42*) and would not likely be the sole mediator of primase/polymerase α redox signaling between [4Fe4S] centers. A major and likely

rate-limiting conformational change for DNA polymerase α binding to DNA has been modeled on a timescale of 100-150 ns using molecular dynamics (*24*). DNA-mediated redox signaling between primase and pol α to promote primase dissociation and primer-template transfer is thus a feasible redox mechanism for the proposed critical step for the primase-to-polymerase α transfer of the primer-template.

Our results support the proposal that the [4Fe4S] cluster in p58C serves as a redox switch governing binding, and therefore initiation and primer length counting, in the first step of replication. We show that oxidation of the $[4Fe4S]^{2+}$ cluster in human DNA primase to the $[4Fe4S]^{3+}$ state facilitates DNA binding by the p58C domain. We demonstrate an electrochemically controlled redox signal for p58C on DNA, dependent on the effective concentration of p58C at the DNA/solution interface, establishing a reversible redox switch. Conserved tyrosine residues in p58C on a pathway between the cluster and DNA mediate the redox reaction, affecting the [4Fe4S] cluster oxidation state and, consequently, DNA association of p58C. Moreover, primase initiation and termination activity, but notably not elongation activity or DNA binding, are compromised in these CT-deficient tyrosine mutants. The p58C domain has been proposed to contact ssDNA in the rate-determining primer initiation step (*12,15,16*), and to play a role in the ability of the enzyme to count the length of the primer and signal for the arrest of further synthesis coupled with hand-off of the initial primed substrate to pol α (*13*).

The recent discovery of [4Fe4S] cluster cofactors in each of the B-family replication-associated polymerases α, ε, δ, and ζ (*17*) is intriguing; combined with our results, this discovery suggests that redox reactions could be driving the DNA-binding switches generally necessary for polymerase handoffs. Moreover, studies similar to the work of Liu and Huang (*54*) investigating

primase [4Fe4S] cluster sensitivity to oxidative stress may further illuminate how this chemistry relates to eukaryotic replication activity in different cellular redox environments. Could the redox switch for primase binding to DNA be part of a larger, DNA-mediated electron transfer relay coordinating the association, transfer, and dissociation steps of replication? Our results illustrate a chemical role for the [4Fe4S] cluster as a DNA-binding redox switch and point towards a new mechanism for coordinating activity within the dynamic replication fork.

References

1. Grodick, M.A., Muren, N.B., Barton, J.K. DNA charge transport within the cell. *Biochemistry*, **2015**, *54*, 962-973.

2. Gorodetsky, A.A., Boal, A.K., Barton, J.K. Direct electrochemistry of Endonuclease III in the presence and absence of DNA. *J. Am. Chem. Soc.* **2006**, *128*, 12082-12083.

3. Boal, A.K., Genereux, J.C., Sontz, P.A., Gralnick, J.A., Newman, D.K., Barton, J.K. Redox signaling between DNA repair proteins for efficient lesion detection. *Proc. Natl. Acad. Sci. U. S. A.,* **2009**, *106,* 15237-15242.

4. Sontz, P.A., Mui, T.P., Fuss, J.O., Tainer, J.A., Barton, J.K. DNA charge transport as a first step in coordinating the detection of lesions by repair proteins. *Proc. Natl. Acad. Sci. USA*, **2012**, *109*, 1856-1861.

5. Pheeney, C.G., Arnold, A.R., Grodick, M.A., Barton, J.K. Multiplexed electrochemistry of DNA-bound metalloproteins. *J. Am. Chem. Soc.,* **2013**, *135*, 11869-11878.

6. Grodick, M.A., Segal, H.M., Zwang, T.J., Barton, J.K. DNA-Mediated Signaling by Proteins with 4Fe-4S Clusters Is Necessary for Genomic Integrity. *J. Amer. Chem. Soc.* **2014**, *136*, 16470-16478.

7. Rees, D.C., Howard, J.B. The Interface Between the Biological and Inorganic Worlds: Iron-Sulfur Metalloclusters., *Science*, **2003**, *300*, 929-931.

8. Rouault, T.A. Mammalian iron-sulphur proteins: novel insights into biogenesis and function. *Nat. Rev. Mol. Cell Biol.*, 2015, *16*, 45-55.

9. Klinge, S., Hirst, J., Maman, J.D., Krude, T., Pellegrini, L. An iron-sulfur domain of the eukaryotic primase is essential for primer synthesis. *Nat. Struct. Mol. Biol.,* **2007**, *14*, 875-877.

10. Weiner, B.E., Huang, H., Dattilo, B.M., Nilges, M.J., Fanning, E., Chazin, W.J. An iron-sulfur cluster in the c-terminal domain of the p58 subunit of human DNA primase. *J. Biol. Chem.*, **2007**, *282*, 33444-33451.

11. Vaithiyalingam, S., Warren, E.M., Eichman, B.F., Chazin, W.J. Insights into eukaryotic priming from the structure and functional interactions of the 4Fe-4S cluster domain of human DNA primase. *Proc. Natl. Acad. Sci. USA*., **2010**, *107*, 13684-13689.

12. Sauguet, L., Klinge, S., Perera, R.L., Maman, J.D., Pellegrini, L. Shared active site architecture between the large subunit of eukaryotic primase and DNA photolyase. *PloS One*. **2010**, *5*, e10083.

13. Agarkar, V.B., Babayeva, N.D., Pavlov, Y.I., Tahirov, T.H. Crystal structure of the c-terminal domain of human DNA primase large subunit. *Cell Cycle,* **2011**, *10*, 926-931.

14. Baranovskiy, A.G., Zhang, Y., Suwa, Y., Babayeva, N.D., Gu, J., Pavlov, Y.I., Tahirov, T.H. Crystal structure of the human primase. *J. Biol. Chem*., **2015**, *290*, 5635-5646.

15. Kilkenny, M.L., De Piccoli, G., Perera, R.L., Labib, K., Pellegrini, L. A conserved motif in the c-terminal tail of DNA polymerase α tethers primase to the eukaryotic replisome. *J. Biol. Chem.,* **2012**, *287*, 23740-23747.

16. Kilkenny, M.L., Longo, M.A., Perera, R.L., Pellegrini, L. Structures of human primase reveal design of nucleotide elongation site and mode of pol α tethering. *Proc. Natl. Acad. Sci. USA*., **2013**, *110*, 15961-15966.

17. Netz, D.J.A., Stith, C.M., Stümpfig, M., Köpf, G., Vogel, D., Genau, H.M., Stodola, J.L., Lill, R., Burgers, P.M.J., Pierik, A.J. Eukaryotic DNA polymerases require an iron-sulfur cluster for the formation of active complexes. *Nature Chemical Biology*., **2012**, *8,* 125-132.

18. Frick, D.N., Richardson, C.C. DNA Primases. *Annu. Rev. Biochem.,* **2001**, *70,* 39-80.

19. Kuchta, R.D., Stengel, G. Mechanism and evolution of DNA primases. *Biochimica et Biophysica Acta*. **2010**, *1804*, 1180-1189.

20. Arezi, B., Kuchta, R.D. Eukaryotic DNA primase. *Trends in Biochemical Sciences*., **2000**, *25*, 572-576.

21. O'Donnell, M.E., Langston, L., Stillman, B. Principles and concepts of DNA replication in bacteria, archaea, and eukarya. *Cold Spring Harbor Perspectives in Biology*., **2013**, *5*, a010108.

22. Baranovskiy, A.G., Babayeva, N.D., Zhang, Y., Gu, J., Suwa, Y., Pavlov, Y.I., Tahirov, T.H. Mechanism of Concerted RNA-DNA Primer Synthesis by the Human Primosome. *J. Biol. Chem.*, **2016**, *291*, 10006-10020.

23. Klinge, S., Núnez-Ramírez, R., Llorca, O., Pellegrini, L. 3D architecture of DNA Pol α reveals the functional core of multi-subunit replicative polymerases. *EMBO J.*, **2009**, *28*, 1978-1987.

24. Perera, R.L., Torella, R., Klinge, S., Kilkenny, M.L., Maman, J.D., Pellegrini, L. Mechanism for priming DNA synthesis by yeast DNA polymerase α. *eLife*, **2013**, *2*, e00482.

25. Vaithiyalingam, S., Arnett, D.R., Aggarwal, A., Eichman, B.F., Fanning, E., Chazin, W.J. Insights into Eukaryotic Primer Synthesis from Structures of the p48 Subunit of Human DNA Primase. *J. Mol. Biol.*, **2014**, *426*, 558-569.

26. Lue, N.F., Chan, J., Wright, W.E., Hurwitz, J. The Cdc13-Stn1-Ten1 complex stimulates pol α activity by promoting RNA priming and primase-to-polymerase switch. *Nature Communications*., **2014**, *5*, 5762.

27. Georgescu, R.E., Schauer, G.D., Yao, N.Y., Langston, L.D., Yurieva, O., Zhang, D., Finkelstein, J., O'Donnell, M.E. Reconstitution of a eukaryotic replisome reveals suppression mechanisms that define leading/lagging strand operation. *eLife*, **2015**, *4*, e04988.

28. Zerbe, L.K., Kuchta, R.D. The p58 subunit of human DNA primase is important for primer initiation, elongation, and counting. *Biochemistry*, **2002**, *41*, 4891-4900.

29. Garg, P., Burgers, P.M.J. DNA polymerases that propagate the eukaryotic DNA replication fork. *Critical Reviews in Biochemistry and Molecular Biology*, **2005**, *40*, 115-128.

30. Fuss, J.O., Tsai, C., Ishida, J.P., Tainer, J.A. Emerging critical roles of Fe-S clusters in DNA replication and repair. *BBA*, **2015**, *1853*, 1253-1271.

31. Slinker, J. D., Muren, N. B., Gorodetsky, A. A., Barton, J. K. Multiplexed DNA-modified electrodes. *J. Am. Chem. Soc.,* **2010**, *132*, 2769-2774.

32. a) Slinker, J.D., Muren, N.B., Renfrew, S.E., Barton, J.K. DNA charge transport over 34 nm. *Nature Chem.* **2011**, *3*, 228-233. b) Laviron, E. General expression of the linear potential sweep voltammogram in the case of diffusionless electrochemical systems. *J. Electroanal. Chem.*, **1979**, *101*, 19-28.

33. Boal, A.K., Yavin, E., Lukianova, O.A., O'Shea, V.L., David, S.S., Barton, J.K. DNA-Bound Redox Activity of DNA Repair Glycosylases Containing [4Fe-4S] Clusters. *Biochemistry,* **2005**, *44*, 8397-8407.

34. Forbes, S.A., Bindal, N., Bamford, S., Cole, C., Kok, C.Y., Beare, D., Jia, M., Shepherd, R., Leung, K., Menzies, A., Teague, J.W., Campbell, P.J., Stratton, M.R., Futreal, P.A. COSMIC: mining complete cancer genomes in the Catalogue of Somatic Mutations in Cancer. *Nucleic Acids Res.,* **2011**, *39*, D945-D950.

35. Cunningham, R.P., Asahara, H., Bank, J.F., Scholes, C.P., Salerno, J.C., Surerus, K., Munck, E., McCracken, J., Peisach, J., Emptage, M.H. Endonuclease III is an iron-sulfur protein. *Biochemistry,* **1989**, *28*, 4450-4455.

36. Holmes, A.M., Cheriathundam, E., Bollum, F.J., Chang, L.M. Initiation of DNA synthesis by the calf thymus DNA polymerase-primase complex. *J. Biol. Chem.*, **1985**, *260*, 10840-10846.

37. Suzuki, M., Savoysky, E., Izuta, S., Tatebe, M., Okajima, T., Yoshida, S. RNA priming coupled with DNA synthesis on natural template by calf thymus DNA polymerase alpha-primase. *Biochemistry*, **1993**, *32*, 12782-12792.

38. Imlay, J.A. Iron-sulphur clusters and the problem with oxygen. *Molecular Microbiology*. **2006**, *59*, 1073-1082.

39. Mui, T.P., Fuss, J.O., Ishida, J.P., Tainer, J.A., Barton, J.K. ATP-Stimulated, DNA-Mediated Redox Signaling by XPD, a DNA Repair and Transcription Helicase. *J. Amer. Chem. Soc.* **2011**, *133*, 16378-16381.

40. Shih, C., Museth, A.K., Abrahamsson, M., Blanco-Rodriguez, A.M., Di Bilio, A.J., Sudhamsu, J., Crane, B.R., Ronayne, K.L., Towrie, M., Vlcek, Jr., A., Richards, J.H., Winkler, J.R., Gray, H.B. Tryptophan-accelerated electron flow through proteins. *Science*, **2008**, *320*, 1760-1762.

41. Gray, H.B., Winkler, J.R. Electron flow through metalloproteins. *Biochim. Biophys. Acta, Bioenerg.*, **2010**, *1797*, 1563-1572.

42. Winkler, J.R., Gray, H.B. Long-range electron tunneling. *J. Am. Chem. Soc.*, **2014**, *136*, 2930-2939.

43. Plekan, O., Feyer, V., Richter, R., Coreno, M., Prince, K.C. Valence photoionization and photofragmentation of aromatic amino acids. *Molecular Physics*., **2008**, *106*, 1143-1153.

44. Stubbe, J., Nocera, D.G., Yee, C.S., Chang, M.C.Y. Radical initiation in the class I ribonucleotide reductase: long-range proton-coupled electron transfer? *Chem. Rev.*, **2003**, *103*, 2167-2202.

45. Stubbe, J., van der Donk, W.A. Protein Radicals in Enzyme Catalysis. *Chem. Rev.*, **1998**, *98*, 705-762.

46. Sheaff, R.J., Kuchta, R.D., Ilsley, D. Calf thymus DNA polymerase-α-primase: "communication" and primer•template movement between the two active sites. *Biochemistry*. **1994**, *33*, 2247-2254.

47. Sheaff, R.J., Kuchta, R.D. Misincorporation of nucleotides by calf thymus DNA primase and elongation of primers containing multiple noncognate nucleotides by DNA polymerase α. *J. Biol. Chem.* **1994**, *269*, 19225-19231.

48. Nunez-Ramirez, R., et al. Flexible tethering of primase and DNA Pol α in the eukaryotic primosome. *Nuc. Acids Res.*, **2011**, *39*, 8187-8199.

49. O'Neill, M.A., Barton, J.K. 2-Aminopurine: a probe of structural dynamics and charge transfer in DNA and DNA:RNA hybrids. *J. Am. Chem. Soc.*, **2002**, *124*, 13053-13066.

50. Boon, E.M., Barton, J.K. DNA Electrochemistry as a probe of base-pair stacking in A-, B-, and Z-form DNA. *Bioconjugate Chem.*, **2003**, *14*, 1140-1147 (2003).

51. Garcia-Diaz, M., Bebenek, K., Krahn, J.M., Pedersen, L.C., Kunkel, T.A. Role of the catalytic metal during polymerization by DNA polymerase lambda. *DNA Repair*, **2007**, *6*, 1333-1340.

52. O'Neill, M.A., Barton, J.K. DNA-Mediated Charge Transport Requires Conformational Motion of the DNA Bases: Elimination of Charge Transport in Rigid Glasses at 77 K. *J. Am. Chem. Soc.*, **2004**, *126*, 13234-13235.

53. O'Neill, M.A., Becker, H.-C., Wan, C., Barton, J.K., Zewail, A.H. Ultrafast Dynamics in DNA-Mediated Electron Transfer: Base Gating and the Role of Temperature. *Angew. Chem. Int. Ed. Engl.*, **2003**, *42*, 5896-5900.

54. Liu, L., Huang, M. Essential role of the iron-sulfur cluster binding domain of the primase regulatory subunit Pri2 in DNA replication initiation. *Protein Cell*, **2015**, *6*, 194-210.

Chapter 3: Redox Switching and Substrate Binding Coordinate Eukaryotic DNA Primase Activity

All electrochemistry and biochemical experiments were performed by E. O'Brien. M.E. Holt and L.E. Salay prepared protein for the experiments.

Introduction

Dynamic, coordinated eukaryotic DNA replication must occur in eukaryotic cells, efficiently duplicating genomes on the scale of 10^6-10^9 bp with error rates of approximately 10^{-9} mismatches per replication cycle. (*1*) The enzyme responsible for beginning this process in eukaryotes is a heterodimeric DNA-dependent RNA polymerase, DNA primase (*2-6*). Primase is a heterodimer containing an RNA polymerase subunit, p48, and a regulatory subunit, p58 (*7-10*). Primase is tethered to the heterodimeric DNA polymerase α in cells; both enzymes putatively contain a [4Fe4S] cluster (*11-13*). The polymerase-α-primase complex executes the first steps of replication through a multistep process (*4-6,14*). First primase binds ssDNA and two nucleotide triphosphates (NTPs) and synthesizes a dinucleotide that becomes the 5'- end of a 8-14nt RNA primer. After dinucleotide synthesis, primase is converted to its active form and can rapidly elongate the primer to appropriate length, before dissociating from the DNA/RNA substrate and allowing polymerase α to bind. Polymerase α then synthesizes ~10-30 deoxynucleotide triphosphates (dNTPs) downstream of the RNA before dissociating and allowing the leading and lagging strand polymerases, polymerase ε and polymerase δ, respectively, (*2,3*) to overtake genome duplication.

All of the core polymerases in eukaryotic replication, as well as the translesion synthesis B-family polymerase ζ (*13*), contain [4Fe4S] clusters, metabolically expensive cofactors associated with biological electron transfer (*15, 16*). The clusters in both DNA polymerase δ and primase (*17,18*) moreover can be oxidized and reduced when bound to DNA, through DNA-mediated charge transport (DNA CT). DNA CT is a long-range, rapid, and mismatch-sensitive biochemical process, (*19-21*) making it interesting to consider as a regulatory mechanism for replication dynamics. DNA CT has previously been demonstrated to occur in nuclei and

nucleosome core particles (*22*,*23*). This process moreover facilitates the first steps of efficient oxidative lesion location *in vitro* and in cells (*24*-*26*) between [4Fe4S] DNA repair enzymes in bacteria.

Here we use DNA-modified Au electrodes to assess the DNA-mediated redox activity of the full-length human DNA primase enzyme, p48/p58. We observe that the full-length enzyme participates in a redox switch, cycling between $[4Fe4S]^{2+}$ and $[4Fe4S]^{3+}$ oxidation states when bound to both DNA and NTPs. This redox activity is moreover DNA-mediated and dependent on the redox pathway of conserved tyrosines through the primase [4Fe4S] domain, p58C (*18*). Anaerobic activity studies additionally demonstrate that the redox switch in primase, which affects primase initiation, affects primase truncation but not catalytic activity. Catalytic activity, but not primase initiation, conversely, is affected by substrate binding prior to the priming reaction. This result suggests that the redox switch works in concert with a conformational switch induced upon substrate binding to regulate each step in primer synthesis.

Materials and Methods.

Oligonucleotide preparation. All standard or modified phosphoramidites and DNA synthesis reagents were purchased from Glen Research. Unmodified DNA oligonucleotides for electrochemical experiments were purchased from Integrated DNA Technologies, Inc. Thiol-modified DNA strands for electrochemistry were made on an Applied Biosystems 3400 DNA synthesizer, with a C6 S-S phosphoramidite incorporated at the 5'- terminus. Single-stranded DNA was purified using standard procedures as described previously. (*27*) High pressure liquid chromatography (HPLC) using a reverse-phase PLRP-S column (Agilent) was used, and oligonucleotide mass confirmed using MALDI-TOF Mass Spectrometry. Thiol-modified strands

were reduced after the initial HPLC purification with 100mM dithiothreitol (Sigma) for 2-3 h in 50 mM Tris-HCl, pH 8.4, 50 mM NaCl. Reduced thiol-modified DNA was purified by size exclusion chromatography (Nap5 Sephadex G-25, GE Healthcare) and subsequent reverse-phase HPLC. Single-stranded oligonucleotides were then desalted using ethanol precipitation and stored in low salt buffer (5 mM Phosphate, pH 7.0, 50 mM NaCl). Duplex DNA for electrochemistry was prepared by quantification of the complementary single-stranded oligonucleotides by UV-Visible spectroscopy, followed by annealing at 90 °C. A mixture of equimolar complementary single-stranded DNA (50 μM) was prepared in low salt buffer. Thiol-modified duplex DNA substrates were then deoxygenated by bubbling argon gas through the solution for 90-180 s. Duplex DNA was annealed on a thermocycler (Beckman Instruments) by initial heating to 90 °C, followed by slow cooling to 4 °C over 90 minutes. DNA was quantified using absorbance at 260 nm, with extinction coefficients at 260 nm for DNA obtained using Integrated DNA Technologies online OligoAnalyzer tool. Single-stranded DNA substrates were quantified using UV-Visible spectroscopy and stored in low salt buffer at a stock concentration for activity assays.

Multiplexed Chip Fabrication. Multiplexed electrode platforms were prepared using standard photolithography techniques, adapted from established protocols. (*21*,*27*,*28*) Nine 1 in. by 1 in. chips were patterned on 525 um thick silicon wafers (SiliconQuest). A thermal oxide layer roughly 4000 Å thick was grown on the silicon wafers using a Tytan tube furnace (Tystar). S1813 photoresist (2 μm layer) was deposited onto the wafers for patterning of the chips before metal deposition. Electron beam evaporation (CHA Industries) was then used to deposit a 3nm titanium adhesion layer followed by a 100nm gold layer, without breaking vacuum between depositions. Metal lift-off using Remover PG (MicroChem) was performed overnight (10-12 h)

at ambient temperature. Wafers were subsequently dried with a nitrogen gun and dehydrated at 140 °C for 10 minutes. A 3 um layer of insulating SU-8 photoresist was deposited and patterned onto the wafer as described previously,(*21*,*27*,*28*) with connective wires between contact pads on the edges of the chips and working electrodes in the center were covered but the contact pads and working electrodes left exposed. This ensured a fixed working electrode surface area of 2 mm^2. SU-8 photoresist was cured (150 °C, 15 minutes) and wafers cleaved into individual chips using a Dynatex Scriber/Breaker or broken manually after scoring with a diamond tip scriber.

DNA Modified Electrode Assembly/Preparation. Multiplexed chips were cleaned using sonication in acetone and isopropyl alcohol as described previously. (*27*) Chips were then dried thoroughly using argon gas and ozone-cleaned for 20 minutes at 20 mW using a Uvo brand ozone cleaner. Clean chips were assembled onto polycarbonate holders with acrylic clamp and Buna-N rubber gasket according to previous protocols, with four quadrants in the chip separated by fastened gasket and clamp. (*27*) Duplex DNA substrates, with a thiol modifier at the 5'- end, (25 μM) were deposited in a 20 μL volume onto each quadrant of the multiplex chip. Substrates incubated for 18-24 hours on the gold surface to allow formation of self-assembled DNA monolayer. DNA monolayers were washed with phosphate buffer (5mM phosphate, pH 7.0, 50mM NaCl, 5% glycerol) and subsequently backfilled with 1mM 6-mercaptohexanol (Sigma) in phosphate buffer for 45 minutes. Monolayers are then washed 10 times per quadrant with phosphate buffer and twice per quadrant with TBP buffer (5 mM phosphate, pH 7.0, 50 mM NaCl, 4 mM $MgCl_2$, 4 mM spermidine) to aid in formation of a monolayer with termini accessible for p58C binding. Assembled chips were transported into an anaerobic glove bag chamber (Coy Products) and washed 5 times per quadrant with p58C buffer (20 mM HEPES, pH 7.2, 75 mM NaCl), which was previously deoxygenated by argon bubbling (at least 1 second/μL

of solution) and allowed to incubate at least 1-2 days in the chamber prior to the experiment. Initial cyclic voltammetry scans of the monolayers in p58C buffer were performed to ensure monolayer formation on each electrode. All washes were performed with 20 μL buffer volumes on each quadrant. Before scanning, a 200 μL volume was deposited over the chip surface, a bulk solution well for completion of a three-electrode circuit with an external reference and counter electrode.

Sample Preparation for Electrochemistry. Wild type and mutant p58C samples were stored prior to experiments in p58C storage buffer (20mM Tris, pH 7.2, 75mM NaCl) or crystallography buffer (20 mM HEPES, pH 6.8, 200 mM NaCl, 2 mM DTT). All p58C variants were transferred to HEPES electrochemistry buffer (20mM HEPES, pH 7.2, 75mM NaCl) using Amicon ultra centrifugal filters (0.5mL, 3MWCO) (Millipore Sigma). Protein was applied in a 90-140μL volume to the filter and centrifuged for 15 minutes at 14000 x g at 4°C. After centrifugation, 400μL of HEPES electrochemistry buffer was applied to the filter and centrifuged at 14000 x g for 20 minutes. This procedure was repeated four times to exchange the p58C protein into HEPES electrochemistry buffer. After buffer exchange and recovery of sample by centrifugation (2 minutes, 1000 x g), concentrations of [4Fe4S] cluster-containing p58C or mutants were measured using UV-Visible spectroscopy, by absorbance of the [4Fe4S] cluster at 410 nm (extinction coefficient = 17000 M^{-1} cm^{-1}). (*29*) Recovered samples (approx. 100-150μL volume) were deoxygenated for 2-3 minutes with argon. Samples were then transferred into the anaerobic chamber (Coy Laboratory products). Before deposition onto the gold electrode surface, p58C/mutant samples were diluted to a molar concentration of 30μM or 57μM [4Fe4S] p58C variant with previously deoxygenated HEPEs electrochemistry buffer. Samples were

deposited onto multiplex chip quadrants in 20 μL volumes initially, with the remaining sample deposited in a well of bulk solution above the chip surface, to a final volume of 200-300μL.

Wild Type/Mutant primase Electrochemistry. All electrochemistry was performed using a CHI620D potentiostat and 16-channel multiplexer (CH Instruments), in an anaerobic glove chamber. Multiplex gold electrodes were part of a three electrode system with an external Ag/AgCl reference electrode (Bioanalytical Systems) and platinum counter electrode. Cyclic voltammetry scans were performed at 100 mV/s scan rates, over a potential range of +0.412 V to -0.288 V vs. NHE or +512mV to -188mV vs NHE. Bulk electrolysis on DNA was performed at an applied potential of +0.412 V vs. NHE for all electrochemical oxidation reactions and -0.188 V vs. NHE for all electrochemical reduction reactions. The oxidizing potential was applied for at least 8.33 minutes for single oxidation reactions on a surface, and 6.67 minutes for the iterative oxidation cycles of p58C variants. The reducing potential was applied for 8.33 minutes in all electrochemical reduction reactions. All bulk electrolysis and cyclic voltammetry was performed in previously deoxygenated p58C storage buffer (20 mM HEPES, pH 7.2, 75 mM NaCl). Charge transfer (nC) in the cathodic peak of oxidized samples CV scans was assessed using the area under the current wave of the reduction signal. Charge transfer was measured for oxidized samples using CHI software, assessing the area under the reductive peak in CV after electrochemical oxidation. Yields for bulk electrolysis were assessed by subtracting the total charge reported in Coulombs from the product of the electrolysis time (s) and the final current value (A). NTP-dependence of electrochemical signals were measured by pipetting a small volume (1-3μL) of 0.1M ATP stock solution into each quadrant of the multiplexed chip setup. Samples were added by quadrant, as physical barriers in the setup prevent diffusion of NTPs between electrode quadrants. After the volume of ATP stock was deposited onto the electrode

quadrant, resulting in a 2.5mM or 5mM concentration of ATP in the quadrant, CV scans were measured (100mV/s scan rate). Charge transfer was assessed using CHI software; charge values were determined by calculation of the area under the reductive and oxidative peak curves. Midpoint potentials of NTP-dependent redox signals were assessed using the peak selection function in CHI software.

Primase Pre-Incubation Initiation Assays. All primase assays were performed anaerobically, with deoxygenated buffers and reagents. Primase was pre-incubated at ambient temperature either in a stock alone, or with the DNA/NTPs used in the reaction. The pre-incubation conditions were 30 minutes at ambient temperature; only DNA or NTPs, not both substrates at once, were incubated with each sample of primase. The α-^{32}P ATP was initially dried (2.5μL of 12μM, eventually diluted to 30μL) *in vacuo* overnight the day preceding the reactions. The ^{32}P ATP-containing tubes were then brought into the anaerobic glove bag chamber, along with concentrated stocks of the unlabeled NTPs, CTP and UTP, and the single-stranded 50-nt initiation substrate, shown in **Table 3.1**. Pre-incubation mixtures consisted of the following: protein-only pre-incubation samples contained 800nM p48/p58 in primase activity buffer (50mM Tris, pH 8.0, 5mM $MgCl_2$), paired with a sample of 500nM ssDNA and 376μM UTP, 224μM CTP, and 2μM α-^{32}P ATP in activity buffer; DNA/ protein pre-incubation samples contained 800nM p48/p58 and 500nM ssDNA and were paired with a sample containing 376μM UTP, 224μM CTP, and 2μM α-^{32}P ATP in primase activity buffer; NTP and protein pre-incubation tubes consisted of a sample containing 800nM p48/p58 with 376μM UTP, 224μM CTP, and 2μM α-^{32}P ATP and paired with a sample containing 500nM ssDNA, all in the Tris activity buffer. These samples were all incubated anaerobically for 30 minutes at ambient temperature. The volume of reagents in each of the two tubes was 15μL for each reaction, making a total

Primase Electrochemistry Substrate I (Well-matched)	3'-CGCGTCTGTGCAACGTCGTG-SH-5'
	5'-TCATCACCACTGGCGCAGACACGTTGCAGCAC-3'
Primase Electrochemistry Substrate II (Well-matched)	3'-TGACTTGGGCAGGACGCAGTTGATGTACTTGTGGAG-SH-5'
	5'-AGCTCTGGTACTGAACCCGTCCTGCGTCAACTACATGAACACCTC-3'
Primase Electrochemistry Substrate II (Abasic Site)	3'-TGACTTGGGCAGGACGCAGTTGATGTACTTGTGGAG-SH-5'
	5'-AGCTCTGGTACTGAACCCGTCCTGCGTCAACTACATGAAC_CCTC-3'
Initiation Substrate	5'-AGAAAA$(GA)_8$ AAT$(A)_{25}$-3'
Elongation Substrate	3'-$(U)_{16}(T)_{15}$-5'
	5'-AGAAAA$(GA)_8$ AAT$A)_{31}$-3'

Table 3.1. DNA substrates used for electrochemistry and DNA primase activity assays. Initial p48/p58 electrochemistry was performed on a 20-nt duplex substrate with a 9-nt 5'-ssDNA overhang (Electrochemistry Substrate I). Electrochemistry of p48/p58 and p48/p58 was performed on self-assembling monolayers of a 36-mer DNA duplex substrate (Electrochemistry Substrate II) with a 9-nt 5'- ssDNA overhang. A 50-nt ssDNA substrate with a single thymine base complementary to the α-^{32}P radiolabeled ATP was used in the primase initiation assay comparing wild type and CT-deficient full-length enzyme. A 2'-OMe RNA-primed ss/dsDNA substrate, containing a 31- nucleotide duplex segment and a 29- nucleotide 5'-ssDNA overhang was used to assay elongation. . U = 2'-OMe rU, SH = -$(CH_2)_6$-SH.

reaction of 30μL when combined and incubated at 37°C. The final reaction conditions were 400nM [4Fe4S] p48/p58, 112μM CTP, 188μM UTP, 1μM α-^{32}P ATP, 250nM ssDNA in 50mM Tris, pH 8.0, 5mM $MgCl_2$. The primase reactions were incubated for 1, 3, 5, 10, and 30 minutes at 37°C in anaerobic conditions, and then quenched by an equal volume per 5.5μL reaction aliquot of 1% SDS, 25mM EDTA quenching solution to stop the reaction. Reactions, when quenched, were then transported out of the anaerobic chamber and heat-denatured for 10 minutes at 70°C, aerobically. Finally, to remove the excess free ^{32}P-labeled nucleotide, the samples were each passed through spin columns (Mini Quick Spin Oligo Columns, Roche) according to manufacturer's protocols, to separate unreacted radioactivity from small products made during primase initiation (7-10nt). Samples were then scintillation-counted and dried overnight *in vacuo*. The samples were then separated using 20% polyacrylamide gel electrophoresis (denaturing gel). Gels were warmed at 1700-2000V (90W) for approximately 1.5 hours before loading samples. Samples were resuspended after drying in 2μL formamide loading dye, vortexed, centrifuged, and heated at 90°C for 1 minute. They were then loaded onto the gel and run at ~2000V (90W) for 3.5 hours. Gels were then exposed to a phosphor screen (GE Healthcare) for 14 hours and imaged on a Typhoon 9000 Phosphorimager (GE Healthcare). Products were quantified using ImageQuant TL software; reported numbers are mean +/- SD values for n = 3 trials.

Pre-Incubation Reactions: Elongation. For primase elongation reactions, pre-incubation, reaction, and purification conditions were generally similar to those of initiation assays. Reagents were prepared in essentially the same manner as for initiation. 2.5μL of 12μM α-^{32}P ATP was dried *in vacuo* overnight for each elongation reaction, then transported into the anaerobic chamber. Pre-incubation mixtures were prepared similarly to those used in initiation

assays; two 15μL fractions of reagents in various combinations were prepared for each reaction and allowed to incubate in the anaerobic chamber for 30 minutes at ambient temperature before being mixed and reacted at 37°C. The primase only pre-incubation samples consisted of 800nM p48/p58 and a paired sample of 1μM dsRNA/DNA and 360μM UTP, 240μM CTP, and 2μM α-^{32}P ATP all in primase activity buffer; DNA/ protein pre-incubation samples consisted of 800nM p48/p58 and 1μM dsRNA/DNA and a paired sample of 360μM UTP, 240μM CTP, and 2μM α-^{32}P ATP all in the primase activity buffer; NTP/primase pre-incubation samples contained 800nM p48/p58 with 360μM UTP, 240μM CTP, and 2μM α-^{32}P ATP and a paired sample of 1μM dsRNA/DNA, all in the Tris activity buffer. The final reaction conditions, consequently, were 400nM p48/p58, 120μM CTP, 180μM UTP, 1μM α-^{32}P ATP and 500nM 2'-OMe RNA-primed DNA in 50mM Tris, pH 8.0, 5mM $MgCl_2$. After pre-incubation and mixing for reaction, each primase assay was incubated anaerobically at 37°C and aliquots of the reaction chemically quenched at 1, 3, 5, 10, and 30 minutes of reaction time. The chemical quencher for each 5.5μL aliquot of reaction was an equal volume of 1% SDS, 25mM EDTA, administered anaerobically. Reactions were further aerobically heat-denatured at 70°C for 10 minutes. Elongation reactions were purified initially using Mini Quick Spin Oligo Columns (Roche) and then using P-6 Micro Bio Spin Columns (BioRad). The Roche columns retain all synthesized products; the initiation products 7-10 nt on the ssDNA segment of the substrate oligonucleotide are purified and quantified with elongation products. The BioRad columns have an exclusion limit of 6kDa, or approximately 20 bases, thus eliminating initiation products from the quantified/purified mixture. This allows for comparison of truncated (30-35nt) products and elongated products (60nt) in the elongation assays.

RESULTS

Reversible, NTP-Dependent p48/p58 Redox Activity on DNA.

Using multiplexed DNA electrochemistry, we investigated whether human DNA primase participates in redox signaling when bound to the necessary substrates for activity (DNA and NTPs). We initially wanted to test whether primase was redox-active when present in the oxidized $[4Fe4S]^{3+}$ form, versus the reduced $[4Fe4S]^{2+}$ form. On a 36-mer duplex DNA substrate with a 9-nt, 5'- ssDNA overhang (**Table 3.1**), we electrochemically oxidized ($E_{applied}$ = 412mV vs. NHE) or electrochemically reduced ($E_{applied}$ = -188mV vs. NHE) a sample of 5μM DNA primase on an electrode surface. We performed these experiments in anaerobic conditions, to ensure full control over the redox state of the sample assayed (*30*). Subsequent cyclic voltammetry (CV) scans after electrochemical oxidation showed little redox activity in the oxidized or reduced samples (**Figure 3.1**). This effect is potentially due to the RNA polymerase domain of DNA primase binding more tightly to the DNA substrate than the p58C domain, which contains the [4Fe4S] cluster. Previous reports of p48/p58 versus p58C DNA binding affinity (*9,18*) suggest that the full-length primase protein containing the RNA polymerase domain binds more tightly than the p58C domain alone; the catalytic subunit may outcompete the [4Fe4S] domain for binding and preclude coupling of the cluster into duplex DNA for redox signaling.

After investigating the redox properties of primase in the presence of DNA but not NTPs, both of which are required substrates for enzymatic activity (*4-6*), we next assayed the redox signaling activity of primase bound to both DNA and NTPs. We observe that primase consistently displays a robust, semi-reversible redox signal in the presence of both substrates.

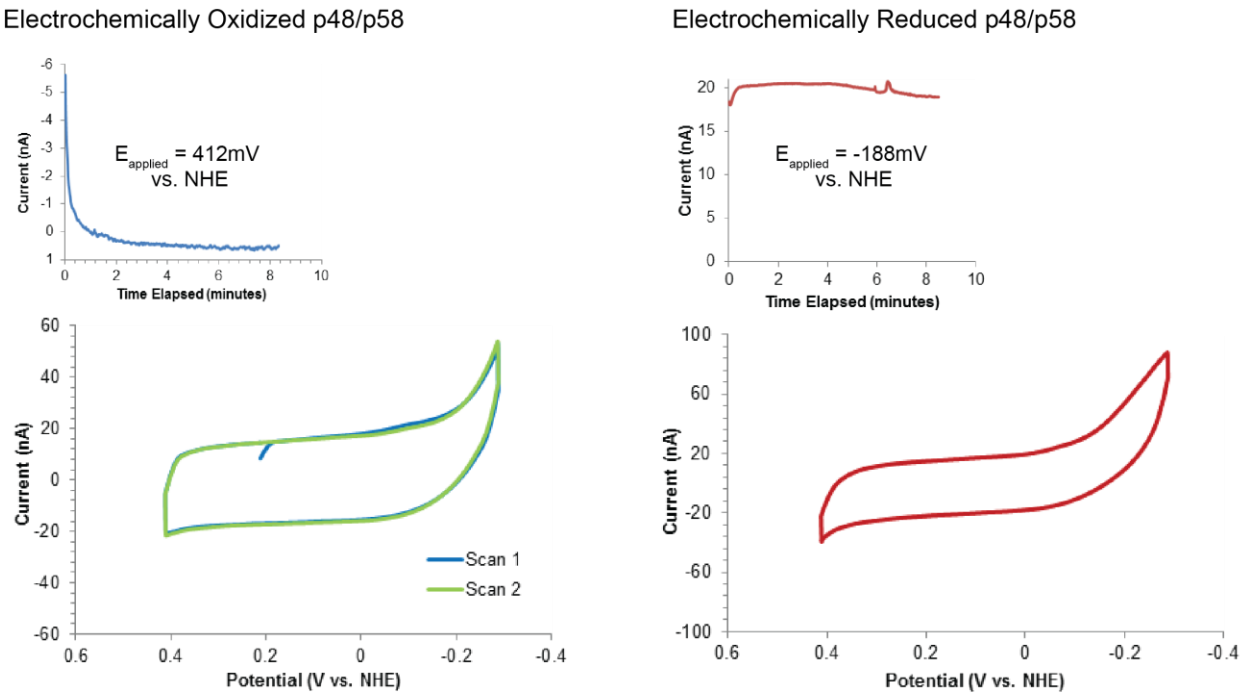

Figure 3.1. Electrochemistry of oxidized and reduced p48/p58 on DNA. Human DNA primase was electrochemically oxidized ($E_{applied}$ = 412mV vs. NHE, top left) or reduced ($E_{applied}$ = -188mV vs. NHE, top right) on a DNA electrode in anaerobic conditions. Subsequent CV scans show that minimal change occurs in this sample upon oxidation or reduction of the enzyme; this protein remains essentially redox-inert in the absence of NTPs. This is likely due to the RNA polymerase domain of p48/p58, a catalytic site distal from the cluster, binding more tightly to DNA and hindering access of the p58C [4Fe4S] domain to the DNA base stack, to couple to for redox activity. This may also be due in part to poor [4Fe4S] cluster loading of the buffer-exchanged sample. Electrochemistry was performed using Electrochemistry Substrate II (Well-matched) in Table 3.1 in anaerobic conditions, on 5µM [4Fe4S] p48/p58 in 20mM HEPES, pH 7.2, 150mM NaCl, 5% glycerol.

We tested two different substrates, a 20-nt DNA duplex with a 9-nt 5'- ssDNA overhang, and a 36-nt DNA duplex with a 9-nt 5'- ssDNA overhang, for NTP-dependent redox activity. We initially measured the redox signal in Tris storage buffer (20mM Tris, pH 7.2, 150mM NaCl, 5% glycerol) on the 20-nt duplex ss/dsDNA substrate. The unaltered p48/p58 displays no redox signal. Upon addition of 5mM [ATP+CTP] to the sample, however, we observe a redox signal in CV centered at 204 ± 5.0 mV vs. NHE, with a charge transfer values of 63±20 nC in the reductive peak. This potential is higher than generally expected (*17,24,25*) for DNA-processing [4Fe4S] enzymes. We hypothesized that the buffer conditions may have been affecting the measured midpoint potential; Tris is a weak buffer which is sensitive to temperature and addition of salts such as NTPs to the sample. (*31*) We therefore exchanged primase into a HEPES buffer and conducted the same NTP-dependent scanning experiment.

In 20mM HEPES, pH 7.2, 150mM NaCl, 5% glycerol, primase in the presence of DNA and 3.33mM [ATP+ CTP] displays a robust, semi-reversible signal centered near 160mV vs. NHE, which is much closer to the reported values for human and yeast p58C (*18,32*) near 140-150mV vs. NHE. This signal was apparent even at 5μM [4Fe4S] enzyme and was measured on a 36-mer duplex with a 9-nt ssDNA overhang, which provides extra space for a larger protein, such as the 110kDa primase, to bind (*17,33*). The signal was attenuated in the presence of an abasic site in the DNA duplex; the primase signal is DNA-mediated. (**Figure 3.2**) The midpoint potential of p48/p58 moreover may be slightly higher than the potential of p58C due to the increased amount of protein matrix surrounding the cluster in the full-length primase enzyme; this can affect cluster environment and alter measured potential. (*34*) Binding of the DNA polyanion and the negatively charged NTPs, importantly, still shifts the cluster potential of full-length primase into the physiological range. This result suggests that the redox switch allowing

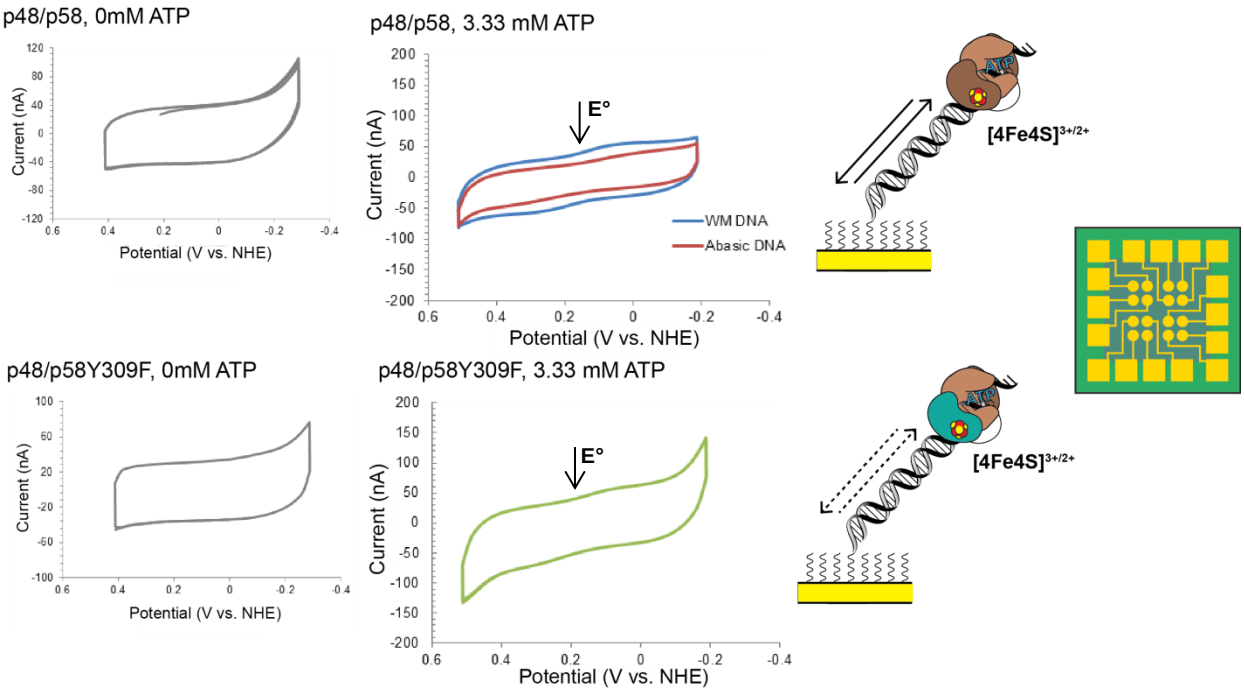

Figure 3.2. NTP-dependent redox signaling in p48/p58. In the absence of NTPs, p48/p58 and p48/p58Y309F are redox-inert on DNA. (left) When 3.3mM [ATP+CTP] is added to the multiplexed DNA electrode platform (right), reversible redox switching between the $[4Fe4S]^{3+}$ and $[4Fe4S]^{2+}$ oxidation states is observed at 160 mV (p48/p58) or 190mV vs. NHE (p48/p58Y309F). The redox signal for WT, CT-proficient primase is attenuated in the presence of an abasic site in the DNA duplex. This suggests that the form of primase bound to both DNA and NTPs, participates in DNA-mediated redox signaling. The single-atom mutant displays a smaller redox signal at a higher potential, which suggests that this variant is CT-deficient and less stabilized in the oxidized form upon substrate binding. Electrochemistry was performed in anaerobic conditions with 5μM [4Fe4S] p48/p58 variant in 20mM HEPES, pH 7.2, 150mM NaCl, 5% glycerol, 100mV/s scan rate.

primase to cycle between the $[4Fe4S]^{3+}$ state and the $[4Fe4S]^{2+}$ state is associated with the active form of primase. In the enzymatically active form, primase performs DNA-mediated redox signaling.

After observing that WT p48/p58 participates in DNA-mediated redox signaling in the presence of DNA and NTPs, we next sought to ascertain whether the p48/p58Y309F variant was CT-deficient. We electrochemically oxidized and reduced 5μM [4Fe4S] p48/p58Y309F as we did with the WT enzyme, and we found surprisingly that the oxidized sample displayed a reductive peak near -100mV vs. NHE, which disappears after one scan. (**Figure 3.3**) No similar peak was seen with p58C, which displays a reductive peak near -135mV vs. NHE after electrochemical oxidation. This signal may be from an oxidized $[4Fe4S]^{3+}$ species, or potentially a $[3Fe4S]^{+}$ cluster, which is a product of oxidation to the $[4Fe4S]^{3+}$ state. The peak is observed at a 35-40mV more positive potential than the p58C oxidized protein peak, which is near the potential observed recently for a $[3Fe4S]^{+}$ cluster in MutYH. (*33*) The signal may also, however, be a $[4Fe4S]^{3+}$ signal not observed in the WT p48/p58 sample. The A_{410}/A_{280} ratios in the UV-Visible spectra for WT p48/p58 and p48/p58Y309F primase in HEPES storage buffer (**Figure 3.4**) indicate that the metal cofactor is better loaded in the mutant sample, which can affect the observation of a redox signal. Interestingly, unlike the $[3Fe4S]^{+}$ reductive peak in MutYH, (*33*) this signal is not persistent in p48/p58Y309F over multiple CV scans. The disappearance of the peak after a single scan to negative, reducing potentials is indicative of redox switching behavior similar to that of p58C.

We finally wanted to observe whether the semi-reversible, NTP-dependent redox activity was observed in the Y309F variant of p48/p58. This result would provide insight into the importance of the tyrosine pathway for mediating primase redox switching in the active form.

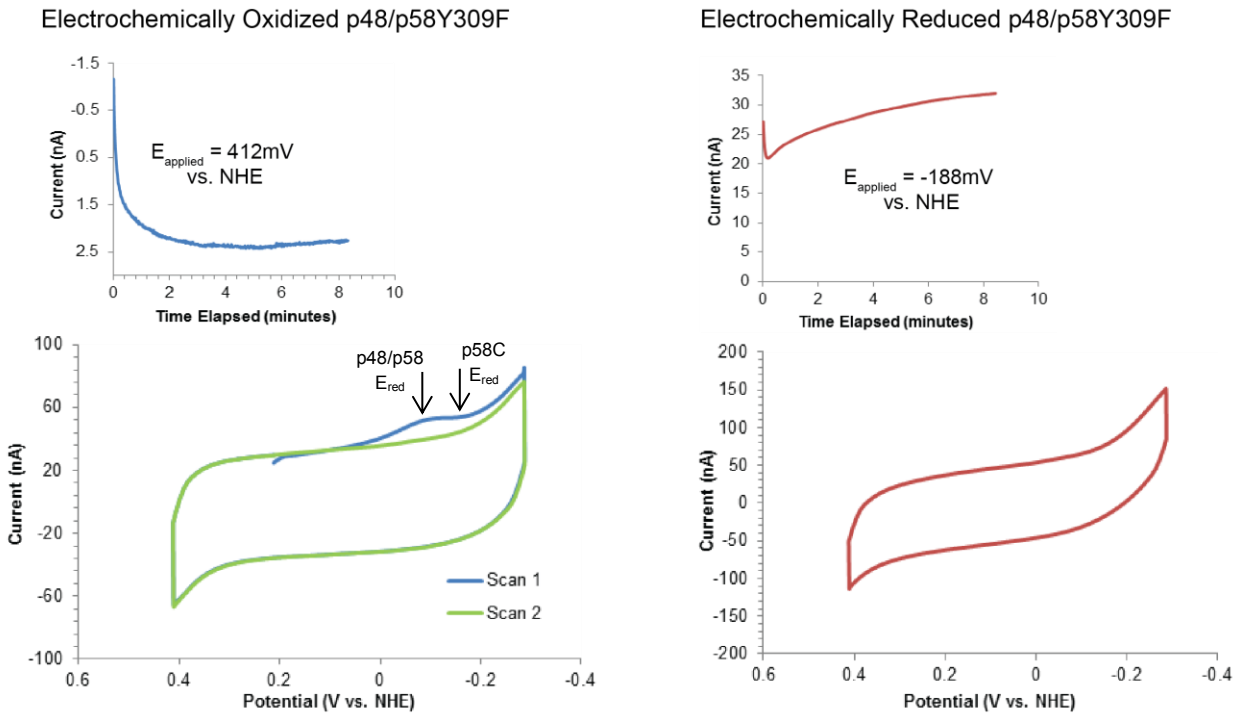

Figure 3.3. Electrochemistry of oxidized and reduced p48/p58Y309F on DNA. The human DNA primase variant was electrochemically oxidized ($E_{applied}$ = 412mV vs. NHE, top left) or reduced ($E_{applied}$ = -188mV vs. NHE, top right) on a DNA electrode in anaerobic conditions. Subsequent CV scans show a small reductive peak in the first scan after oxidation near ~-100mV vs. NHE in the oxidized sample and no redox signal after reduction. It is possible that this variant, which is redox-deficient when bound to NTPs, generated a redox signal after oxidation due to oxidative degradation to a $[3Fe4S]^{+}$ cluster, or it may have generated a redox signal upon oxidation due to increased [4Fe4S] cofactor loading, relative to p48/p58. Electrochemistry was performed using Electrochemistry Substrate II (Well-matched) in Table 3.1 in anaerobic conditions, on 5µM [4Fe4S] p48/p58 in 20mM HEPES, pH 7.2, 150mM NaCl, 5% glycerol.

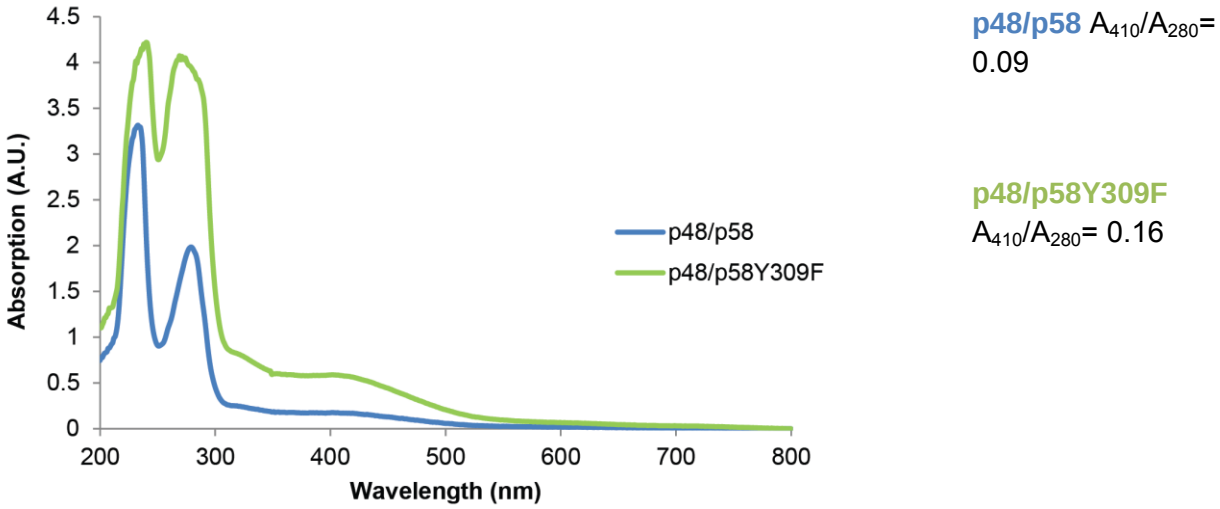

Figure 3.4. UV-Visible Spectra of p48/p58 (blue) and p48/p58Y309F (green) after exchange into 20mM HEPES, pH 7.2, 150mM NaCl, 5% glycerol from the original Tris storage buffer. The loading of the mutant protein was slightly higher than that of the WT, as judged by the ratio of absorbance at 410nm/280nm.

We observe that 5μM [4Fe4S] p48/p58Y309F does display a semi-reversible redox signal in the presence of a 36-mer DNA duplex with a 9-nt 5'- ssDNA overhang in the presence of 3.3mM [ATP + CTP]. (**Figure 3.2**) The redox signal however, displays decreased charge transfer (**Figure 3.2, 3.5**) relative to WT primase. The midpoint potential, moreover, was interestingly centered approximately 30mV more positive on average than the WT primase potential, near 190mV vs. NHE in HEPES storage buffer. This suggests that the redox pathway mutant of primase is further outside the potential range measured for other DNA-processing [4Fe4S] enzymes (*17,24-26,33*). This mutant is thus less capable of being oxidized upon substrate binding, which affects initiation activity (*35*) and primer truncation. The higher potential is likely to affect redox signaling with other [4Fe4S] enzymes and may have implications for the coordination of primase activity during replication.

P48/p58Y309F is Deficient in Primer Truncation, but not in Catalytic Activity.

The Y309F mutation in human p48/p58, which is near the cluster but approximately 15-20Å from the DNA binding interface of p58C (*7,8*), was previously demonstrated to attenuate redox switching activity in p58C and abrogate initiation activity on ssDNA in full-length primase. (*35*) This variant only synthesized 21-26% of WT products on average in anaerobic conditions, supporting the previous evidence that the redox switch is crucial for primase initiation on ssDNA. Attenuation of initiation activity in p48/p58Y345F and p48/p58Y345C is not a result of simply perturbing substrate binding interactions; the CT pathway regulates the ability of primase to synthesize products on ssDNA.

To assess the effect of the redox pathway mutation at Y309 on human primase elongation activity, we measured the product synthesis by WT primase and p48/p58 on an exogenously

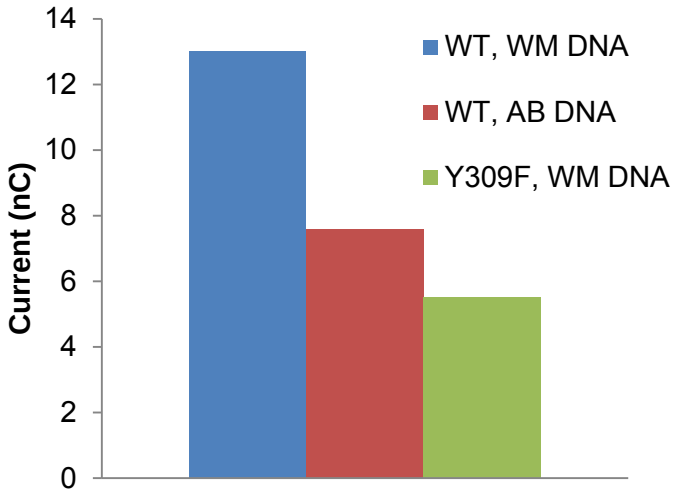

	E° (mV vs. NHE)	E_{ox} - E_{red} (mV)
WT (WM DNA)	160 ± 4.0	230 ± 20
WT (AB DNA)	170 ± 5.0	280 ± 20
Y309F (WM DNA)	190 ± 4,0	200 ± 30

Figure 3.5. Charge transport for primase electrochemistry reductive peak signals, in the presence of DNA and NTPs. WT p48/p58 displays an attenuated signal on average in the presence of a DNA duplex substrate with an abasic site. The signal is also attenuated in the presence of a single-atom redox pathway mutation in the [4Fe4S] domain. The redox potential values are similar to those measured for human p58C (*18*) for WT primase; the mutant however displays a more positive potential, indicating less stabilization of the $[4Fe4S]^{3+}$ enzyme relative to WT upon substrate binding. The large peak splitting values observed indicate a semi-reversible electron transfer process. The values reported are the mean +/- s.d. for n= at least 3 trials.

primed substrate. We used the same 31nt RNA/DNA primer/60nt template substrate used previously with WT and Y345F/Y345C primase variants. The single-atom Y309F mutation affects primer truncation but not catalytic activity, as the gel and product quantifications in **Figure 3.6** show. No appreciable difference between 60-nt product synthesis is apparent for WT and Y309F mutant primase, but the average percentage of truncated products for WT and mutant primase diverge. WT truncates 67-78% of products on average and Y309F mutant truncates only 8-24% of products on average. This result interestingly is different from the result with Y345 mutants, which both truncated to an extent similar to WT. The observed result suggests that primase truncation depends on the redox pathway to some degree, although it was not as easily observed with the Y345 mutants. Potentially, mutation of a residue near the cluster, as opposed to the DNA binding interface, facilitates more consistent redox deficiency due to dynamic substrate interactions occurring further from Y309 during the initiation/elongation assays.

Substrate Binding Enhances Primase Catalytic Activity but Does Not Affect Initiation. Primase binding of the anionic DNA and NTP substrates required for activity dramatically affects the redox properties of the [4Fe4S] cluster. (**Figure 3.2**) Structural evidence suggests that DNA and NTP binding is necessary to induce a conformation in which the DNA/NTP binding interfaces of p48 and p58C are close enough to one another for synthesis of a short stretch of RNA on the genomic template (*7*). This binding has indeed recently been demonstrated (*36*) to change the conformation of the p48/p58 heterodimer, which likely alters the [4Fe4S] cluster environment. Substrate binding thus may cause a conformational change that alters the environment and potential of the [4Fe4S] cluster (*34*) and promotes catalytic activity. We have established that the redox pathway which promotes efficient cycling between the $[4Fe4S]^{3+}$ and

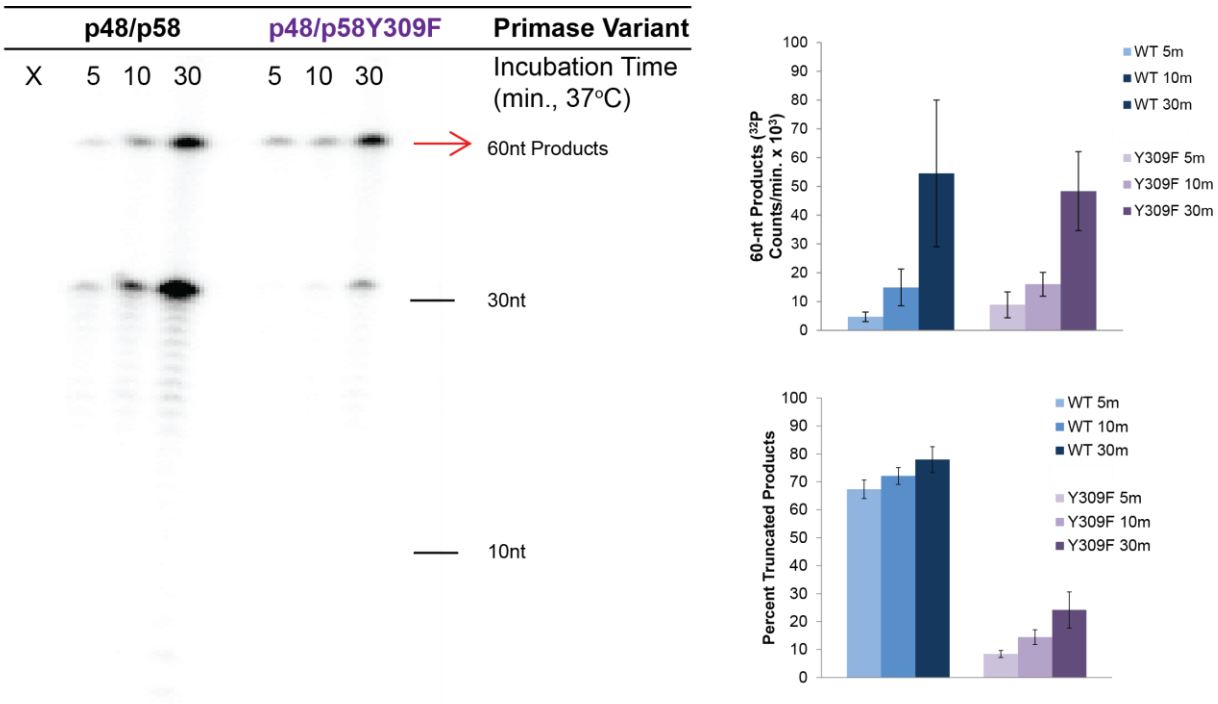

Figure 3.6. Primer Truncation, but not catalysis, is affected by the single-atom Y309F redox pathway mutation in primase. The Y309F mutant of human DNA primase is proficient in synthesis of full-length products (60 nt length), but it is deficient in synthesis of truncated products (32-35nt). The deficiency in truncation (graph, bottom right) is more pronounced in this mutant than in the Y345F/Y345C primase variants. This suggests strongly that the charge transfer pathway in DNA primase is important for initiation activity on single-stranded DNA. The redox switch in primase is integral to initiation activity. All primase initiation assays contain 400nM primase variant, 500nM ssDNA, 1μM α-^{32}P ATP, 180μM UTP, 120μM CTP, at 37°C in anaerobic conditions in 50mM Tris, pH 8.0, 3mM $MgCl_2$. Product quantifications are mean +/- s.d. of n= 3 trials for WT and Y309F primase variants.

$[4Fe4S]^{2+}$ states is crucial for primase initiation and truncation (*35*, **Figure 3.6**) but not for catalytic activity. It is possible that DNA/NTP binding prior to the primer synthesis reaction may enhance primase initiation or elongation.

To assess how substrate binding affects primase activity, we pre-incubated one sample of p48/p58 in the presence of neither DNA or NTPs, one sample in the presence of DNA, and one sample in the presence of NTPs for 30 minutes in an anaerobic chamber at ambient temperature prior to initiation or elongation reactions. We then began the reactions by adding the remaining necessary substrates for activity to each sample and incubating the mixtures at 37°C. All pre-incubation samples contained the same concentration of primase in the same total volume (15μL). The final initiation reaction conditions were 400nM [4Fe4S] p48/p58, 112μM CTP, 188μM UTP, 1μM α-^{32}P ATP, 250nM ssDNA (initiation substrate in **Table 3.1**) in 50mM Tris, pH 8.0, 5mM $MgCl_2$, and the final elongation reaction conditions were 320nM p48/p58, 500nM primed DNA (elongation substrate in **Table 3.1**), 180μM [UTP], 120μM [CTP], 1μM α-^{32}P ATP in 50mM Tris, pH 8.0, 5mM $MgCl_2$. We measured the products synthesized after quenching reaction mixtures at t = 1, 3, 5, 10, and 30 minutes.

We observe that pre-incubation of DNA or NTPs with primase does not affect the efficiency of an initiation reaction outside of the margin of error. (**Figures 3.7, 3.8**) Both total products on a 50-nt ssDNA substrate and primer-length (7-10nt) products were measured in similar quantities across all time points collected. This similarity suggests that the conformational switch associated with substrate binding (*36*) is not enough to affect primase initiation activity. These data contrast, interestingly, with the previously observed effect when DNA primase is incubated aerobically on a poly(dT) substrate with ATP. (*37*) Pre-incubation assays under these conditions suggested that primase was not active if primase was pre-incubated

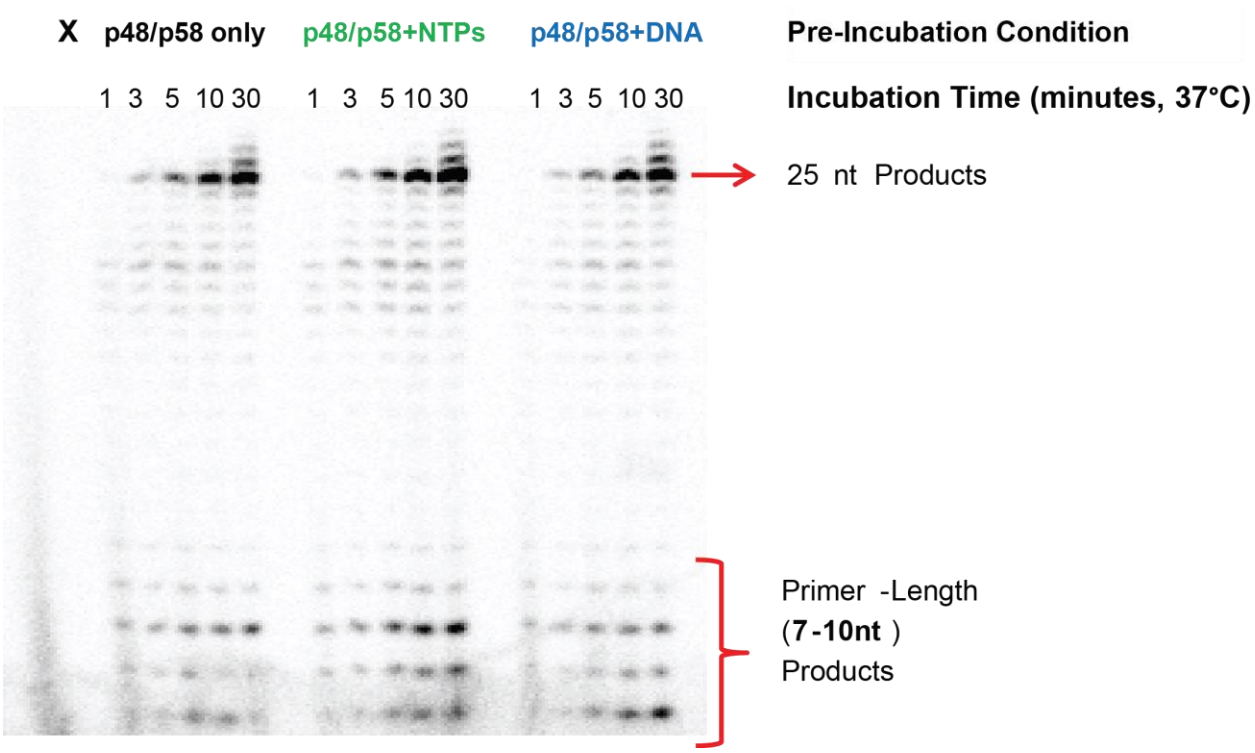

Figure 3.7. Substrate Binding Order Does not Affect Primase Initiation. Gel separation of products for three primase initiation reactions. Primase alone (p48/p58 only, grey), primase pre-incubated with NTPs was added to DNA (p48/p58 + NTPs, green), or primase pre-incubated with DNA was added to NTPs (p48/p58 + DNA, blue) to start the reaction. Pre-incubation times were 30 minutes in anaerobic conditions; all pre-incubation volumes were equal. All experiments were performed in anaerobic conditions, with 400 nM p48/p58, 250nM primed DNA, 188μM [UTP], 112μM [CTP], 1μM α-^{32}P ATP in 50mM Tris, pH 8.0, 3mM $MgCl_2$, 37°C.

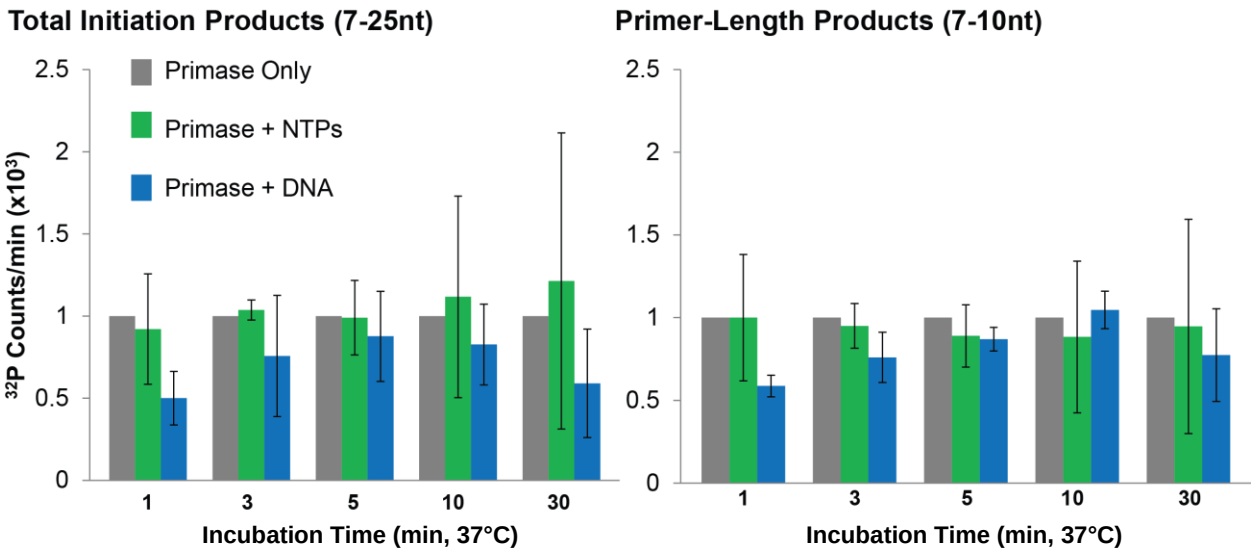

Figure 3.8. Quantification of primase initiation products in the pre-incubation assay. Total products (left) and primer-length (7-10nt) products (right) do not differ within error for the majority of time points assayed in the pre-incubation reaction under anaerobic conditions. This similarity suggests that substrate binding alone does not drive primase initiation, though it appears to drive elongation activity. All measurements are mean +/- S.D. for n= 3 trials.

with ATP. The effect was likely different in the presence of aerobic oxygen, which may have non-specifically oxidized ATP-bound p48/p58, inhibiting initiation activity dependent on the redox switch.

Primase elongation, in contrast, was aided by pre-incubation with NTPs in our conditions (**Figure 3.9**). Incubation with NTPs increases the number of total products on primed DNA by a factor of approximately 1.5 to 3, with primase only pre-incubation products normalized to 1. Incubation with DNA does not increase total products to the same degree; t= 1 minute showed no difference in products under these conditions, and t = 30 minutes showed the largest increase, a factor of 1.87 relative to primase only pre-incubation. These numbers increase slightly (**Figure 3.9**) when only elongation products (32-60 nt) are quantified and compared to primase only pre-incubation conditions. We also conducted these assays under aerobic conditions and saw the same general pattern with more error, likely due to nonspecific oxidation of the primase cluster over time (*30*). (**Figure 3.10, 3.11**) These results suggest that binding DNA or NTPs does induce a

conformational change that enhances primase catalytic activity, but this change alone cannot drive the activation of primase for initiation on ssDNA.

DISCUSSION

The redox switch function of the [4Fe4S] cluster cofactor in human DNA primase regulates DNA binding affinity of the enzyme and plays a critical role in the multistep primer synthesis process. Here we show using DNA electrochemistry that the redox switch function is relevant not only for the [4Fe4S] domain of human DNA primase, but for the full-length, catalytically active p48/p58 heterodimer. We show evidence for a redox switch for full-length

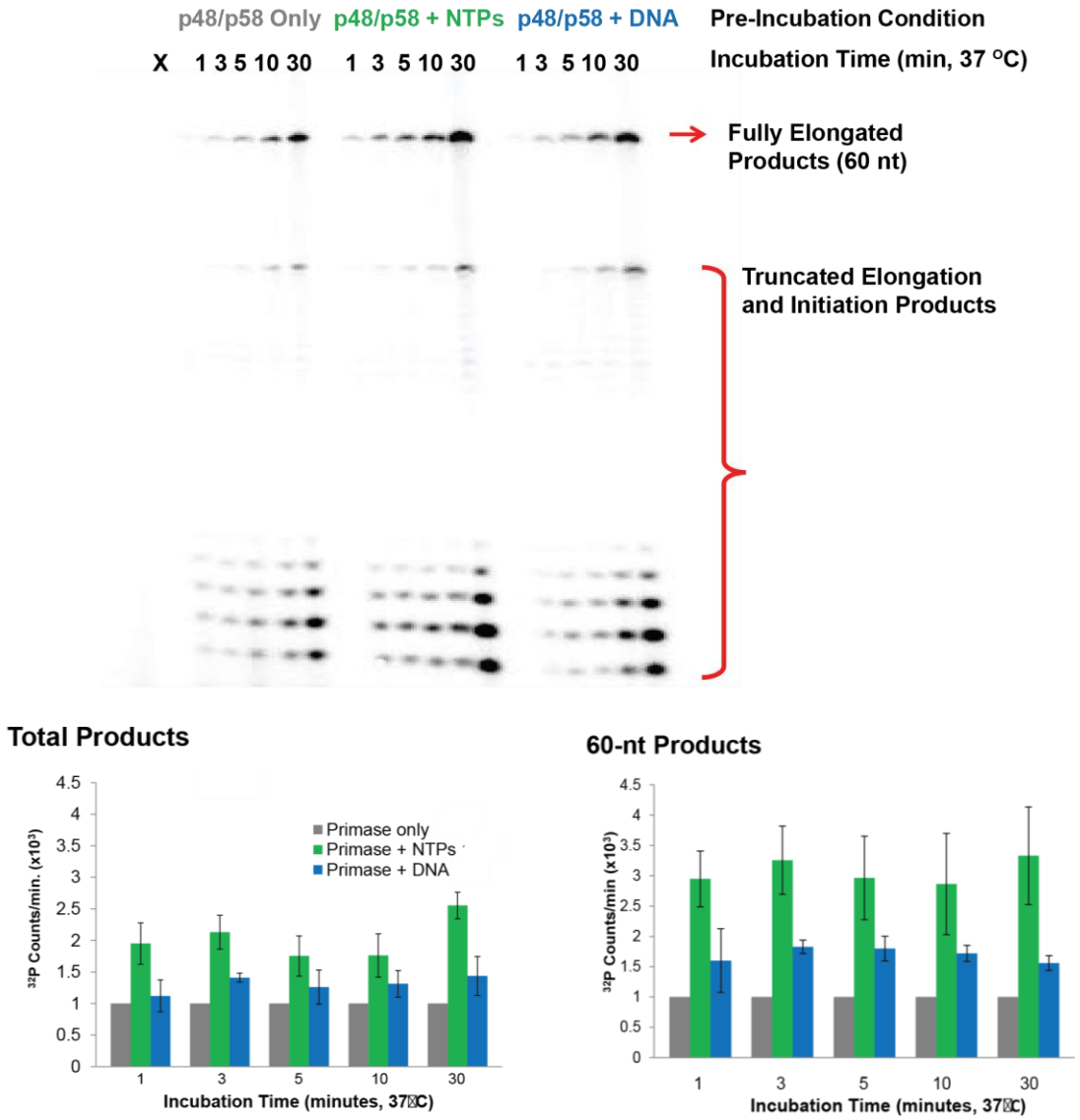

Figure 3.9. Primase elongation after pre-incubation with DNA and NTPs. Primase pre-incubation with DNA and NTPs increases elongation product production significantly. Catalytic activity, as measured by elongation products, is most greatly enhanced on average by pre-incubation with NTPs, but pre-incubation with DNA also enhances product formation. A representative gel for the pre-incubation conditions is shown above. Quantifications for the total elongation products synthesized (bottom left) and full elongation prodcuts (bottom right) are shown. All experiments were performed in anaerobic conditions, with 320nM p48/p58, 500nM primed DNA, 180µM [UTP], 120µM [CTP], 1µM α-^{32}P ATP in 50mM Tris, pH 8.0, 5mM $MgCl_2$ in anaerobic conditions. Quantifications are the mean +/- s.d. of n= 3 trials.

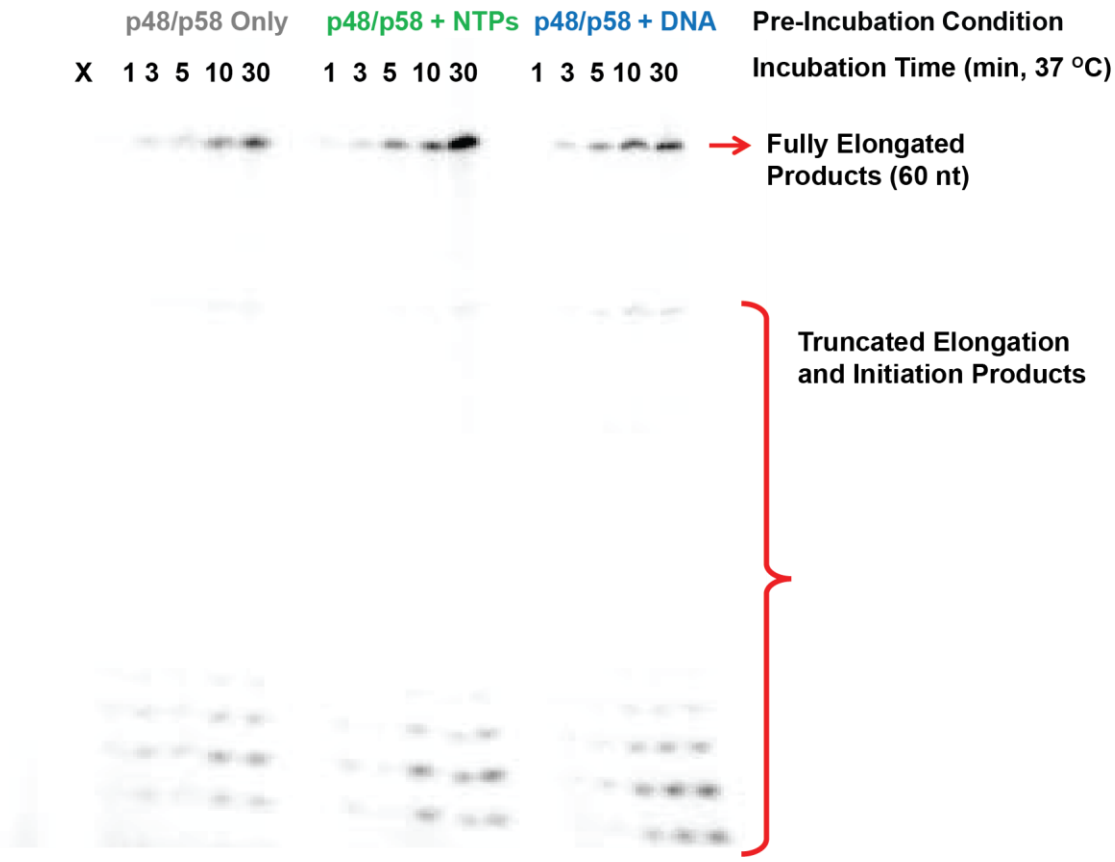

Figure 3.10. Pre-Incubation Assay for primase elongation in aerobic conditions. Gel separation of products for three primase initiation reactions. Primase alone (p48/p58 only, grey), primase pre-incubated with NTPs was added to DNA (p48/p58 + NTPs, green), or primase pre-incubated with DNA was added to NTPs (p48/p58 + DNA, blue) to start the reaction. Pre-incubation times were 30 minutes in anaerobic conditions; all pre-incubation volumes were equal. Experiments were performed in aerobic conditions, with 400 nM p48/p58, 500nM primed DNA, 180μM [UTP], 120μM [CTP], 1μM α-^{32}P ATP in 50mM Tris, pH 8.0, 3mM $MgCl_2$. 37°C.

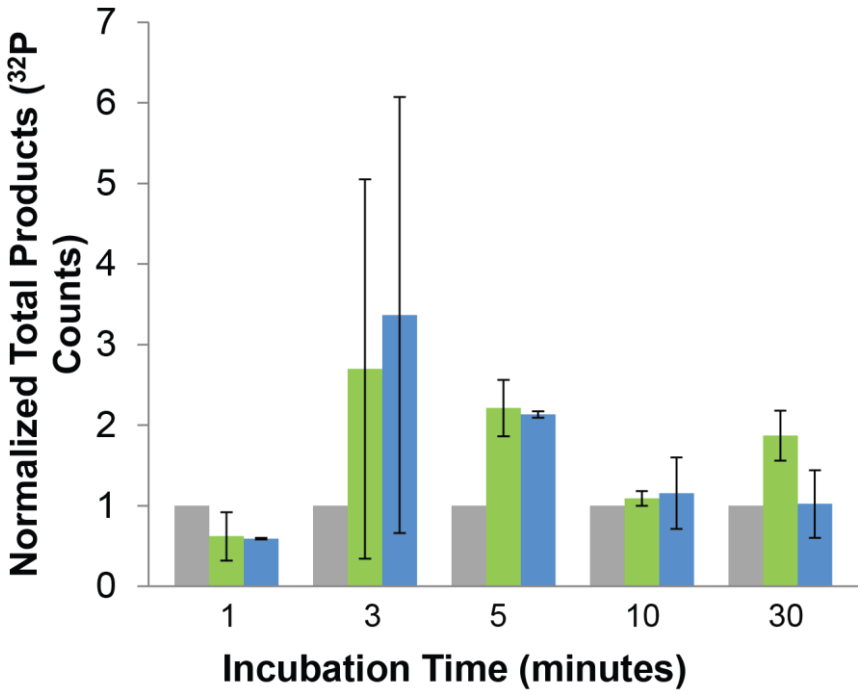

Figure 3.11. Quantification of primase elongation products in the pre-incubation assay, under aerobic conditions. The same general pattern was observed as in the anaerobic elongation assays, but the error is higher in the presence of atmospheric oxygen, due to nonspecific oxidation of the primase [4Fe4S] cluster. All measurements are mean +/- S.D. for n= 3 trials.

primase variants in the presence of an oxidizing applied potential, and we demonstrate that there is robust, semi-reversible redox activity centered near 160mVvs. NHE when primase is bound to both DNA and NTPs, the substrates required for primer synthesis on a ssDNA template. This semi-reversible activity is DNA-mediated, and the signal is attenuated and shifted ~30mV positive in the presence of a single-atom Y309F mutation along the primase redox pathway. This Y309F mutation, which is known to affect initiation activity (*35*), also affects primer truncation on an exogenously primed substrate but does not alter catalytic activity. Finally, we show that binding of anionic substrates (DNA or NTPs) prior to a priming reaction enhances primase catalytic activity but does not affect initiation.

Our electrochemical results on the full-length p48/p58 enzyme corroborate the redox switching mechanism observed in human and yeast p58C; the oxidized form of the protein is bound tightly and is redox-active, and the reduced form is loosely associated with the substrates and is redox-inert. Bulk electrolysis in the primase variants, in spite of poor loading for WT primase, suggests that the different oxidation states of the cluster have different redox signaling properties on DNA. The semi-reversible NTP-dependent signals further suggest that the oxidized and reduced forms have different levels of activity. Disparate amounts of charge transfer in the reductive versus oxidative peaks during CV, as well as large peak splitting values, suggest that the DNA and NTP-bound primase displays more redox signaling capacity when oxidized than when reduced. The large ΔE_p value exceeding 200mV suggests a slow and somewhat irreversible redox reaction in primase. (*38*) The larger cathodic peak indicates that more primase is bound and coupled to DNA when converted from the initial $[4Fe4S]^{3+}$ state to the $[4Fe4S]^{2+}$ state in the cathodic sweep, than when converted from $[4Fe4S]^{2+}$ to $[4Fe4S]^{3+}$ state in the anodic sweep. The relatively slow redox activity observed in primase, compared to

polymerase δ (*17*), is consistent with the slower activity of primase during DNA replication (*39*). Redox switching in this enzyme thus fits the general pattern of primase activity.

The primase activity results presented in this study suggest that different regulatory switches act in tandem to coordinate primase activity. The redox switch reaction, which is dependent on the tyrosine pathway perturbed in the Y309F mutant, regulates initiation and truncation activity in human DNA primase. The effect on initiation has now been demonstrated with primase variants containing tyrosine pathway mutations close to the DNA binding interface (*18*), as well as the [4Fe4S] cluster (*35*). None of the tyrosine pathway mutations tested, however, affected catalytic activity. In order to gain insight into a regulatory switch that may affect catalytic activity, we assayed primase activity when the enzyme was allowed to bind either DNA or NTPs before beginning a primer synthesis reaction on an exogenously primed substrate. Previous structural and spectroscopic work (*7*,*36*) suggested that a conformational change in primase occurred upon substrate binding and could encourage catalytic activity. Our findings indicate that NTP binding before a reaction, and to a lesser extent DNA binding, enhance primase catalytic activity but do not affect initiation on ssDNA. These results, along with the 60Å separation of the DNA binding interfaces for p48 and p58C in the isolated primase enzyme, suggest that a large structural change is connected to catalytic activity.

This conformational change in DNA primase is expected to change the redox environment of the cluster and thus the redox potential by altering solvent exposure, for example, (*34*) The electrostatic change in cluster environment upon DNA and NTP binding, however, is likely to play the largest role in affecting the primase redox switch. Since DNA charge transport, and intraprotein charge transport (*40*,*41*), occur on the ps and μs timescale, respectively. This timescale is faster than the 10μs-1ms timescale for many biologically important protein

conformational changes that occur in cells (*42*). The redox switch activation in the primase cluster is thus more rapid than the conformational change that may promote catalytic activity; the effects are likely not measureable on the timescale of the activity studies, without inhibiting the redox switch through site-directed mutagenesis. We therefore propose that the redox switch in the primase [4Fe4S] cluster allows the protein to bind tightly to DNA initially. The conformational switch promoting catalytic activity can then occur and allow for primer synthesis on the bound substrate.

Redox switching driven by a change in [4Fe4S] oxidation state has now been demonstrated to modulate the DNA binding affinity of several DNA-processing [4Fe4S] enzymes in a manner which regulates activity (*25*,*26*,*43-45*). The primase redox switch fits this pattern and may be important for coordinating the early steps of replication. The combination of a redox switch driven by a change in primase electrostatic environment upon binding DNA and NTPs, in concert with a conformational switch affecting catalytic activity, allow for efficient and regulated primer synthesis and handoff to DNA polymerase α, another putative [4Fe4S] enzyme. Structural analysis and modeling performed on polymerase α has moreover suggested that this enzyme also undergoes significant conformational shifts during priming (*46*). The lagging strand polymerase, DNA polymerase δ, which contains a redox-active [4Fe4S] cluster (*13*,*17*) also adopts different conformations bound to and dissociated from DNA, which are related to polymerase δ interactions with the proliferating cell nuclear antigen (PCNA) processivity clamp (*47*).

Redox switching in [4Fe4S] enzymes, including DNA primase, is a rapid and effective mechanism for stabilizing a DNA-bound enzyme. Oxidation of the resting $[4Fe4S]^{2+}$ enzyme to a $[4Fe4S]^{3+}$ state increases DNA binding affinity, creating a stable DNA:protein complex that

can then stall during stress conditions, as observed for DNA polymerase δ. The same stabilization of the DNA:oxidized protein complex may also allow for primase to bind substrates and undergo a conformational change to promote activity on ssDNA. The redox switch thus serves as a gating mechanism to coordinate enzymatic activity of these enzymes under normal and stress conditions within the crowded, dynamic nuclear environment.

References

1. Moran, U., Phillips, R., Milo, R. SnapShot: Key Numbers in Biology. *Cell*, **2010**, *141*, 1262.

2. O'Donnell, M.E., Langston, L., Stillman, B. Principles and concepts of DNA replication in bacteria, archaea, and eukarya. *Cold Spring Harbor Perspectives in Biology*, **2013**, *5*, a010108.

3. Burgers, P.M.J., Kunkel, T.A. Eukaryotic DNA Replication Fork. *Annu. Rev. Biochem.*, **2017**, *86*, 417-438.

4. Frick, D.N., Richardson, C.C. DNA Primases. *Annu. Rev. Biochem.,* **2001**, *70,* 39-80.

5. Kuchta, R.D., Stengel, G. Mechanism and evolution of DNA primases. *Biochimica et Biophysica Acta*. **2010**, *1804*, 1180-1189.

6. Arezi, B., Kuchta, R.D. Eukaryotic DNA primase. *Trends in Biochemical Sciences*., **2000**, *25*, 572-576.

7. Baranovskiy, A.G., Zhang, Y., Suwa, Y., Babayeva, N.D., Gu, J., Pavlov, Y.I., Tahirov, T.H. Crystal structure of the human primase. *J. Biol. Chem*., **2015**, *290*, 5635-5646.

8. Vaithiyalingam, S., Warren, E.M., Eichman, B.F., Chazin, W.J. Insights into eukaryotic priming from the structure and functional interactions of the 4Fe-4S cluster domain of human DNA primase. *Proc. Natl. Acad. Sci. USA*., **2010**, *107*, 13684-13689.

9. Sauguet, L., Klinge, S., Perera, R.L., Maman, J.D., Pellegrini, L. Shared active site architecture between the large subunit of eukaryotic primase and DNA photolyase. *PloS One*. **2010**, *5*, e10083.

10. Kilkenny, M.L., Longo, M.A., Perera, R.L., Pellegrini, L. Structures of human primase reveal design of nucleotide elongation site and mode of pol α tethering. *Proc. Natl. Acad. Sci. USA*., **2013**, *110*, 15961-15966.

11. Weiner, B.E., Huang, H., Dattilo, B.M., Nilges, M.J., Fanning, E., Chazin, W.J. An iron-sulfur cluster in the c-terminal domain of the p58 subunit of human DNA primase. J. Biol. Chem., **2007**, 282, 33444-33451.

12. Klinge, S., Hirst, J., Maman, J.D., Krude, T., Pellegrini, L. An iron-sulfur domain of the eukaryotic primase is essential for primer synthesis. *Nat. Struct. Mol. Biol.,* **2007**, *14*, 875-877.

13. Netz, D.J.A., Stith, C.M., Stümpfig, M., Köpf, G., Vogel, D., Genau, H.M., Stodola, J.L., Lill, R., Burgers, P.M.J., Pierik, A.J. Eukaryotic DNA polymerases require an iron-sulfur cluster for the formation of active complexes. *Nature Chemical Biology*., **2012**, *8,* 125-132.

14. Nunez-Ramirez, R., et al. Flexible tethering of primase and DNA Pol α in the eukaryotic primosome. *Nuc. Acids Res.*, **2011**, *39*, 8187-8199.

15. Rouault, T.A. Mammalian iron-sulphur proteins: novel insights into biogenesis and function. *Nat. Rev. Mol. Cell Biol.*, **2015**, *16*, 45-55.

16. Beinert, H.; Holm, R.H.; Münck, E. Iron-Sulfur Clusters: Nature's Modular, Multipurpose Structures. *Science* **1997**, *277*, 653-659.

17. Bartels, P.L., Stodola, J.L., Burgers, P.M.J., Barton, J.K. A Redox Role for the [4Fe4S] Cluster of Yeast DNA Polymerase δ. *J. Am. Chem. Soc.*, **2017**, *139*, 18399-18348.

18. O'Brien, E., Holt, M.E., Thompson, M.K., Salay, L.E., Ehlinger, A.C., Chazin, W.J., Barton, J.K. The [4Fe4S] cluster of human DNA primase functions as a redox switch using DNA charge transport. *Science*, **2017**, *355*, eaag1789.

19. Nunez, M.E., Hall, D.B., Barton, J.K. Long-range oxidative damage to DNA: effects of distance and sequence. *Chem. Biol. (Oxford, U. K.)*, **1999**, *6*, 85-97.

20. Kelley, S.O., Boon, E.M., Barton, J.K., Jackson, N.M., Hill, M.G. Single-base mismatch detection based on charge transduction through DNA. *Nuc. Acids Res.*, **1999**, *27*, 4830-4837.

21. Slinker, J.D., Muren, N.B., Renfrew, S.E., Barton, J.K. DNA charge transport over 34 nm. *Nature Chem.* **2011**, *3*, 228-233.

22. Nuñez, M.E., Noyes, K.T., Barton, J.K. Oxidative Charge Transport through DNA in Nucleosome Core Particles. *Chemistry and Biology*, **2002**, *9*, 403-415.

23. Nuñez, M.E., Holmquist, G.P., Barton, J.K. Evidence for DNA Charge Transport in the Nucleus. *Biochemistry*, **2001**, *40*, 12465-12471.

24. Boal, A.K., Yavin, E., Lukianova, O.A., O'Shea, V.L., David, S.S., Barton, J.K. DNA-Bound Redox Activity of DNA Repair Glycosylases Containing [4Fe-4S] Clusters. *Biochemistry* **2005**, *44*, 8397-8407.

25. Grodick, M.A., Segal, H.M., Zwang, T.J., Barton, J.K. DNA-Mediated Signaling by Proteins with 4Fe-4S Clusters Is Necessary for Genomic Integrity. *J. Amer. Chem. Soc.* **2014**, *136*, 16470-16478.

26. Boal, A.K., Genereux, J.C., Sontz, P.A., Gralnick, J.A., Newman, D.K., Barton, J.K. Redox signaling between DNA repair proteins for efficient lesion detection. *Proc. Natl. Acad. Sci. U. S. A.*, **2009**, *106,* 15237-15242.

27. Pheeney, C.G., Arnold, A.R., Grodick, M.A., Barton, J.K. Multiplexed electrochemistry of DNA-bound metalloproteins. *J. Am. Chem. Soc.,* **2013**, *135*, 11869-11878.

28. Slinker, J. D., Muren, N. B., Gorodetsky, A. A., Barton, J. K. Multiplexed DNA-modified electrodes. *J. Am. Chem. Soc.,* **2010**, *132*, 2769-2774.

29. Cunningham, R.P., Asahara, H., Bank, J.F., Scholes, C.P., Salerno, J.C., Surerus, K., Munck, E., McCracken, J., Peisach, J., Emptage, M.H. Endonuclease III is an iron-sulfur protein. *Biochemistry,* **1989**, *28*, 4450-4455.

30. Imlay, J.A. Iron-sulphur clusters and the problem with oxygen. *Molecular Microbiology*. **2006**, *59*, 1073-1082.

31. Durst, R.A., Staples, B.R. Tris/Tris-HCl: A Standard Buffer for Use in the Physiologic pH Range. *Clinical Chemistry*, **1972**, *18*, 206-208.

32. O'Brien, E.,* Salay, L.E.*, Epum, E.A., Friedman, K.L., Chazin, W.J., Barton, J.K. Yeast Require Redox Switching in DNA Primase. *Manuscript in preparation. 2018.*

33. McDonnell, K.J.,* Chemler, J.A.,* Bartels, P.L.,* O'Brien, E., Marvin, M.L., Ortega, J., Stern, R.H., Raskin, L., Li, G., Sherman, D.H., Barton, J.K., Gruber, S.B. A Novel Human MUTYH Variant Causing Colonic Polyposis through Redox Degradation of the $[4Fe4S]^{2+}$ Cluster. Nature Chemistry, **2018**, in press.

34. Dey, A., et al. Solvent tuning of electrochemical potentials in the active sites of HiPIP versus ferredoxin. *Science,* **2007**, *318*, 1464-1468**.**

35. O'Brien, E., Holt, M.E., Thompson, M.K., Salay, L.E., Ehlinger, A.C., Chazin, W.J., Barton, J.K. Response to 'Comment on "The [4Fe4S] cluster of human DNA primase functions as a redox switch using DNA charge transport."' *Science*, **2017**, *357*, 6348.

36. Holt, M.E., Thompson, M.K., Chazin, W.J. *manuscript in preparation.*

37**.** Sheaff, R.J., Kuchta, R.D. Mechaniam of Calf Thymus DNA Primase: Slow Initiation, Rapid Polymerization, and Intelligent Termination. *Biochemistry*, **1993**, *32*, 3027-3037.

38. Nicholson, R.S. Theory and Application of Cyclic Voltammetry for Measurement of Electrode Reaction Kinetics. *Anal. Chem.*, **1965**, *37*, 1351-1355.

39. Lee, J.-B., et al. DNA primase acts as a molecular brake in DNA replication. *Nature*, **2006**, *439*, 621-624.

40. Gray, H.B., Winkler, J.R. Electron flow through metalloproteins. *Biochim. Biophys. Acta, Bioenerg.*, **2010**, *1797*, 1563-1572.

41. O'Neill, M.A., Becker, H.-C., Wan, C., Barton, J.K., Zewail, A.H. Ultrafast Dynamics in DNA-Mediated Electron Transfer: Base Gating and the Role of Temperature. *Angew. Chem. Int. Ed. Engl.*, **2003**, *42*, 5896-5900.

42. Shaw, D.E., et al. Atomic-Level Characterization of the Structural Dynamics of Proteins. *Science*, **2010**, *330*, 341-346.

43. Tse, E.C.M., Zwang, T.J., Barton, J.K. The Oxidation State of [4Fe4S] Clusters Modulates the DNA-Binding Affinity of DNA Repair Proteins. *J. Am. Chem. Soc.*, **2017**, *139*, 12784-12792.

44. Gorodetsky, A.A., Boal, A.K., Barton, J.K. Direct electrochemistry of Endonuclease III in the presence and absence of DNA. *J. Am. Chem. Soc.* **2006**, *128*, 12082-12083.

45. Bartels, P.L., Zhou, A., Arnold, A.R., Nunez, N.N., Crespilho, F.N., David, S.S., Barton, J.K. Electrochemistry of the [4Fe4S] Cluster in Base Excision Repair Proteins: Tuning the Redox Potential with DNA. *Langmuir.*, **2017**, *33*, 2523-2530.

46. Perera, R.L., Torella, R., Klinge, S., Kilkenny, M.L., Maman, J.D., Pellegrini, L. Mechanism for priming DNA synthesis by yeast DNA polymerase α. *eLife*, **2013**, *2*, e00482.

47. Johansson, E., Garg, P., Burgers, P.M.J. The Pol32 Subunit of DNA Polymerase Contains Separable Domains for Processive Replication and ProliferatingCell Nuclear Antigen (PCNA) Binding, *J. Biol. Chem.*, **2004**, *279*, 1907-1915.

Chapter 4: Yeast Require Redox Switching in DNA Primase

Adapted from: O'Brien, E.*, Salay, L.E.*, Epum, E.A., Friedman, K.L., Chazin, W.J., Barton, J.K. Yeast Require Redox Switching in DNA Primase. 2018, draft.

*Equal contribution.

E. O'Brien wrote the manuscript and performed all electrochemistry experiments. E. O'Brien performed hydrogen peroxide liquid culture assay and methylene blue sensitivity assay. L.E. Salay prepared p58C protein, X-ray crystallography, and yeast temperature/hydrogen peroxide/tetrad analysis assays. K.L. Friedman and E.A. Epum performed tetrad analysis and constructed yeast strains.

Introduction

DNA replication requires the coordinated activity of an array of polymerase enzymes. (*1-3*) DNA primase initiates the synthesis on both the leading and lagging strands of the DNA template. Primase synthesizes a short (8-12 nt) RNA primer before handing off the primed template to DNA polymerase α. Primase contains an RNA polymerase subunit (p48) and a regulatory subunit (p58). (*4-6*) Primase (*7,8*) and many other, if not all, replicative polymerases contain at least one [4Fe4S] cluster (*9,10*), a metal cofactor associated with biological redox chemistry. (*11*) Given the high metabolic expense associated with incorporation of a cluster into one of these proteins (*12,13*), this cofactor is presumed to play a functional role in the enzyme. Interestingly, the clusters in both human DNA primase (*14*) and yeast DNA polymerase δ (*15*) have been demonstrated to perform redox chemistry when bound to DNA.

The [4Fe4S] cluster in eukaryotic primases is essential for primer synthesis on a ssDNA substrate *in vitro* (*7,8*) and in cells. (*16*) The cluster is located in the C-terminal domain of the regulatory subunit, p58C, which is flexibly tethered to the N-terminal domain (*17,18*) and can bind DNA independently of the rest of the primase enzyme (*19,20*). In human DNA primase, the cluster acts as a redox switch, modulating the affinity of p58C for its substrate. (*14*) Human p58C is tightly bound to DNA and redox-active in the $[4Fe4S]^{3+}$ state, but more loosely associated with DNA and redox-inert in the $[4Fe4S]^{2+}$ state. Other DNA-processing [4Fe4S] enzymes exhibit similar behavior. Endonuclease III in *E. coli*, for example, undergoes approximately a 1000-fold increase in DNA binding affinity upon oxidation to the $[4Fe4S]^{3+}$ state from the resting $[4Fe4S]^{2+}$ state. (*19,20*) The redox switch in human primase may facilitate rapid, efficient binding and substrate handoff during priming, through DNA-mediated electron transfer. (*14*)

Charge shuttling between bound DNA and the distant metal cofactor is mediated by pathways through the protein. (*14,21,22*) These pathways are often comprised of aromatic residues, which have comparatively low ionization energies and can transfer charge (*23-25*) through an insulating protein matrix. Site-directed mutagenesis altering these aromatic residues can create enzymatically functional, redox-deficient variants (*14,21,22*) of the [4Fe4S] enzyme. In human primase, the redox switch is mediated by conserved tyrosine residues, Y309, Y345, and Y347. Substitution of these residues with phenylalanine leads to redox-deficient mutants that are defective for initiation of primer synthesis. In yeast primase, residues Y395 and Y397 are conserved and orthologous to Y345 and Y347 in human primase. Though positioned differently than their human orthologues within the respective p58C crystal structures, they are spaced within feasible distance of the cluster and other aromatic residues that comprise a redox pathway. (*23,24*) We hypothesized that yeast and human p58C have similar redox switch mechanisms, despite their different tyrosine constellations. Establishing that a yeast primase redox pathway exists also provides an opportunity to construct and assay the viability of yeast cells expressing redox-deficient primase variants.

Materials and Methods

Protein Expression and Purification. Yeast p58C (Pri2) residues 316-512 were cloned into pGB100 using the BamHI and NotI restriction sites. This plasmid was transformed into Rosetta DE3 cells. The cells were grown to an OD_{600} of 1.0 at 37°C. They were then induced with 1 mM isopropyl β-D-1-thiogalactopyranoside (IPTG) and transferred to 20°C for 16 hr. The cells were harvested and stored at -80°C.

For purification, the cells pellets were thawed and resuspended in 50 mM NaH_2PO_4 (pH 7.8), 500 mM NaCl, 10 mM imidazole. Dnasin and lysozyme were added at 2 mg/g of cells.

Protease inhibitor tablets (Roche) were added to the suspension. The suspension was homogenized using a Dounce homogenizer and then sonicated on ice for 10 min. The solution was spun at 50,000 rcf for 20 min at 4°C. The supernatant was filtered and passed over a Ni-NTA column (GE Healthcare). The column was washed with 3 column volumes of 50 mM NaH_2PO_4 (pH 7.8), 500 mM NaCl, 20 mM imidazole. The protein was eluted with 50 mM NaH_2PO_4 (pH 7.8), 500 mM NaCl, 250 mM imidazole. The eluent was dialyzed overnight at 4°C into 50 mM NaH_2PO_4 (pH 7.8), 500 mM NaCl, 10 mM imidazole and the 6xHis tag was cleaved using H3C protease. The dialyzed protein was repassed over the Ni-NTA column as in the previous step. The flow-through and wash fractions were collected. These fractions were dialyzed into 20 mM HEPES (pH 7.2), 50 mM NaCl, 2 mM dithiothreitol (DTT) (Heparin Buffer A). This was filtered and passed over a 5 ml Hi-Trap HP heparin column (GE Healthcare) that had been pre-equilibrated with Heparin Buffer A. Heparin Buffer B was prepared 20 mM HEPES (pH 7.2), 1 M NaCl, 2 mM DTT. The protein was eluted using a linear gradient of 0 to 100% of Heparin Buffer B over 40 column volumes. The protein typically eluted ~20% Heparin Buffer B (250 mM NaCl). The protein dialyzed into 20 mM HEPES (pH 6.8), 2 mM DTT, 200 mM NaCl, flash frozen in N_2, and stored at -80°C.

Site Directed Mutagenesis. Site directed mutagenesis for single-site and multi-site variants was performed using a Q5 mutagenesis kit (New England Biolabs). The primers to create the mutations are listed below. The same reverse primer was used for all mutations. The annealing temperature for amplification was 58°C.

Site directed mutagenesis primers

Mutation	Primer
Y395F	5'GAGAAGTTCAATAAAGAATTCCGTTACAGCTTCAGGC
Y397L	5'GAGAAGTTCAATAAAGAACTGCGTTACAGCTTCAGGC
Y397F	5'GAGAAGTTCAATAAAGAATACCGTTTCAGCTTCAGGC
Y397L	5'GAGAAGTTCAATAAAGAATACCGTCTGAGCTTCAGGC
Reverse primer	5'CATTGTCATGTTCCCATTTCTTGTAAATGC

Oligonucleotide preparation. All standard or modified phosphoramidites and DNA synthesis reagents were purchased from Glen Research. Unmodified DNA oligonucleotides for electrochemical experiments were purchased from Integrated DNA Technologies, Inc. DNA sequences for electrochemistry assays are shown in **Table 4.1**. Thiol-modified DNA strands for electrochemistry were made on an Applied Biosystems 3400 DNA synthesizer, with a C6 S-S phosphoramidite incorporated at the 5'- terminus. Single-stranded DNA was purified using standard procedures as described previously. (*25*) High pressure liquid chromatography (HPLC) using a reverse-phase PLRP-S column (Agilent) was used, and oligonucleotide mass confirmed using MALDI-TOF Mass Spectrometry. Thiol-modified strands were reduced after the initial HPLC purification with 100mM dithiothreitol (Sigma) for 2-3 h in 50 mM Tris-HCl, pH 8.4, 50 mM NaCl. Reduced thiol-modified DNA was purified by size exclusion chromatography (Nap5 Sephadex G-25, GE Healthcare) and subsequent reverse-phase HPLC. Single-stranded oligonucleotides were then desalted using ethanol precipitation and stored in low salt buffer (5 mM Phosphate, pH 7.0, 50 mM NaCl). Duplex DNA for electrochemistry was prepared by quantification of the complementary single-stranded oligonucleotides by UV-Visible

DNA Substrates	
p58C Electrochemistry	3'-CGCGTCTGTGCAACGTGCTG-SH-5' 5'-CATGCGCAGACACGTTGCACGAC-3'
p58C Fluorescence Anisotropy	3'-GAGAGTTT-5' 5'-[FitC]-TCTCTCTCTCAAA-3'

Table 4.1. Electrochemistry and fluorescence anisotropy DNA substrates used. Electrochemistry of p58C was performed on self-assembling monolayers of a 20-mer DNA duplex substrate with a 3-nt 5'- ssDNA overhang. Fluorescence anisotropy was performed on a 8-mer DNA duplex with a 5-nt ssDNA overhang. SH = $-(CH_2)_6$-SH, FitC = FITC.

spectroscopy, followed by annealing at 90 °C. A mixture of equimolar complementary single-stranded DNA (50 μM) was prepared in low salt buffer. Thiol-modified duplex DNA substrates were then deoxygenated by bubbling argon gas through the solution for 90-180 s. Duplex DNA was annealed on a thermocycler (Beckman Instruments) by initial heating to 90 °C, followed by slow cooling to 4 °C over 90 minutes. DNA was quantified using absorbance at 260 nm, with extinction coefficients at 260 nm for DNA obtained using Integrated DNA Technologies online OligoAnalyzer tool. Single-stranded DNA substrates were quantified using UV-Visible spectroscopy and stored in low salt buffer at a stock concentration for activity assays. Notes on DNA preparation and purification are detailed in **Chapter 2.**

Multiplexed Chip Fabrication. Multiplexed electrode platforms were prepared using standard photolithography techniques, adapted from established protocols. (*25-27*) Nine 1 in. by 1 in. chips were patterned on 525 um thick silicon wafers (SiliconQuest). A thermal oxide layer roughly 4000 Å thick was grown on the silicon wafers using a Tytan tube furnace (Tystar). S1813 photoresist (2 μm layer) was deposited onto the wafers for patterning of the chips before metal deposition. Electron beam evaporation (CHA Industries) was then used to deposit a 3nm titanium adhesion layer followed by a 100nm gold layer, without breaking vacuum between depositions. Metal lift-off using Remover PG (MicroChem) was performed overnight (10-12 h) at room temperature. Wafers were subsequently dried with a nitrogen gun and dehydrated at 140 °C for 10 minutes. A 3 um layer of insulating SU-8 photoresist was deposited and patterned onto the wafer as described previously,(*25-27*) with connective wires between contact pads on the edges of the chips and working electrodes in the center were covered but the contact pads and working electrodes left exposed. This ensured a fixed working electrode surface area of 2 mm^2.

SU-8 photoresist was cured (150 °C, 15 minutes) and wafers cleaved into individual chips using a Dynatex Scriber/Breaker or broken manually after scoring with a diamond tip scriber.

DNA Modified Electrode Assembly/Preparation. Multiplexed chips were cleaned using sonication in acetone and isopropyl alcohol as described previously; procedure is detailed in **Chapter 2**. (*25*) Chips were then dried thoroughly using argon gas and ozone-cleaned for 20 minutes at 20 mW using a Uvo brand ozone cleaner. Clean chips were assembled onto polycarbonate holders with acrylic clamp and Buna-N rubber gasket according to previous protocols, with four quadrants in the chip separated by fastened gasket and clamp. (*25*) Duplex DNA substrates, with a thiol modifier at the 5'- end, (25 μM) were deposited in a 20 μL volume onto each quadrant of the multiplex chip. Substrates incubated for 18-24 hours on the gold surface to allow formation of self-assembled DNA monolayer. DNA monolayers were washed with phosphate buffer (5mM phosphate, pH 7.0, 50mM NaCl, 5% glycerol) and subsequently backfilled with 1mM 6-mercaptohexanol (Sigma) in phosphate buffer for 45 minutes. Monolayers are then washed 10 times per quadrant with phosphate buffer and twice per quadrant with TBP buffer (5 mM phosphate, pH 7.0, 50 mM NaCl, 4 mM $MgCl_2$, 4 mM spermidine) to aid in formation of a monolayer with termini accessible for p58C binding. Assembled chips were transported into an anaerobic glove bag chamber (Coy Products) and washed 5 times per quadrant with p58C buffer (20 mM HEPES, pH 7.2, 75 mM NaCl), which was previously deoxygenated by argon bubbling (at least 1 second/μL of solution) and allowed to incubate at least 1-2 days in the chamber prior to the experiment. Initial cyclic voltammetry scans of the monolayers in p58C buffer were performed to ensure monolayer formation on each electrode. All washes were performed with 20 μL buffer volumes on each quadrant. Before scanning, a 200 μL volume was deposited over the chip surface, a bulk solution well for completion of a

three-electrode circuit with an external reference and counter electrode. Chip assembly, preparation, and reagent storage is detailed more in **Chapter 2.**

Sample Preparation for Electrochemistry. Wild type and mutant p58C samples were stored prior to experiments in p58C storage buffer (20mM Tris, pH 7.2, 75mM NaCl) or crystallography buffer (20 mM HEPES, pH 6.8, 200 mM NaCl, 2 mM DTT). All p58C variants were transferred to HEPES electrochemistry buffer (20mM HEPES, pH 7.2, 75mM NaCl) using Amicon ultra centrifugal filters (0.5mL, 3MWCO) (Millipore Sigma). Protein was applied in a 90-140µL volume to the filter and centrifuged for 15 minutes at 14000 x g at 4°C. After centrifugation, 400µL of HEPES electrochemistry buffer was applied to the filter and centrifuged at 14000 x g for 20 minutes. This was repeated four times to exchange the p58C protein into HEPES electrochemistry buffer. After buffer exchange and recovery of sample by centrifugation (2 minutes, 1000 x g), concentrations of [4Fe4S] cluster-containing p58C or mutants were measured using UV-Visible spectroscopy, by absorbance of the [4Fe4S] cluster at 410 nm (extinction coefficient = 17000 M^{-1} cm^{-1}). (*28*) Recovered samples (approx. 100-150µL volume) were deoxygenated for 2-3 minutes with argon. Samples were then transferred into the anaerobic chamber (Coy Laboratory products). Before deposition onto the gold electrode surface, p58C/mutant samples were diluted to a molar concentration of 30µM or 57µM [4Fe4S] p58C variant with previously deoxygenated HEPEs electrochemistry buffer. Samples were deposited onto multiplex chip quadrants in 20 µL volumes initially, with the remaining sample deposited in a well of bulk solution above the chip surface, to a final volume of 200-300µL.

Wild Type/Mutant p58C Electrochemistry. All electrochemistry was performed using a CHI620D potentiostat and 16-channel multiplexer (CH Instruments), in an anaerobic glove chamber. Multiplex gold electrodes were part of a three electrode system with an external

Ag/AgCl reference electrode (Bioanalytical Systems) and platinum counter electrode. Cyclic voltammetry scans were performed at 100 mV/s scan rates, over a potential range of +0.412 V to -0.288 V vs. NHE or +512mV to -188mV vs NHE. Bulk electrolysis on DNA was performed at an applied potential of +0.412 V vs. NHE or +512mV vs. NHE for all electrochemical oxidation reactions and -0.188 V vs. NHE for all electrochemical reduction reactions. The oxidizing potential was applied for at least 8.33 minutes for single oxidation reactions on a surface, and 6.67 minutes for the iterative oxidation cycles of p58C variants. The reducing potential was applied for 8.33 minutes in all electrochemical reduction reactions. All bulk electrolysis and cyclic voltammetry was performed in previously deoxygenated p58C storage buffer (20 mM HEPES, pH 7.2, 75 mM NaCl). Charge transfer (nC) in the cathodic peak of oxidized samples CV scans was assessed using the area under the current wave of the reduction signal. Variants of p58C were compared for charge transfer proficiency using at least three trials of oxidation at +0.412 V vs. NHE or +512mV vs. NHE, after at least 8.33 minutes of oxidation at the applied potential. Charge transfer was measured for oxidized samples using CHI software, assessing the area under the reductive peak in CV after electrochemical oxidation. Yields for bulk electrolysis were assessed by subtracting the total charge reported in Coulombs from the product of the electrolysis time (s) and the final current value (A). NTP-dependence of electrochemical signals were measured by pipetting a small volume (1-3μL) of 0.1M ATP stock solution into each quadrant of the multiplexed chip setup. These stocks should be added by quadrant, rather than into the bulk solution. Divide the NTP stock into quarters and pipet ¼ of the total solution onto a quadrant. Samples were added by quadrant, as physical barriers in the setup prevent diffusion of NTPs between electrode quadrants. After the volume of ATP stock was deposited onto the electrode quadrant, resulting in a 2.5mM or 5mM concentration of ATP in the quadrant, CV

scans were measured (100mV/s scan rate), followed by square wave voltammetry in both reductive and oxidative sweeps (15 Hz frequency). Charge transfer was assessed using CHI software; charge values were determined by calculation of the area under the reductive and oxidative peak curves. Midpoint potentials of NTP-dependent redox signals were assessed using the peak selection function in CHI software.

Mutant Selection and Design. Mutations in the p58C domain of human DNA primase were designed based on previously determined structural data (*18-20, 29*) bioinformatics (*19*) compiled for conserved residues in this domain. Chimera software was used to analyze the relevant residues in the 1.54 Å resolution structure of yeast p58C (*30*) (PDB 3LGB). Distances between tyrosine residues were measured between centroids.

Circular Dichroism. Near-UV circular dichroism was performed as described in (*31*).

Fluorescence anisotropy. Fluorescence anisotropy was performed as described in (*14*). Yeast p58C and the related mutants were assayed in 20 mM HEPES (pH 6.8), 2 mM DTT, 75 mM NaCl.

X-ray crystallography. The protein was dialyzed into 20 mM HEPES (pH 6.8), 2 mM DTT, 75 mM NaCl and concentrated to ~5 mg/ml. Crystals were grown at 16°C by mixing 1:1 yeast p58C variants (~5 mg/ml) and mother liquor (100 mM TRIS (pH 8.5), 40-65% MPD) using hanging drop vapor diffusion. Crystals formed after 2 days. They were then looped, transferred to a cryo-protectant containing the mother liquor and 20% glycerol.

Data collection for yeast p58C Y397F was performed at 100 K using an in-house Bruker Microstar rotating anode x-ray generator with a Bruker Proteum PT135 CCD area detector at a wavelength of 1.54 Å. Sulfur single anomalous dispersion (SAD) was used to phase this data set

with the program suite HKL2MAP. (*32*) The model was built using arp/Warp in the CCP4 suite of programs (*33*) followed by iterative rounds of refinement using Phenix (*34*) and *Coot* (*35*)**.**

Crystallographic data for the remaining variants were collected at the Advanced Photon Source (Argonne National Laboratory, Chicago, IL) on Life Sciences Collaborative Access Team beamlines. Data were indexed and scaled using HKL2000. (*36*) Molecular replacement using Phaser (*37*) with the model of the yeast p58C variant Y397F was used to solve the phases of the remaining mutants. The models were refined iteratively using Phenix (34) and *Coot*. (*35*)

Yeast Strain Construction. *PRI2* mutations were introduced into diploid strain DKF206 (*MAT***a**/*MAT*α *trp1/trp1 leu2/leu2 ura3/ura3 his7/his7*) (*38*) by two-step gene replacement (*39*). Integration plasmids were created by subcloning a ___ fragment of plasmid PRI2-3HA (*40,16*) into the pRS406 vector (*41*) and mutations were created using overlap-extension PCR (*42*). Silent nucleotide changes were included to create restriction site polymorphisms tightly linked to each mutation. Plasmids linearized with ___ were transformed into DKF206 and Ura+ transformants were subsequently plated on media containing 5-fluoroorotic acid. Chromosomal integration of all mutations was verified by restriction digestion and sequencing (cells losing the *URA3* marker by recombination also lost the 3HA tag). Diploid strains heterozygous for integrated alleles were sporulated and tetrads were dissected by standard methods. Complementing plasmid pRS416-*PRI2* contains a ___kb fragment amplified from yeast genomic DNA inserted at the BamHI and EcoRI sites of pRS416. *PRI2* alleles were C-terminally tagged with a 13Myc tag by PCR-mediated integration using pFA6a-13Myc *TRP1* as template as described (*43*). PCR amplification and sequencing was used to determine which allele was tagged within diploid strains. Sequences of oligonucleotides utilized for cloning and mutagenesis are available by request.

Yeast Spot Assays. Overnight cultures of strains were diluted to an OD_{600} of 1. Four microliters of this culture and of four serial dilutions were spotted onto YPD agar containing 100μM methylene blue. Differences in growth were recorded after an incubation at 30°C for 2 days.

Yeast Liquid Culture Growth. Three single colonies of *PRI2*, *pri2Y395F*, and *pri2Y397F* were picked and grown overnight in YPD media (230 RPM, 30°C). Colonies were monitored for OD_{600} using an Ultrospec 10 Cell Density Meter. Overnight cultures were then diluted to an OD_{600} of 0.05 in fresh YPD liquid media and grown until mid-log phase. Cultures were normalized to OD_{600} = 0.5 and aliquoted into 1mL volumes. These 1mL fractions were dosed with a stock of filter-sterilized H_2O_2 to a final concentration of 2mM H_2O_2. They were deposited into a sterile, 96-well plate in 200μL aliquots, with 3 technical replicates of each colony (3/strain). Cells were then scanned every 20 minutes for 24 hours in a 96-well plate reader. OD_{600} values were plotted as an average of n= 3 trials for 3 colonies of each strain, for a total of 9 samples/strain. Values shown are the average OD_{600} +/- s.d.

Results

Redox Switch through a Tyrosine Pathway in Yeast p58C.

Human and yeast p58C have similar overall structures (**Figure 4.1**) with a backbone RMSD of only 0.82Å. Both proteins bind DNA with micromolar affinity. (*19,20*) Yeast and human p58C contain [4Fe4S] clusters buried within the protein, approximately 25 Å from the DNA binding interface (*19,20*) (**Figure 4.1**). Despite having only 40% identical sequences, yeast and human p58C notably have multiple conserved tyrosine residues located between the cluster and the DNA binding interface. In human p58C, these tyrosines shuttle charge through the insulating protein matrix and mediate the redox switch. (*14*) (**Figure 4.1**)

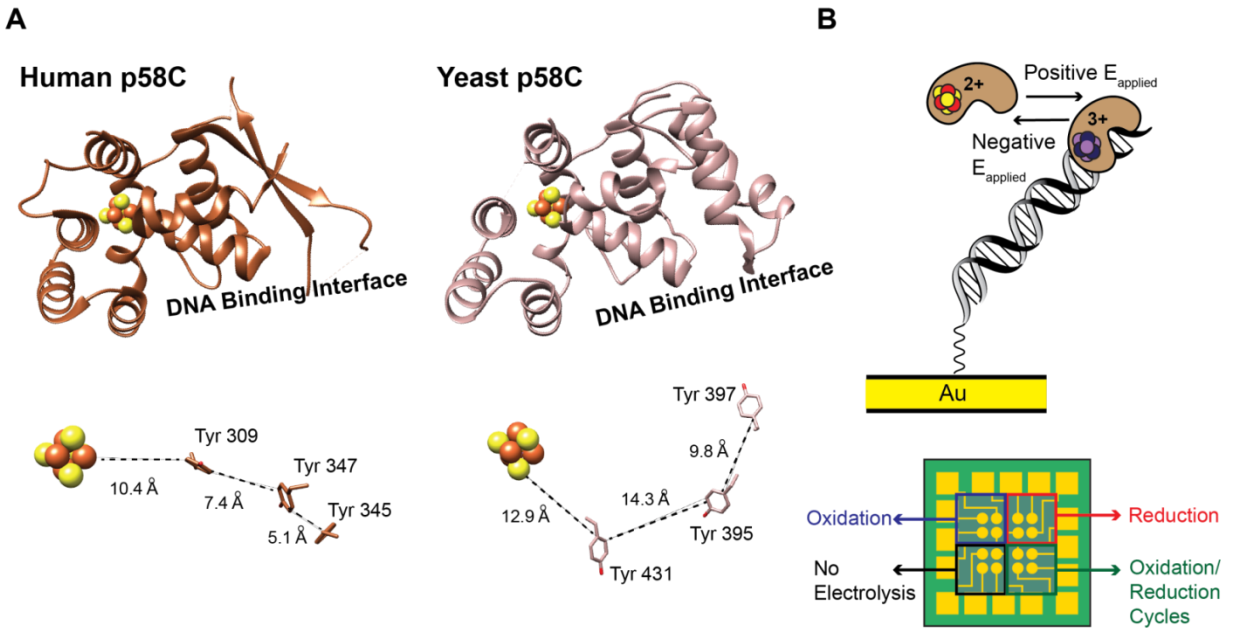

Figure 4.1. The structures of yeast and human p58C can support a common redox switch when bound to DNA. A) Comparison of p58C structures and conserved tyrosine residues near the [4Fe4S] cluster for yeast p58C (light brown) and human p58C (dark brown). Both proteins contain a [4Fe4S] cluster cofactor and several conserved tyrosine residues positioned between the DNA binding interface of p58C and the [4Fe4S] cluster that are within feasible distance for charge transfer. (*24*, *44*) Conserved tyrosine residues in each protein are shown below the respective p58C structures. Structures rendered using human p58C (PDBID 3L9Q) (*20*) and the yeast p58C structure from this study (PDBID N/A). B) Cartoon depicting the change in DNA binding and activity associated with [4Fe4S] cluster redox. (Below) Diagram of the multiplexed, sixteen-electrode DNA electrochemistry platform used for observation of electrochemistry under different conditions with replicates on a single surface.

We sought to determine whether the yeast p58C [4Fe4S] cluster has a similar redox switching capability to human p58C using DNA-mediated electrochemistry. We identified several tyrosine residues conserved in yeast p58C, which are within feasible charge transport distance of the yeast p58C cluster or DNA-binding interface, as possible mediators of a redox switch. Residues Y395 and Y397 in yeast p58C (**Figure 4.1**), orthologous to Y345 and Y347, respectively, in the human p58C redox pathway, are prime candidates for a redox role.(*14*) A third tyrosine in human p58C, Y309, is conserved in the yeast protein structure but not in the sequence. Distances between tyrosine centroids are larger on average in the yeast protein crystal structure (12.9-15.3Å) (*19*) than in the human protein crystal structure (5.1-10.4Å), (*20*) but nonetheless fall securely within the distance for feasible microsecond electron transfer. As the distance between centroids, rather than the relative positions of tyrosines in the protein, is the primary factor determining the feasibility of charge transfer through protein, we predicted that both pathways could mediate redox switching.

To test whether a change in the oxidation state of the [4Fe4S] cluster in yeast p58C affects DNA binding as with human p58C, we compared electrochemical behavior of oxidized $[4Fe4S]^{3+}$ p58C and reduced $[4Fe4S]^{2+}$ p58C on multiplexed DNA electrodes in an anaerobic environment (**Figure 4.1**). Multiplex DNA electrodes were modified with a 20-nt DNA duplex substrate containing a 3-nt, 5'- ssDNA overhang (**Table 4.1**) identical to the substrate used in the study of human p58C electrochemistry. (*14*) Electrochemically unaltered yeast p58C displays no redox signal in cyclic voltammetry scans (**Figure 4.2**), suggesting that the isolated form of the protein is not coupled to the DNA base pairs to participate in redox signaling.

WT p58C was then electrochemically oxidized by applying a positive potential (412 or 512 mV vs. NHE; see **Table 4.2**) or electrochemically reduced by applying a negative potential

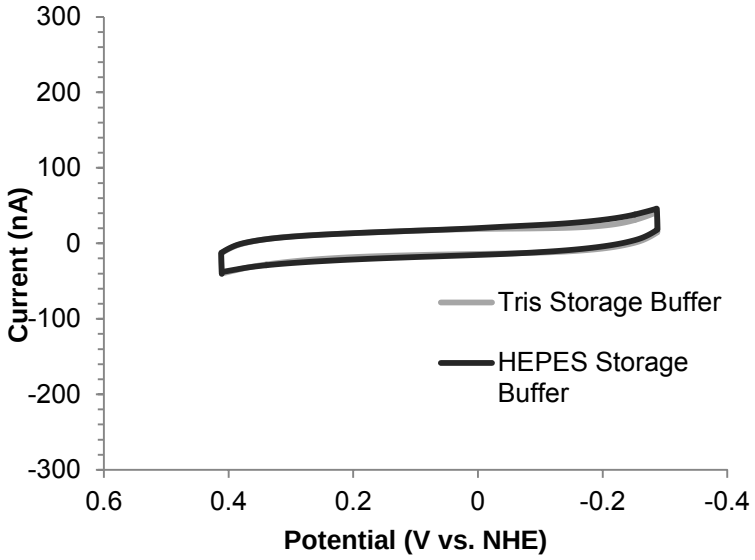

Figure 4.2. P58C does not produce a redox signal on ss/dsDNA in the absence of electrochemical alteration. CV performed on 30μM [4Fe4S] p58C in Tris storage buffer (light grey trace) and 40μM [4Fe4S] p58C in HEPES storage buffer (dark grey trace) using a Ag/AgCl reference electrode is shown. Buffer conditions were 20mM Tris buffer, pH 7.2, 75mM NaCl or 20mM HEPES, pH 7.2, 75mM NaCl. CV scanning was performed in anaerobic conditions, at a 100mV/s scan rate, for both samples.

(-188 mV vs. NHE) to the electrode surface. To ensure that all of the protein at the solution/electrode interface was converted to the desired redox state, bulk electrolysis was performed until the current reached a constant value (approximately 8.3 minutes). Oxidized or reduced samples were scanned by CV immediately after bulk electrolysis. The electrochemically oxidized sample displays a large cathodic peak near ⁻130 - ⁻150 mV vs. NHE in Tris storage buffer (20 mM Tris, pH 7.2, 75 mM NaCl). After a single scan to negative, reducing potential values, the redox signal disappears, indicating a loss of coupling between the [4Fe4S] cluster and the DNA bases sufficient for redox switching. (**Figure 4.3**). The electrochemically reduced protein, conversely, does not display any redox signal after bulk electrolysis is performed. This result suggests that oxidized $[4Fe4S]^{3+}$ yeast p58C is tightly bound to DNA and electronically coupled into the bases for DNA-mediated redox signaling. When yeast p58C is reduced to the $[4Fe4S]^{2+}$ state, however, the protein is loosely associated with DNA and does not participate in DNA-bound redox activity.

Human p58C can be electrochemically converted from the oxidized and redox-active state, to the reduced and redox-inert state. (*14*) We performed iterative oxidations of yeast p58C on a single DNA electrode to test whether the yeast protein redox switch was also electrochemically controlled. (**Figure 4.3**) Oxidation of yeast p58C to the $[4Fe4S]^{3+}$ state during bulk electrolysis converts the protein to a redox-active form, producing a large reductive CV signal. CV scanning to negative potentials then converts the protein back to the resting, (*7,8*) redox-inert $[4Fe4S]^{2+}$ state, but a second oxidation of the same sample regenerates the reductive peak in CV. The redox switch in yeast p58C is thus similar to the redox switch in human p58C, i.e. a change in [4Fe4S] cluster oxidation state allows conversion between two forms of p58C with dramatically different DNA-binding and redox signaling properties.

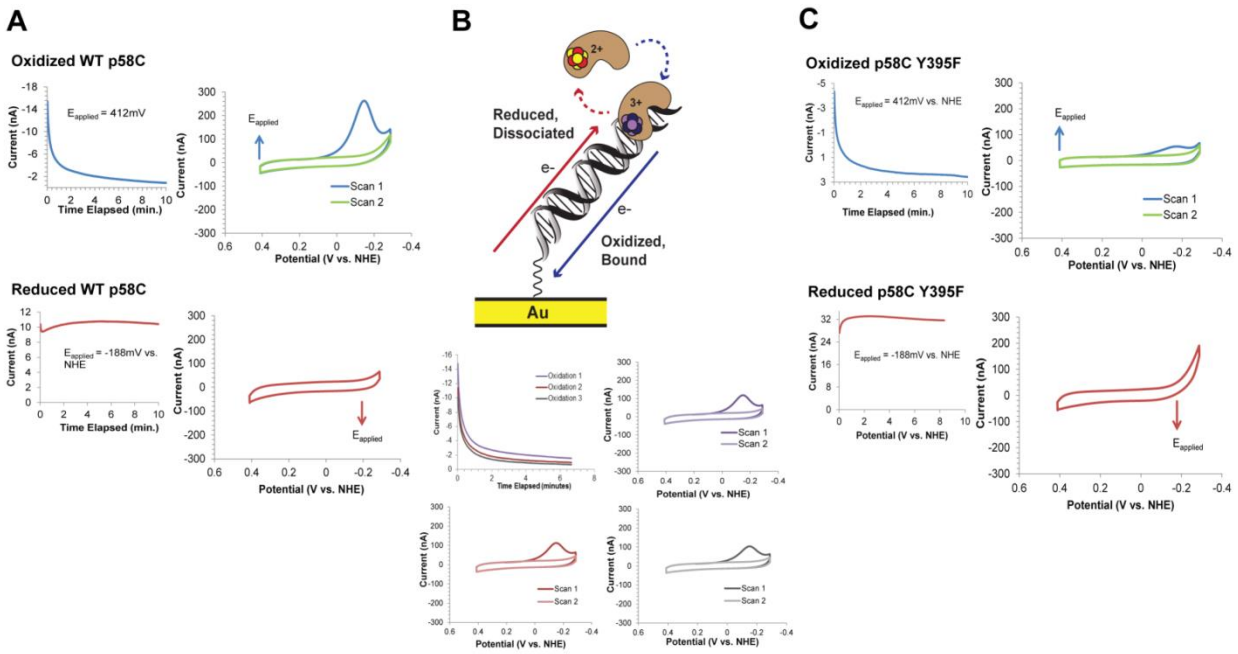

Figure 4.3. A redox switch in yeast p58C is mediated by the pathway of conserved tyrosine residues. A) Electrochemical oxidation and subsequent CV scans of yeast wild type p58C. A large reductive peak is observed in the initial scan of the oxidized protein, but disappears after a single scan to negative potentials. The reduced p58C is electrochemically inactive on a DNA-modified surface. B) Cartoon (above) illustrates the electrochemically reversible switch between the oxidized, electrochemically active p58C in the $[4Fe4S]^{3+}$ state with tighter binding to the DNA substrate and the reduced electrochemically inactive p58C in the $[4Fe4S]^{2+}$ state with weaker DNA binding affinity. Iterative electrochemical oxidation and CV after each oxidation on a single DNA-modified surface. The p58C signal is regenerated upon oxidation at a positive applied potential. C) Electrochemically oxidized and reduced p58C Y395F. Y395F (Y345 ortholog in human p58C) and Y397F (**Figure 4.6**) (Y347F ortholog in human p58C) were electrochemically oxidized and reduced, then scanned using CV on a DNA electrode. Both mutants showed similar behavior to WT p58C, but the charge transfer efficiency of the electrochemically oxidized protein was decreased for the Y395F variant and variable for the Y397F variant. The electrochemically reduced protein was not electrochemically active after electrochemical reduction. All scans were performed in anaerobic conditions, on 30 µM [4Fe4S] p58C (WT, Y395F, or Y397F), 20 mM Tris, pH 7.2, 75 mM NaCl. All CV was performed at 100 mV/s scan rate.

Upon observing that the yeast p58C [4Fe4S] cluster functions as a redox switch modulating DNA binding, we investigated whether the yeast p58C redox switch is dependent on a pathway of conserved tyrosine residues. We constructed yeast p58C variants with mutations at Y395 or Y397, designed to perturb the tyrosine-mediated redox pathway. All generated p58C variants (Y395F, Y397F, Y395L, and Y397L) load the [4Fe4S] cluster comparably to WT, as assessed by the ratio of absorption at 410nm/280nm in UV-Visible spectroscopy (**Figure 4.4**). Electrochemical assays show moreover that single-atom Y395F (**Figure 4.3**) and Y397F (**Table 4.2**) yeast p58C mutants have diminished charge transfer abilities compared to WT p58C during both oxidation by bulk electrolysis and reduction by CV. WT p58C samples also displayed increased charge transfer in bulk electrolysis and CV than p58C Y395L (**Figure 4.5**) and Y397L (**Figure 4.6**) compared in the same electrochemical conditions. The WT displays more charge transfer in bulk electrolysis and CV than mutants across all conditions tested, as summarized in **Table 4.2**. Small variations in the side chains (*23, 24, 44*) thus cause large changes in the efficacy of the [4Fe4S] cluster redox role.

Tyrosine Pathway Mutations Do Not Change Yeast p58C Structure or DNA Binding.

X-ray crystal structures of the WT yeast p58C and tyrosine mutants demonstrate that CT pathway mutations do not change the overall structure of the protein. (**Figure 4.7, Figure 4.8**) The overlays of WT yeast p58C and p58C Y395F, Y397F, Y395L, and Y397L, all of which are within 0.5 Å RMSD of the WT, show that all variants have nearly identical structures. The F395 and F397 aromatic rings in Y395F and Y397F, respectively, are oriented in nearly the exact same position as the aromatic rings in the tyrosine side chains of the WT protein, as observed for the human p58C Y345F and Y347F mutants (*14*). Notably, the more drastic substitution of the tyrosine aromatic ring with the leucine aliphatic chain in the Y395L and Y397L variants also has

p58C Variant	Buffer	Concentration ([4Fe4S] protein)	E_{ox} (mV vs. NHE)	Q_{BE} (nC)	Q_{CV} (nC)
WT	Tris	30 µM	412	553±61	145±41
Y395F	Tris	30 µM	412	340.0±50.0	9.03±5.3
Y397F	Tris	30 µM	412	136±1.4	44.9±13
WT	HEPES	57 µM	512	392±160	2.19±0.33
Y395L	HEPES	57 µM	512	371±240	0.266±0.17
Y397L	HEPES	40 µM	512	624±170	0.248±0.07

Table 4.2. Summary of bulk electrolysis/CV conditions for yeast p58C variant electrochemical assays. Buffer conditions are 20mM Tris, pH 7.2, 75mM NaCl (Tris in table) or 20mM HEPES, pH 7.2, 75mMNaCl (HEPES in table). In HEPES buffer, protein samples were generally less redox-active than in Tris, which is likely due to some loss of [4Fe4S] cluster after buffer exchange. The charge transferred during bulk electrolysis (Q_{BE}) and subsequent CV (Q_{CV}) is reported for each variant. Under every set of conditions tested, WT p58C displayed comparable or greater Q_{BE} than tyrosine mutants. WT moreover displayed greater Q_{CV} than variants tested at comparable conditions, suggesting that yeast p58C is less redox-efficient than human p58C but the redox activity depends on tunneling of charge through conserved tyrosines. Values reported are mean +/- S.D. for n=at least 3 trials.

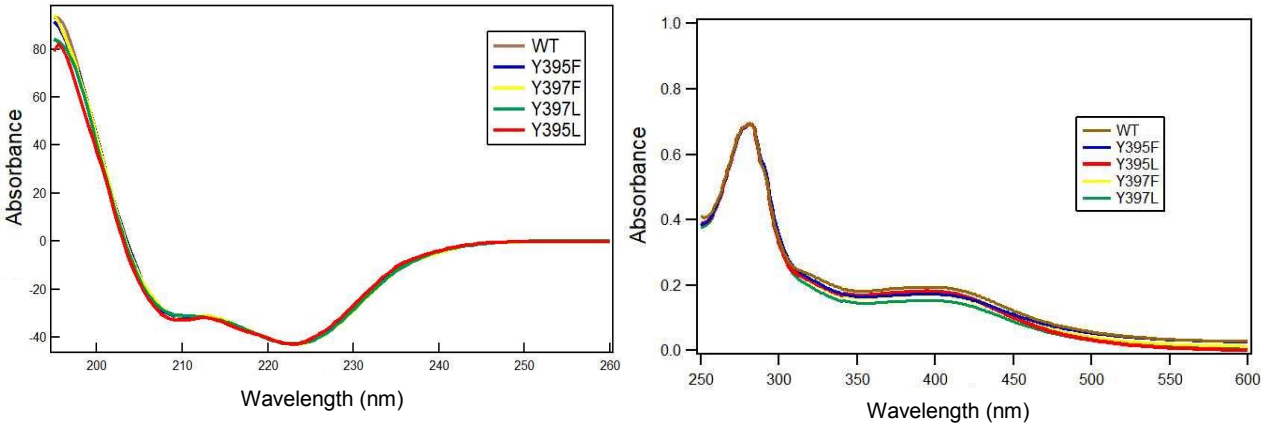

Figure 4.4. WT and mutant yeast p58C biophysical characterization. left) Circular dichroism (CD) spectroscopy of WT and mutant p58C indicate the mutations do not perturb any of the elements of secondary structure. All spectra normalized to WT at 222 nm. right) UV-Visible spectroscopy of WT and mutant p58C shows similar 280 nm/410 nm absorbance ratios, indicating similar degrees of [4Fe4S] cluster cofactor loading in all variants. All spectra normalized to WT at 410 nm.

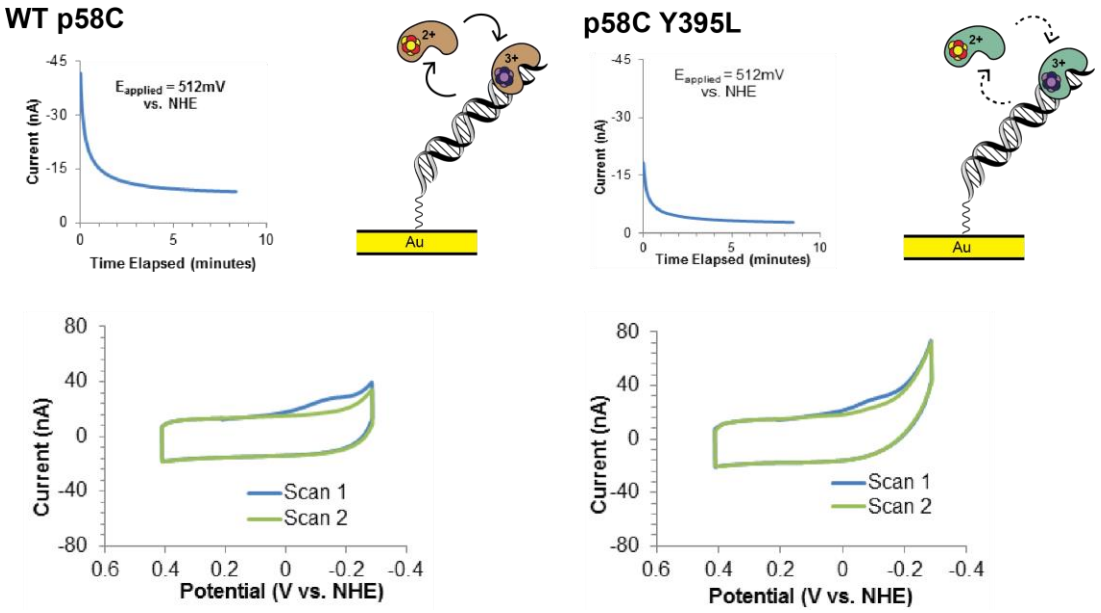

Figure 4.5. Tyrosine to leucine p58C mutants are redox-deficient. A) Electrochemical oxidation and subsequent CV scan of yeast wild type p58C. A reductive peak is observed in the initial scan of the oxidized protein, but this peak disappears after scanning to negative potentials. B) Electrochemical oxidation and subsequent CV of yeast p58C Y395L. The leucine mutant displays decreased redox activity, relative to WT p58C, during bulk electrolysis and in CV after electrochemical oxidation. The electrochemically reduced protein was not electrochemically active after electrochemical reduction. All scans were performed in anaerobic conditions, on 57 µM [4Fe4S] p58C (WT or Y395L), 20 mM HEPES, pH 7.2, 75 mM NaCl. All CV was performed at 100 mV/s scan rate.

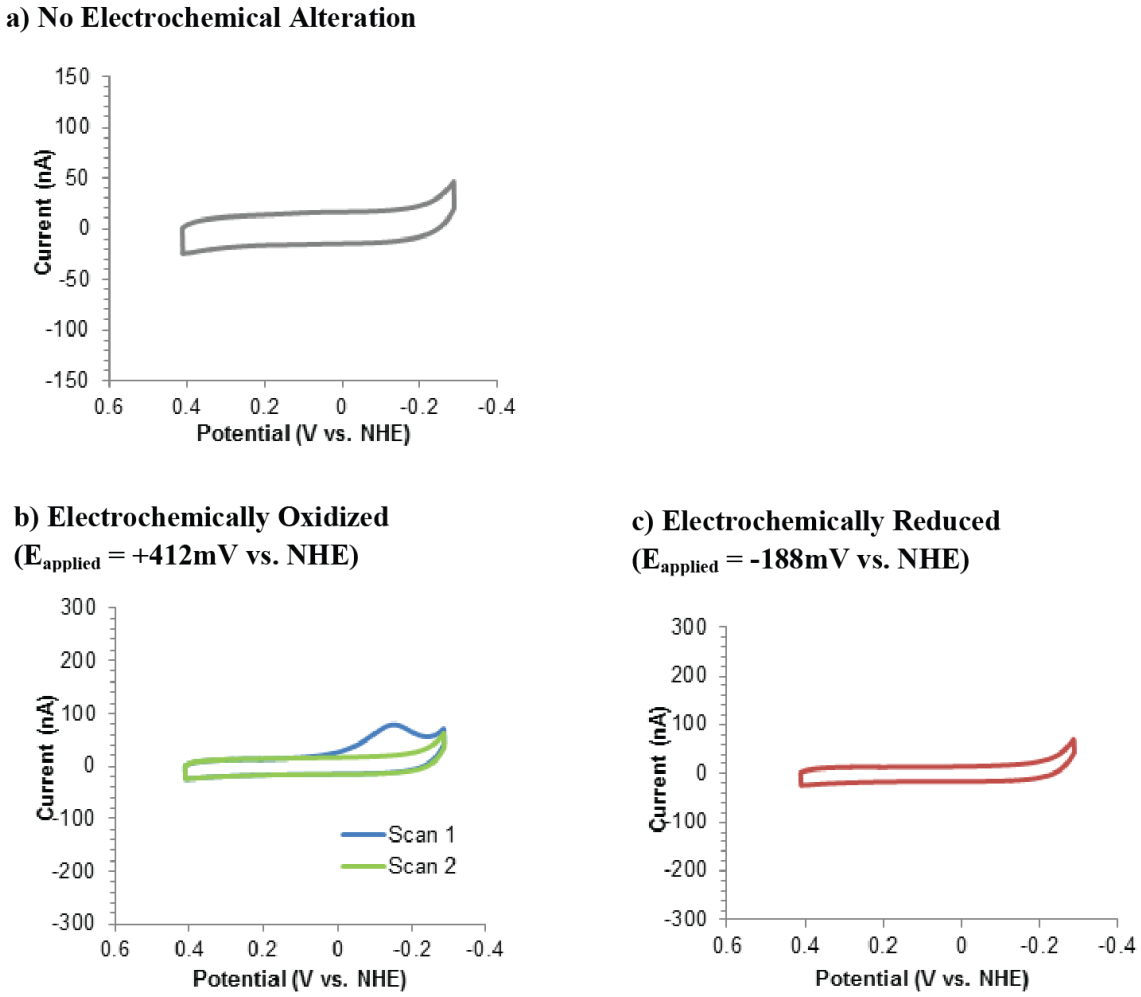

Figure 4.6. CV scans of yeast p58C Y397F. a) Electrochemically unaltered p58C Y397F mutant displays no electrochemical signal on DNA. b) p58C Y397F tyrosine mutant displays a cathodic peak after oxidation at an applied potential of +412mV vs. NHE, but the peak is significantly smaller than that observed for wild type. c) p58C Y397F displays no redox signal on DNA after electrochemical reduction at an applied potential of -188mV vs. NHE. All scans performed on 30μM [4Fe4S] p58C variant, in 20mM Tris, pH 7.2, 75mM NaCl, at a 100mV/s scan rate.

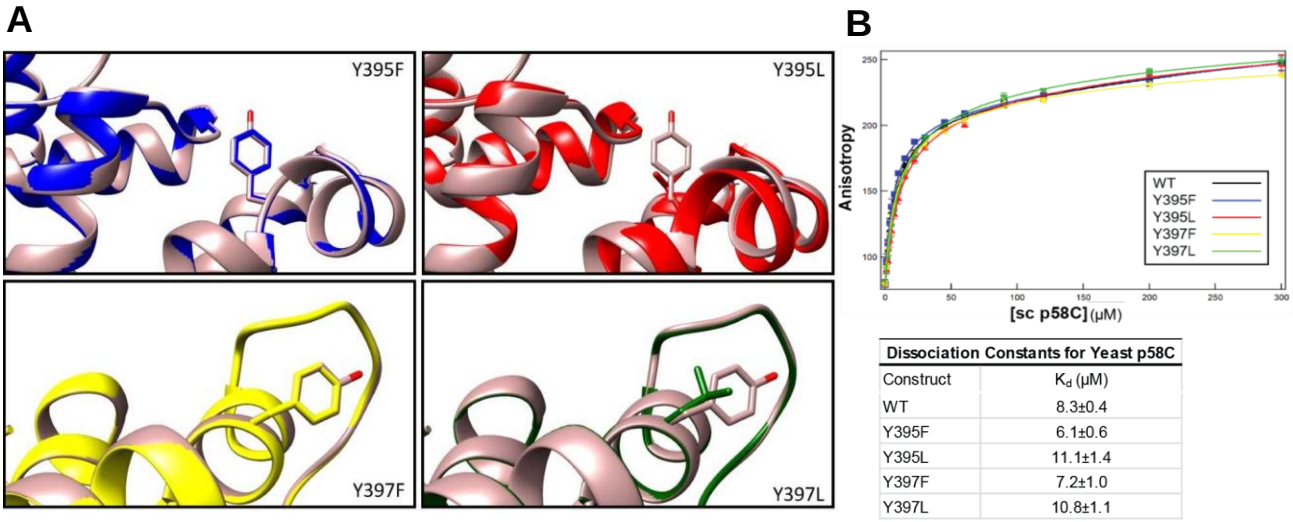

Dissociation Constants for Yeast p58C	
Construct	K_d (μM)
WT	8.3±0.4
Y395F	6.1±0.6
Y395L	11.1±1.4
Y397F	7.2±1.0
Y397L	10.8±1.1

Figure 4.7. DNA binding and structure are preserved upon mutation of conserved tyrosine residues Y395 and Y397 in yeast p58C. A) Crystal structures of WT and yeast p58C tyrosine mutants show minimal structural perturbation of the overall protein structure with redox pathway mutations. The WT yeast p58C (green) crystal structure is overlaid with each redox-deficient mutant. Mutation of tyrosines to either aromatic phenylalanine or aliphatic leucine do not produce significant changes in the structure. B) DNA binding of yeast p58C variants measured using fluorescence anisotropy. WT yeast p58C and tyrosine mutants bind substrate with similar affinities, suggesting that differences in electrochemical signals are due to differences in redox proficiency rather than differences in ability to bind DNA.

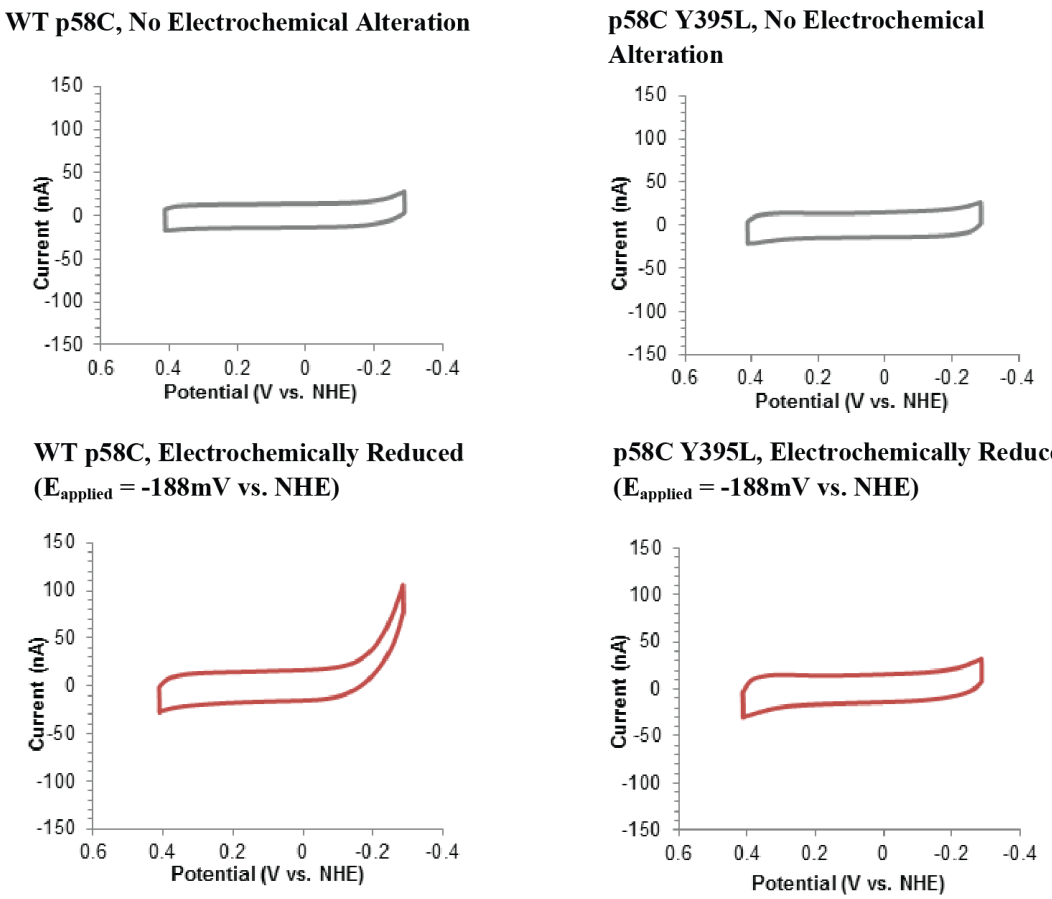

Figure 4.8. Cyclic voltammetry of electrochemically unaltered WT p58C (top left, grey trace) and p58C Y395L (top right, grey trace) and electrochemically reduced WT p58C (bottom left, red trace) and p58C Y395L (bottom right, red trace). Electrochemically unaltered and electrochemically reduced variants under identical conditions display no redox activity, suggesting that the unaltered samples is predominantly in the redox-inert, $[4Fe4S]^{2+}$ form. All CV scans were performed in anaerobic conditions, with 57µM [4Fe4S] p58C Y395L in 20mM HEPES, pH 7.2, 75mM NaCl. Scans were performed at 100mV/s scan rate.

very little effect on the structure, including the orientation of the leucine side chains. Thus, redox pathway mutations do not change the overall structure of p58C.

We also compared *in vitro* DNA binding capabilities of WT and mutant yeast p58C. (**Figure 4.7, Figure 4.8**) As for human p58C, these experiments were performed under aerobic conditions, since attempts to alter the redox state using chemical reagents degrades the cluster. A fluorescence anisotropy assay was performed using a substrate that contains a 5'-ssDNA overhang similar to the substrate used in p58C electrochemistry. The WT and all variants bind DNA with affinities in the low micromolar range (**Table 4.1, Figure 4.7, Figure 4.8**). Notably, both the tyrosine and leucine mutants are indistinguishable from the WT protein. This result indicates that the difference in redox signal magnitude observed on the DNA electrodes WT and mutant p58C is a result of differences in the redox switching ability and not the ability to bind DNA. Overall, the similar structural and biophysical properties of the tyrosine mutants relative to WT p58C support the conclusion that different behavior observed for these variants is solely due to differences in their chemical/electronic properties.

Reversible, NTP-Dependent Redox Activity in Yeast p58C.

Yeast p58C displays an NTP-dependent redox signal on DNA electrodes in anaerobic conditions. (**Figure 4.9**) A semi-reversible CV signal centered at 149±14 mV vs. NHE is generated for 57 μM [4Fe4S] p58C in the presence of DNA and 1.25 mM ATP. Importantly this is within the biological redox potential range (*45*) and is comparable to the potential values observed for other DNA-processing [4Fe4S] proteins, suggesting that active primase has the potential to signal other DNA-bound [4Fe4S] proteins during replication. (*1,15, 46-49*) The signal observed in CV displays an average charge transfer value of 8.7 ± 4 nC in the reductive

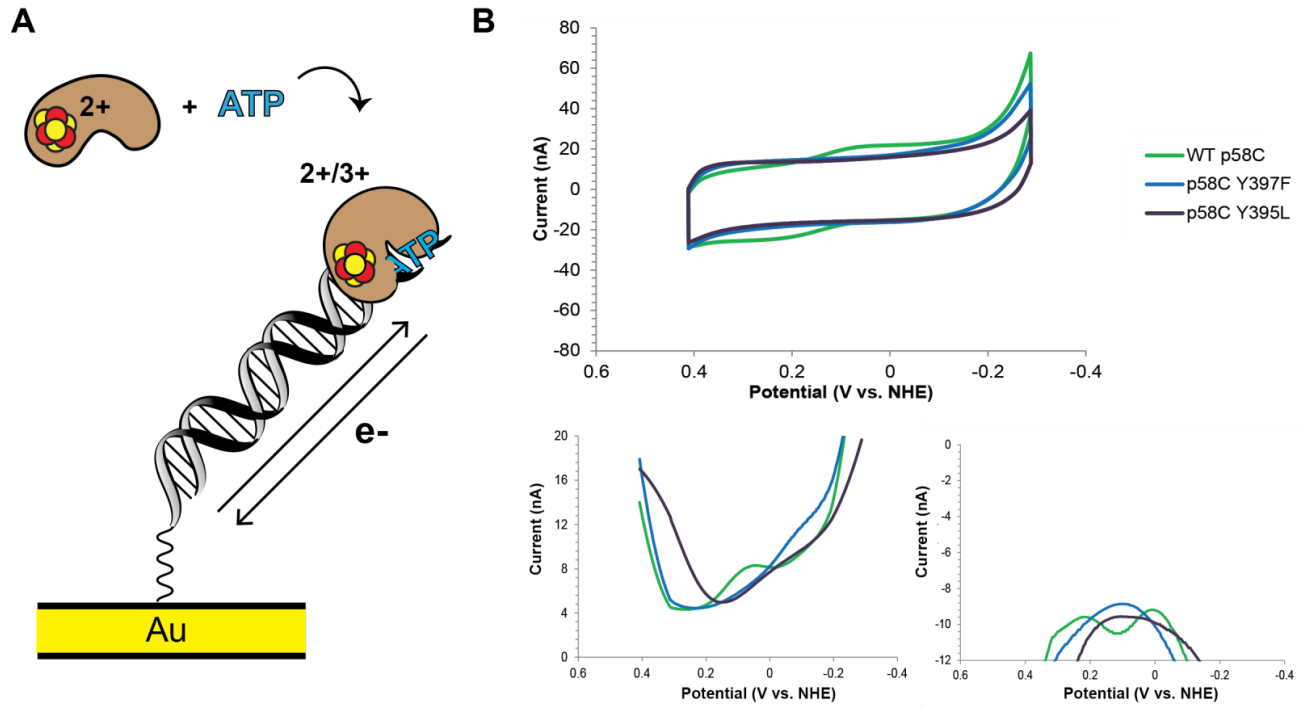

Figure 4.9. NTP binding promotes a reversible redox switch in yeast p58C. A) Cartoon depicts redox activity of yeast p58C bound to DNA and a nucleotide triphosphate (NTP). The protein can reversibly cycle between the $[4Fe4S]^{3+}$ and $[4Fe4S]^{2+}$ state when bound to all substrates essential for primase activity. B) CV scans of WT yeast p58C (green trace), p58C Y397F (blue trace), and p58C Y395L (purple) in the presence of 1.25 mM ATP (WT). Both proteins show reversible redox signals centered at 149 ± 14 mV vs. NHE (WT). The WT protein signal is 70 ± 10% reversible. Mutant p58C does not have a measurable signal, suggesting that the redox pathway is important for redox switching in the presence of all native primase substrates. Square Wave Voltammetry (Reduction sweep, left; oxidation sweep, right) of WT and tyrosine mutant p58C. Square Wave voltammetry in the reductive sweep show a small signal for the Y397F variant near -80 mV vs. NHE, which is attributed to a $[3Fe4S]^{+}$ degradation product. (*50*) These data suggest that the tyrosine pathway and reversible redox switching is integral for activity and cluster stability. All scans were performed in anaerobic conditions, on 57 µM [4Fe4S] p58C variant and 1.25 mM ATP in 20 mM HEPES, pH 7.2, 75 mM NaCl. All CV was performed at 100 mV/s scan rate. Square Wave voltammetry was performed at 15 Hz frequency. Potentials reported are mean values +/- s.d. of at least three trials.

peak and 5.8 ± 2 nC in the oxidative peak. This result suggests that NTP binding promotes a redox switch in p58C in the absence of electrochemical alteration.

The larger cathodic wave in CV is consistent with the oxidized $[4Fe4S]^{3+}$ protein having a higher binding affinity and being more strongly coupled to the DNA bases for redox activity than the reduced $[4Fe4S]^{2+}$ protein. The reductive peak corresponds to the electrochemical conversion of $[4Fe4S]^{3+}$ p58C to $[4Fe4S]^{2+}$ p58C, and the oxidative peak is a measurement of the reverse process. Comparison of the reductive and oxidative sweeps in square wave voltammetry (SWV) (**Figure 4.9**) show a similar disparity in signal size; the reductive sweep signal displays an average current of 2.8±1 nA; the oxidative wave displays an average current of 0.90±0.5 nA. The redox switch model predicts that more oxidized protein is bound in the p58C:DNA:NTP complex than reduced protein, generating a larger reductive peak than oxidative peak in CV and SWV.

To assess whether this reversible signal depends on the p58C charge transfer pathway, we measured the NTP-dependent signals of yeast p58C Y395L and Y397F mutants. The assays were performed in the presence of 1.25 mM ATP under identical conditions to those used for the WT protein. Neither variant (**Figure 4.9**) displays a reversible redox signal, which suggests that the conserved tyrosine pathway is important for redox switching. Interestingly, the CV and SQWV scans of the single-atom mutant p58C Y397F (**Figure 4.9**) display a reductive peak, which indicates some redox activity may occur in this mutant. The reductive peak is detected for Y397F at -86 ± 13 mV vs. NHE with a current averaging 0.36 ± 0.3 nA, in 73% of the measured scans. Moreover, a similar signal was observed on DNA electrodes for p58C Y397F in the presence of 2.5 mM ATP. (**Figure 4.10**) The secondary peak in the reductive wave can also be

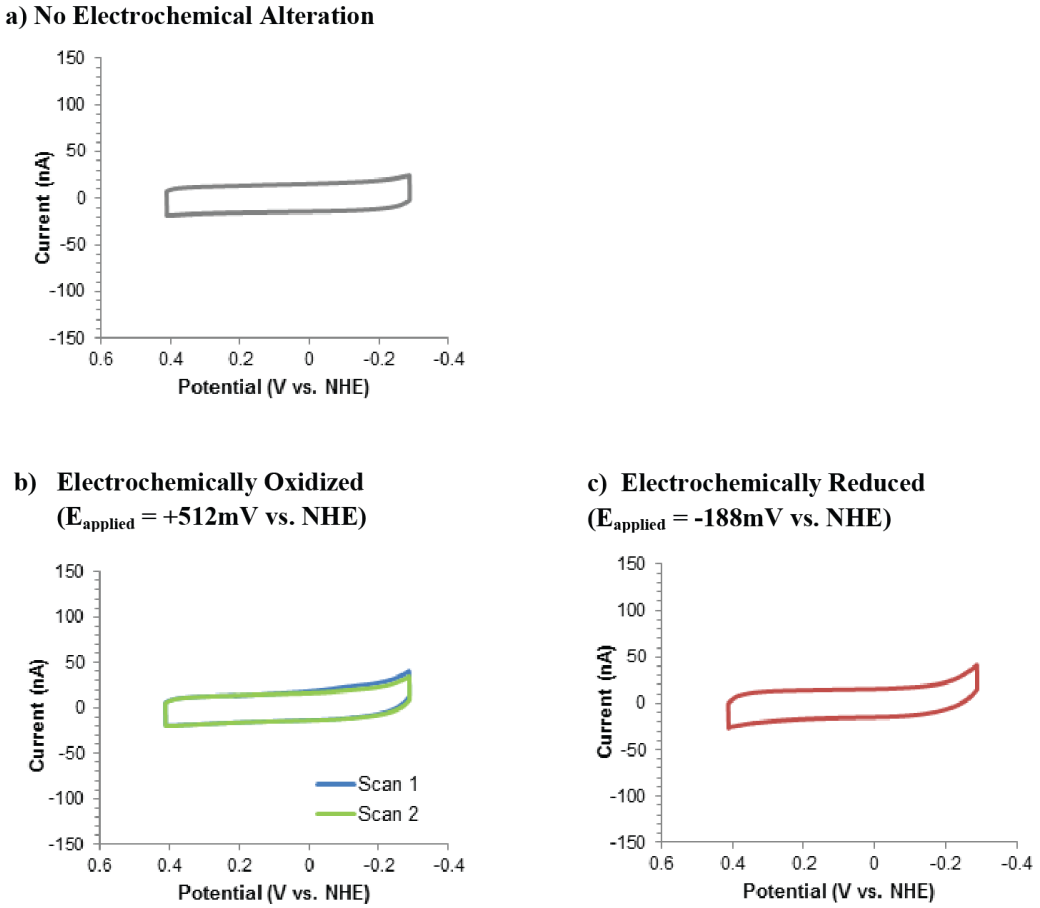

Figure 4.10. CV scans of yeast p58C Y397L. a) Electrochemically unaltered p58C Y397L mutant displays no electrochemical signal on DNA. b) p58C Y397L tyrosine mutant displays a cathodic peak after oxidation at an applied potential of +512mV vs. NHE, but the peak is significantly smaller than that observed for wild type. c) p58C Y397L displays no redox signal on DNA after electrochemical reduction at an applied potential of -188mV vs. NHE. All scans performed on 40µM [4Fe4S] p58C variant, in 20mM HEPES, pH 7.2, 75mM NaCl, at a 100mV/s scan rate.

observed in WT yeast p58C, alongside the primary wave centered at 150mV vs. NHE, in the presence of a large excess of ATP (**Figure 4.11**).

This reductive peak likely corresponds to the presence of the $[3Fe4S]^{+}$ degradation product (*50*) of the [4Fe4S] cofactor. A signal in the reductive wave at comparable potentials was recently observed electrochemically and spectroscopically in a variant of human MutYH, a base excision repair protein, when exposed to atmospheric oxygen (*51*). The $[3Fe4S]^{+}$ degradation product is produced by oxidation from the resting $[4Fe4S]^{2+}$ state to the $[4Fe4S]^{3+}$ state (*47,51*) in a mutant with a destabilized metal cofactor. Tyrosine pathway variants cannot efficiently undergo the switch back to the reduced form once oxidized. Hence, the deficient redox activity of these p58C variants may 'trap' the high energy $[4Fe4S]^{3+}$ form until it becomes unstable and degrades. This result suggests that efficient redox switching is essential not only for regulation of activity, but also for the stability of the active protein.

The Yeast p58C Redox Switch is Necessary for Viability.

After characterizing the redox switch in yeast DNA primase, we sought to investigate the consequences of this chemistry in yeast cells. Both subunits of yeast primase are essential; partially defective alleles compromise DNA synthesis and yeast cell growth (*52*). Liu and Huang (*16*) additionally have shown that mutations of the cysteine residues ligating the p58C [4Fe4S] cluster cause growth defects in cells, suggesting the importance of the primase cluster for viability. We have shown that mutations at p58 residues Y395 or Y397 along the redox pathway impair the Fe-S redox switch *in vitro* and hypothesized that these mutations would compromise cell growth. Single-site mutations were introduced into the chromosomal gene encoding the p58 subunit of DNA primase of *S. cerevisiae* (*PRI2*, *53*) at positions Y395 and

Y397 under control of the endogenous promoter. Introducing these redox pathway mutations that do not affect [4Fe4S] cluster loading or DNA binding of p58C *in vitro* allowed us to test the effect of the cluster redox switch on cellular fitness.

We predicted that mutation of Y395 or Y397 to an aliphatic leucine residue would decisively inhibit the redox switch in primase. Although Y395L and Y397L mutants of p58C are structurally intact and bind DNA with WT affinity, they more strongly inhibit the redox switching of p58C on a DNA electrode than the single-atom Y395F or Y397F mutants (**Figure 4.5, Table 4.2**). Strikingly, the *pri2Y397L* single-residue mutation confers lethality in yeast (**Table 4.3**). This result underscores the importance of an aromatic redox pathway within the primase protein for DNA replication and cell survival.

We next sought to observe whether single-atom Y395F and Y397F mutations in p58C, which diminish but do not eliminate redox switching in primase, affect cellular fitness. Strains expressing the *pri2Y395F* and *pri2Y397F* alleles were viable at 30˚C and grew comparably to the parental *PRI2* strain (**Figure 4.12**). Since it has been suggested that the presence of the [4Fe4S] cluster makes primase sensitive to oxidative stress (*16*), we grew the WT *PRI2*, *pri2Y395F*, and *pri2Y397F* strains in the presence of 2 mM hydrogen peroxide, a chemical oxidative stress inducer. We observe that *pri2Y395F* strain grows slower on average than the WT or Y397F strain, in liquid culture or on solid rich media after exposure to hydrogen peroxide in liquid culture. (**Figure 4.14**) Strains containing the *pri2Y395F* mutations grew with more variability than WT or *pri2Y397F* strains, however. Yeast strain growth in the presence of 100 μM methylene blue (**Figure 4.15**), a redox dye that reacts with visible light to generate singlet oxygen and induce stress (*54*), follows a similar pattern. We see a slight defect in growth for the *pri2Y395F* strain in the presence of methylene blue and light, which is not present in a dark

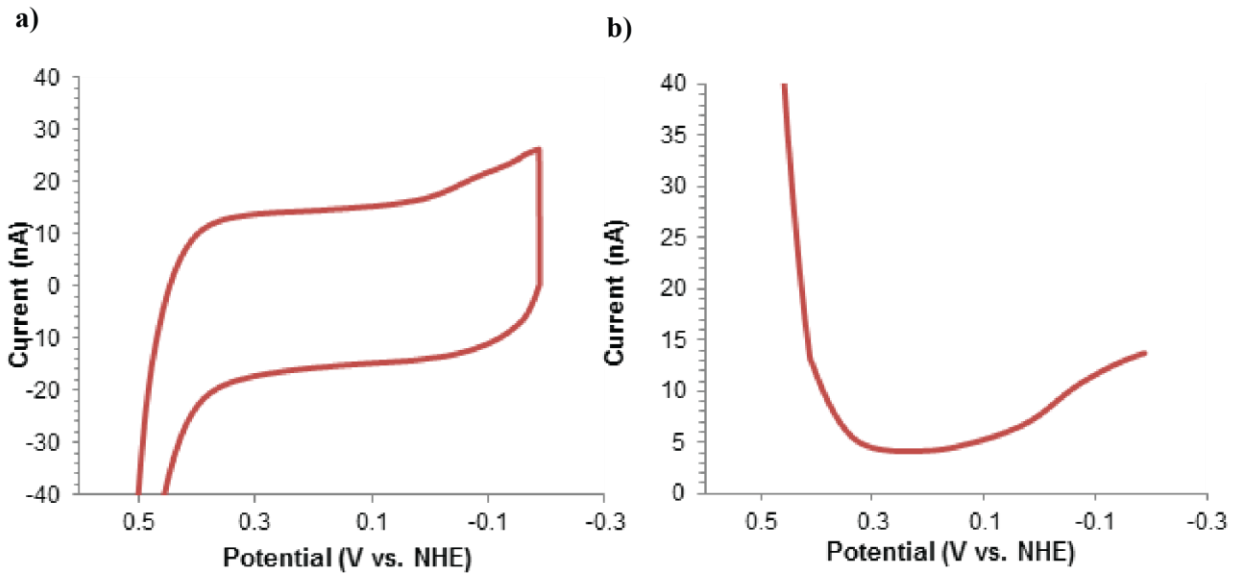

Figure 4.11. Electrochemistry of yeast p58C Y397F in the presence of 2.5mM ATP. a) CV scans show a small peak in the reductive wave near -80mV vs. NHE, which is likely a $[3Fe4S]^{+}$ oxidative degradation product. b) SWV of yeast p58C Y397F in the presence of 2.5mM ATP. All scans performed in anaerobic conditions on 57µM [4Fe4S] p58C Y397F and 2.5mM ATP, in 20mM HEPES, pH 7.2, 75mM NaCl, at a 100mV/s scan rate for CV or a 15 Hz frequency for SWV.

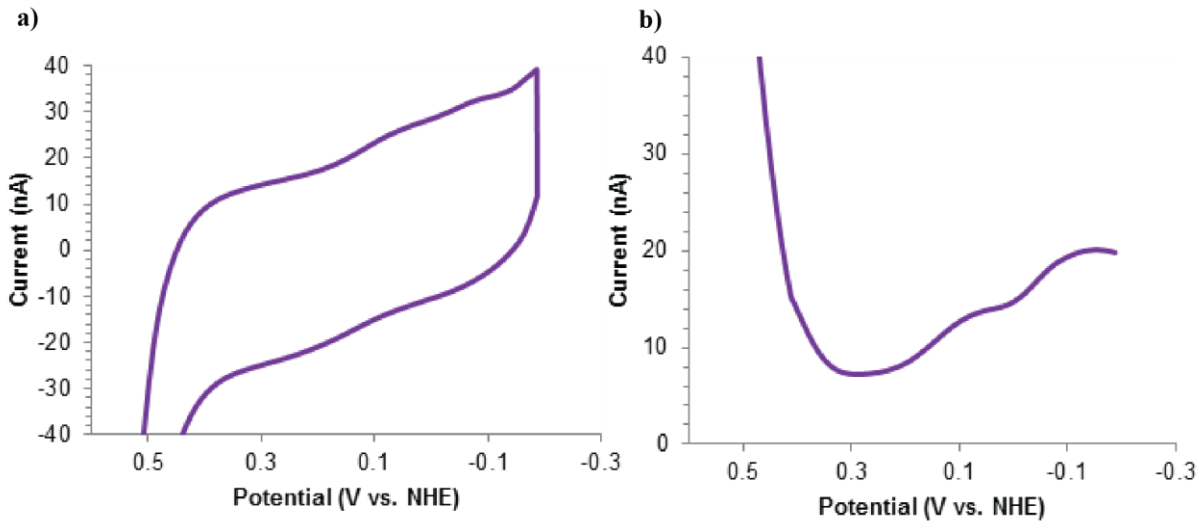

Figure 4.12. Electrochemistry of WT yeast p58C in the presence of 5mM ATP. a) CV scans show a small peak in the reductive wave near -80mV vs. NHE, likely a $[3Fe4S]^{+}$ oxidative degradation product. b) SWV of yeast p58C in the presence of 5mM ATP. All scans performed in anaerobic conditions on 40µM [4Fe4S] p58C and 5mM ATP, in 20mM HEPES, pH 7.2, 75mM NaCl, at a 100mV/s scan rate for CV or a 15 Hz frequency for SWV.

Yeast Strain	Growth Phenotype
PRI2	WT growth at all temperatures
pri2-Y395F	Some Sensitivity to Oxidative Stress, WT growth at 30°C
pri2-Y397F	WT growth at all temperatures
pri2-Y395L	Not Available
pri2-Y397L	**Lethal**

Table 4.3. The aromatic pathway mediating the primase redox switch is essential for cell viability as reflect in growth phenotypes of different yeast primase tyrosine mutants. The Y395F mutation confers some sensitivity to oxidative stress conditions (2 mM hydrogen peroxide, 100 μM methylene blue). A single-residue mutation changing conserved, aromatic tyrosine 397 to aliphatic leucine residues confer lethality in yeast.

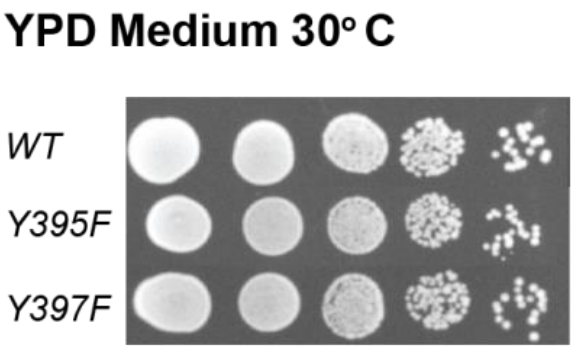

Figure 4.13. Yeast strains coding for WT *PRI2*, *pri2Y395F*, *or pri2Y397F*. Strains were grown in liquid rich medium overnight, normalized to OD_{600}= 1, and plated in ten-fold serial dilutions. Plated samples grew on agar plates for 2 days. All strains grew comparably in rich medium at permissive temperature (30°C).

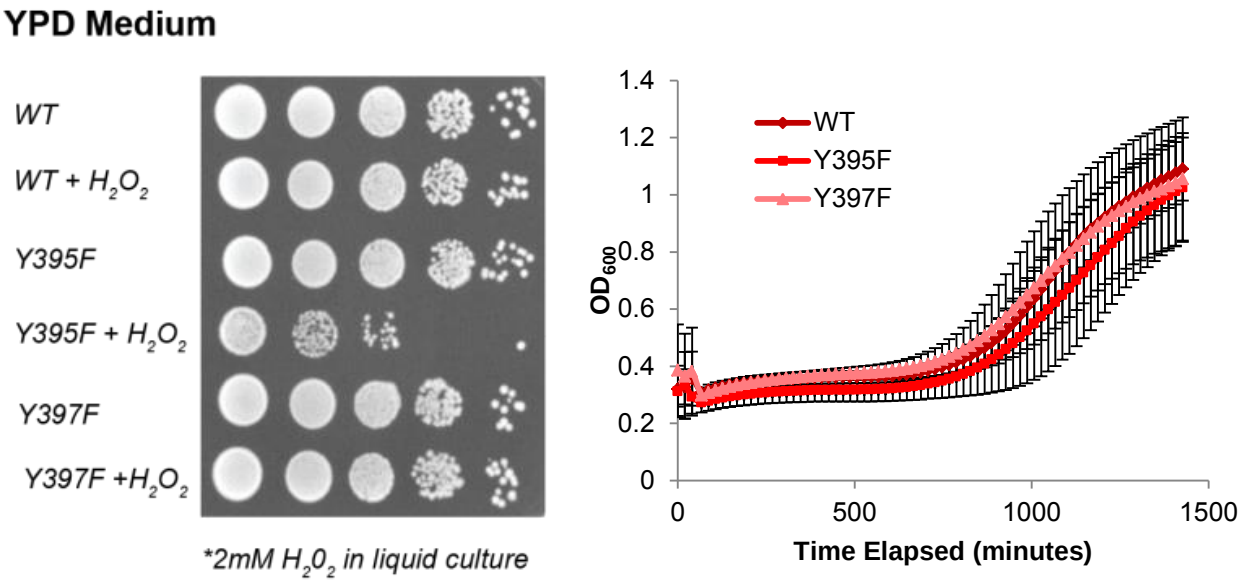

Figure 4.14. Y395F strains display some sensitivity to hydrogen peroxide, relative to WT and Y397F strains. (left) Spot assay with normalized (OD_{600}= 1) strains plated in ten-fold serial dilutions on rich agar plates. Cells were grown in media overnight, normalized to mid-log phase, and dosed with 2mM hydrogen peroxide, and grown in the presence of 2mM hydrogen peroxide overnight. Cells were then grown for 2 days on solid rich media at 30°C. (right) Yeast strains were grown overnight and normalized to mid-log phase, then dosed with 2mM H_2O_2 and grown for 24 hours at 30°C, in liquid culture. Growth curves over a 24 hour period, measuring OD_{600} every 20 minutes, show that Y395F grows more slowly on average. The wide range of error may be due to adaptive suppressor mutations in the mutant strains. Average growth of n= 3 colonies +/- s.d. is shown for each variant.

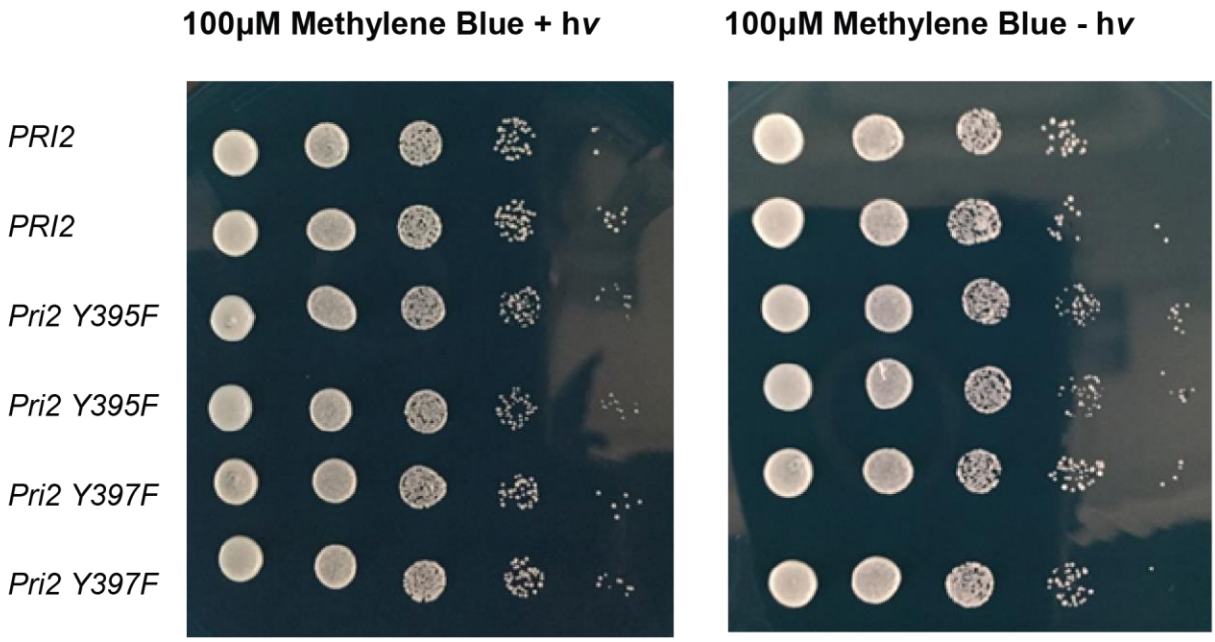

Figure 4.15. Yeast strains coding for WT *PRI2, pri2Y395F, or pri2Y397F*. Strains were grown in liquid rich medium overnight, normalized to OD_{600}= 1, and plated in ten-fold serial dilutions on YPD solid media with 100µM methylene blue. Plated samples grew on agar plates for 2 days at 30°C, in the presence (+h*ν*) or absence (-h*ν*) of visible light. Y395F showed a very slight defect in the presence of light, which was not observed in the absence of light.

control. (**Figure 4.15**) The small effect of the Y395F mutation suggests that the p58C redox pathway contributes to oxidative stress sensitivity. In the presence of this mutation, yeast may acquire suppressor mutations (*55*) to compensate for the defects caused by redox switch inhibition, resulting in variation of growth between colonies of the *pri2Y395F* strain.

Small-molecule reactive oxygen species (ROS) such as hydrogen peroxide or singlet oxygen can damage the [4Fe4S] cluster directly, causing degradation to the $[3Fe4S]^{+}$ form (*50,51*) directly or indirectly through DNA charge transport. We have observed, for example, that guanine radicals in oxidized duplex DNA induce redox switching in a bound [4Fe4S] Endonuclease III protein. (*56*) Independent of the cluster oxidation mechanism, the results suggest that efficient switching between the $[4Fe4S]^{2+}$ and $[4Fe4S]^{3+}$ redox states is important for survival. WT p58C, as DNA electrochemistry demonstrates, can more easily cycle between the $[4Fe4S]^{2+}$ and $[4Fe4S]^{3+}$ states than the tyrosine mutants. Once oxidized, WT p58C can convert readily back to the $[4Fe4S]^{2+}$ state, avoiding further oxidation and degradation to the $[3Fe4S]^{+}$ cluster. The mutants are not as capable of cycling between redox states and therefore are likely to be more susceptible to degradation from the $[4Fe4S]^{3+}$ to the $[3Fe4S]^{+}$ species. A single-atom tyrosine to phenylalanine mutation in the primase aromatic redox pathway modestly increases yeast sensitivity to oxidative stress; a more drastic leucine mutation at position 397, however, abrogates the pathway and confers lethality. It is possible that a phenylalanine residue in the pathway may have enough redox capacity to partially affect a redox switch and primase activity. Like tyrosine and tryptophan, phenylalanine is relatively more common in oxidoreductase enzymes; (44) tyrosine to phenylalanine mutants may retain some electron transfer function. Hence, single-atom mutants that *compromise* the redox pathway in primase

cause increased sensitivity to stress, but more drastic tyrosine to leucine mutation that *eliminates* the redox pathway causes cell death.

Discussion

Reversible, redox-driven switches control DNA binding affinity in [4Fe4S] enzymes central to both DNA repair and replication, facilitating rapid and efficient substrate binding and dissociation (*15,45, 57*). The oxidized $[4Fe4S]^{3+}$ bacterial glycosylase Endonuclease III, for example, binds the DNA polyanion 550-fold more tightly than the reduced, $[4Fe4S]^{2+}$ Endonuclease III. Reversible cluster oxidation and reduction facilitates DNA-mediated redox signaling between Endonuclease III and other [4Fe4S] repair proteins in the first steps of locating oxidative DNA damage. (*57*) The [4Fe4S] enzyme yeast DNA polymerase δ is DNA-bound and active in the $[4Fe4S]^{2+}$ state, when associated with Proliferating Cell Nuclear Antigen (PCNA) (*58*). When oxidized to the $[4Fe4S]^{3+}$ state, however, PCNA-associated polymerase δ binds DNA even more tightly, stalling DNA synthesis. (*15*) This change in binding may allow polymerase δ to sense and respond to oxidative stress in the cell. Efficient, reversible switching between [4Fe4S] redox states thus plays important roles in coordinating the activity of diverse, specialized DNA-processing [4Fe4S] enzymes. Here we have established a general redox switching mechanism, dependent on a change in oxidation state of the [4Fe4S] cluster, that regulates DNA binding and redox signaling in eukaryotic DNA primases. This switch regulates primer synthesis, but not catalytic activity, in human primase (*14*). Conserved tyrosine residues shuttle charge through the insulating protein matrix, between the metal cofactor and bound DNA. Here, we show that a similar redox switch exists in yeast primase, despite a different arrangement of tyrosines for DNA-protein electron transfer, and that this redox switch in primase is essential for cell growth.

The primase redox switch, driven by a change in [4Fe4S] cluster oxidation state, is mediated by a constellation of conserved tyrosines in the yeast and human (*14*) proteins. Although these residues are positioned differently in yeast and human orthologues, our results show that they perform the same chemistry. Conserved tyrosines between the cluster and DNA binding interface are spaced $\leq$ 15Å apart in both proteins, facilitating microsecond electron transfer. (*23, 24, 44, 46*) Despite previous arguments that structural differences in yeast and human primase preclude a general redox role for these residues (*59*), the electrochemical and biological data unequivocally demonstrate that the electron transfer pathway is conserved in these eukaryotic primases. Our results also suggest that the role of these tyrosine residues is much more significant than their contributions to any network of p58C/substrate hydrogen bonds (*18*), as we observe electrochemical attenuation of the p58C redox signal on DNA and lethality in yeast due to a single-residue redox pathway mutation.

The general redox pathway through primase depends crucially on the side chain chemistry of key residues. Single-atom mutations p58Y395F and p58Y397F weaken the aromatic charge transfer pathway through yeast primase, and the Y395F mutation causes some increased sensitivity to oxidative stress. The more drastic side chain modifications in the p58 Y397L mutant, while yielding little structural perturbation in the protein or effect on DNA binding affinity, eliminate the aromatic pathway and is lethal in cells. These tyrosines are not located near the primase catalytic site, yet a mutation at a position between the [4Fe4S] cluster and DNA-binding domain affects the regulatory electron transfer redox switch and prohibits cell growth. These observations support our proposal that the conserved redox chemistry of the [4Fe4S] cluster in DNA primase plays a central role in coordinating the initial steps of eukaryotic DNA priming.

References

1. O'Brien, E., Silva, R.M.B., Barton, J.K. Redox Signaling through DNA. *Isr. J. Chem.*, **2016**, *56*, 705-723.

2. O'Donnell, M.E., Langston, L., Stillman, B. Principles and concepts of DNA replication in bacteria, archaea, and eukarya. *Cold Spring Harbor Perspectives in Biology*., **2013**, *5*, a010108.

3. Burgers, P.M.J., Kunkel, T.A. Eukaryotic DNA Replication Fork. *Annu. Rev. Biochem.,* **2017**, *86*, 417-438.

4. Frick, D.N., Richardson, C.C. DNA Primases. *Annu. Rev. Biochem.,* **2001**, *70,* 39-80.

5. Kuchta, R.D., Stengel, G. Mechanism and evolution of DNA primases. *Biochimica et Biophysica Acta*. **2010**, *1804*, 1180-1189.

6. Arezi, B., Kuchta, R.D. Eukaryotic DNA primase. *Trends in Biochemical Sciences*., **2000**, *25*, 572-576.

7. Weiner, B.E., Huang, H., Dattilo, B.M., Nilges, M.J., Fanning, E., Chazin, W.J. An iron-sulfur cluster in the c-terminal domain of the p58 subunit of human DNA primase. *J. Biol. Chem.*, **2007**, *282*, 33444-33451.

8. Klinge, S., Hirst, J., Maman, J.D., Krude, T., Pellegrini, L. An iron-sulfur domain of the eukaryotic primase is essential for primer synthesis. *Nat. Struct. Mol. Biol.,* **2007**, *14*, 875-877.

9. Fuss, J.O., Tsai, C., Ishida, J.P., Tainer, J.A. Emerging critical roles of Fe-S clusters in DNA replication and repair. *BBA*, **2015**, *1853*, 1253-1271.

10. Netz, D.J.A., Stith, C.M., Stümpfig, M., Köpf, G., Vogel, D., Genau, H.M., Stodola, J.L., Lill, R., Burgers, P.M.J., Pierik, A.J. Eukaryotic DNA polymerases require an iron-sulfur cluster for the formation of active complexes. *Nature Chemical Biology*., **2012**, *8,* 125-132.

11. Rees, D.C., Howard, J.B. The Interface Between the Biological and Inorganic Worlds: Iron-Sulfur Metalloclusters., *Science*, **2003**, *300*, 929-931.

12. Rouault, T.A. Mammalian iron-sulphur proteins: novel insights into biogenesis and function. *Nat. Rev. Mol. Cell Biol.*, **2015**, *16*, 45-55.

13. Netz, D.J.A., Mascarenhas, J., Stehling, O., Pierik, A.J., Lill, R. Biogenesis of cytosolic and nuclear iron-sulfur proteins. *Trends Cell Biol.,* **2014**, *24*, 303-312.

14. O'Brien, E., Holt, M.E., Thompson, M.K., Salay, L.E., Ehlinger, A.C., Chazin, W.J., Barton, J.K. The [4Fe4S] cluster of human DNA primase functions as a redox switch using DNA charge transport. *Science*, **2017**, *355*, eaag1789.

15. Bartels, P.L., Stodola, J.L., Burgers, P.M.J., Barton, J.K. A Redox Role for the [4Fe4S] Cluster of Yeast DNA Polymerase δ. *J. Am. Chem. Soc.*, **2017**, *139*, 18399-18348.

16. Liu, L., Huang, M. Essential role of the iron-sulfur cluster binding domain of the primase regulatory subunit Pri2 in DNA replication initiation. *Protein Cell*, **2015**, *6*, 194-210.

17. Nunez-Ramirez, R., et al. Flexible tethering of primase and DNA Pol α in the eukaryotic primosome. *Nuc. Acids Res.*, **2011**, *39*, 8187-8199.

18. Baranovskiy, A.G., Babayeva, N.D., Zhang, Y., Gu, J., Suwa, Y., Pavlov, Y.I., Tahirov, T.H. Mechanism of Concerted RNA-DNA Primer Synthesis by the Human Primosome. *J. Biol. Chem.*, **2016**, *291*, 10006-10020.

19. Sauguet, L., Klinge, S., Perera, R.L., Maman, J.D., Pellegrini, L. Shared active site architecture between the large subunit of eukaryotic primase and DNA photolyase. *PloS One*. **2010**, *5*, e10083.

20. Vaithiyalingam, S., Warren, E.M., Eichman, B.F., Chazin, W.J. Insights into eukaryotic priming from the structure and functional interactions of the 4Fe-4S cluster domain of human DNA primase. *Proc. Natl. Acad. Sci. USA*., **2010**, *107*, 13684-13689.

21. Boal, A.K., Yavin, E., Lukianova, O.A., O'Shea, V.L., David, S.S., Barton, J.K. DNA-Bound Redox Activity of DNA Repair Glycosylases Containing [4Fe-4S] Clusters. *Biochemistry*, **2005**, *44*, 8397-8407.

22. Sontz, P.A., Mui, T.P., Fuss, J.O., Tainer, J.A., Barton, J.K. DNA charge transport as a first step in coordinating the detection of lesions by repair proteins. *Proc. Natl. Acad. Sci. USA*, **2012**, *109*, 1856-1861.

23. Plekan, O., Feyer, V., Richter, R., Coreno, M., Prince, K.C. Valence photoionization and photofragmentation of aromatic amino acids. *Molecular Physics*., **2008**, *106*, 1143-1153.

24. Gray, H.B., Winkler, J.R. Electron flow through metalloproteins. *Biochim. Biophys. Acta, Bioenerg.*, **2010**, *1797*, 1563-1572.

25. Pheeney, C.G., Arnold, A.R., Grodick, M.A., Barton, J.K. Multiplexed electrochemistry of DNA-bound metalloproteins. *J. Am. Chem. Soc.*, **2013**, *135*, 11869-11878.

26. Slinker, J. D., Muren, N. B., Gorodetsky, A. A., Barton, J. K. Multiplexed DNA-modified electrodes. *J. Am. Chem. Soc.*, **2010**, *132*, 2769-2774.

27. Slinker, J.D., Muren, N.B., Renfrew, S.E., Barton, J.K. DNA charge transport over 34 nm. *Nature Chem.* **2011**, *3*, 228-233.

28. Cunningham, R.P., Asahara, H., Bank, J.F., Scholes, C.P., Salerno, J.C., Surerus, K., Munck, E., McCracken, J., Peisach, J., Emptage, M.H. Endonuclease III is an iron-sulfur protein. *Biochemistry*, **1989**, *28*, 4450-4455.

29. Agarkar, V.B., Babayeva, N.D., Pavlov, Y.I., Tahirov, T.H. Crystal structure of the c-terminal domain of human DNA primase large subunit: implications for the primase-polymerase α switch. *Cell Cycle,* **2011**, *10*, 926-931.

30. Pettersen, E.F., et al. UCSF chimera - A visualization system for exploratory research and analysis. *J Comput Chem*, **2004**, *25*, 1605-1612.

31. Holt, M.E., Salay, L.E., Chazin, W.J. A Polymerase with Potential: The Fe-S Cluster in Human DNA Primase. *Methods in Enzymology*, **2017**, *595*, 361-390.

32. Pape, T., Schneider, T.R. HKL2MAP: a graphical user interface for macromolecular phasing with SHELX programs. *J Appl Crystallogr*., **2004**, *37*, 843-844.

33. Perrakis, A., Sixma, T.K., Wilson, K.S., Lamzin, V.S. wARP: Improvement and extension of crystallographic phases by weighted averaging of multiple-refined dummy atomic models. *Acta Crystallogr D,* **1997**, *53*, 448-455.

34. Adams, P.D., et al. PHENIX: a comprehensive Python-based system for macromolecular structure solution. *Acta Crystallogr D Biol Crystallogr.,* **2010**, *66*, 213-221.

35. Emsley, P., Lohkamp, B., Scott, W.G., Cowtan, K. Features and development of Coot. *Acta Crystallogr D Biol Crystallogr*, **2010**, *66*, 486-501.

36. Otwinowski, Z., Minor, W. Processing of X-ray diffraction data collected in oscillation mode. *Methods Enzymol,* **1997**, *276*, 307-326.

37. Mccoy, A.J., et al. Phaser crystallographic software. J *Appl Crystallogr,* **2007**, *40*, 658-674.

38. Ji, H., Platts, M.H., Dharamsi, L.M., Friedman, K.L. Regulation of Telomere Length by an N-Terminal Region of the Yeast Telomerase Reverse Transcriptase. *Mol Cell Biol,* **2005**, *25* 9103-9114.

39. Scherer, S., David R.W. Replacement of chromosome segments with altered DNA sequences constructed *in vitro*." *Proc. Natl. Acad. Sci. USA*, **1979**, *76*, 4951-4955.

40. Ricke, R. M., Bielinsky, A.K. A conserved Hsp10-like domain in Mcm10 is required to stabilize the catalytic subunit of DNA polymerase-alpha in budding yeast. *J Biol Chem*, **2006**, *281*, 18414-18425.

41. Sikorski, R. S., Hieter, P. A system of shuttle vectors and yeast host strains designed for efficient manipulation of DNA in *Saccharomyces cerevisiae*. *Genetics*, **1989**, *122*, 19-27.

42. Warrens, A. N., Jones, M.D., Lechler, R.I. Splicing by overlap extension by PCR using asymmetric amplification: an improved technique for the generation of hybrid proteins of immunological interest. *Gene*, **1997**, *186*, 29-35.

43. Longtine M.S., McKenzie, A., Demarini, D.J., Shah, N.G., Wach, A., Brachat, A., Philippsen, P., Pringle, J.R. Additional modules for versatile and economical PCR-based gene deletion and modification in *Saccharomyces cerevisiae*. *Yeast*, **1998**, *14*, 953-961.

44. Winkler, J.R., Gray, H.B. Long-range electron tunneling. *J. Am. Chem. Soc.*, **2014**, *136*, 2930-2939.

45. Bartels, P.L., Zhou, A., Arnold, A.R., Nunez, N.N., Crespilho, F.N., David, S.S., Barton, J.K. Electrochemistry of the [4Fe4S] Cluster in Base Excision Repair Proteins: Tuning the Redox Potential with DNA. *Langmuir.*, **2017**, *33*, 2523-2530.

46. Grodick, M.A., Muren, N. B., Barton, J. K., DNA charge transport within the cell. *Biochemistry*, **2015**, *54*, 962-973.

47. Boal, A.K., Genereux, J.C., Sontz, P.A., Gralnick, J.A., Newman, D.K., Barton, J.K. Redox signaling between DNA repair proteins for efficient lesion detection. *Proc. Natl. Acad. Sci. U. S. A.*, **2009**, *106,* 15237-15242.

48. Mui, T.P., Fuss, J.O., Ishida, J.P., Tainer, J.A., Barton, J.K. ATP-Stimulated, DNA-Mediated Redox Signaling by XPD, a DNA Repair and Transcription Helicase. *J. Amer. Chem. Soc.* **2011**, *133*, 16378-16381.

49. Grodick, M.A., Segal, H.M., Zwang, T.J., Barton, J.K. DNA-Mediated Signaling by Proteins with 4Fe-4S Clusters Is Necessary for Genomic Integrity. *J. Amer. Chem. Soc.* **2014**, *136*, 16470-16478.

50. McDonnell, K.J.,* Chemler, J.A.,* Bartels, P.L.,* O'Brien, E., Marvin, M.L., Ortega, J., Stern, R.H., Raskin, L., Li, G., Sherman, D.H., Barton, J.K., Gruber, S.B. A Novel Human MUTYH Variant Causing Colonic Polyposis through Redox Degradation of the $[4Fe4S]^{2+}$ Cluster. Nature Chemistry, **2018**, in press.

51. Imlay, J.A. Iron-sulphur clusters and the problem with oxygen. *Molecular Microbiology*. **2006**, *59*, 1073-1082.

52. Francesconi, S., Longhese, M.P., Piseri, A., Santocanale, C., Lucchini, G., Plevani, P. Mutations in conserved yeast DNA primase domains impair DNA replication *in vivo*. *Proc. Natl. Acad. Sci. USA*, **1998**, *88*, 3877-3881.

53. Foiani, M., Santocanale, C., Plevani, P., Lucchini, G. A single essential gene, PRI2, encodes the large subunit of DNA primase in *Saccharomyces cerevisiae*. *Mol. Cell Biol.*, **1989**, *9*, 3081-3087.

54. DeRosa, M.C., Crutchley, R.J. Photosensitized singlet oxygen and its applications. *Coordination Chemistry Reviews*, **2002**, *233-234*, 351-371.

55. Prelich, G. Suppression mechanisms: themes from variations. *Trends in Genetics*, **1999**, *15*, 261-266.

56. Yavin, E., Boal, A.K., Stemp, E.D.A., Boon, E.M., Livingston, A.L., O'Shea, V.L., David, S.S., Barton, J.K. Protein-DNA Charge Transport: Redox Activation of a DNA Repair Protein by Guanine Radical. *Proc. Nat. Acad. Sci.USA*, **2005**, *102*, 3546-3551.

57. Tse, E.C.M., Zwang, T.J., Barton, J.K. The Oxidation State of [4Fe4S] Clusters Modulates the DNA-Binding Affinity of DNA Repair Proteins. *J. Am. Chem. Soc*., **2017**, *139*, 12784-12792..

58. Johansson, E., Majka, J., Burgers, P.M.J. Structure of DNA Polymerase δ from *Saccharomyces cerevisiae*. *J. Biol. Chem*, **2001**, *276*, 43824-43828.

59. Baranovskiy, A.G., Babayeva, N.D., Zhang, Y., Blanco, L., Pavlov, Y.I., Tahirov, T.H. Comment on "The [4Fe4S] cluster of human DNA primase functions as a redox switch using DNA charge transport." *Science*, **2017**, *357*, 6348.

Chapter 5: A human MUTYH variant linking colonic polyposis to redox degradation of the [4Fe4S]$^{2+}$ cluster

Adapted from: McDonnell, K.J.; Chemler, J.A.; Bartels, P.L.; O'Brien, E.; Marvin, M.L.; Ortega, J.; Stern, R.H.; Raskin, L.; Li, G.; Sherman, D.H.; Barton, J.K.; Gruber, S.B. A Human MUTYH Variant Linking Colonic Polyposis to Redox Degradation of the $[4Fe4S]_{2+}$ Cluster. *Nature Chemistry*, **2018**, in press.

P. Bartels carried out all electrochemistry and UV-visible, circular dichroism, and EPR spectroscopy. **E. O'Brien assisted with protein preparation for electrochemistry, electrochemistry. experiments, and DNA substrate preparation.** K. McDonnell and J. Chemler identified the C306W mutation, purified proteins, and carried out characterization of the latter (activity assays, biolayer interferometry, and iron quantification).

Introduction

In cells sustaining oxidative damage, genomic guanine residues are frequently oxidized to 8-oxo-7,8-dihydroguanine (8-oxoG). Unlike guanine, 8-oxoG can pair effectively with either cytosine or adenine bases, with potentially serious mutagenic consequences (*1*). A DNA glycosylase conserved among species from bacteria to humans, known in humans as MUTYH, removes adenine from these 8-oxoG:A mispairs as part of the base excision repair pathway. In humans, germline *MUTYH* mutations that impair enzymatic activity lead to an increase in G:C>T:A transversions that have been shown to result in missense mutations in the *APC* tumour suppressor gene in epithelial cells lining the colon. Mutations in *APC* are the first recognizable genetic events that initiate malignant transformation of normal colonic epithelia into polyps, specifically adenomas, before the acquisition of other mutations that complete the neoplastic conversion sequence from normal tissue through adenoma to carcinoma (*2*). Bi-allelic mutations of *MUTYH* give rise to the autosomal recessive cancer genetic syndrome, *MUTYH*-associated polyposis (MAP) (*3*). Typically, by their fifth decade, MAP patients develop 10–100 colonic polyps (*4*). *MUTYH* variants are common, with a prevalence of at least 1–2% among western Europeans (*5*), and the colorectal cancer risk increases nearly 2- and 100-fold for mono- and bi-allelic *MUTYH* mutations, respectively (*6*).

The MUTYH protein comprises three major regions (*7*): the N terminus, which contains the endonuclease III six-helix barrel catalytic domain, the interdomain connector (IDC) and the C terminus, corresponding to protein residues 1–306, 315–366 and 368–500, respectively. The MUTYH N terminus contains a [4Fe4S] cluster ligated by four cysteine residues; although metabolically expensive, the cluster is conserved in MutY homologues across all domains of life (*8*). A rare exception is the yeast endonuclease III homologue Ntg1, which has no cluster, but

one is present in a second yeast homologue (Ntg2) (*9*). Indeed, the only organisms lacking a cluster in any MutY homologue are specialized anaerobes subject to lower levels of oxidative stress (*10*). Studies performed on *Escherichia coli* MutY and its homologue endonuclease III (EndoIII) have demonstrated that the cluster is unnecessary for structural integrity and is largely redox-inert in solution (*11*, *12*). However, when *E. coli* MutY and EndoIII were incubated on duplex DNA-modified gold electrodes, a reversible redox signal centred near 80 mV versus normal hydrogen electrode (NHE) was observed for both proteins, and was identified as the [4Fe4S] couple, an assignment supported by electron paramagnetic resonance (EPR) spectroscopy (*13*). Subsequent experiments with EndoIII on a graphite electrode in the presence and absence of DNA revealed that binding to the negatively charged DNA backbone shifts the redox potential of these proteins by about −200 mV, activating the cluster towards oxidation and resulting in a significant increase in binding affinity of the oxidized [4Fe4S] form of the enzyme relative to the native [4Fe4S] form (*14*).

These studies have led to a model in which [4Fe4S] base excision repair (BER) proteins with similar DNA-bound redox potentials use reversible redox exchanges to signal to one another across the genome, taking advantage of the unique ability of DNA to conduct charge across the π-stacked base pairs (bps) in a process known as DNA-mediated charge transport (DNA CT) (*15, 16*). DNA CT has both a very shallow distance dependence and an exquisite sensitivity to even slight disruptions in base pair stacking, making it an ideal lesion reporter. In our CT signalling model, oxidative stress generates highly reactive species, such as guanine radicals, which can then oxidize proteins including MutY (*17*). If another [4Fe4S] protein is bound at a distal site and the intervening DNA is undamaged, it can send an electron through the DNA to reduce the first protein. Following reduction, the protein's affinity for DNA is decreased

and the protein dissociates to another region of the genome, while the oxidized protein remains bound. In the presence of a lesion, DNA CT is impaired, and the oxidized protein will remain bound and diffuse towards the site of damage. Thus, DNA CT constitutes a means for [4Fe4S] proteins to scan a vast genome on a relevant timescale and redistribute in the vicinity of lesions. In the case of *E. coli*, long-range signalling by DNA CT has been estimated to reduce the damage search time from 45 min to 10 min or less (*18*).

In the present study, we describe a novel MUTYH variant, p.C306W, identified in a patient exhibiting colonic polyposis. Using an *E. coli* overexpression system, this variant was generated together with wild-type (WT) MUTYH and the well-characterized pathologic variants Y179C and G396D. We used electrochemistry, UV– vis and EPR spectroscopy to compare the redox properties of these four MUTYH variants. Enzymatic activity and DNA binding parameters were determined using glycosylase assays and biolayer interferometry (BLI), respectively. Together, these results provide strong evidence for a primary function of the [4Fe4S] cluster in DNA-mediated redox signalling and establish MUTYH C306W as a pathogenic variant, enhancing our understanding of the role of the [4Fe4S] cluster in human disease.

Materials and Methods

Determination of Trans Chromosomal Configuration of MUTYH Gene Variants

Germline DNA was amplified using the polymerase chain reaction (PCR) to generate a 935 base pair amplicon that includes the open reading frame positions c.918C>G (p.C306W) and c.1187G>A (p.G396D). The PCR reaction used the forward primer 5′-CCA GGA GAT TTC AAC CAA GC-3′ and the reverse primer 5′ -AAG GGT CAA GGG GTT CAA AT-3′. The c.1187G>A mutation creates a unique BglII restriction endonuclease site which allowed

generation of a 719 base pair fragment from the parent 935 base pair amplicon. The shorter 719 base pair fragment was resolved using agarose gel electrophoresis, purified and its DNA sequence determined (University of Michigan (U-M) Sequencing Core) to establish the identity of the c.918 position.

Identification of APC gene G:C → T:A Transversions

Tumor DNA was extracted from a formalin-fixed, paraffin-embedded colonic adenoma originating from the proband using the RecoverAll Total Nucleic Acid isolation kit (Ambion). A portion of the mutation cluster region of the *APC* gene (*19*) was amplified using PCR with the forward primer 5′-TGC CAC AGA TAT TCC TTC ATC A-3′ and the reverse primer 5′-CAT GGT TTG TCC AGG GCT AT-3′. The PCR product was subsequently sequenced (U-M Sequencing Core).

Cloning of wild type and Mutant MUTYH expression plasmids

A plasmid containing the open reading frame for the beta3 isoform of *MUTYH* (NM_001048174.1) was obtained from OriGene (Catalog #: RC201376-OR, Rockville, MD.) and used as a template for the cloning of derivative constructs. Mutant *MUTYH* construct synthesis was accomplished using PCR-based site-directed mutagenesis of wild type MUTYH. The wild type and mutants were then cloned as maltose binding protein (MBP) fusions into pMCSG19 (*20*) between the KpnI and XbaI restriction sites to increase protein solubility (*21*). The plasmids were further modified by removing the first fourteen codons encoding the mitochondrial recognition sequence, which alleviated heterologous protein toxicity. Furthermore, to decrease the capture of truncated heterologous protein, the N-terminus His_6 tag located between the MBP sequence and the TEV cleavage site was removed and a C-terminus His_{10} tag was attached with a flexible $(SG)_7$ linker to increase solvent exposure.

Preparation of Protein

Heterologous MUTYH proteins in *Escherichia coli* strain BL21(DE3) were initially purified in accordance with previously published protocols using nickel affinity chromatography with 1 mM DTT (*22*). To improve yields and purity, the expression plasmids were transformed into the *E. coli* expression strain for toxic proteins, BL-AI (Invitrogen) also harboring the rare codon plasmid pRARE2-CDF (*23*). One liter of fresh Terrific Broth modified with 4% glycerol and 50 μg/mL of antibiotics (ampicillin and streptomycin) in a three L baffled flask was inoculated with 25 mL of overnight cultures in the same medium. Cultures were grown at 37 ºC in a horizontal shaker at 175 rpm until the OD_{600} reached approximately 2.5. The temperature was adjusted to 15 ºC, and after 90 minutes, 0.25 mM IPTG and 0.2% arabinose were added. After 12-16 hours, cells were harvested by centrifugation, flash frozen in liquid nitrogen, and stored at -80 °C until processing. Cell pellets were thawed in an ice bath and re-suspended in 80 mL of ice cold 10% glycerol before the addition of 53 mg/mL of CelLytic Express (Sigma), one tablet of Protease Inhibitor Cocktail (Sigma) and 20 mM imidazole. The samples were clarified on a nutator for 30 minutes at 4ºC before the addition of 20 mM of β-mercaptoethanol. The crude cell lysate was passed through a 0.45 μm filter in preparation for nickel affinity chromatography. His-tagged proteins were loaded onto a 5 mL HisTrap HP column (GE Healthcare) at 2 mL/min using an AKTA Explorer FPLC instrument (GE Healthcare) at 4 ºC. The columns were first washed with 20 column volumes of 93% Buffer A (20 mM Tris-HCl, pH 7.4, 1 M NaCl, 20 mM β-mercaptoethanol, 10% glycerol) and 7% Buffer B (20 mM Tris-HCl, pH 7.4, 100 mM NaCl, 500 mM imidazole, 10% glycerol) and the proteins were eluted using a 7-100% Buffer B gradient over 10 column volumes. Fractions containing MBP-MUTYH protein (as determined by SDS-PAGE), were pooled. Typical yields of purified protein for MBP-MUTYH wild type,

Y179C and G396D were between 10-20 mg from one liter cultures and 0.5-1.5 mg of soluble protein was obtained for MUTYH p.C306W. Monomeric protein was obtained by size exclusion chromatography using a Superdex 200 10/300 GL column (GE Healthcare) in Buffer C (20 mM Tris-HCl, 100 mM NaCl, 1 mM DTT, 10% glycerol). Fractions eluting near the expected molecular weight (104 kD) were collected, partitioned into aliquots, flash frozen in liquid nitrogen and stored at -80 ºC until further use.

DNA Substrates for Glycosylase and Binding Assays

All oligonucleotides (Integrated DNA Technologies, Coralville, Iowa) were purchased PAGE purified. Duplexes were obtained by heating 50 µl 50 µM complementary strands at 85 ºC then decreasing the temperature by 0.5 ºC every 30 seconds until attaining room temperature. The FAM labelled 8-oxoG:A duplex used in the DNA glycosylase assay consisted of 5′-ACA AAG AAC TTA TAG CTC CTC CTT GAG CAC ACA GAG GTG TTC GAT GTA GTT G/A/C GCA GGA CGG GTT CAG T/6-FAM/-3′ and 3′-TGT TTC TTG AAT ATC GAG GAG GAA CTC GTG TGT CTC CAC AAG CAT GAT CAA C/8oxoG/G CGT CCT GCC CAA GTC A-5′. The biotin labeled 8-oxoG:A duplex used in the binding assay consisted of 5′-/BiotinTEG/AC AAA GAA CTT ATA GCT CCT CCT TGA GCA CAC AGA GGT GTT CAT GTA GTT G/A/C GCA GGA CGG GTT CAG T-3′ and the 8-oxoG oligomer.

DNA Glycosylase Assay

The DNA glycosylase assay was adapted as previously reported (*22,24,25*). The activity was evaluated by providing 10 nM of DNA substrate containing a single 8-oxoG:A mismatch to wild type or mutant MBP-MUTYH proteins (0-1000 nM) at 37ºC in a buffer (20 mM Tris-HCl, pH 8.0, 100 mM NaCl, 1 mM EDTA, 1 mM DTT, and 0.1 mg/mL BSA). Reactions were

quenched after 1 hour with 80 mM NaOH followed by heating the samples to 90 ºC for 4 minutes, cooled and then diluted with three volumes of formamide spiked with GeneScan™ 500 LIZ™ Size Standard (Invitrogen). DNA fragmentation was determined employing capillary electrophoresis (U-M DNA Sequencing Core, ABI 3730 DNA Analyzer). Traces were analyzed using Peak Scanner^{TM} Software (version 1.0, Applied Biosystems). The percent of excised DNA was calculated as the ratio of the 6-FAM peak area migrating at 44 oligonucleotides to the total peak area (at 44 and 66 oligonucleotides).

Multiple Turnover assay: Active Site Titration

The multiple turnover assay was adapted as previously reported (*22,24,25*). Reactions were analyzed for scission of 10 nM FAM-labeled 8-oxoG duplex DNA after the addition of MUTYH protein. The total protein concentrations, selected to give a burst amplitude in a detectible range, were 25, 2670, 500 and 25 nM of MUTYH wild type, Y179C, C306W and G396D, respectively. Samples were drawn over a 20 minute time course and processed as described above. The cleaved product concentration, [P], was fitted with Equation 1 to determine the amplitude of the burst (A_0), k_B (rate constant during the burst phase) and k_L (rate constant for the linear phase).

Equation 1: $[P] = A_0[1-\exp(-k_Bt)]+k_Lt$

The percent of active protein was calculated as a ratio of the A_0 to total protein concentration.

Binding Kinetics (Biolayer Interferometry)

All biolayer interferometry measurements were made on an Octet RED instrument (Pall ForteBio, Menlo Park, CA) using streptavidin (SA) biosensors (26). Assays were performed in 96-well black microplates at 25 ºC and 1000 rpm. All volumes were 200 µL. All proteins were

buffer exchanged using PD-10 columns (GE Healthcare) pre-equilibrated with PBS then serial diluted (25, 12.5, 6.25, 3.125, 0.78125 nM) into working volumes with 1X Kinetics Buffer (Pall FortBio;10 mM Phosphate, pH 7.4, 150 mM NaCl, 0.02% Tween-20, 1 mg/mL BSA). The biotinylated duplex DNA was first immobilized onto the SA biosensors for 300 seconds and then equilibrated in 1X Kinetics Buffer for 300 seconds. Protein association was performed for 150-300 seconds followed by dissociation into 1X Kinetics Buffer for 900 seconds. A reference sensor with immobilized dsDNA was subtracted from each data set. Shift data was analyzed with ForteBio's Analysis software (version 7.1). Kinetic parameters k_{on} and k_{off} and affinity (K_D) were determined from a global non-linear regression of association and dissociation binding kinetics using a 1:1 Langmuir binding model.

Fe Elemental Analysis

The presence of elemental Fe within MUTYH protein samples was determined using a Thermo Scientific Element2 ICP-HRMS (*27*). Purified proteins were dialyzed overnight to remove glycerol and to allow equilibration with blank buffer (20 mM Tris-HCl, pH 7.5, 100 mM NaCl and 1 mM DTT) using a 10K MWCO Slide-A-Lyzer dialysis cassettes (Thermo Scientific).

DNA synthesis and purification for electrochemistry

Thiol, FA, and OG modified DNA strands were prepared on an automated DNA synthesizer (Applied Biosystems) and purified by HPLC on a PLRPS column (Agilent) as described in previously published protocols (*28*); unmodified strands were ordered from IDT and purified by HPLC. DNA purification from solid-phase synthesis is performed as described in **Chapter 2**. For electrochemistry, 50 μL 50 μM complementary DNA strands were degassed and annealed in storage buffer (5 mM sodium phosphate, pH 7.0, 50 mM NaCl) in equimolar

amounts by a 5 minute incubation at 95°C followed by slow cooling (1.5 hours) to RT on a thermocycler. Well-matched (WM) duplex DNA, DNA with an FA:OG lesion, and substrates containing an abasic site were all prepared in this way. Duplex sequences were as follows:

WM DNA

5′ – ACT GAA CCC GTC CTG GCT CAA CTA CAT GAA CAC CTC – 3′
3′ – TGA CTT GGG CAG GAC GCA GTT GAT GTA CTT GTG GAG – 5′ – C6 Thiol

FA:OG DNA

5′ – ACT GAA CCC GTC CTG GC**OG** CAA CTA CAT GAA CAC CTC – 3′
3′ – TGA CTT GGG CAG GAC GC**FA** GTT GAT GTA CTT GTG GAG – 5′ – C6 Thiol

Abasic DNA

5′ – ACT GAA CCC GTC CTG GCT CAA CTA CAT GAA C**Ab**C CTC – 3′
3′ – TGA CTT GGG CAG GAC GCA GTT GAT GTA CTT GTG GAG – 5′ – C6 Thiol

OG = 8-oxoguanine, FA = 2′-fluoroadenine, Ab = abasic site

Electrochemistry on DNA self-assembled monolayers (SAMs)

Electrochemical characterization of MUTYH was carried out on a multiplexed chip platform consisting of 16 individually-addressable gold electrodes separable into four quadrants (*28*). Self-assembled DNA monolayers were formed by adding 25 μL 25 μM duplexed DNA in phosphate buffer (5 mM sodium phosphate, pH 7.0, 50 mM NaCl) to each quadrant of the chip and incubating overnight. After monolayer formation, gaps in the film were eliminated by backfilling for 45 minutes at RT with 1 mM 6-mercapto-1-hexanol in phosphate buffer with 5% glycerol. The surface was then extensively rinsed in phosphate buffer, followed by protein storage buffer (described below). To compare different monolayer morphologies, DNA was incubated in phosphate buffer as described to generate low-density DNA monolayers (surface coverage of ~15 pmol/cm^2) or in the presence of 100 mM $MgCl_2$ to form high-density

monolayers (surface coverage of ~40 pmol/cm^2) (*29*,*30*). Bulk electrolysis experiments were performed using gold rod electrodes in a custom-made electrochemical cell. Experiments were carried out in air unless otherwise noted; anaerobic experiments were performed in a glove bag (Coy) under a 95% N_2/5% H_2 atmosphere. Reagent storage, surface preparation, and preparation for anaerobic electrochemistry are described in detail in **Chapter 2**.

MUTYH concentration was determined by UV-vis, using an extinction coefficient of 17000 $M^{-1}cm^{-1}$ at 410 nm to determine [4Fe4S] cluster concentration and 102330 $M^{-1}cm^{-1}$ at 280 nm to determine total protein concentration; cluster loading was determined by dividing [4Fe4S] cluster concentration by total protein concentration, and was typically around 15%. Initial characterization was carried out in Tris storage buffer (20 mM Tris, pH 7.4, 100 mM NaCl, 1 mM DTT, 10% glycerol v/v), while later electrochemical and spectroscopic experiments used a HEPES buffer (20 mM HEPES, pH 7.4, 100 mM KCl, 1 mM DTT, 0.5 mM EDTA, 10% glycerol v/v). MUTYH was transferred into HEPES using Amicon 10 kDa MW cutoff spin tubes (Millipore Biomedicals) at 4^{o}C.

Once in an appropriate buffer, MUTYH was added to a multiplexed chip and incubated for several hours with cyclic and square wave voltammetry (CV and SQWV, respectively) scans taken once per hour. In typical experiments, CV scans were taken in a potential window of -0.188 to 0.412 V vs NHE at a scan rate of 100 mV/s, while SQWV scans were taken at a frequency of 15 Hz with 0.025 V amplitude. To plot the scan rate dependence of CV current, scans in the same window were carried out at 20, 50, 80, 100, 200, 500, 750, and 1000 mV/s. All experiments were performed on a CH Instruments potentiostat with a Ag/AgCl reference in 3 M NaCl and Pt wire counter electrode. Potentials were converted to NHE by adding 212 mV to the measured potentials, accounting for both the salt concentration (209 mV according to BASi®)

and ambient temperature. (*31*) Bulk electrolysis was carried out at 0.412 mV versus NHE, and yields were estimated by subtracting the total charge passed with only buffer present from that passed when MUTYH was included. All buffer components were purchased from Sigma-Aldrich, the Ag/AgCl reference electrode was purchased from BASi®, and the Pt wire counter electrode was purchased from the Kurt J. Lesker Company. Ag/AgCl reference and Pt counter electrode setup constructions are described in **Chapter 2**.

EPR spectroscopy

Continuous wave X-band EPR was carried out at 10 K on a Bruker EMX instrument. Samples were prepared aerobically, using 150 μL 5 – 15 μM MUTYH in parallel with a storage buffer blank. Spectra were taken from the summation of 9 sweeps at 12.88 mW microwave power, 2 G modulation amplitude, and a receiver gain of 5.02 $x10^3$.

Results

Identification and functional deficiencies of a novel MUTYH variant

A novel germline *MUTYH* variant, ~c.918C>G (p.C306W), together with the previously well-described *MUTYH* mutation ~c.1187G>A (p.G396D), were identified in a patient with colonic polyposis whose family history was significant for early-age colon cancer. The cysteine at position 306 represents one of the four cysteine residues that mediate integration of the conserved MUTYH [4Fe4S] cluster. In bacterial MutY, cluster loss is associated with decreased protein function (*12*), which suggests that in MUTYH the C306W variant may affect the integrity of the [4Fe4S] cluster and represent a pathologic mutant (**Figure 5.1** illustrates the structure of bacterial MutY and identifies corresponding residues in MUTYH).

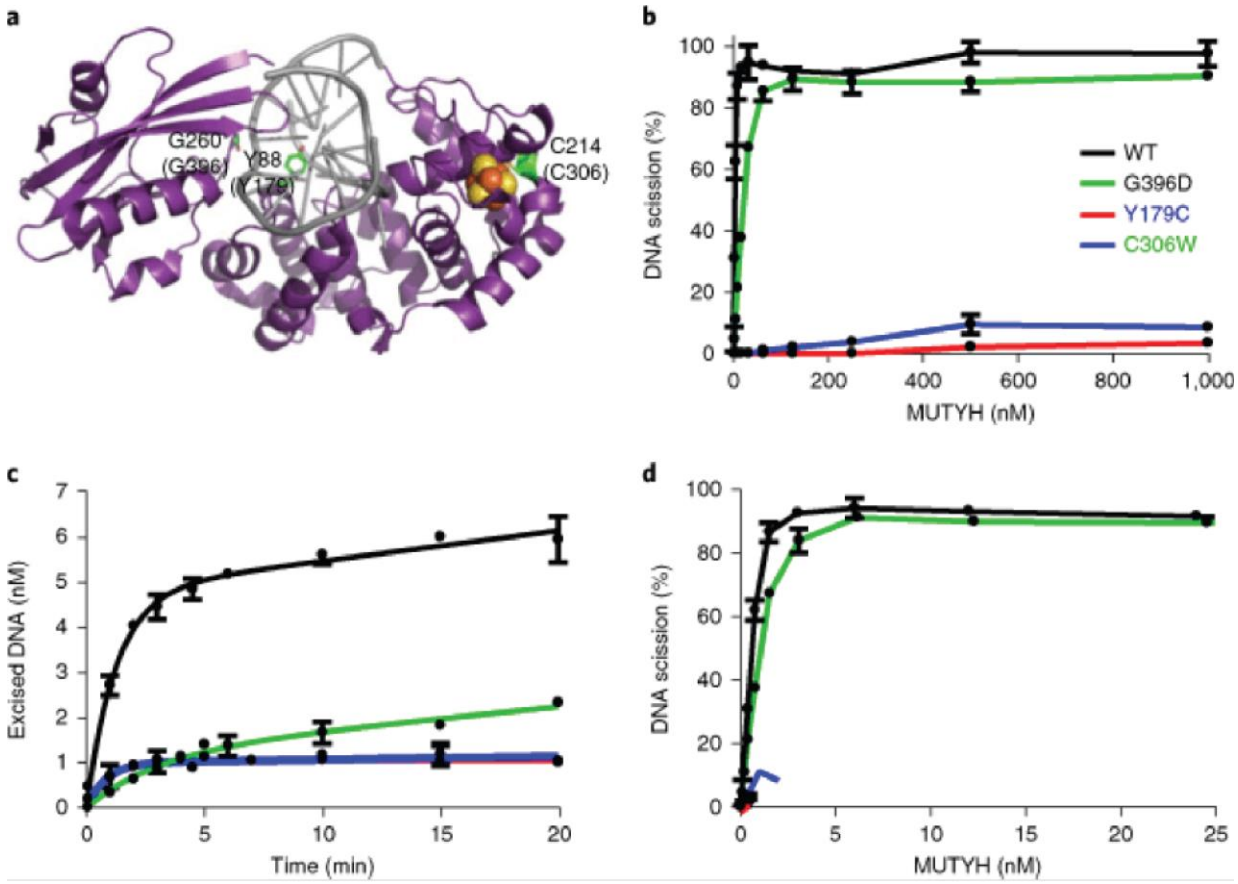

Figure 5.1 A novel human MUTYH variant, C306W, lacks glycosylase activity.a) Ribbon-model structure of MutY/DNA complex illustrating two pathogenic, well-characterized MAP-relevant residues Y179C and G396D, as well as the newly identified variant C306W. All three amino acids are conserved from bacteria to humans. Their relative positions are illustrated using a *Geobacillus stearothermophilus* MutY/DNA complex, with the corresponding residue numbers from human MUTYH isoform β3 in parentheses (structure from PDB ID 1RRQ). The novel C306W mutation occurs in one of four cysteine residues that ligate the conserved [4Fe4S] cluster in MUTYH. Black lines, wild-type MUTYH; green lines, G396D; red lines, Y179C; blue lines, C306W. All data are presented as mean + s.d., $n = 3$. b) Glycosylase assay using soluble, monomeric MUTYH. Relative to WT and G396D MUTYH, Y179 and C306 proteins demonstrate severely attenuated DNA scission activity. c) Multiple turnover reaction conditions define the concentration of active protein within a purified protein sample. The glycosylase assay was performed with sufficient MUTYH protein to generate reaction burst amplitudes (A) within the detectable range. MUTYH active fractions, A , and k and k rate constants of the excision reaction during the exponential and linear phase, respectively, were determined by fitting the data points to the equation $[P] = A\,[1 - \exp(-k\,)t] + k\,t$. d, Adenine excision activity of WT and mutant MUTYH proteins after correcting for active fractions, A . The correction for active MUTYH C306W and Y179C proteins shifted their assay concentrations below 2.5 nM.

Supporting the potential pathogenicity of the novel ~918C>G variant, we established that this variant is situated in a trans chromosomal configuration relative to the ~1187G>A *MUTYH* mutation (**Figure 5.2**) Further evidence of the pathogenic nature of the ~918C>G variant was apparent in the sequence of the *APC* gene in somatic DNA originating from a colonic adenoma from the patient. This sequencing revealed the presence of a G:C>T:A transversion in the *APC* gene, which is the hallmark genetic lesion indicative of deficient *MUTYH*-mediated DNA enzymatic repair (*2*) (**Figure 5.3**).

Four MUTYH proteins (WT, the well-characterized mutants G396D and Y179C, and the novel variant C306W) were overexpressed in *E. coli* and purified by nickel affinity chromatography. Monomeric MUTYH proteins were produced by treatment with 20 mM β mercaptoethanol, followed by size exclusion fast protein liquid chromatography with validation by UV spectroscopy (**Figures 5.4**). Relative to WT MUTYH, G396D MUTYH demonstrated a significant decrease in glycosylase activity and Y179C a severe deficiency; comparative assessment of C306W MUTYH revealed a virtual absence of activity, thus establishing its pathogenicity (**Figure 5.1 b**). The glycosylase activities of aggregated MUTYH proteins were also assessed; in these experiments C306W was similarly deficient in glycosylase activity (**Figure 5.5**).

For a more complete functional comparison of the four MUTYH variants, we conducted time-course glycosylase assays under multiple turnover conditions in order to quantitatively determine the proportion of active enzyme in each sample (*22,24*). These assays were performed using dsDNA containing an 8-oxoG:A mispair together with varying concentrations of MUTYH proteins. The experimental results demonstrate an initial burst of adenine excision activity proportional to the active fraction, A , of the protein sample (**Figure 5.1c** and **Table 5.1**). The

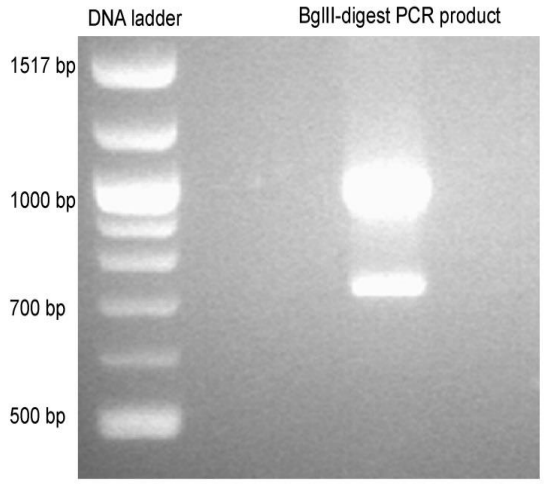

Figure 5.2. ***The c.918C>G MUTYH variant is situated trans relative to the c.1187G>A MUTYH mutation.*** The c.1187G>A (p.G396D) *MUTYH* mutation creates a unique BglII restriction enzyme site which we employed to isolate the chromosomal DNA strand containing the c.1187G>A *MUTYH* mutation. A 957 bp fragment encompassing the *MUTYH* open reading frame nucleotide positions 918 and 1187 was generated with PCR and then restriction enzyme digested with BglII. The digestion products were resolved on 1.5% agarose gel and the lower molecular weight DNA band isolated (arrow). Sequencing of the lower molecular weight band demonstrated the wildtype cytosine nucleotide at position 918 consistent with a trans configuration of the c.1187G>A and c.918C>G *MUTYH* alterations.

Normal Colonic Tissue

Colonic Adenoma

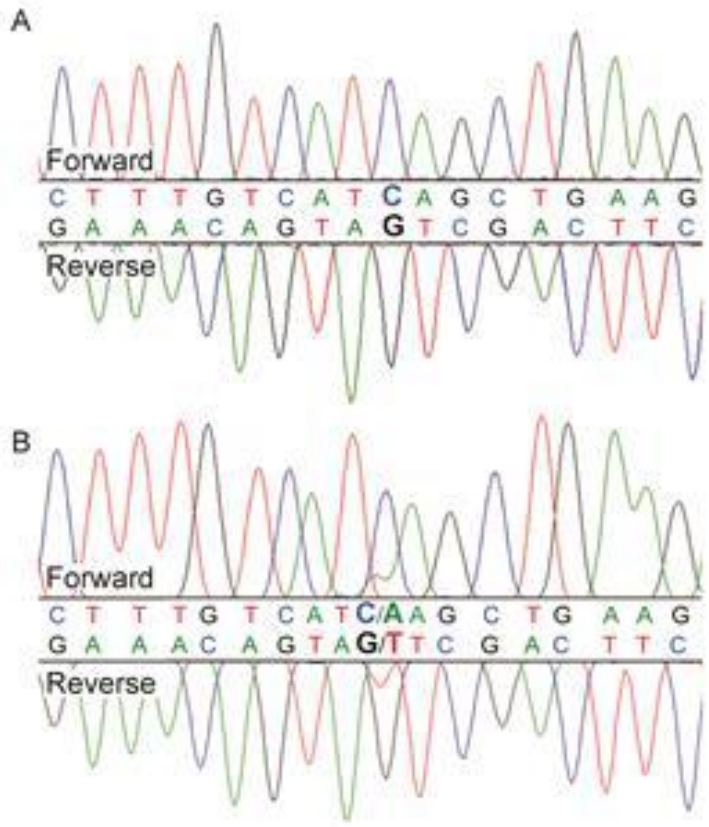

Figure 5.3. ***Trans c.1187G>A (p.G396D) and c.918C>G (p.C306W) MUTYH Mutations are Associated with the Signature G:C to T:A Transversion Distinctive of Deficient MUTYH DNA Repair.*** From one of the patient's adenomatous polyps we extracted DNA to assess for the presence of the signature G:C to T:A nucleotide transversion which results from deficient MUTYH DNA repair. The figure depicts a portion of the germline nucleotide sequence from the mutation cluster region of the APC gene (upper tracing); this sequence reveals the normal wildtype *APC* sequence. In comparison, the lower tracing depicts the forward and reverse nucleotide sequence from DNA extracted from one of the patient's colonic polyps for this same mutation cluster region of the *APC* gene; there is identified a G:C to T:A transversion (arrow) resulting in a premature stop codon in the *APC* open reading frame and pathologic APC protein product.

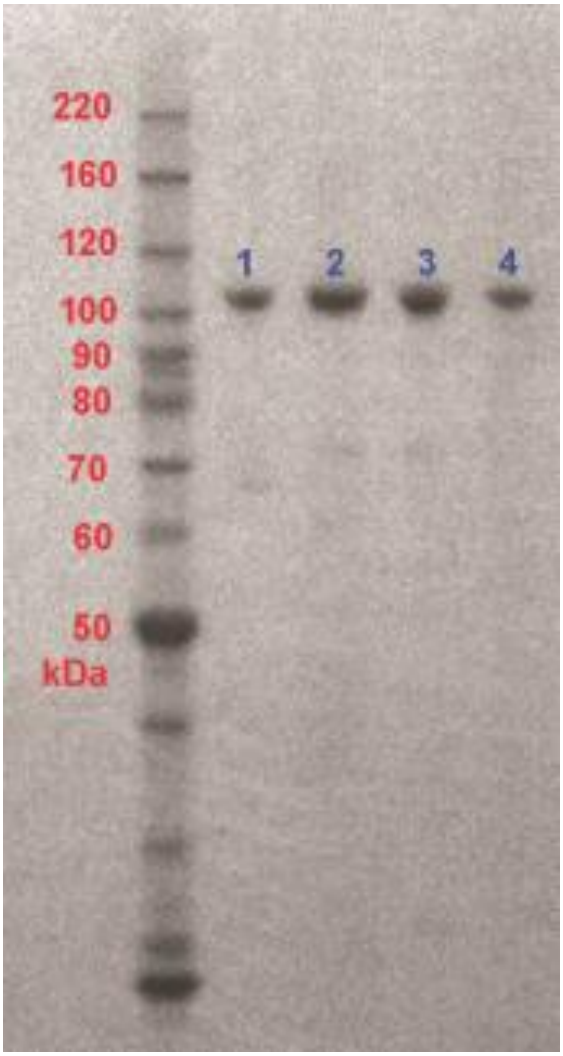

Figure 5.4. SDS-PAGE gel of purified monomeric MUTYH proteins. The left lane contains the protein molecular weight ladder. The lanes 1-4 contain 1ug of MUTYH wild type, Y179C, C306W, and G396D, respectively.

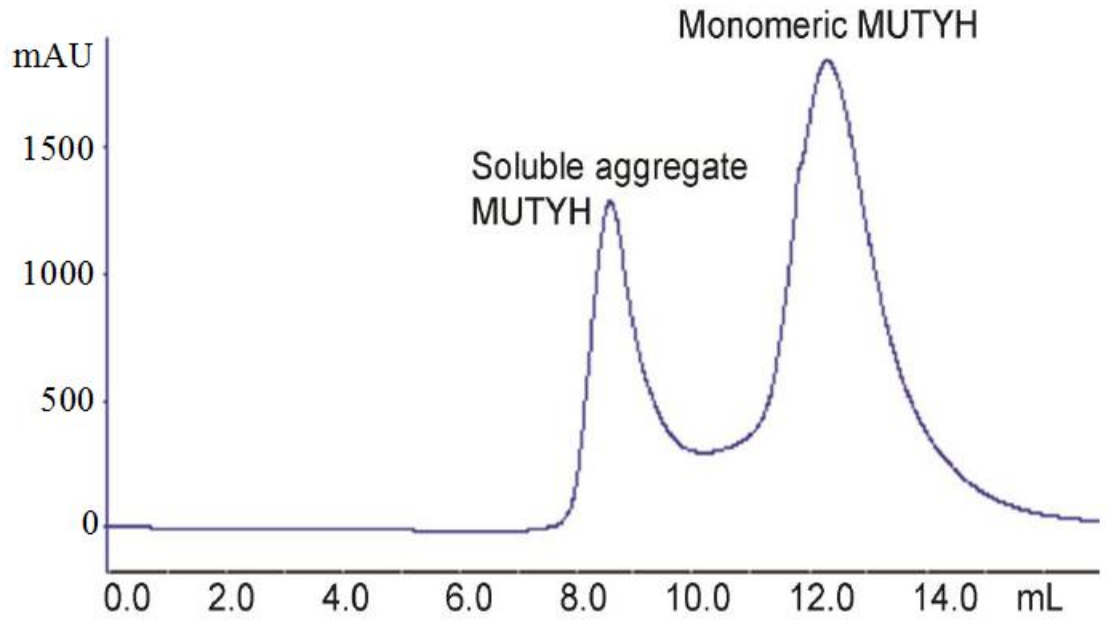

Figure 5.5. SEC-FPLC UV_{260} trace of WT MUTYH following treatment with 20 mM β-mercaptoethanol. While some soluble aggregates still occur in the void volume, the majority of the purified protein is monomeric.

excision reaction rate constants, k_B and k_L, were determined for the exponential and linear phases of the reaction, respectively (**Table 5.1**). Both WT MUTYH and G396D proteins had comparable linear rates for turnover and the highest fraction of active protein. In contrast, the

C306W MUTYH mutant was essentially devoid of adenine excision activity and Y179C had no detectable turnover. The fractions of active MUTYH were then used to correct for the total amount of protein used in the glycosylase assay, confirming that WT MUTYH and G396D mutant had comparable activities, while C306W and Y179C mutants displayed poor activity. The poor activity observed in MUTYH C306W could have two possible explanations: either that this mutant was catalytically inactive or it was unable to bind specifically to DNA (as is the case with low activity in the weakly bound Y179C).

To help distinguish between these possibilities, we used BLI (*26*) to measure the binding parameters of the MUTYH proteins. We compared the binding of WT MUTYH and the G396D, Y179C and C306W mutants to DNA containing an 8-oxoG:A mispaired duplex. **Table 5.1** summarizes the binding kinetics. Relative to WT MUTYH, the G396D and Y179C variants demonstrated increasing values of primarily due to decreased association rates. There was no detectable binding for the C306W mutant within the protein concentration range tested, suggesting that the low activity levels observed in this mutant were due primarily to ineffective DNA binding.

Together, these data demonstrate the functional deficiency and establish the pathogenicity of the C306W MUTYH variant. In bacterial MutY, [4Fe4S] cluster loss is associated with decreased protein function (*12*), which suggests that in MUTYH the C306W variant may affect the integrity of the [4Fe4S] cluster, accounting for the pathogenicity of this mutant. To assess the integrity of the [4Fe4S] cluster, iron loading of the clusters of WT

Multiple Turnover Experiment					
Enzyme ID	**[protein] (nM)**	**A_0**	**A_0/[protein]**	**k_B (min^{-1})**	**k_L (min^{-1} nM)**
Wild type	25	4.8 ± 0.2	19.20%	0.8 ± 0.1	0.07 ± 0.01
Y179C	2670	1.1 ± 0.1	0.04%	1.0 ± 0.2	0
C306W	500	1.0 ± 0.1	0.20%	1.2 ± 0.2	0.01 ± 0.01
G396D	25	1.2 ± 0.2	4.90%	0.3 ± 0.1	0.05 ± 0.01

Enzyme/DNA kinetic binding data obtained from biolayer interferometry			
Enzyme ID	**k_{on} ($M^{-1}s^{-1}$) x 10^4**	**k_{off} (10^{-4} s^{-1})**	**K_D (10^{-9} M)**
Wild type	43 ± 0.4	2.7 ± 0.03	0.6 ± 0.01
Y179C	2.9 ± 0.4	5.0 ± 0.21	17 ± 2.57
C306W	No binding		
G396D	10 ± 0.5	5.3 ± 0.12	5.2 ± 0.27

Top: Deterimination of rate constants from multiple turnover experiment.

Bottom: Determination of binding constants with BLI. k_B and $k_L$are the association and dissociation rates and K_D is the equilibrium dissociation constant.

Data show mean + s.d., n= 3.

Table 5.1 Determination of rate and binding constants.

MUTYH and mutants Y179C, G396D and C306W were compared by quantifying the iron present in each sample using inductively coupled plasma–high-resolution mass spectrometry (ICP-HRMS) for elemental analysis (*27*). Consistent with disruption of the Fe–S cluster loop in the C306W variant, this protein exhibited substantially lower iron content relative to the other MUTYH proteins tested (**Table 5.2**). However, UV–vis spectra taken from disrupted aggregates of all four variants distinctly showed the broad peak centred at 410 nm that is characteristic of a [4Fe4S] cluster, indicating that MUTYH C306W is still capable of binding an intact cluster and further suggesting that loading by cellular machinery is still effective. In addition, circular dichroism (CD) spectra of WT MUTYH and the C306W mutant were indistinguishable, confirming that no global conformational changes were induced by this mutation (**Figure 5.6**). Thus, the low cluster content, as measured by ICP-HRMS, was instead tentatively associated with decreased protein stability in this mutant, and subsequent electrochemical and EPR experiments were used to more reliably examine the [4Fe4S] cluster properties in detail.

DNA-bound electrochemistry of WT and mutant MUTYH

Having observed that MUTYH C306W appeared to incorporate less iron despite its capacity to bind an intact cluster, we next assessed its redox properties on DNA-modified gold electrodes alongside WT, G396D and Y179C MUTYH (**Figure 5.7**). We reasoned that electrochemical analysis would aid these studies for two reasons: first, access to highly purified WT MUTYH allowed us to determine if the human protein behaved in a manner similar to its bacterial counterpart, and, second, electrochemical monitoring would provide an effective way to assess the stability of MUTYH C306W over time. Specifically, we expected that the predicted instability of MUTYH C306W would result in electrochemical signals that were either smaller than WT or less stable over time.

Enzyme ID	[Fe] (µM)	[MUTYH] (µM)	% Ratio 4Fe/ Enzyme
Wild type	6.42 ± 0.32	1.36	115%
Y179C	6.40 ± 0.32	1.65	95%
C306W	0.78 ± 0.03	1.63	9%
G396D	6.59 ± 0.33	1.62	99%
Buffer	0.17 ± 0.03		

Data show mean ± s.d., n= 3.

Table 5.2. Elemental iron analysis of MUTYH proteins by ICP-HRMS.

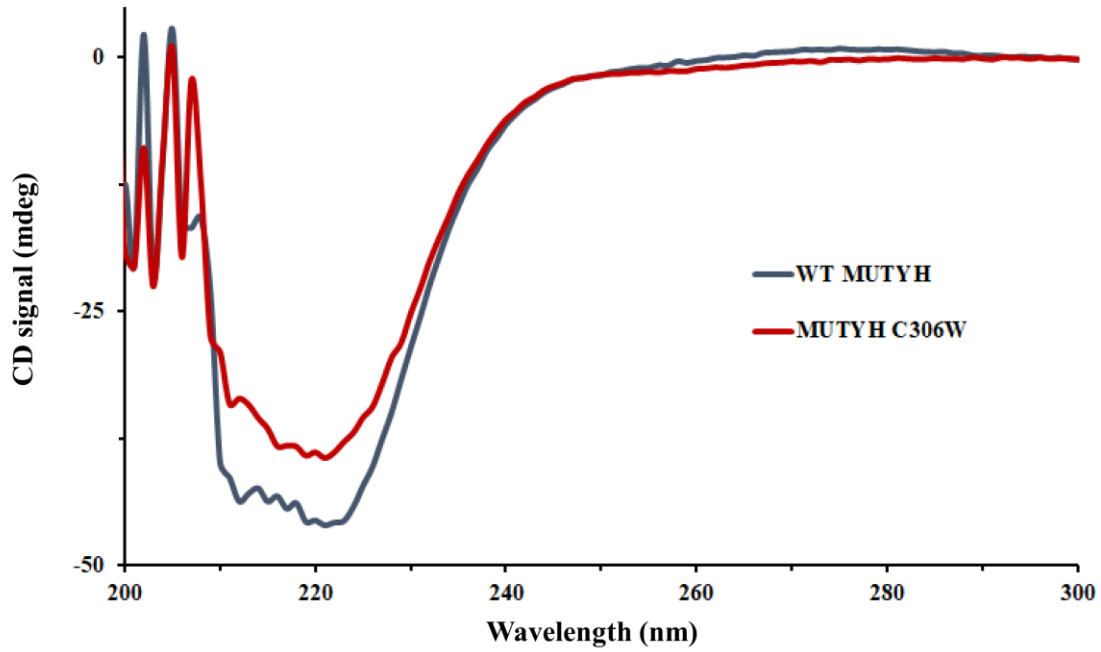

Figure 5.6. Circular dichroism (CD) spectra of WT MUTYH and MUTYH C306W. The similarity in spectra suggest that the C306W mutation does not result in significant global structural perturbations. These experiments were performed in HEPES storage buffer (30 mM HEPES, 100 mM KCl, 1 mM DTT, 0.5 mM EDTA, 10% glycerol v/v, pH 7.4).

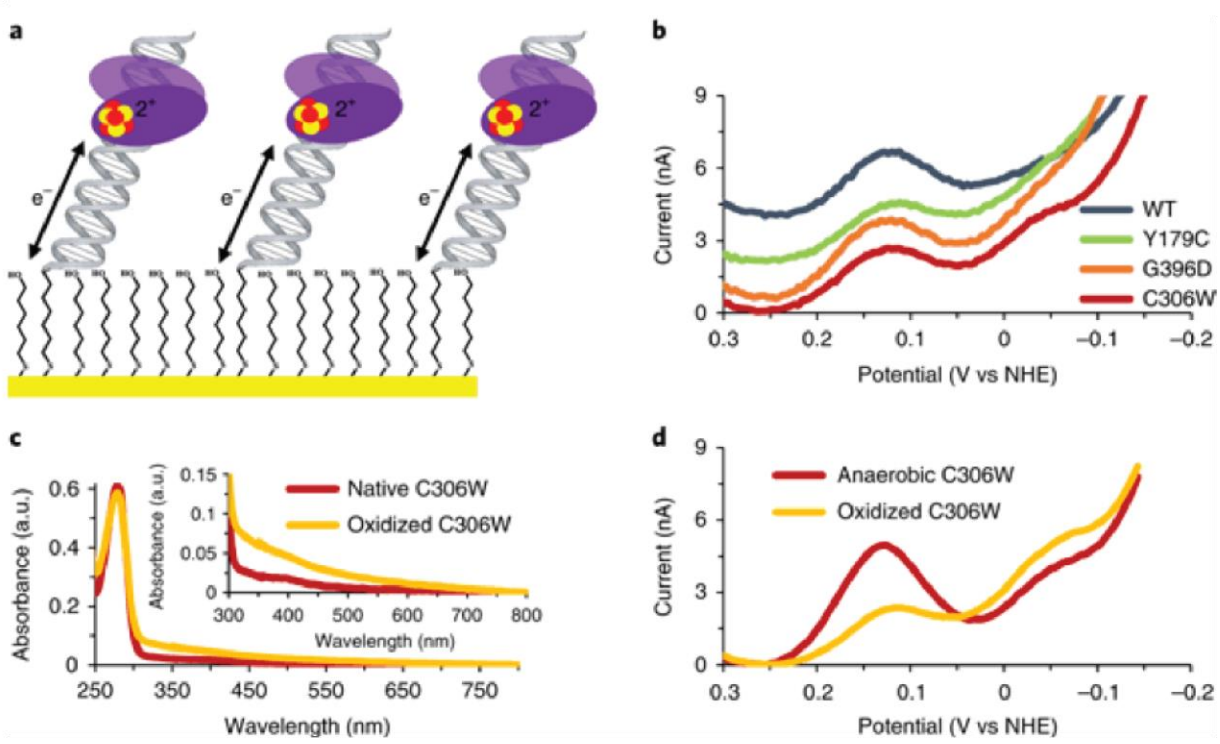

Figure 5.7. Initial electrochemical and spectroscopic characterization of MUTYH variants. **a**) Electrochemistry is carried out on DNA-modified gold electrodes, which allow controlled reduction or oxidation of the [4Fe4S] cluster. **b**) Incubation of 2–2.5 μM WT, Y179C, G396D or C306W MUTYH on a DNA-modified electrode in storage buffer (20 mM Tris, 100 mM NaCl, 1 mM dithiothreitol (DTT), 0.5 mM EDTA, 10% glycerol vol/vol, pH 7.4) resulted in a reversible signal with a midpoint potential of ~105 mV versus NHE. C306W uniquely exhibited an irreversible reductive peak around −50 mV versus NHE, which we presumed to be some form of oxidative degradation product. **c**) After aerobic oxidation by bulk electrolysis, the UV–vis spectrum of C306W showed no evidence of aggregation but did display a broad increase in absorption from 700 to 300 nm, suggestive of cluster oxidation. **d**) Consistent with cluster degradation in the presence of oxygen, aerobic bulk electrolysis of C306W enhanced the size of the irreversible peak relative to the reversible signal, while anaerobic incubation provided a protective effect. All square wave voltammetry (SQWV) measurements were obtained at a frequency of 15 Hz and 0.025 V amplitude, and the signals shown are an average from at least four separate electrodes on a multiplexed chip. The SQWV background current levels in **b**) were all comparable and have been adjusted for ease of visualization. Bulk electrolysis was performed for 1 h at 0.412 V versus NHE on a DNA-modified gold rod electrode in a glass cell.

In these experiments, MUTYH was incubated in storage buffer (20 mM Tris, pH 7.4, 100 mM NaCl, 1 mM DTT, 10% glycerol vol/vol) and periodically scanned by cyclic voltammetry (CV) and square wave voltammetry (SQWV). Aggregated protein preparations were treated with 20 mM β-mercaptoethanol and exchanged into storage buffer with fresh DTT immediately before electrochemical analysis. UV–vis spectroscopy confirmed that treated proteins were monomeric and contained intact [4Fe4S] clusters. Notably, cluster loading in monomeric WT MUTYH prepared from disassembled aggregates was significantly lower than expected (~15% as determined from the *A* :*A* ratio), but the low loading actually turned out to be advantageous for these experiments. Because apoproteins may bind some available DNA on the surface and thus decrease signal amplitude, the most important factor in making direct comparisons between different MUTYH proteins on an electrode is not absolute loading (although high levels are ideal) but that each variant is similarly loaded with a [4Fe4S] cluster. Fortunately, this turned out to be the case, with the MUTYH C306W samples also ~15% loaded as determined by UV–vis spectroscopy (**Figure 5.6**). To test multiple conditions simultaneously, DNA monolayers were prepared on multiplexed gold electrodes, which enabled up to four experiments to be conducted in parallel (*28*). In this case, half of the available quadrants consisted of unmodified well-matched (WM) DNA and half of substrate trap 2'-fluoro-2'-deoxyadenosine: 8- oxoguanine (FA:OG) DNA, which was included in an effort to enhance the signal amplitude by increasing the DNA binding affinity. In addition, both high-density (formed in the presence of 100 mM MgCl) and low-density monolayers were compared on a single chip. DNA surface density is an important parameter for protein experiments (*28*): high density films have more DNA on the surface (30–50 pmol/cm), which can improve DNA-mediated signalling by sterically hindering large proteins, while low-density films contain less DNA (15–20 pmol cm

), which can be more readily accessible to proteins (*29*,*30*). Overall, the effect of each type of film is likely to depend strongly on the particular protein being studied, and both have been used in previous studies (*28*). In the case of WT MUTYH at a concentration of ~2.5 μM [4Fe4S] cluster, a reversible redox signal with a midpoint potential of 106 ± 1 mV versus NHE was immediately apparent, and increased over the course of the experiment (**Figure 5.6**). The midpoint potential was similar to the 65–95 mV (versus NHE) range reported for other [4Fe4S] proteins bound to DNA, with the slightly higher potential of MUTYH most probably attributable to the distinct buffer conditions. Although the signals were relatively small, they were readily quantifiable: on low-density films containing WM DNA, CV peak areas were 31 ± 1 × 10 nC for the reductive peak and −33 ± 2 × 10 nC for the oxidative peak, while the equivalent values on high-density films were 25 ± 2 × 10 nC and −27 ± 3 × 10 nC, respectively. Interestingly, no significant differences in signal intensity were observed between WM and FA:OG DNA, with CV reductive and oxidative peak charges of 28 ± 1 × 10 nC and −34 ± 4 × 10 nC on low-density FA:OG DNA films and 24 ± 2 × 10 nC and −24 ± 1 × 10 nC on high-density films. The FA:OG substrate trap is known to increase the binding affinity of the very similar murine Mutyh on a 30-mer duplex by an order of magnitude (*25*), and the absence of any clear change in signal intensity suggests that our system is not sufficiently sensitive to detect this difference. Several possible explanations exist for this insensitivity. First, it may be that the absolute amount of accessible DNA on either surface is too low to detect a difference between WM and FA:OG substrates. Alternatively, the significant amount of apoprotein present may have blocked some of the accessible DNA from fully loaded protein. A further complicating factor may be the presence of DNA tethered to a surface rather than in solution, which might

lower the chances of protein encounter. Despite these potential limitations, we were able to definitively observe and quantify signals from DNA-bound MUTYH.

The signal from MUTYH C306W (also at the ~2.5 μM [4Fe4S] cluster) was comparable in both potential and maximum size to WT, although the signal size was considerably more variable between experiments. Although it was not clearly CT-deficient, as might have been expected, the C306W signal decreased in size at a steady rate after 1–2 h of incubation, consistent with the loss of iron seen by ICP-HRMS. In addition, the intensity of a second, irreversible peak centered around −50 mV versus NHE increased as the reversible [4Fe4S] signal decayed. This secondary peak was unprecedented among BER proteins on DNA-modified electrodes, but its growth in parallel with loss of the reversible signal suggested that it was some form of degradation product. Although all of the DNA-processing enzymes studied thus far have shown stabilization of the [4Fe4S] form on DNA binding to yield a reversible [4Fe4S] signal on an electrode, loss of iron by the oxidized [4Fe4S] species to form the [3Fe4S] cluster has been reported in bacterial MutY and EndoIII when the samples were frozen for EPR under aerobic conditions (*13*). As this is the first step in cluster degradation, we considered the [3Fe4S] cluster to be a likely candidate for the identity of this unexpected MUTYH C306W species. At approximately −50 mV versus NHE, the MUTYH C306W secondary peak fell within the range of reported [3Fe4S] cluster potentials (*32*), supporting assignment to this species. The irreversible nature of the signal was unusual, given that [3Fe4S] clusters can typically access a reversible 1 /0 redox couple, but, given the significant effect of even a single unit of cluster charge on DNA binding affinity (*14*), irreversibility could be explained as protein dissociation from DNA on reduction to the neutral [3Fe4S] cluster.

Confirming that the [4Fe4S] cluster degradation observed in MUTYH C306W was unique to this mutant, electrochemical analysis of DNA-bound Y179C and G396D (both 2.5 μM in storage buffer) yielded reversible signals at nearly the same potential as WT with no secondary peak present (**Table 5.3**). Like WT, the signals from both of these variants increased over time and remained stable for several hours (**Figure 5.6**). Notably, the Y179C signal was only about half as large as that for the WT, which is consistent with the reported lower binding affinity of this mutant relative to both WT and G396D (7.5 nM for Y179C versus 2.2 and 4.9 nM for WT and G396D, respectively) (*33*). Overall, however, both mutants were more similar to WT than C306W in their redox properties, which was unsurprising given that the cluster in these variants is unaltered. The propensity for the MUTYH C306W cluster to degrade by redox activity provides a possible explanation for the low DNA-binding affinity observed with BLI binding studies, as previous MutY studies have demonstrated that apoprotein lacking cluster remains structurally intact, but exhibits defective DNA binding (*12*).

Electrochemical characterization of MUTYH in HEPES buffer

To verify that the electrochemical properties of MUTYH were not altered in HEPES buffer, electrochemical analysis was performed with each variant as was done previously in Tris buffer (**Figure 5.8**). In HEPES buffer, WT MUTYH underwent a slight decrease in midpoint potential from 105 ± 1 mV vs NHE in Tris to 93 ± 1 mV vs NHE in HEPES (**Table 5.3**), but the overall signal shape and properties remained unaltered. Unsurprisingly, the addition of more concentrated protein to the electrode (~5 μM for all electrochemical experiments in HEPES) gave substantially larger signals, with WT MUTYH yielding a reductive peak area of 7.6 ± 3 nC and an oxidative peak area of -5.6 ± 3 nC on low density monolayers. Remarkably, although the protein was only about twice as concentrated compared with previous experiments, the signal

MUTYH variant	E_{mdpt} in Tris (mV)	E_{mdpt} in HEPES (mV)
WT	106 ± 1	93 ± 1
C306W	114 ± 3	97 ± 1
Y179C	105 ± 0.8	100 ± 2
G396D	115 ± 0.1	99 ± 4

Potentials are the average of at least three independent measurements, and error is s.d. of the mean.

Table 5.3 Midpoint potentials of MUTYH and mutants as measured by CV.

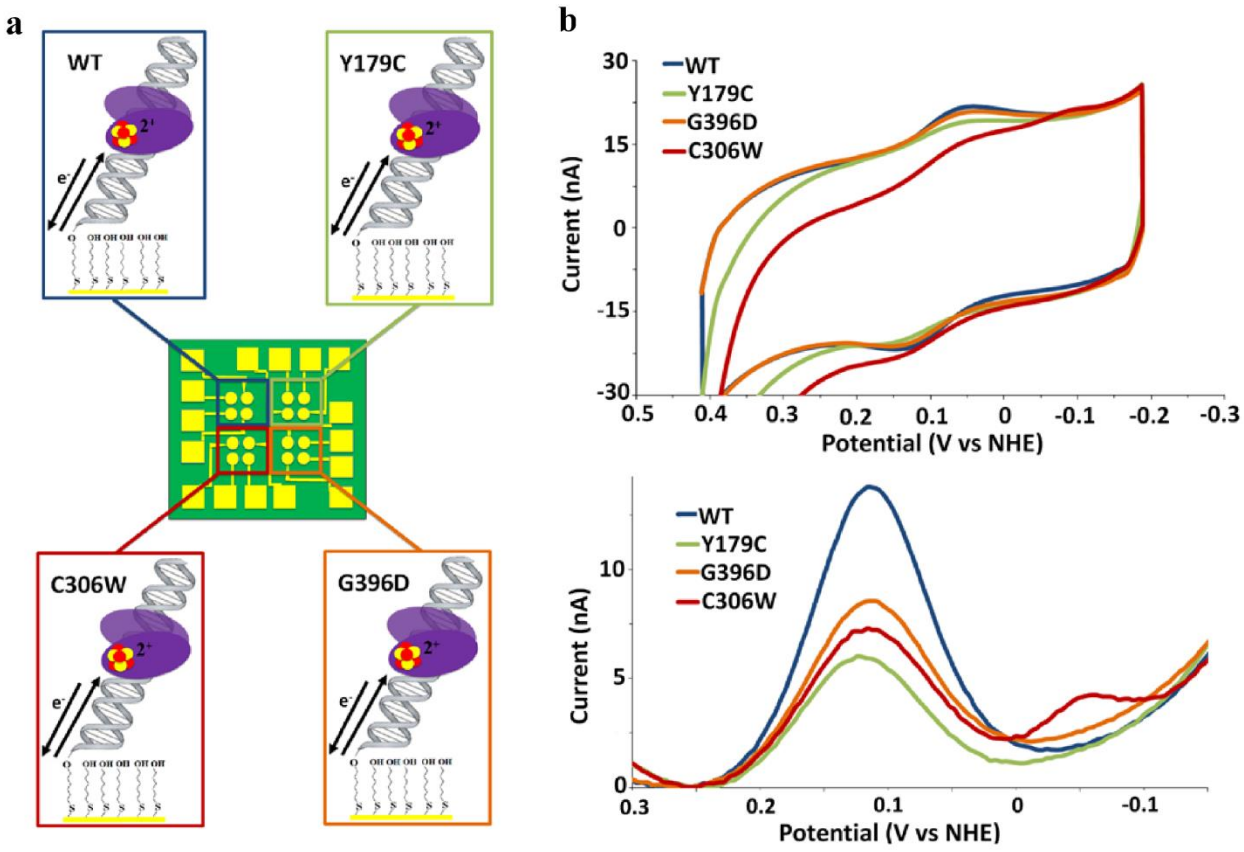

Figure 5.8. Electrochemical characterization of MUTYH variants in HEPES buffer. (**a**) Arrangement of MUTYH variants on a multiplexed chip. (**b**) CV (top) and SQWV (bottom) scans of 5 μM WT, Y179C, G396D, and C306W variants in HEPES storage buffer (30 mM HEPES, 100 mM KCl, 1 mM DTT, 0.5 mM EDTA, 10% glycerol v/v, pH 7.4). Under these conditions, substantial signals occur even by CV. The MUTYH C306W secondary peak is readily apparent in both CV and SQWV. CV scans were taken at a scan rate of 100 mV/s, while SQWV scans were taken at a frequency of 15 Hz with 0.025 V amplitude. All scans shown are an average obtained from at least seven separate electrodes.

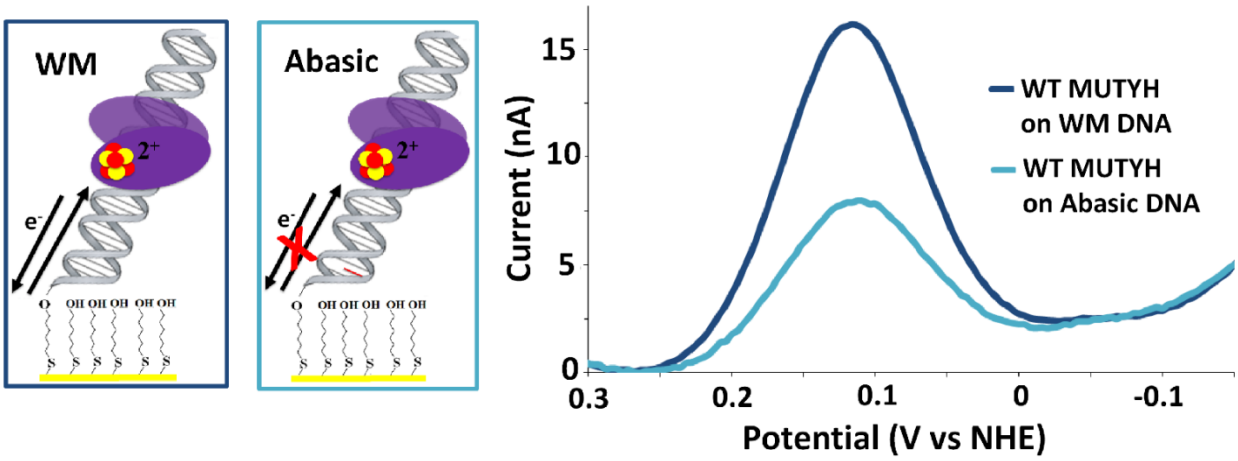

Figure 5.9. Abasic site discrimination by WT MUTYH. 5.0 μM WT MUTYH was incubated in HEPES buffer (30 mM HEPES, 100 mM KCl, 1 mM DTT, 0.5 mM EDTA, 10% glycerol v/v, pH 7.4) on a single multiplexed chip with half of the available quadrants containing DNA with an abasic site (light blue) near the electrode and the other half containing well matched (WM) DNA (dark blue). As is apparent from the SQWV voltammetry, the signal on WM DNA was comparable in size to previously observed signals (**Figure 5.6**), but the total peak area on abasic DNA was decreased by ~40%, indicating that the signal was DNA-mediated. The SQWV voltammograms were obtained at 15 Hz, and signal shown is the average of at least seven separate electrodes from two quadrants.

was over 10 times larger, indicating that some of this increase could be attributed to the distinct buffer conditions.

Like WT, all of the mutants showed ~10-fold larger signals when concentrated in HEPES, and their midpoint potentials decreased by a similar margin, placing all variants in the same potential window (**Table 5.3**). The signal from the MUTYH Y179C protein was still noticeably smaller than WT (reductive and oxidative peaks at 48 ± 18% and 33 ± 17% of WT), again most likely as a result of lower binding affinity of this mutant, while G396D was not significantly different from WT (reductive and oxidative peaks at 77 ± 32% and 76 ± 41% of WT). To ensure accurate comparison with EPR spectra, electrochemistry for the less stable C306W mutant was performed on the same day as EPR, and using the same sample stock. Consistent with the oxidation indicated in the UV-visible spectrum and the presence of a $[3Fe4S]^{+}$ cluster in the EPR spectra, the reversible signal in this sample was significantly smaller than any other mutant (reductive and oxidative peaks 35 ± 15% and 26 ± 14% of WT) and a very prominent secondary reductive peak was present centered at -88 ± 6 mV vs NHE (**Figure 5.8**). The larger signals made this peak much more readily quantifiable compared with Tris buffer, and the total charge of this irreversible peak was found to represent ~20% of either peak of the reversible $[4Fe4S]^{3+/2+}$ couple. The area in this case was lower than estimated for the C306W sample aerobically oxidized in Tris buffer, where the secondary peak was roughly equal in magnitude to the main peak, which suggested that the concentrated sample in HEPES was not 100% oxidized. Overall, UV-visible and EPR spectra obtained from the same MUYH C306W protein strongly supported the identification of the irreversible peak as a $[3Fe4S]^{+/0}$ redox couple. When compared to WT MUTYH, or even the Y179C and G396D mutants, the susceptibility of the C306W [4Fe4S] cluster to degradation upon oxidation during redox signaling was apparent,

and the irreversibility of the degradation product signal indicates that the resultant $[3Fe4S]^{+/0}$ species does not bind DNA effectively.

Based on the measured midpoint potentials in Tris buffer (**Table 5.3**), electrochemical signals from dilute MUTYH samples were most likely DNA-bound (*28*); however, the small signal sizes made it impossible to determine if the signal was DNA-mediated. The substantially larger signals recorded in HEPES buffer with concentrated samples allowed this issue to be addressed, and chips containing half well-matched DNA and half DNA containing an abasic site were prepared for this purpose. Earlier work with DNA-mediated EndoIII signals showed a dependence on monolayer morphology (*28*); thus, to see if this was also the case for MUTYH, the abasic site discrimination studies were carried out on both high and low density monolayers.

On abasic DNA, a maximum charge attenuation of 38% for the reductive peak and 46% for the oxidative peak was obtained on low density monolayers (**Figure 5.9**); in contrast, no appreciable discrimination was observed on high density monolayers. The observed abasic site discrimination confirmed that MUTYH can take part in DNA-mediated signaling, and the differences in high and low density DNA monolayers emphasize the importance of surface accessibility to large proteins. The sterically hindered high density films clearly do not provide sufficient access to DNA in an appropriate conformation to observe such a signal, and the peaks seen in this case are likely attributable to DNA-bound proteins signaling directly through the monolayer surface (*28*).

Interestingly, the pattern of abasic site discrimination observed here is opposite to previously published data for *E. coli* EndoIII (*28*); this difference can be rationalized by considering two important factors. First, the DNA used in the EndoIII experiments was only 15

bp, while EndoIII has a binding footprint of 12 bp. Thus, the protein would have taken up much of the available space and the cluster could readily bypass the mismatch on fully accessible low density DNA (*34*). In contrast, the DNA substrate chosen for MUTYH was 36 bp while the binding footprint is likely close to the 16 bp reported for mouse MUTYH (*35*), making bypass of the abasic site on low density monolayers less likely. Second, a considerable size discrepancy exists between the two proteins: unmodified MUTYH is 61 kDa, while EndoIII is only 24 kDa. Thus, steric hindrance in high density films would be expected to have a greater impact on MUTYH, a notion supported by the observation that the largest signals obtained on high density monolayers containing WM DNA were ~30% smaller than the equivalent signals on low density films.

Characterization of the C306W degradation product

In an effort to characterize the MUTYH C306W cluster degradation product more fully, we proceeded to assess its dependence on oxygen, which is often involved in [3Fe4S] cluster formation (*13*). Specifically, we employed electrochemical and UV–vis spectroscopic analysis to compare aerobically oxidized proteins with those maintained in an anaerobic environment. For an effective comparison, a single C306W sample was concentrated and one half of the sample was diluted to 2.5 μM in degassed buffer and placed on a chip containing low-density WM DNA in an anaerobic glove bag (95% N /5% H atmosphere), while the other half was maintained in aerobic conditions and oxidized on a DNA-modified gold rod electrode held at 0.412 V versus NHE. The anaerobic sample was scanned periodically by CV and SQWV, and, following electrolysis, the oxidized sample was transferred to the glove bag and added to a separate quadrant on the same chip. In addition to electrochemistry, UV–vis spectra were recorded before

and after electrolysis both to observe changes in the 410 nm peak and to ensure that the oxidized sample did not aggregate.

Quantification of the total charge passed during electrolysis indicated near-complete oxidation of the aerobic protein by ~60 min. Before electrolysis, the UV–vis spectrum showed the broad peak centred at 410 nm characteristic of a [4Fe4S] cluster, but, after oxidation, the absorbance increased over a broad range from 700 to 300 nm, with a poorly defined peak around 410 nm and a substantial shoulder between 400 and 300 nm (**Figure 5.6**). Such absorbance features are a general characteristic of cluster oxidation, although UV–vis spectra alone are insufficient to precisely identify the oxidized species generated (*36*). Importantly, the 280 nm peak remained sharp and distinct even after oxidation, and the spectrum was not elevated at 800 nm, demonstrating that the protein had not aggregated and confirming that all changes were due solely to cluster oxidation. This result stands in stark contrast to the soluble MUTYH aggregates observed in both WT and C306W in the absence of DTT, which were visibly cloudy with a U-shaped UV–vis spectrum characteristic of aggregation, highly elevated absorbance at 800 nm, no distinct [4Fe4S] peak, and a very slight 280 nm peak visible only as a shoulder (**Figure 5.6**). CV of the aerobically oxidized C306W MUTYH variant revealed an irreversible peak comparable in size to the main reversible peaks; in contrast, the equivalent peak in the anaerobic sample was much smaller than the main peak and had not changed from initial levels (**Figure 5.6**). Furthermore, the reversible signal of the anaerobic sample increased over time and exceeded even the strongest signals observed for aerobically incubated WT MUTYH, which was even more intriguing given that the anaerobic sample had been incubating on the electrode for several hours. Supporting greater instability of the C306W [4Fe4S] cluster, aerobic oxidation of WT

MUTYH gave low bulk electrolysis yields, and no readily apparent irreversible peak was present by CV. In addition, the UV–vis spectra of WT before and after oxidation were indistinguishable. Taken together, the apparent sensitivity of MUTYH C306W to oxidation and degradation in air along with the absence of any observable degradation in aerobically oxidized WT MUTYH supported the assignment of the secondary peak to a [3Fe4S] cluster, although these techniques alone could not verify this identity.

EPR spectroscopy of MUTYH

Having confirmed that the C306W degradation product was an oxidized species forming under aerobic conditions, we turned to EPR spectroscopy as a final step towards its definitive identification. EPR provides a means of distinguishing among different paramagnetic species and is commonly used to study Fe–S proteins (*32*,*36*,*37*). Although EPR analysis can be very informative, there were two general concerns with respect to MUTYH. First, EPR experiments are generally performed with significantly higher levels of concentrated protein than those used in our electrochemical experiments with MUTYH: signals have been reported for 10 μM *E. coli* EndoIII (*13*) and ~9 μM DNA polymerase δ (ref. (*38*)), but even these were still three to four times more concentrated than the MUTYH samples. Second, the low temperatures necessary to resolve signals from [4Fe4S] clusters (10–35 K) require the samples to be frozen before analysis,which can impact protein stability if the buffer pH changes with temperature, as is the case for the Tris buffers used in our MUTYH studies (*39*).

Therefore, before attempting EPR, all MUTYH variants were concentrated and exchanged into a HEPES buffer (20 mM HEPES, pH 7.4, 100 mM KCl, 1 mM DTT, 10% glycerol vol/vol, pH 7.4), and potassium was used in place of sodium as a further precaution to stabilize the pH at low temperature (*40*). UV–vis spectroscopy and electrochemistry (**Figure 5.8**)

were used to confirm protein stability in HEPES and to verify that the redox properties remained comparable. As observed in the UV–vis spectra (**Figure 5.10**), all MUTYH variants maintained their monomeric form in this buffer, although they could not be concentrated beyond 15 μM without forming soluble aggregates. When such aggregates did form, they were readily resolved by simple dilution, and the UV–vis spectra of WT MUTYH and mutants Y179C and G396D all retained a sharp 410 nm peak with ~15% cluster loading even after an additional freeze–thaw cycle one week after buffer exchange (**Figure 5.10**). In contrast, the spectrum of the MUTYH C306W protein closely resembled the aerobically oxidized sample described previously (**Figure 5.10**). Oxidation may have occurred over the extended aerobic buffer exchange process or during the freeze–thaw cycle on the day of EPR experiments. Because the extinction coefficient at 410 nm was unknown for the MUTYH C306W product, we estimated cluster loading in this mutant by comparing the magnitude of absorbance with the earlier aerobically oxidized sample, yielding a concentration comparable to the other variants.

All EPR spectra of MUTYH proteins were obtained with 15 μM WT and C306W and 5 μM G396D and Y179C (the latter mutants were not available in larger amounts). From the broadened UV–vis absorption, we predicted that the corresponding EPR spectrum would show evidence of either the [3Fe4S] cluster or a more advanced degradation product, while WT, Y179C and G396D were expected to be diamagnetic and thus EPR silent. Unexpectedly, all of the samples showed a small, broad signal with a shoulder at $g = 2.04$ (**Figure 5.10**) most likely attributable to oxidation during the aerobic freezing process, as reported previously for *E. coli* EndoIII and MutY. Nonetheless, MUTYH C306W protein displayed a much sharper signal with a clear peak centred at $g = 2.018$ (**Figure 5.10**), which is characteristic of [3Fe4S] clusters (*32*,*37*). Importantly, the C306W EPR signal, but not the broad signals of WT and the other

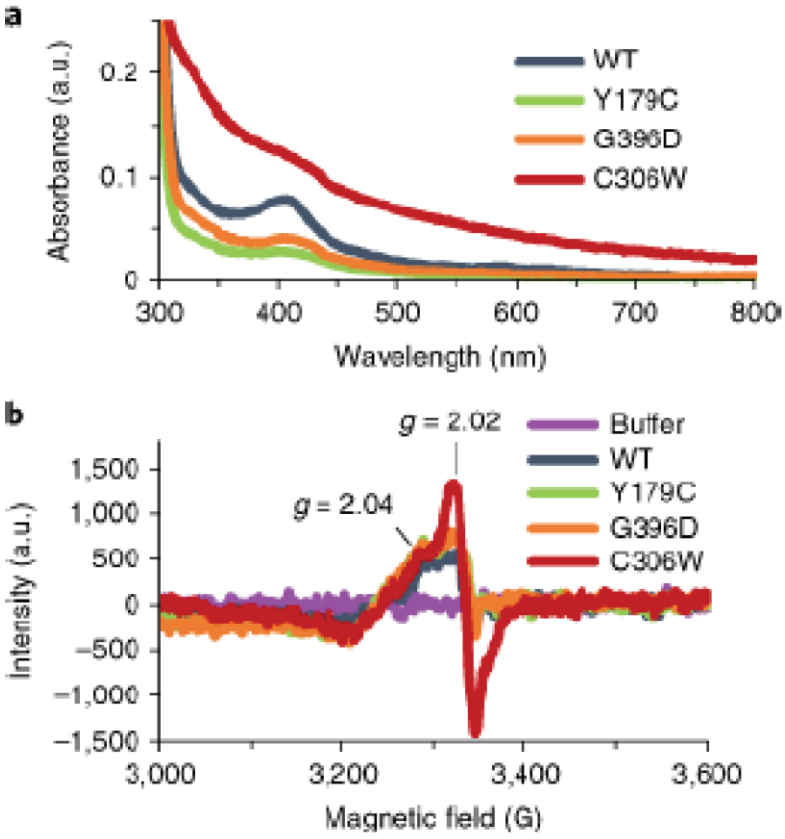

Figure 5.10. Characterization of MUTYH in HEPES and analysis of the C306W decay product. **a**) UV–vis spectra of concentrated WT, Y179C and G396D exchanged into HEPES buffer (20 mM HEPES, 100 mM KCl, 1 mM DTT, 0.5 mM EDTA, 10% glycerol vol/vol, pH 7.4) all displayed the characteristic [4Fe4S] cluster absorption band centred at 410 nm. In contrast, the C306W spectrum showed broadly increased absorbance associated with oxidation. **b**) EPR spectra of 15 μM (WT and C306W) or 5 μM (Y179C and G396D) MUTYH variants. The C306W EPR spectrum shows a sharp peak at $g = 2.018$ with a shoulder at $g = 2.04$, supporting identification of the degradation product as a [3Fe4S] cluster. Continuous-wave X-band EPR spectra were measured at 10 K with 12.88 mW microwave power, 2 G modulation amplitude, and 5.02 × 10 receiver gain.

MUTYH variants, closely resembled spectra from chemically oxidized *E. coli* EndoIII and MutY that were also assigned to the [3Fe4S] cluster (*13*). Although some of the C306W [4Fe4S] degradation may have occurred during sample freezing, the significantly larger and sharper EPR signal relative to the other variants, coupled with the UV–vis spectrum indicating previous oxidation, contradict this notion.

Discussion

In the present study we describe a novel MUTYH variant, C306W, and its association with the development of colonic polyposis and a family history of colon cancer. We determined that the C306W variant lacks DNA abscission activity and has decreased ability to bind target DNA, establishing the pathogenicity of this variant. In C306W MUTYH there is loss of a cysteine residue that ligates the MUTYH [4Fe4S] cluster. This finding raised the possibility that the loss of the cysteine might disrupt the integrity of the [4Fe4S] cluster and provide an explanation for the pathogenicity associated with MUTYH C306W. The observation by ICP-HRMS that the [4Fe4S] cluster of C306W exhibits significantly lower iron content further bolstered this hypothesis and prompted an electrochemical, mechanistic investigation of the MUTYH [4Fe4S] cluster and the effect of cysteine loss in the C306W variant.

Towards this end, we present direct evidence of redox signalling in eukaryotic MUTYH. DNA-modified electrochemical analysis revealed the redox potentials of all MUTYH variants studied to be in general agreement with earlier work (**Table 5.3**), with the potentials as measured in HEPES buffer almost identical to those obtained for *E. coli* MutY in phosphate buffer (*13*). The similarity of the WT MUTYH electrochemical signals to those of the *E. coli* protein strongly supports the notion that the primary function of the conserved [4Fe4S] cluster is redox activity in all organisms. Furthermore, the DNA-mediated nature of this signal in MUTYH suggests that a

process akin to the DNA-mediated redox-based damage search observed in bacteria may also be present and operating in humans.

Unlike WT MUTYH, the C306W mutant showed an unexpected, and irreversible, reduction between −50 and −100 mV versus NHE, in combination with loss of the reversible signal at ~100 mV versus NHE; EPR spectroscopy confirmed this additional signal to be the [3Fe4S] couple. The observed degradation and poor DNA binding in MUTYH C306W are consistent with the higher DNA binding affinity associated with increasing charge in [4Fe4S] clusters, in which coulombic effects cause the [4Fe4S] cluster to bind the DNA polyanion significantly more tightly than the [4Fe4S] [3Fe4S] and [3Fe4S] degradation products, with one and zero net charges, would bind much more weakly to DNA than the $[4Fe4S]^{2+}$ form, consistent with the irreversible reduction observed in degraded MUTYH C306W. Overall, our results suggest that, for MUTYH C306W, ordinary redox activity on DNA would lead to oxidation to the [4Fe4S] state, as is typical in these proteins, but the lower stability of the cluster would promote the loss of an iron atom and irreversible dissociation following a second redox signalling cycle. Ultimately, this process could result in the low iron content measured by ICP-HRMS, an effect that might well be exacerbated if the dissociated [3Fe4S] form degraded further when removed from the protective environment of DNA. Cluster degradation in MUTYH C306W is also consistent with the low levels of glycosylase activity and poor DNA binding affinity as measured by BLI (**Table 5.1**), which are attributes of bacterial MutY following cluster removal (*12*). This inherent instability of the C306W [4Fe4S] cluster and consequent loss of function we propose to be a source of pathogenicity in this MUTYH variant.

With regard to other potential sources of pathogenicity, we recognize that MUTYH is also regulated by post-translational modifications, including phosphorylation and ubiquitination,

that could be altered by this mutation (*41,42*). However, these sites are in different regions of the protein relative to the [4Fe4S] domain, and are thus unlikely to be affected by this particular mutation. Thus, redox-stimulated cluster degradation is most likely the primary cause of pathogenicity in MUTYH C306W.

The irreversible [3Fe4S] cluster signal seen in MUTYH C306W has not been observed previously in electrochemical studies of DNA-processing [4Fe4S] proteins, but the signal was within the same redox potential range reported for the [3Fe4S] couple of bacterial Ni–Fe hydrogenase and fumarate reductase enzymes(*43,44*). In *E. coli* MutY, [4Fe4S] cluster ligand substitution of the corresponding cysteine residue has been shown to be defective in DNA binding, similar to the situation with MUTYH C306W (*45*). We note, however, that none of the substitutions involving *E. coli* MutY occurred with a residue as bulky as tryptophan (*45*).

Given the results obtained for MUTYH C306W, it appears probable that mutations in other residues that alter the region around the [4Fe4S] cluster will be similarly deficient in their ability to mediate repair of oxidatively damaged DNA in vivo (*46-50*). Indeed, both germline and somatic alterations in other cysteines comprising the [4Fe4S] cluster and the four arginines that participate in hydrogen bonding to the cysteines coordinating the cluster (*51*) (**Table 5.4**) have been identified and are associated with colorectal as well as other cancers (*7*). It is probable that these mutations also result in instability, degradation and dysfunction of the [4Fe4S] cluster secondary to the same mechanisms detailed above. The effects of these lesions as well as the C306W variant underscore the importance of the [4Fe4S] cofactor in establishing competent MUTYH-mediated DNA repair.

The current study advances our basic electrochemical understanding of the redox chemistry, function and integrity of the [4Fe4S] cluster, as well as providing insight into the

Residue	Reported Variant
C290	C290W[55]
C297	not reported
C300	not reported
C306	C306W (this study)
R241	R241W[53,55] R241G [14]
R245	R245L [56] R245C [14] R245H [14,54]
R247	R247G [14]
R309	R309C [9,57]

Table 5.4. The four coordinating cysteines and surrounding arginines predicted or reported [14] to be associated with MAP.

pathologic sequelae resulting from disruption of the cluster. Specifically, we have documented and provided an explanation for a novel mechanism of colonic polyposis and cancer predisposition linked to electrochemical compromise of the MUTYH [4Fe4S] cluster. Future studies, we anticipate, will provide additional clarification of the central role of the [4Fe4S] cluster in MUTYH-mediated DNA repair and its underlying electrochemistry.

References

1. Markkanen, E., Dorn, J., Hubscher, U. MUTYH DNA glycosylase: the rationale for removing undamaged bases from the DNA. *Front. Genet.,* **2013**, *4*, 18.

2. Al-Tassan, N., et al. Inherited variants of MYH associated with somatic G:C→T:A mutations in colorectal tumors. *Nat. Genet,* **2002**, *30*, 227–232.

3. Sampson, J. R., et al. Autosomal recessive colorectal adenomatous polyposis due to inherited mutations of MYH. *Lancet,* **2003**, *362*, 39–41.

4. Sieber, O. M., et al. Multiple colorectal adenomas, classic adenomatous polyposis, and germ-line mutations in MYH. *N. Engl. J. Med,* **2003**,. *348*, 791–799.

5. Cleary, S. P., et al. Germline MutY human homologue mutations and colorectal cancer: a multisite case–control study. *Gastroenterology,* **2009**, *136*, 1251–1260.

6. Jones, N., et al. Increased colorectal cancer incidence in obligate carriers of heterozygous mutations in MUTYH. *Gastroenterology*, **2009**, *137*, 489–494.

7. Out, A. A. et al. Leiden Open Variation Database of the MUTYH gene. *Human Mutat,* **2010**,. *31*, 1205–1215.

8. Maio, N., Rouault, T. A. Iron–sulfur cluster biogenesis in mammalian cells: new insights into the molecular mechanisms of cluster delivery. *Biochim. Biophys. Acta,* **2015**, *1853*, 1493–1512.

9. Alseth, I., et al. The *Saccharomyces cerevisiae* homologues of endonuclease III from *Escherichia coli*, Ntg1 and Ntg2, are both required for efficient repair of spontaneous and induced oxidative DNA damage in yeast. *Mol. Cell Biol.,* **1999**, *19*, 3779–3787.

10. Trasvina-Arenas, C. H., Lopez-Castillo, L. M., Sanchez-Sandoval, E. & Brieba, L. G. Dispensability of the [4Fe-4S] cluster in novel homologues of adenine glycosylase MutY. *FEBS J.,* **2016**, *283*, 521–540.

11. Cunningham, R. P., et al. Endonuclease III is an iron–sulfur protein. *Biochemistry,* **1989**, *28*, 4450–4455.

12. Porello, S. L., Cannon, M. J., David, S. S. A substrate recognition role for the [4Fe-4S] cluster of the DNA repair glycosylase MutY. *Biochemistry*, **1998**, *37*, 6465–6475.

13. Boal, A. K., et al. DNA-bound redox activity of DNA repair glycosylases containing [4Fe-4S] clusters. *Biochemistry,* **2005**, *44*, 8397–8407.

14. Gorodetsky, A. A., Boal, A. K., Barton, J. K. Direct electrochemistry of endonuclease III in the presence and absence of DNA. *J. Am. Chem. Soc.*, **2006**, *128*, 12082–12083.

15. Arnold, A. R., Grodick, M. A., Barton, J. K. DNA charge transport: from chemical principles to the cell. *Cell Chem. Biol.*, **2016**, *23*, 183–197.

16. O'Brien, E., Silva, R. M. & Barton, J. K. Redox signaling through DNA. *Isr. J. Chem.*, **2016**, *56*, 705–723.

17. Yavin, E., et al. Protein–DNA charge transport: redox activation of a DNA repair protein by guanine radical. *Proc. Natl Acad. Sci. USA,* **2005**, *102*, 3546–3551.

18. Boal, A. K., et al. Redox signaling between DNA repair proteins for efficient lesion detection. *Proc. Natl Acad. Sci. USA*, **2009**, *106*, 15237–15242.

19. Miyoshi, Y., *et al.* Somatic mutations of the APC gene in colorectal tumors: mutation cluster region in the APC gene. *Hum Mol Genet.,* **1992**, *1*, 229-233.

20. Donnelly, M. I. *et al.* An expression vector tailored for large-scale, high-throughput purification of recombinant proteins. *Protein Expr Purif,* **2006**, *47*, 446-454, doi:S1046-5928(06)00014-3 [pii]10.1016/j.pep.2005.12.011.

21. Kapust, R. B., Waugh, D. S. Escherichia coli maltose-binding protein is uncommonly effective at promoting the solubility of polypeptides to which it is fused. *Protein Sci.,* **1999**, *8*, 1668-1674, doi:10.1110/ps.8.8.1668.

22. D'Agostino, V. G. *et al.* Functional analysis of MUTYH mutated proteins associated with familial adenomatous polyposis. *DNA Repair (Amst),* **2010**, *9*, 700-707, doi:10.1016/j.dnarep.2010.03.008S1568-7864(10)00103-5 [pii].

23. Whicher, J. R. *et al.* Cyanobacterial polyketide synthase docking domains: a tool for engineering natural product biosynthesis. *Chemistry & biology,* **2013**, *20*, 1340-1351, doi:10.1016/j.chembiol.2013.09.015S1074-5521(13)00356-6 [pii].

24. Kundu, S., Brinkmeyer, M. K., Livingston, A. L., David, S. S. Adenine removal activity and bacterial complementation with the human MutY homologue (MUTYH) and Y165C, G382D, P391L and Q324R variants associated with colorectal cancer. *DNA Repair (Amst),* **2009**, *8*, 1400-1410, doi:10.1016/j.dnarep.2009.09.009S1568-7864(09)00250-X [pii].

25. Porello, S. L., Leyes, A. E., David, S. S. Single-turnover and pre-steady-state kinetics of the reaction of the adenine glycosylase MutY with mismatch-containing DNA substrates. *Biochemistry,* **1998**, *37*, 14756-14764, doi:10.1021/bi981594+bi981594+ [pii].

26. Rich, R. L., Myszka, D. G. Higher-throughput, label-free, real-time molecular interaction analysis. *Anal Biochem,* **2007**, *361*, 1-6, doi:S0003-2697(06)00803-7 [pii] 10.1016/j.ab.2006.10.040.

27. Profrock, D., Prange, A. Inductively coupled plasma-mass spectrometry (ICP-MS) for quantitative analysis in environmental and life sciences: a review of challenges, solutions, and trends. *Appl Spectrosc.,* **2012**, *66*, 843-868, doi:10.1366/12-06681660817 [pii].

28. Pheeney, C. G., Arnold, A. R., Grodick, M. A., Barton, J. K. Multiplexed electrochemistry of DNA-bound metalloproteins. *J Am Chem Soc.*, **2013**, *135*, 11869-11878, doi:10.1021/ja4041779.

29. Boon, E. M., Salas, J. E., Barton, J. K. An electrical probe of protein-DNA interactions on DNA-modified surfaces. *Nat Biotechnol.,* **2002**, *20*, 282-286, doi:10.1038/nbt0302-282nbt0302-282 [pii].

30. Kelley, S. O., Barton, J. K., Jackson, N. M., Hill, M. G. Electrochemistry of methylene blue bound to a DNA-modified electrode. *Bioconjug Chem.,* **1997**, *8*, 31-37, doi:10.1021/bc960070obc960070o [pii].

31. Greeley, R. S., Smith, W. T., Stoughton, R. W., Lietzke, M. H. Electromotive Force Studies in Aqueous Solutions at Elevated Temperatures .1. The Standard Potential of the Silver-Silver Chloride Electrode. *J Phys Chem-Us,* **1960**, *64*, 652-657, doi:Doi 10.1021/J100834a031.

32. Johnson, M. K., Duderstadt, R. E., Duin, E. C. Biological and synthetic [Fe S] clusters. *Adv. Inorg. Chem.*, **1999**, *3 4 47*, 1–82.

33. D'Agostino, V. G., et al. Functional analysis of MUTYH mutated proteins associated with familial adenomatous polyposis. *DNA Repair,* **2010**, *9*,700–707.

34. O'Handley, S., Scholes, C. P., Cunningham, R. P. Endonuclease III interactions with DNA substrates. 1. Binding and footprinting studies with oligonucleotides containing a reduced apyrimidinic site. *Biochemistry,* **1995**, *34*, 2528-2536.

35. Pope, M. A., David, S. S. DNA damage recognition and repair by the murine MutY homologue. *DNA Repair (Amst),* **2005**, *4*, 91-102, doi:S1568-7864(04)00239-3 [pii]10.1016/j.dnarep.2004.08.004.

36. Sweeney, W. V. & Rabinowitz, J. C. Proteins containing 4Fe-4S clusters: an overview. *Annu. Rev. Biochem,* **1980**, *49*, 139–161.

37. Duff, J. L. C., Breton, J. L. J., Butt, J. N., Armstrong, F. A., Thomson, A. J. Novel redox chemistry of [3Fe-4S] clusters: Electrochemical characterization of the all-Fe(II) form of the [3Fe-4S] cluster generated reversibly in various proteins and its spectroscopic investigation in *Sulfolobus acidocaldarius* ferredoxin. *J. Am. Chem. Soc.,* **1996**, *118*, 8593–8603.

38. Netz, D. J. A., et al. Eukaryotic DNA polymerases require an iron–sulfur cluster for the formation of active complexes. *Nat. Chem. Biol.,* **2012***, 8*, 125–132.

39. Good, N. E., et al. Hydrogen ion buffers for biological research. *Biochemistry,* **1966**, *5*, 467.

40. Ugwu, S. O. The effect of buffers on protein conformational stability. *Pharm. Technol.,* **2004**, *28*, 86–108.

41. Kundu, S., Brinkmeyer, M. K., Eigenheer, R. A. Ser 524 is a phosphorylation site in MUTYH and Ser 524 mutations alter 8-oxoguanine (OG): a mismatch recognition. *DNA Repair,* **2010**, *9*, 1026–1037.

42. Dorn, J., Ferrari, E., Imhof, R., Ziegler, N., Hubscher, U. Regulation of human MutYH DNA glycosylase by the E3 ubiquitin ligase mule. *J. Biol. Chem.,* **2014**, *289*, 7049–7058.

43. Asso, M., Guigliarelli, B., Yagi, T., Bertrand, P. EPR and redox properties of *Desulfovibrio vulgaris* Miyazaki hydrogenase: comparison with the Ni–Fe enzyme from *Desulfovibrio gigas*. *Biochim Biophys. Acta,* **1992**, *1122*, 50–56.

44. Kowal, A. T., et al. Effect of cysteine to serine mutations on the properties of the [4Fe-4S] center in *Escherichia coli* fumarate reductase. *Biochemistry,* **1995**, *34*, 12284–12293.

45. Golinelli, M. P., Chmiel, N. H., David, S. S. Site-directed mutagenesis of the cysteine ligands to the [4Fe-4S] cluster of *Escherichia coli* MutY. *Biochemistry,* **1999**, *38*, 6997–7007.

46. Bai, H., et al. Functional characterization of two human MutY homolog (hMYH) missense mutations (R227W and V232F) that lie within the putative hMSH6 binding domain and are associated with hMYH polyposis. *Nucleic Acids Res.,* **2005**, *33*, 597–60.

47. Ali, M., et al. Characterization of mutant MUTYH proteins associated with familial colorectal cancer. *Gastroenterology,* **2008**, *135*, 499–507.

48. Bai, H., et al. Functional characterization of human MutY homolog (hMYH)

missense mutation (R231L) that is linked with hMYH-associated polyposis. *Cancer Lett.,* **2007**, *250*, 74–81.

49. Goto, M., et al. Adenine DNA glycosylase activity of 14 human MutY homolog (MUTYH) variant proteins found in patients with colorectal polyposis and cancer. *Human Mutat.,* **2010**, *31*, E1861–1874.

50. Fleischmann, C., et al. Comprehensive analysis of the contribution of germline MYH variation to early-onset colorectal cancer. *Int. J. Cancer,* **2004**, *109*, 554–558.

51. Luncsford, P. J., et al. A structural hinge in eukaryotic MutY homologues mediates catalytic activity and Rad9-Rad1-Hus1 checkpoint complex interactions. *J. Mol. Biol.,* **2010**, *403*, 351–370.

Chapter 6: Summary and Perspectives

DNA-mediated charge transport (DNA CT) is an interesting and effective means of regulating biological processes. This chemistry occurs over long molecular distances, in a manner that is rapid and sensitive to mismatches, oxidative lesions, and other perturbations that affect the base stacking interactions of the DNA duplex. (*1-3*) DNA CT moreover can be used by a number of enzymes for redox signaling through metal cofactors, primarily [4Fe4S] clusters. (*4-6*) DNA-processing, [4Fe4S] enzymes throughout all domains of life employ these metabolically expensive cofactors (*7*) for redox regulation of processes ranging from DNA repair to genome duplication.

The surprise discovery of [4Fe4S] clusters in DNA repair enzymes (*8*) initially prompted the hypothesis that these cofactors were a structural relic without a functional purpose. The isolated [4Fe4S] proteins were redox-inert, and there was not an obvious purpose for the cofactors to serve. DNA electrochemistry was used to show, however, that DNA-bound [4Fe4S] repair enzymes were able to convert between the $[4Fe4S]^{2+}$ and $[4Fe4S]^{3+}$ oxidation states. Binding of the polyanionic DNA substrate shifts the redox potential of the $[4Fe4S]^{3+/2+}$ couple approximately 200mV negative, stabilizing the $[4Fe4S]^{3+}$ form of the protein. This shift corresponds to an increase of 2-3 orders of magnitude in DNA binding affinity for the $[4Fe4S]^{3+}$ form, relative to the $[4Fe4S]^{2+}$ form. (*9-11*) The difference in binding affinity for the two redox states of the cluster allows for a redox-driven DNA binding switch that can affect rapid binding/dissociation of these proteins to their native substrate. This chemistry has been demonstrated to facilitate DNA-mediated redox signaling between [4Fe4S] repair enzymes *in vitro* and in cells. (*4-6*) Iteratively, DNA-mediated redox signaling leads to a redistribution of [4Fe4S] repair enzymes to damaged segments of the genome, coordinating the first steps of repair.

Though this redox role for the [4Fe4S] cluster was well-characterized in bacterial repair enzymes, it was not immediately obvious what role [4Fe4S] clusters were playing in the dozens of replication, transcription, and repair enzymes from bacteria to humans containing the cofactor. How does the redox-gated DNA binding switch affect other proteins with different enzymatic functions? How might this chemistry be coordinating complex and rapid processes in the crowded cellular environment?

In this work, we address the functional role of the [4Fe4S] cluster in eukaryotic DNA primase, the heterodimeric enzyme responsible for initiating replication on single-stranded genomic DNA, and in human MUTYH, the adenine glycosylase in the base excision repair pathway homolgous to previously characterized [4Fe4S] bacterial MutY. (*12*,*13*) Using DNA electrochemistry, biochemical studies, and X-ray crystallography, we show that the [4Fe4S] cluster in DNA primase serves as a redox switch governing DNA binding in the human (Ch. 2) and yeast (Ch. 4) systems. The redox switch reaction in primase is mediated by conserved tyrosine residues positioned between the [4Fe4S] cluster and the DNA binding interface. We show that the redox switch regulates initiation and truncation but not catalytic activity in human primase (Ch. 2, Ch. 3). The switch regulates DNA binding and signaling activity for both the [4Fe4S] domain of primase (p58C) (Ch. 2) and the full-length p48/p58 primase heterodimer (Ch.3). The redox switch in yeast primase, moreover, is essential for viability; a single-residue mutation to the redox pathway confers lethality in cells (Ch. 4). Human MUTYH, finally, participates in DNA-mediated redox signaling similarly to the bacterial MutY, and destabilized redox signaling for the DNA-bound protein results in a severe phenotype linked with hereditary colorectal cancer. (Ch. 5)

Investigation of the role of the cluster in human DNA primase began with electrochemical characterization of the primase [4Fe4S] domain, p58C. We show using DNA electrochemistry in anaerobic conditions that oxidized $[4Fe4S]^{3+}$ p58C is tightly bound to DNA and redox-active, whereas reduced $[4Fe4S]^{2+}$ p58C is loosely associated with DNA and redox-inert. This electrochemically reversible redox switch, moreover, is mediated by three conserved tyrosine residues in human p58C, Y309, Y345 and Y347. Single-atom mutations of these pathway residues result in decreased electrochemical activity but no change in DNA binding or structural properties. Engineering these mutations into full-length primase results in decreased initiation on single-stranded DNA but no change in catalytic activity. Truncation of primer synthesis, finally, is abrogated for the WT enzyme in the presence of a single-base mismatch in the nascent primer; truncation is gated by DNA CT. The redox activity of p58C suggests a role for the DNA binding switch in coordinating replication, possibly during primer handoff to the putative [4Fe4S] enzyme DNA polymerase α. Primase and polymerase α have similar measured DNA binding affinities, yet polymerase α must take the primer-template from primase at the appropriate point in replication, after RNA primer synthesis. This reversible redox-driven [4Fe4S] chemistry provides a potential explanation for the binding/dissociation/transfer steps that coordinate the first steps of replication.

We show using DNA electrochemistry that reversible cycling between the $[4Fe4S]^{2+}$ and $[4Fe4S]^{3+}$ redox states is important not only for p58C but for the full-length human DNA primase enzyme. When bound to both DNA and NTPs, necessary substrates for activity, primase undergoes reversible redox chemistry at a physiological potential similar to the DNA- and NTP-bound p58C. This potential, interestingly, shifts positive approximately 20mV in the presence of the single-atom redox pathway mutation Y309F in the full-length primase dimer.

The Y309F mutation is closer to the cluster than to the DNA-binding interface of the p58C domain, and this mutation abrogates initiation and truncation of primers *in vitro*. Though the redox pathway does not appear to be important for catalytic activity, binding of either DNA or NTPs before a reaction enhances catalytic activity *in vitro*. These results suggest that the redox switch driven by the cluster, along with a conformational change associated with primase substrate binding, work together to regulate the steps of primer synthesis during replication.

We next investigated whether the redox switch mechanism was conserved in different eukaryotic primases and of biological consequence. We electrochemically characterized the yeast p58C domain, which contains a cluster that, similarly to human p58C, acts as a switch regulating DNA binding and signaling activity. We found that mutation of conserved tyrosines Y395 and Y397 in yeast p58C decreased redox activity without affecting DNA binding or structure. These tyrosines are positioned differently than their human orthologues within the p58C protein, yet they perform the same chemistry. We finally assayed growth of yeast containing single atom Y395F and Y397F mutations, and single-residue Y395L and Y397L mutations in p58C. The single-atom Y395F mutants display some additional sensitivity to oxidative stress relative to WT cells, but the effects are small and difficult to consistently measure. The effect of the Y395L mutation in yeast primase is not yet clear, but the Y397L mutation is lethal in yeast. These results suggest that the redox switch in primase is conserved across several eukaryotic organisms and is important for cell viability.

A human analogue to the bacterial base excision repair pathway, which utilizes DNA-mediated redox signaling to search the genome for damage, is known to contain several DNA-binding [4Fe4S] enzymes. Homolgous proteins to the bacterial MutY and Endonuclease III, [4Fe4S] enzymes MUTYH and NTHL1 respectively, are part of this pathway for example.

(*13,14*) It was not previously clear whether these [4Fe4S] enzymes also participated in redox signaling on DNA. We show using DNA electrochemistry that human MUTYH participates in DNA-mediated redox signaling at essentially the same potential as bacterial [4Fe4S] repair proteins. We moreover demonstrate using DNA electrochemistry and Electron Paramagnetic Resonance (EPR) spectroscopy that the C306W variant of MUTYH, which is linked to MUTYH-associated polyposis (MAP), undergoes oxidative degradation of the [4Fe4S] cluster to the $[3Fe4S]^{+}$ form when participating in DNA-mediated redox signaling. This variant, which is deficient in DNA binding and glycosylase activity, could effectively load the [4Fe4S] cluster but does not retain the intact cofactor during the DNA CT-driven search for genomic damage. These results demonstrate that human base excision repair enzymes also participate in redox signaling that is consequential in maintaining genome integrity and preventing disease.

The work in this thesis has expanded the understanding of how [4Fe4S] clusters can function as redox switches to regulate DNA binding and redox signaling in the context of different pathways and enzymes. We are now learning of several new roles for these cofactors in DNA primase, and in other eukaryotic replication proteins. Redox switching driven by the [4Fe4S] cluster moreover helps regulate bacterial and human base excision repair. We look forward to exciting future discoveries which will further illuminate the role that DNA CT plays in coordinating activity in the crowded and dynamic nuclear environment.

References

1. Nunez, M.E., Hall, D.B., Barton, J.K. Long-range oxidative damage to DNA: effects of distance and sequence. *Chem. Biol. (Oxford, U. K.)*, **1999**, *6*, 85-97.

2. Kelley, S.O., Boon, E.M., Barton, J.K., Jackson, N.M., Hill, M.G. Single-base mismatch detection based on charge transduction through DNA. *Nuc. Acids Res.*, **1999**, *27*, 4830-4837.

3. Boal, A.K., Barton, J.K. Electrochemical Detection of Lesions in DNA. *Bioconj. Chem.*, **2005**, *16*, 312-321.

4. Boal, A.K., Genereux, J.C., Sontz, P.A., Gralnick, J.A., Newman, D.K., Barton, J.K. Redox signaling between DNA repair proteins for efficient lesion detection. *Proc. Natl. Acad. Sci. U. S. A.* **2009**, *106,* 15237-15242.

5. Sontz, P.A., Mui, T.P., Fuss, J.O., Tainer, J.A., Barton, J.K. DNA charge transport as a first step in coordinating the detection of lesions by repair proteins. *Proc. Natl. Acad. Sci. USA*, **2012**, *109*, 1856-1861.

6. Grodick, M.A., Segal, H.M., Zwang, T.J., Barton, J.K. DNA-Mediated Signaling by Proteins with 4Fe-4S Clusters Is Necessary for Genomic Integrity. *J. Amer. Chem. Soc.* **2014**, *136*, 16470-16478.

7**.** Rouault, T.A. Mammalian iron-sulphur proteins: novel insights into biogenesis and function. *Nat. Rev. Mol. Cell Biol.*, **2015**, *16*, 45-55.

8**.** Cunningham, R.P., Asahara, H., Bank, J.F., Scholes, C.P., Salerno, J.C., Surerus, K., Munck, E., McCracken, J., Peisach, J., Emptage, M.H. Endonuclease III is an iron-sulfur protein. *Biochemistry*, **1989**, *28*, 4450-4455.

9**.** Gorodetsky, A.A., Boal, A.K., Barton, J.K. Direct electrochemistry of Endonuclease III in the presence and absence of DNA. *J. Am. Chem. Soc.* **2006**, *128*, 12082-12083.

10. Tse, E.C.M., Zwang, T.J., Barton, J.K. The Oxidation State of [4Fe4S] Clusters Modulates the DNA-Binding Affinity of DNA Repair Proteins. *J. Am. Chem. Soc*., **2017**, *139*, 12784-12792.

11. Bartels, P.L., Zhou, A., Arnold, A.R., Nunez, N.N., Crespilho, F.N., David, S.S., Barton, J.K. Electrochemistry of the [4Fe4S] Cluster in Base Excision Repair Proteins: Tuning the Redox Potential with DNA. *Langmuir.*, **2017**, *33*, 2523-2530.

12. O'Brien, E., Holt, M.E., Thompson, M.K., Salay, L.E., Ehlinger, A.C., Chazin, W.J., Barton, J.K. The [4Fe4S] cluster of human DNA primase functions as a redox switch using DNA charge transport. *Science*, **2017**, *355*, eaag1789.

13. McDonnell, K.J.,* Chemler, J.A.,* Bartels, P.L.,* O'Brien, E., Marvin, M.L., Ortega, J., Stern, R.H., Raskin, L., Li, G., Sherman, D.H., Barton, J.K., Gruber, S.B. A Novel Human MUTYH Variant Causing Colonic Polyposis through Redox Degradation of the [4Fe4S]2+ Cluster. Nature Chemistry, **2018**, in press.

14. Bartels, P.L., O'Brien, E., Barton, J.K. DNA Signaling by Iron-Sulfur Cluster Proteins. *Iron-Sulfur Clusters in Chemistry and Biology (ed. T. Rouault, de Gruyter, Berlin/Boston)*, **2017**, *2*, 405-423.